High-Order Discontinuous Galerkin Method on Hexahedral Elements for Aeroacoustics

High-Order Discontinuous Galerkin Method on Hexahedral Elements for Aeroacoustics
H. Özdemir

HIGH-ORDER DISCONTINUOUS GALERKIN METHOD ON HEXAHEDRAL ELEMENTS FOR AEROACOUSTICS

PROEFSCHRIFT

ter verkrijging van
de graad van doctor aan de Universiteit Twente,
op gezag van de rector magnificus,
prof.dr. W.H.M. Zijm,
volgens besluit van het College voor Promoties
in het openbaar te verdedigen
op vrijdag 7 juli 2006 om 13:15 uur

door

Hüseyin Özdemir

geboren op 3 maart 1973
te Yıldızeli

Dit proefschrift is goedgekeurd door de promotoren:
prof.dr.ir. H.W.M. Hoeijmakers
prof.dr.ir. A. Hirschberg
en de assistent-promotor:
dr. ir. R. Hagmeijer

ışığım, hayat arkadaşım Belgin'e...
biricik kızım Duru'ya...

TABLE OF CONTENTS

INTRODUCTION

1.1   Acoustics and aeroacoustics

Acoustics is defined as the science of sound, its production, transmission and effects [6]. The most familiar acoustics phenomenon is that associated with the sensation of sound. For the average young person, a vibrational disturbance is interpreted as sound if its frequency lies in the range between about 20 to 20,000 Hz (1Hz = 1 hertz = 1 cycle/second). However, in a broader sense acoustics also includes the *ultrasonic* frequencies above 20,000 Hz and *infrasonic* frequencies below 20 Hz. Acoustics is distinguished from optics in that sound is a mechanical, rather than an electromagnetic, wave motion.

Sound is characterized by its intensity, expressed in decibels (dB). On the logarithmic decibel scale, an increase of 3 dB means that the intensity of noise has doubled. The human ear is able to distinguish a large range of noise intensity, from 1 dB to about 125 dB (threshold of pain).

The mathematical theory of sound propagation began with Isaac Newton (1643-1727), whose Principia (1686) included a mechanical interpretation of sound as being "pressure" pulses transmitted through neighboring fluid particles. Substantial progress towards the development of a viable theory of sound propagation, resting on a firmer mathematical and physical concepts, was made during the eighteenth century by Euler (1707-1783), Lagrange (1736-1813) and d'Alembert (1717-1783) [88]. In the nineteenth century the science of acoustics was developed thoroughly, Stokes and Rayleigh being the subject's greatest contributors.

In his two famous papers [73, 74] Lighthill (1927-1998) described the phenomenon of sound production by a turbulent flow, which marked the beginning of aeroacoustics. The analogy, that Lighthill derived, identifies aerodynamic sources of sound by representing the complex fluid mechanical process that acts as an acoustic source by an acoustical equivalent source term for the non-homogeneous wave equation. In this approach, the sound is generated by the deviation between the actual flow and a reference ideal acoustical field which is an extrapolation of the acoustical field at the position of listener. Lighthill's analogy is a very general definition that Hirschberg

[55] led to state "*aeroacoustics is the art of finding approximations which are optimal for the calculation of the sound produced by a flow*".

1.2   Computational Aeroacoustics

Sound generated by flow is a serious problem in many engineering applications. Most of the sounds of engineering interest cause human discomfort. The most notorious examples are flow noise by powerful machinery and jet engines. The tightening regulations of airport noise also make the area interesting from an engineering point of view. With advances in jet-noise reduction (e.g. by increasing the bypass ratio of turbofan engines), other components of overall noise have increased in significance namely, fan noise, airframe noise (including noise from flaps, slats and landing gear) especially during landing (at lower speeds). Other examples of flow-generated sound include the noise from wind turbines, fans in rotating machines and helicopter rotors, as well as automobile noise and noise from combustion instabilities and wind instruments.

In the light of the mentioned engineering problems the broad goal of Computational Aeroacostics (CAA) can be identified as to enable aeroacoustics predictions in these variety of flows and engineering devices and to advance our understanding of the sound generation process in general [37].

When these variety of flows are considered it is necessary to make some simplifications in order to attack a CAA problem. Classifying the problem according to the sound generation mechanism, is a first step. Problem types could be grouped as linear and nonlinear in general. Linear problems involve for example sound propagation in a uniform medium including reflecting/absorbing surfaces and the propagation of sound in a non-uniform medium. The non-uniformity also includes the state of the flow about which it is linearized which does not need to be uniform. In some cases small perturbations may lead to phenomena for which the linear approximation no longer holds. This includes problems of nonlinear wave propagation, scattering of nonlinear disturbances into sound, noise from turbulent boundary layers, flow separation and acoustically induced instabilities and resonances. Some examples of the nonlinear propagation problems involve nonlinear steepening of waves leading to the formation of shock waves, viscous effects at high sound intensities, sound propagation in multi-phase flows, thermo-acoustics, propagation of the sonic boom through atmospheric turbulence, etc. Airframe noise and rotorcraft noise are some examples of nonlinear scattering problems.

Computational techniques for sound generation problems can be classified depending on whether or not the sound is computed together with the flow field that includes the fluid dynamic sources of sound. In case the aim is to compute the unsteady flow and the sound together a direct computational approach is used. In this approach the

flow region including the source field and at least a part of the near-acoustic-field must be included. There are two direct computational approaches, the direct numerical simulation (DNS) and the large eddy simulation (LES). DNS resolves the dynamics of all flow scales of the turbulent flow including the small dissipative scales. LES resolves the range of the scales of the energy-containing eddies that are dynamically important flow scales and models the smaller scales and their effect on the resolved scales by a subgrid model. DNS directly provides the near-acoustic-field while LES gives the sound field associated with the dynamics that have been captured. By using different analytical and numerical techniques it is possible to extend the near-fields obtained by direct computation to the acoustical far-field. Numerical techniques involve solutions of simplified equations (such as linearized Euler equations, LEE) in extended domain around the near-field region. In the extended domain a mesh is used that is more appropriate for far-field sound propagation. If the wave equation is satisfied at the edge of the simulation, domain the Kirchoff integral can be used to solve the wave equation analytically. In any case the computational cost is large due to the need of sufficiently fine meshes covering a large computational domain.

An alternative to the direct computation is using a hybrid method in which the computation of the flow is decoupled from the computation of the sound field. The computation of the sound field is achieved by using an aeroacoustic theory or flow-field decomposition. It is assumed that there is no feedback from the sound field to the flow field, i.e. a one-way coupling is assumed. This assumption leads to a restriction of the flow types to flows at low fluctuating Mach numbers. In the hybrid method the space-time history of the flow field is calculated with methods like DNS, LES, unsteady Reynolds-averaged Navier-Stokes (RANS), and vortex methods, from which time-accurate turbulence data is also extracted. The sound sources are then calculated using the time-accurate turbulence data. As a last step the radiated sound field is predicted either by an acoustic analogy or by solving the LEE with the calculated sound sources included as the source terms within LEE. An alternative approach is to use a steady RANS instead of time-accurate flow simulation and calculate the acoustic source terms with a statistical model in order to reduce the high computational cost of the time-accurate flow simulation. For broader reviews on CAA the reader is referred to a number of review articles such as Colonius & Lele[38], Colonius[37], Kurbatskii & Mankbadi[69], Tam[103, 105], Wang et al.[112] and Wells & Renaut[113].

1.3 Objective and motivation

The objective of this thesis is to develop and verify a higher-order numerical method to compute the propagation of acoustic information in a three-dimensional domain which may involve complex geometries.

In most applications the acoustic amplitude is small compared to the mean pressure

level and the sound propagation can be studied by the use of the linearized equations describing the fluid motion. Although attenuation of sound waves increases with increasing frequency, the effect of viscosity on the propagation of sound can be neglected, as a first approximation, so that we can utilize the flow model based on LEE.

Computational methods for aeroacoustics require more accuracy than the usual second-order computational fluid dynamics methods. Although finite-difference methods could be used for higher-order accuracies, they need special treatments at the boundaries and usually require a smooth, structured mesh. This requirement is a problem when complex geometries are present within the computational domain.

In this thesis a quadrature-free implementation of the discontinuous Galerkin method, as developed by Atkins & Shu[8, 10], is used for the spatial discretization of the three-dimensional LEE. For the time integration a multi-stage low-storage Runge-Kutta scheme is employed.

The discontinuous Galerkin method has some remarkable advantages due to the flexibility in discretization of domains with complex geometries. The discontinuous Galerkin method is a highly compact formulation that perfectly suited for obtaining the high accuracy desired for computational aeroacoustics on non-smooth unstructured grids. The boundary conditions can be treated relatively simple, which is of importance in order to obtain uniform high order accuracy at the boundaries of complex geometries.

In the discontinuous Galerkin approximation the solution domain is divided into non-overlapping elements and the solution in each element is approximated via a local basis function set. Thus the governing equations are solved in a finite element space of discontinuous functions. The degree of the approximating polynomials (local basis function set) determines the order of accuracy of the method and, if desired, the degree of the polynomials used can be easily changed from element to element. In the present thesis the LEE are solved on a hexahedral mesh and the order of accuracy of the spatial discretization (degree of approximating polynomials) is arbitrary. The discontinuity between the elements can be treated by introducing the solution of the Riemann problem at the element interfaces.

Another advantage of the method is that it is highly parallelizable. The mass matrix can be inverted once and for all and in order to update the solution in each element only the elements sharing the same interface are involved, so the communication between the CPU-units of a parallel system can be kept to a minimum.

The developed numerical method is the third step of the so-called three-step method in order to predict the sound field due to an unsteady flow field. As explained above in the first step the flow field is computed either with a time-accurate computational method or a time averaged RANS method and in the second step the aeroacoustic sources are obtained from the results of the first step and used as sound sources input for the developed method for solving the LEE in the third step.

The present research builds on the earlier work of Blom[25] who developed a second-order method for solving the LEE on unstructured tetrahedral meshes employing the discontinuous Galerkin method.

1.4   Outline of the thesis

In chapter 2 the equations of motion and the equation of state are described and the dimensionless form of the equations is presented. Furthermore the approximations that lead to the Euler equations are given and finally the linearization process is described that results in the linearized Euler equations (LEE).

In chapter 3 the discontinuous Galerkin finite-element formulation used for the spatial discretization is presented for an arbitrary order of accuracy in terms of the truncation error. Furthermore the evaluation of integrals involving products of the basis functions are described. Also the treatment of boundary and initial conditions is given. Finally the multi-stage low-storage Runge-Kutta time discretization method is described.

Verification is always the first goal in developing a numerical algorithm. Convection of a one-dimensional Gaussian pulse, chosen as a verification problem, is discussed in chapter 4. The analytical solution of the problem is presented in two alternative routes and the numerical results are compared with the analytical solution. Chapter 4 also includes studies on the numerical dispersion and the CPU-time requirements of the method.

In chapter 5 the problem of acoustic radiation from a vibrating wall segment inside an infinite rectangular duct is considered. The relation between the wall motion and the normal velocity profile used as a linearized boundary condition for the vibrating wall segment is explained in some detail. The numerical solution that is obtained for a hexahedral mesh, which is used throughout this thesis is compared to the results obtained by Blom[25, 26] using a similar method for a tetrahedral mesh. Comparison between the numerical result and the analytical solution is also presented. Furthermore a grid convergence (h-refinement) and a p-refinement study is reported on.

Effects of non-parallelepiped elements, i.e. of grid distortion is investigated in chapter 6, considering two cases. In the first case the grid is skewed at a certain angle while keeping the shape of the elements as parallelepiped and in the second case the grid is randomly distorted, violating the present restriction of the implementation of the method to cases for which the transformation of the elements in the physical space to the unit element in computational space is linear. This implies that the present mapping is exact for parallelepiped elements but approximate for more elements of a more general shape.

In chapter 7 the discontinuous Galerkin method is applied to an acoustic liner

problem. Here we consider a single orifice in a plate inside a long duct. The results are compared to the analytical solution obtained by Kooijman et al.[64].

Finally in chapter 8 concluding remarks and recommendations for future research are presented .

LINEARIZED EULER EQUATIONS

2.1 Introduction

In general, flows can be described by means of the equations of motion, describing transport of e.g. mass, momentum and energy. This also holds for the acoustic problems. However, (aero-)acoustic problems considered in this thesis concerned with the sound propagation in air where the viscosity does not play a significant role (as described in section 2.4). Under this assumption the equations of motion, loosely called the Navier-Stokes equations (formally only the momentum equation is named after Navier (1785-1836) and Stokes (1819-1903)), reduces to the Euler equations.

In most application the acoustic amplitude is very small relative to the mean pressure ([42, 75, 95]) and the sound propagation can be studied by the use of the linearized approximation of the equations describing the fluid motion.

The equations of motion and the equations of state are described in section 2.2 and the dimensionless form of equations of motion are presented in section 2.3. The Euler equations and the linearization process is shown in sections 2.4 and 2.5 respectively.

2.2 Conservation Laws and Constitutive Equations

In continuum fluid dynamics, the equations governing physical quantities such as velocity, density, pressure and temperature, will be considered to vary continuously from point to point throughout the fluid. We assume that we can define a "fluid particle" which we can assign these macroscopic properties that we associate with the fluid in bulk. In addition the fluid particle is assumed to be large compared to molecular scales but small compared to the global length scales. We then can describe the fluid motion by using the laws of mass, momentum and energy conservation applied to an elementary fluid particle.

Employing index notation and Cartesian coordinates, we have for the mass conservation in differential form

$$\frac{\partial \rho}{\partial t} + \frac{\partial}{\partial x_i}(\rho u_i) = S_m, \tag{2.1}$$

where ρ is the fluid density, $\mathbf{u}_i$ is the flow velocity and S_m is the mass source term. In general the mass source term, $S_m = 0$, however, some processes like the action of a pulsating sphere or of mass injection are represented by the mass source term S_m.

The momentum conservation law is

$$\frac{\partial}{\partial t}(\rho u_i) + \frac{\partial}{\partial x_j}(P_{ij} + \rho u_j u_i) = S_i, \quad i = 1, 2, 3, \tag{2.2}$$

where, S_i is an external force density and P_{ij} is

$$P_{ij} = p\delta_{ij} - \tau_{ij}, \tag{2.3}$$

with p pressure, δ_{ij} is the Kronecker* delta and τ_{ij} is the viscous stress tensor. When the relation between τ_{ij} and the deformation rate of the fluid element is linear the fluid is described as Newtonian and the resulting momentum conservation equation Eq. (2.2) is referred to as the Navier-Stokes equation. Employing Stokes' hypothesis, that the fluid is in local thermodynamic equilibrium, so that the pressure p and the thermodynamic pressure are equivalent, which leads to the viscous stress tensor of the form

$$\tau_{ij} = \mu \left(\frac{\partial u_i}{\partial x_j} + \frac{\partial u_j}{\partial x_i} \right) - \frac{2}{3}\mu \left(\frac{\partial u_k}{\partial x_k} \right) \delta_{ij}, \tag{2.4}$$

where, μ is the dynamic viscosity and depends on temperature and pressure. μ is assumed constant throughout this study.

The energy conservation law is given by

$$\frac{\partial \rho E}{\partial t} + \frac{\partial}{\partial x_j}(\rho H u_j - \tau_{ij} u_i + q_j) = S_e, \tag{2.5}$$

where, the internal energy, e, is related to the total energy, E, and total enthalpy, H, by:

$$E \equiv e + \frac{1}{2}u_k u_k, \tag{2.6}$$

and

$$H \equiv E + \frac{p}{\rho}. \tag{2.7}$$

---

*$\delta_{ij} = 1$ if $i = j$, $\delta_{ij} = 0$ if $i \neq j$.

In Eq. (2.5), q_j is the heat flux due to heat conduction and is for example defined by Fourier's law as

$$q_j = -\kappa \frac{\partial T}{\partial x_j},$$ (2.8)

where κ is the heat conductivity coefficient which depends on pressure.

We will assume air to behave as a calorically perfect gas, i.e. the following relations are valid:

$$p = \rho R T,$$ (2.9)

$$e = c_v T,$$ (2.10)

where R is the specific gas constant, with $R = c_p - c_v$ and c_p and c_v are the specific heats at constant pressure and volume, respectively.

2.3   Navier-Stokes Equations in Dimensionless Form

The Navier-Stokes equations can be written in dimensionless form by introducing scaling parameters for length, mass, time and temperature. Here we choose as reference quantities: length L, density ρ_0, velocity U and temperature T_0. This analysis results in the following set of dimensionless equations:

$$\frac{\partial \bar{\rho}}{\partial \bar{t}} + \frac{\partial}{\partial \bar{x}_j}(\bar{\rho}\bar{u}_j) = \bar{S}_m,$$ (2.11)

$$\frac{\partial(\bar{\rho}\bar{u}_i)}{\partial \bar{t}} + \frac{\partial}{\partial \bar{x}_j}(\bar{\rho}\bar{u}_j\bar{u}_i + \bar{p}\delta_{ij} - \bar{\tau}_{ij}) = \bar{S}_i, \quad i = 1,2,3,$$ (2.12)

$$\frac{\partial(\bar{\rho}\bar{E})}{\partial \bar{t}} + \frac{\partial}{\partial \bar{x}_j}(\bar{\rho}\bar{H}\bar{u}_j - \bar{\tau}_{ij}\bar{u}_i + \bar{q}_j) = \bar{S}_e,$$ (2.13)

with, the dimensionless source terms:

$$\bar{S}_m = \frac{S_m L}{\rho_0 U}, \quad \bar{S}_i = \frac{S_i L}{\rho_0 U^2}, \quad \bar{S}_e = \frac{S_e L}{\rho_0 U^3}.$$ (2.14)

The dimensionless viscous stress term is written as

$$\bar{\tau}_{ij} = \bar{\mu}\left(\frac{\partial \bar{u}_i}{\partial \bar{x}_j} + \frac{\partial \bar{u}_j}{\partial \bar{x}_i} - \frac{2}{3}\frac{\partial \bar{u}_k}{\partial \bar{x}_k}\delta_{ij}\right),$$ (2.15)

with,

$$\bar{\mu} = \frac{\mu}{\rho_0 U L} \equiv \frac{1}{Re_L},$$ (2.16)

and the heat flux

$$\bar{q}_j = -\bar{\kappa}\frac{\partial \bar{T}}{\partial \bar{x}_j}, \tag{2.17}$$

with,

$$\bar{\kappa} = \frac{\kappa T_0}{\rho_0 U^3 L}. \tag{2.18}$$

Upon identifying λ as a characteristic length scale and λf as a characteristic velocity scale, $\bar{\mu}^{-1}$ can be interpreted as an *acoustic Reynolds number* Re_λ:

$$Re_\lambda = \frac{\rho_0(\lambda f)\lambda}{\mu} = \frac{\rho_0 \lambda^2 f}{\mu} = \frac{\lambda^2 f}{\nu}, \tag{2.19}$$

where,

$$\lambda \equiv \frac{\sqrt{c_v T_0}}{f}, \tag{2.20}$$

and $\lambda f = \sqrt{c_v T_0}$ represents a characteristic velocity scale with f, the frequency of an acoustic wave. By these scaling factors $\bar{\kappa}$ can be rewritten in the following form

$$\bar{\kappa} = \frac{\mu}{\rho_0 \lambda^2 f}\frac{\kappa T_0}{\mu}\frac{1}{\lambda^2 f^2}. \tag{2.21}$$

$\bar{\kappa}$ can be rearranged to get

$$\bar{\kappa} = \frac{1}{Re_\lambda}\frac{\gamma}{Pr}, \tag{2.22}$$

where, the Prandtl number is defined as

$$Pr = \frac{\mu c_p}{\kappa}, \tag{2.23}$$

and the ratio of the specific heats, γ:

$$\gamma = \frac{c_p}{c_v}. \tag{2.24}$$

2.4   Euler Equations

In a sound field the pressure represents a far greater stress field than that induced by viscosity at frequencies of most practical interest. The ratio of the two stresses is the Reynolds number which is given in Eq. (2.19). For air $\nu = 1.5 \cdot 10^{-5}\,m^2/s$ so that for $f = 1\,kHz$ we have $Re_\lambda = 4 \cdot 10^7$ so sound has to travel $\lambda = 10^7$ wave

lengths or more for the viscosity to play a significant role. Schreier [97] has analyzed the effect of viscosity on a small pressure wave propagating into a medium at rest in 1D and concluded that in air, at any rate, the viscosity has very little effect on the velocity at which the sound wave propagates. In practice the kinematic viscosity appears to be a rather unimportant effect in the attenuation of waves in free space. Therefore, neglecting the viscosity effects results in the Euler equations of the form:

$$\frac{\partial \bar{\rho}}{\partial \bar{t}} + \frac{\partial}{\partial \bar{x}_j}(\bar{\rho}\bar{u}_j) = \bar{S}_m, \tag{2.25}$$

$$\frac{\partial(\bar{\rho}\bar{u}_i)}{\partial \bar{t}} + \frac{\partial}{\partial \bar{x}_j}(\bar{\rho}\bar{u}_j\bar{u}_i + \bar{p}\delta_{ij}) = \bar{S}_i, \quad i = 1, 2, 3, \tag{2.26}$$

$$\frac{\partial(\bar{\rho}\bar{E})}{\partial \bar{t}} + \frac{\partial}{\partial \bar{x}_j}(\bar{\rho}\bar{H}\bar{u}_j) = \bar{S}_e, \tag{2.27}$$

2.5   Linearization of the Euler Equations

A sound wave disturbs the fluid from its mean state while it propagates. When we consider the state of the fluid at rest with a uniform pressure p_0 and density ρ_0 the sound wave perturbs the pressure by $p_0 + p'(\mathbf{x}, t)$ and the density by $\rho_0 + \rho'(\mathbf{x}, t)$. The ratios $|p'/p_0|$ and $|\rho'/\rho_0|$ are much less than unity so the disturbances are small.

Although always weak, the range of amplitudes commonly experienced in sound waves is very great, e.g. typical audible sound power level for human hear range from $10^{-12}\,W$ to about $10^5\,W$ [42, 95]. Because of this very wide range of levels it is customary to describe sound powers through the use of logarithmic scales known as *sound levels*. The Sound Power Level (PWL) is given in decibels (dB) by:

$$PWL = 10\,log_{10}\,(P/P_{ref}). \tag{2.28}$$

with P the Power in W and $P_{ref} = 10^{-12}W$. The Sound Pressure Level (SPL) is a measure of the mean square level of the acoustic fluctuation and is defined as

$$SPL = 20\,log_{10}\,\left(\frac{|p'|}{p_{ref}}\right), \tag{2.29}$$

where, the reference pressure $p_{ref} = 2 \times 10^{-5}\,N/m^2$. When the pressure fluctuations are equal in magnitude to the mean pressure, $|p'| = p_0 \equiv 1\,atmosphere$ ($= 10^5\,N/m^2$) the sound pressure level is equivalent to $194\,dB$. The threshold of pain is between $130\,dB$ and $140\,dB$ [42, 75, 95] corresponding to a pressure variation of amplitude around $|p'|/p_0 = 10^{-3}$.

As can be seen from these examples in most applications the acoustic amplitude is very small relative to the mean pressure p_0 ($|p'|/p_0 \ll 1$), and the sound propagation can be studied by the use of the linearized approximation of the equations describing the fluid motion.

The Euler equations can be written in terms of primitive variables in index notation as follows:

$$\frac{\partial \rho}{\partial t} + u_j \frac{\partial \rho}{\partial x_j} + \rho \frac{\partial u_j}{\partial x_j} = S_m, \tag{2.30}$$

$$\frac{\partial u_i}{\partial t} + u_j \frac{\partial u_i}{\partial x_j} + \frac{1}{\rho} \frac{\partial p}{\partial x_i} = \frac{1}{\rho}(S_i - u_i S_m), \quad i = 1, 2, 3, \tag{2.31}$$

$$\frac{\partial p}{\partial t} + u_j \frac{\partial p}{\partial x_j} + \gamma p \frac{\partial u_j}{\partial x_j} = (\gamma - 1)\left\{ S_e - u_i S_i + \frac{1}{2} u_i u_i S_m \right\}. \tag{2.32}$$

The Euler equations can be linearized assuming the aeroacoustic perturbations (ρ', u_i', p') to be small compared to the mean flow properties (ρ_0, u_{i0}, p_0). As an example, assuming ρ_0 to be of the order $\mathcal{O}(1)$, it can be written that $|\rho'| = |\rho_0|\mathcal{O}(\varepsilon)$, with $\varepsilon \ll 1$. In order to linearize the Euler equations the following expressions will be used:

$$\begin{aligned} \rho &= \rho_0 + \rho', & u_i &= u_{i0} + u_i', \\ p &= p_0 + p', & \mathcal{S} &= \mathcal{S}_0 + \mathcal{S}'. \end{aligned} \tag{2.33}$$

It will also be assumed that the mean flow quantities satisfy the Euler equations and the terms higher than order $\mathcal{O}(\varepsilon)$ can be neglected.

Substituting (2.33) into Eq. (2.30) and linearizing gives for the continuity equation:

$$\mathcal{O}(1) \quad : \quad \frac{\partial \rho_0}{\partial t} + u_{j0} \frac{\partial \rho_0}{\partial x_j} + \rho_0 \frac{\partial u_{j0}}{\partial x_j} = S_{m_0},$$

$$\mathcal{O}(\varepsilon) \quad : \quad \frac{\partial \rho'}{\partial t} + u_j' \frac{\partial \rho_0}{\partial x_j} + u_{j0} \frac{\partial \rho'}{\partial x_j} + \rho' \frac{\partial u_{j0}}{\partial x_j} + \rho_0 \frac{\partial u_j'}{\partial x_j} = S_m'. \tag{2.34}$$

The momentum equation can be written in linearized form as:

$$\mathcal{O}(1) \quad : \quad \frac{\partial u_{i0}}{\partial t} + u_{j0} \frac{\partial u_{i0}}{\partial x_j} + \frac{1}{\rho_0} \frac{\partial p_0}{\partial x_i} = \frac{1}{\rho_0}(S_{i0} - u_{i0} S_{m_0}),$$

$$\begin{aligned} \mathcal{O}(\varepsilon) \quad : \quad & \frac{\partial u_i'}{\partial t} + u_j' \frac{\partial u_{i0}}{\partial t} + u_{j0} \frac{\partial u_i'}{\partial t} + \frac{1}{\rho_0} \frac{\partial p'}{\partial x_i} - \frac{\rho'}{\rho_0} \frac{\partial p_0}{\partial x_i} \\ & = \frac{1}{\rho_0}(u_{i0} S_{m0}' + u_i' S_{m0}) + \frac{\rho'}{\rho_0^2}(u_{i0} S_{m_0} - u_{i0} S_{i0}) \end{aligned} \tag{2.35}$$

Finally the energy equation in linearized form is

$$
\mathcal{O}(1) \quad : \quad \frac{\partial p_0}{\partial t} + u_{j0}\frac{\partial p_0}{\partial x_i} + \gamma p_0 \frac{\partial u_{j0}}{\partial x_j} = (\gamma - 1)(S_{e0} - u_{i0}S_{i0} + \frac{1}{2}u_{i0}u_{i0}S_{m_0}),
$$

$$
\mathcal{O}(\varepsilon) \quad : \quad \frac{\partial p'}{\partial t} + u'_j\frac{\partial p_0}{\partial x_i} + u_{j0}\frac{\partial p'}{\partial x_i} + \gamma p_0 \frac{\partial u'_j}{\partial x_j} + \gamma p'\frac{\partial u_{j0}}{\partial x_j}
$$

$$
= (\gamma - 1)(S'_e - u_{i0}S'_i - u'_iS_{i0}
$$

$$
+ \frac{1}{2}(u_{i0}u_{i0}S'_m + u_{i0}u'_iS_{m0} + u'_iu_{i0}S_{mo})). \quad (2.36)
$$

In this thesis the mean flow will be assumed to be uniform (or piecewise constant in discrete form) so that the derivatives of the mean flow properties are zero. Under this assumption combining Eq.(2.34, 2.35 and 2.36) the three-dimensional linearized Euler equations can be written as:

$$
L(\mathbf{u}) = \frac{\partial \mathbf{u}}{\partial t} + \frac{\partial \mathbf{f}_i(\mathbf{u})}{\partial x_i} = \mathbf{s}, \quad \mathbf{u}(\vec{x}, t) \in \mathbb{R}^5, \quad \vec{x} \in \Omega, t \in I_t. \quad (2.37)
$$

The solution vector $\mathbf{u} = (\rho', u'_1, u'_2, u'_3, p')$ where ρ', u'_1, u'_2, u'_3, and p' denote the aeroacoustic density, velocities and pressure perturbations, respectively and $\mathbf{s}$ ($\in \mathbb{R}^5$) is the source term for the LEE. The perturbation $\mathbf{u}$ can be described with respect to the mean flow $\mathbf{u}_0$ where,

$$
\mathbf{f}_i(\mathbf{u}) = A_i(\mathbf{u}_0)\mathbf{u}, \quad A_i \in \mathbb{R}^5 \times \mathbb{R}^5. \quad (2.38)
$$

The matrices $A_i = (A_1, A_2, A_3)^T$ are defined as:

$$
A_i(\mathbf{u}_0) = \begin{bmatrix} u_{0i} & \delta_{i1}\rho_0 & \delta_{i2}\rho_0 & \delta_{i3}\rho_0 & 0 \\ 0 & u_{0i} & 0 & 0 & \delta_{1i}/\rho_0 \\ 0 & 0 & u_{0i} & 0 & \delta_{2i}/\rho_0 \\ 0 & 0 & 0 & u_{0i} & \delta_{3i}/\rho_0 \\ 0 & \delta_{i1}\gamma p_0 & \delta_{i2}\gamma p_0 & \delta_{i3}\gamma p_0 & u_{0i} \end{bmatrix}, \quad i = 1, 2, 3, \quad (2.39)
$$

ρ_0, u_{01}, u_{02}, u_{03} and p_0 are the mean flow density, velocities and pressure, respectively.

Here, the linearization has been performed starting from the Euler equations in primitive variables form. It is also possible to linearize the Euler equations in different forms. For further details the reader is referred to the PhD thesis by Blom [25] where such a detailed analysis has been performed. Blom discussed the linearization of the Euler equations starting from conservation form for conservative variables, quasi-linear form for conservative variables and for primitive variables. Furthermore

he derived three different formulations for linearizing the Euler equations in conservation form for conservative variables.

DISCONTINUOUS GALERKIN FORMULATION

3.1 Introduction

Compared to computational fluid dynamics the accuracy of numerical methods for aeroacoustics require special attention in the sense that numerical dispersion and dissipation errors are much more critical. Although finite-difference methods could be used to achieve higher-order accuracy, they need special treatments at the boundaries and usually require smooth, structured meshes. Especially when the problem of interest involves complex geometries this requirement cannot be met. The Discontinuous Galerkin (DG) method [8, 30, 62] has some remarkable advantages with respect to flexibility in discretization of domains with complex geometries.

The DG method is a highly compact finite-element projection method. The solution within an element is reconstructed by looking at the element itself and the communication is achieved only with the direct neighbors through the approximate Riemann flux. The size of the stencil is fixed and independent of the desired order of accuracy.

The method is better suited than the finite-difference methods to handle complicated geometries. Moreover, the treatment of the boundary conditions is relatively simple (no special treatment required), and obtaining uniform high-order accuracy at the boundaries involving complex geometries is feasible. The method can be easily applied to both structured and unstructured meshes.

The DG method provides a practical framework for the development of a higher-order method desired for computational aeroacoustics on non-smooth unstructured grids [9, 24, 59, 82, 83, 84, 85]. The high-order accuracy can be obtained by employing high-degree of approximating polynomials within an element. The degree of the approximating polynomials can be easily changed from one element to the other. The local grid refinement (*h*-refinement) and the local-degree-variation (*p*-refinement) (Flaherty et al. [46], van der Vegt & van der Ven [109] and Süli et al. [100]) can be applied.

The discontinuity in the elements leads to a block diagonal matrix and since the size of the blocks is equal to the number of degrees of freedom inside the element considered the block can be inverted easily once and for all. This simple handling of

the mass matrix makes the method highly parallelizable.

Although the original DG method introduced by Reed and Hill [91] in 1973, the method has increasingly become popular since the beginning of 1990s. Reed and Hill applied the method in the framework of transport of neutrons. In 1974 LeSaint and Raviart [72] made the first analysis of the DG method and proved its rate of convergence to be at least h^p for general triangulations and h^{p+1} for Cartesian grids employing basis polynomials up to order p, where h is a length scale that represents the size of elements. In 1986, Johnson and Pitkäranta [62] proved a rate of convergence of at least $h^{p+\frac{1}{2}}$ for general triangulations and in 1988 Richter [93] obtained the optimal rate of convergence of h^{p+1} for a semi-uniform triangulation. In 1991 Peterson [87] numerically confirmed that this rate of convergence cannot be improved within the class of quasi-uniform meshes.

All the above mentioned studies are confined to linear equations. The first analysis of the DG method as applied to a non-linear scalar hyperbolic equation is due to Chavent and Cockburn [29]. Cockburn et al. [31] extended their analysis to a one-dimensional system of conservation laws, and Cockburn et al. [32] further extended it to the multidimensional scalar case, and in 1998 Cockburn and Shu [34] treated the multidimensional systems. In 1998 Atkins and Shu [10] performed the first quadrature-free implementation of the DG method and showed that this formulation requires less storage and computational time.

Biswas, Devine and Flaherty [20] and Adjerid, Affia and Flaherty [3] showed super-convergence of the method on Gauss-Radau points. Lowrie [77] also reported numerical results of order h^{2p+1} convergence. Recently, Cockburn et al. showed the possibility of obtaining a rate of convergence of h^{2p+1} by a suitable post processing of the numerical solution.

Concerning the issue of wave propagation of the DG method there have been relatively fewer works. Johnson & Pitkäranta [62] performed a Fourier analysis of the DG method for the case of $p = 1$. Lowrie [78] performed a Fourier analysis of a space-time discontinuous Galerkin scheme for a one-dimensional scalar advection equation up to $p = 3$. In [59], Hu, Hussaini and Rasetarinera studied numerical dissipation and dispertion errors of the DG method for one- and two-dimensional wave equations. In a recent work by Rasetarinera, Hussaini and Hu [90], it was further demonstrated numerically that dissipation errors of the DG method decay at order h^{2p+2} (locally) when the exact characteristic splitting formula is used. Sherwin [98] has carried out a Fourier analysis which gave exact expression of the numerical frequency analytically up to $p = 3$ and numerically for $p = 10$.

In Hagmeijer et al. [50], the governing characteristic polynomial is identified for any order p for the semi-discrete algorithm obtained from applying the DG method to the one-dimensional scalar advection equation, where the exact formulation of the Riemann problem at element interfaces is used. Blom [25] has extended this work

employing Lax-Friedrichs flux at element interfaces rather than the exact solution of the Riemann problem. Blom showed that as long as the basis function span the same approximate solution space, the characteristic polynomial is identical regardless of the kind of polynomial basis used.

There are also some examples of the DG method applied to CFD problems. Halt and Agarwal [51] applied the method of moments which is similar to the DG method, to the steady two-dimensional Euler equations for subsonic flows. Bassi and Rebay first applied the DG method to two-dimensional Euler equations in transonic flows ([15]) and than extended to the Navier-Stokes equations ([16]). The DG method applied to three-dimensional Euler equations by van der Vegt [107]. Later, van der Vegt and van der Venn [108, 109] applied the space-time discontinuous Galerkin method for the solution of the Euler equations in time-dependent flow domains.

In section 3.2 the discontinuous Galerkin space discetization of the linearized Euler equations is presented. In section 3.3 and section 3.4 the treatment of boundary conditions and initial condition are presented respectively. Finally the multi-stage low-storage Runge-Kutta time integration algorithm is described in section 3.5.

3.2 Discontinuous Galerkin Discretization

We would like to discretise the Linearized Euler Equations (LEE) (Eq. 2.37) in space, employing the Discontinuous Galerkin (DG) method in a region Ω. We consider a solution $\mathbf{u}(\cdot, t)$ such that for each time $t \in I_t$, $\mathbf{u}(\cdot, t)$ belongs to the function space U of the form

$$\mathbf{u}(\cdot, t) \in U^5, \quad U \equiv L^2(\Omega), \tag{3.1}$$

where $L^2(\Omega)$ denotes a Hilbert space of all square integrable functions on Ω with an associated inner product defined by ([65]):

$$(f, g)_\Omega \equiv \int_\Omega f(\mathbf{x}) g(\mathbf{x}) d\Omega, \qquad f, g \in L^2(\Omega). \tag{3.2}$$

The weak formulation of the LEE can now be written as ([27])

$$(L(\mathbf{u}(\cdot, t)), \mathbf{v}) = (\mathbf{s}, \mathbf{v}), \quad \forall \mathbf{v} \in U^5. \tag{3.3}$$

In order to discretise the LEE we divide the solution domain Ω into non-overlapping hexahedral elements Ω_j such that

$$\bar{\Omega} = \bigcup_{j=1}^{N_e} \bar{\Omega}_j, \tag{3.4}$$

where $\overline{\Omega}_j = \Omega_j \cup \partial\Omega_j$ is the closure of Ω_j and the boundary $\partial\Omega_j$ belongs to at most two elements and N_e denotes the number of elements. We consider an approximate solution $\mathbf{u}_h(\cdot, t)$ to the solution $\mathbf{u}(\cdot, t)$ in the following form

$$\mathbf{u}_h(\cdot, t) \in U_h^5, \quad U_h = span\{b_{jk}\} \subset U, \tag{3.5}$$

where U_h is a finite-dimensional subspace of U. The functions $\{b_{jk}\}$ are linearly independent basis functions defined such that

$$b_{jk} \equiv \begin{cases} \overline{b}_{jk}(\mathbf{x}), & \mathbf{x} \notin \partial\Omega_j, \\ 0, & \mathbf{x} \in \partial\Omega_j. \end{cases} \tag{3.6}$$

$$\overline{b}_{jk}(\mathbf{x}) = 0, \quad \mathbf{x} \notin \overline{\Omega}_j, \tag{3.7}$$

The functions $\overline{b}_{jk}$ and b_{jk} differ only in that $b_{jk} = 0$ on the boundary $\partial\Omega_j$ while in general $\overline{b}_{jk} \neq 0$ on the boundary $\partial\Omega_j$. The basis functions are continuous in Ω_j and $k = 0, 1, .., M$ is the index of the polynomials where the upper limit is defined as;

$$M(p, d) = \frac{1}{d!} \prod_{l=1}^{d} (p + l), \tag{3.8}$$

with d the number of space dimensions and p the highest degree of the polynomials used, with j fixed. We consider the approximate solution $\mathbf{u}_h(\cdot, t)$, in Ω_j, of the solution $\mathbf{u}(\cdot, t)$ as an expansion on to the basis set $\{b_{jk}\}$

$$\mathbf{u}_h(\mathbf{x}, t) = \mathbf{u}_{jk}(t) b_{jk}(\mathbf{x}), \quad \mathbf{u}_{jk}(t) \in L^2(I_t), \quad b_{jk} \in L^2(\Omega), \tag{3.9}$$

where, $\mathbf{u}_{jk}$ are the solution expansion coefficients or the degrees of freedom for the solution on Ω_j and functions of time only in this semi-discrete approach.

It is noted that we employ the Einstein summation convention throughout this thesis, except for the index "j". Hence in Eq. (3.9) summation over k is implied, while there is no summation over j.

We approximate the weak formulation (Eq. (3.3)) by replacing the solution $\mathbf{u}(\cdot, t)$ with the approximate solution $\mathbf{u}_h(\cdot, t)$

$$(L(\mathbf{u}_h(\cdot, t)), \mathbf{v}_h) = (\mathbf{s}, \mathbf{v}_h), \quad \forall \mathbf{v}_h \in U_h^5. \tag{3.10}$$

Since Eq. (3.10) holds for *any* function $\mathbf{v}_h \in U_h^5$ we can replace $\mathbf{v}_h$ by $b_{jm} \in U_h^5$ to get

$$(L(\mathbf{u}_h(\cdot, t)), b_{jm}) = (\mathbf{s}, b_{jm}), \quad \forall j \in (1, 2, .., N_e), \quad \forall m \in (0, 1, .., M). \tag{3.11}$$

Inserting Eq. (3.11) into Eq. (2.37) and integrating over Ω leads to

$$\int_\Omega L(\mathbf{u}_h(\mathbf{x},t))b_{jm}d\Omega = \int_\Omega \mathbf{s}b_{jm}d\Omega, \tag{3.12}$$

Integration by parts we get:

$$\int_{\Omega_j} \frac{\partial \mathbf{u}_{jk}}{\partial t}b_{jk}b_{jm}d\Omega - \int_{\Omega_j} \mathbf{f}_i \frac{\partial b_{jm}}{\partial x_i}d\Omega + \int_{\Omega_j} \frac{\partial}{\partial x_i}(\mathbf{f}_i b_{jm}) = \int_{\Omega_j} \mathbf{s}b_{jm}d\Omega, \tag{3.13}$$

and applying Gauss' theorem to the third term gives,

$$\int_{\Omega_j} \frac{\partial \mathbf{u}_{jk}}{\partial t}b_{jk}b_{jm}d\Omega - \int_{\Omega_j} \mathbf{f}_i \frac{\partial b_{jm}}{\partial x_i}d\Omega + \int_{\partial\Omega_j} b_{jm}\mathbf{f}_i n_{ji}dS = \int_{\Omega_j} \mathbf{s}b_{jm}d\Omega. \tag{3.14}$$

where n_{ji} denotes i^{th} component of the unit outward normal vector on $\partial\Omega_j$. For each j, Eq. (3.14) contains only the unknowns $\mathbf{u}_{jk}(t)$, $k = 0, .., M$, giving rise to N_e sets of $(M+1)$ ordinary differential equations for the functions $\mathbf{u}_{jk}(t)$. The coupling of the functions $\mathbf{u}_{jk}(t)$ in neighboring elements is achieved by replacing the (normal component of the) flux $\mathbf{f}_i$ in the surface integral term by a numerical flux

$$\mathbf{f}_i(\mathbf{u}_j)n_{ji}|_{\mathbf{x}\in\partial\Omega_{jl}} = \mathbf{h}(\bar{\mathbf{u}}_j, \bar{\mathbf{u}}_l, \mathbf{n}_j) \tag{3.15}$$

where $\bar{\mathbf{u}}_j(\mathbf{x},t) \equiv u_{jk}(t)\bar{b}_{jk}(\mathbf{x})$ and $l \in I_j$ with

$$\begin{aligned} j &\notin I_j \\ l &\in I_j \Leftrightarrow \partial\Omega_j \cap \partial\Omega_l \neq \emptyset, \quad j \neq l, \end{aligned} \tag{3.16}$$

where, $I_j = \{r_1, r_2, r_3, r_4, r_5, r_6\}$ is the set of global indices, describing the direct neighborhood elements Ω_{r_l} and/or the domain boundary which coincides with the element boundary $\partial\Omega_{r_l}$ of element Ω_j. The common edges are denoted by $\partial\Omega_{jl} = \partial\Omega_j \cap \partial\Omega_l$, $l \in I_j$. The set I_j has six elements. When one or more edges of the hexahedra Ω_j belongs to the domain boundary $\partial\Omega$, the global index in the set I_j then refers to the boundary index. With Eq. (3.9) and Eq.(3.15), Eq. (3.14) is recast as:

$$\int_{\Omega_j} \frac{\partial \mathbf{u}_{jk}}{\partial t}b_{jk}b_{jm}d\Omega - \int_{\Omega_j} \mathbf{f}_i \frac{\partial b_{jm}}{\partial x_i}d\Omega + \int_{\partial\Omega_j} b_{jm}\mathbf{h}dS = \int_{\Omega_j} \mathbf{s}b_{jm}d\Omega, \quad \forall m, j. \tag{3.17}$$

LeSaint and Raviart [72] made the first analysis of the Discontinuous Galerkin method and proved its rate of convergence to be at least h^p for general triangulations

and h^{p+1} for Cartesian grids employing basis polynomials up to order p, where h is a length scale that represents the size of elements. Later, Johnson and Pitkäranta [62] proved a rate of convergence of at least $h^{p+\frac{1}{2}}$ for general triangulations and Peterson [87] numerically confirmed that this rate of convergence cannot be improved within the class of quasi-uniform meshes. Richter [93] obtained the optimal rate of convergence of h^{p+1} for a semi-uniform triangulation. Hence, when the method is applied to a hexahedral mesh, the analysis of LeSaint and Raviart indicates that the method is $(p+1)^{th}$-order accurate.

3.2.1 Numerical flux

At any interface between two elements, since the solution is allowed to be discontinuous, there is a left state and a right state leading to a Riemann problem which is represented by the flux vector as shown in Eq. (3.15). Solving the Riemann problem will provide the coupling and handle the discontinuity at element interfaces. Various kinds of flux formulas have been proposed and used in the literature to approximate the solution of the Riemann problem. In this study we will consider two commonly used flux formulas: the *characteristics-based* flux formula and the *Lax-Friedrich* flux formula.

The numerical flux $h(\cdot, \cdot, \cdot)$ is assumed to be Lipschitz continuous[§] and consistent with $\mathbf{f}_i n_{ji}$, that is,

$$\mathbf{h}(\mathbf{u}, \mathbf{u}, \mathbf{n}_j) = \mathbf{f}_i(\mathbf{u})n_{ji}, \quad \forall \mathbf{u}, \tag{3.19}$$

and conservative, that is,

$$\mathbf{h}(\bar{\mathbf{u}}_j, \bar{\mathbf{u}}_l, \mathbf{n}_j) = -\mathbf{h}(\bar{\mathbf{u}}_l, \bar{\mathbf{u}}_j, -\mathbf{n}_j). \tag{3.20}$$

The *characteristics-based* flux formula is of the form

$$\mathbf{h}(\bar{\mathbf{u}}_j, \bar{\mathbf{u}}_l, \mathbf{n}_j) = \frac{1}{2}\{f(\bar{\mathbf{u}}_j) + f(\bar{\mathbf{u}}_l) - \theta\mathbf{A}^n(\bar{\mathbf{u}}_l - \bar{\mathbf{u}}_j)\}, \quad \theta \geq 0, \tag{3.21}$$

where θ is a scalar parameter and $\mathbf{A}^n$ is the normal component of the matrix $\mathbf{A}$. Choosing $\theta = 1$ leads to an *exact characteristics splitting* (the exact Roe solver) where, on the other hand, choosing $\theta = 0$ will result in a symmetric averaged scheme.

[§]If $(X, ||\cdot||)$ is a metric space, a function $W : X \to \mathbb{R}$ is said to be Lipschitz continuous, or Lipschitzian, if for some $M \in \mathbb{R}$,

$$|W(x) - W(x')| \leq M\|x - x'\|, \tag{3.18}$$

$\forall x, x' \in X$. M is said to be a Lipschitz constant for W. It is noted that this condition is stronger than the more usual continuity condition.

The *Lax-Friedrich* flux formula is of the form

$$\mathbf{h}(\bar{\mathbf{u}}_j, \bar{\mathbf{u}}_l, \mathbf{n}_j) = \frac{1}{2}\{f(\bar{\mathbf{u}}_j) + f(\bar{\mathbf{u}}_l) - \theta|a|_{max}(\bar{\mathbf{u}}_l - \bar{\mathbf{u}}_j)\}, \quad \theta \geq 0, \qquad (3.22)$$

where, $|a|_{max}$ is the maximum (absolute value) of the eigenvalues of the (5×5) matrix $\mathbf{A}^n$.

The boundary integral term in Eq. (3.17) can be evaluated numerically by applying numerical quadrature formulas of the required order [36]. However, application of quadrature rules is costly [10]. Atkins and Shu [8, 10] introduced the quadrature-free implementation where the fluxes and source terms are expanded onto the basis functions as follows:

$$\mathbf{f}_i(\mathbf{u}(\mathbf{x}, t)) \approx (\mathbf{f}_i)_h = \sum_{j=1}^{N_e}(\mathbf{f}_i)_{jk}b_{jk}, \qquad (3.23)$$

$$\mathbf{s}(\mathbf{x}, t) \approx \mathbf{s}_h = \sum_{j=1}^{N_e}\mathbf{s}_{jk}b_{jk}, \qquad (3.24)$$

with $k = 0, 1, .., \bar{M}$, where the number of terms in the expansion, $\bar{M}$, depends on the form of the nonlinearity in $\mathbf{f}_i$. When the flux (and or the source) term are linear functions of $\mathbf{u}$, the expansion is trivial and exact and $\bar{M} = M(p, d)$ where M is given in Eq. (3.8). When the flux is non-linear or linear with non-constant coefficients, the flux can be expanded in a Taylor series, can be defined in terms of the projection operator or alternatively the projection method can be used to determine the flux expansion directly. The details of these approaches can be found in [8] and [10]. In the non-linear case the degree of the flux expansion has to be at least $p + 1$ leading to $\bar{M} > M$ [8, 10].

3.2.2   Polynomial basis functions

The basis functions are defined on the "master" or "reference" element $\hat{\Omega}$, in the computational space. The local coordinates in the master element are given by $\boldsymbol{\xi} = (\xi, \eta, \zeta)^T$ and the coordinate system has its origin at the centroid of the hexahedron. The physical coordinates in element Ω_j are related to the computational coordinates of the master element by the invertible map:

$$\mathbf{x}^j : \quad \overline{\hat{\Omega}} \mapsto \overline{\Omega}_j,$$
$$\mathbf{x}^j(\boldsymbol{\xi}) = \mathbf{x}_{j0} + J_j\boldsymbol{\xi}, \quad J_j \in \mathbb{R}^3 \times \mathbb{R}^3. \qquad (3.25)$$

Here $\mathbf{x}_{j0} = (x_{j0}, y_{j0}, z_{j0})_j^T$ denotes the location of the centroid of element Ω_j (see also Fig.(3.1)), relative to the fixed coordinate system $\mathbf{x} = (x, y, z)^T$, defined for the
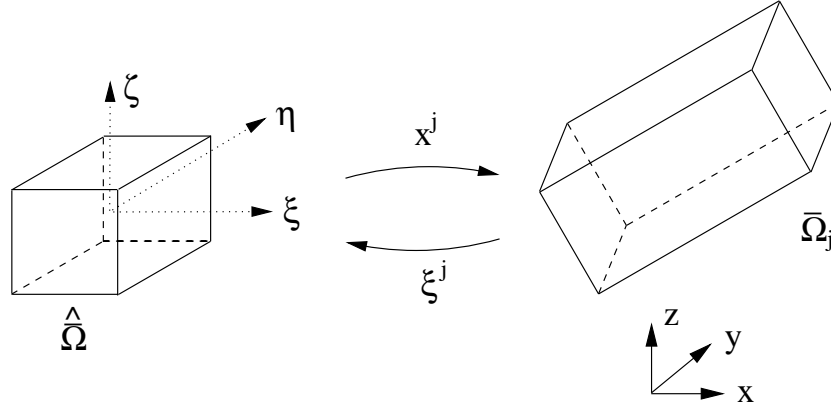
FIGURE 3.1: *Transformation from physical to computational space coordinates.*

whole domain Ω and J_j is the Jacobian, a non-singular (3×3)-matrix with constant coefficients. The Jacobians J_j are in general different for each element.

The map $\boldsymbol{\xi}^j$ is the inverse of $\mathbf{x}^j$:

$$\boldsymbol{\xi}^j : \quad \overline{\Omega}_j \mapsto \overline{\hat{\Omega}},$$
$$\boldsymbol{\xi}^j(\mathbf{x}) = J_j^{-1}(\mathbf{x} - \mathbf{x}_{j0}), \quad \Rightarrow \quad \boldsymbol{\xi}^j(\mathbf{x}^j(\boldsymbol{\xi})) = \boldsymbol{\xi}. \tag{3.26}$$

In general the maps $\mathbf{x}^j$ and $\boldsymbol{\xi}^j$ are nonlinear when completely general hexahedral elements are used, so the elements are restricted to parallelepiped which can be linearly mapped into a cube. A schematic of both maps is given in Fig. (3.1).

On $\overline{\hat{\Omega}}$ we define a set of linearly independent polynomials $\{b_k(\xi, \eta, \zeta)\}$ of degree $\leq p$:

$$\{b_k\} = \{\xi^{k_1} \eta^{k_2} \zeta^{k_3} \mid 0 \leq k_1 + k_2 + k_3 \leq p, \ k_i \geq 0\}. \tag{3.27}$$

The set $\{b_k\}$ is complete in the sense that it spans $\hat{\mathcal{P}}_p(\overline{\hat{\Omega}})$, the space of all polynomials on $\overline{\hat{\Omega}}$ with real coefficients and with a degree $\leq p$:

$$\hat{\mathcal{P}}_p(\hat{\Omega}) = \text{span}\{b_0, b_1, \dots, b_M\}. \tag{3.28}$$

The set of basis functions $\overline{b}_{jk}$ are induced by the set b_k as:

$$\overline{b}_{jk}(\mathbf{x}) \equiv b_k(\boldsymbol{\xi}^j(\mathbf{x})), \quad \mathbf{x} \in \overline{\Omega}_j. \tag{3.29}$$

3.2.3 Evaluation of integrals

Employing the linear representations given by Eq.(3.9) and Eq.(3.24), the individual terms in Eq.(3.17) can be evaluated.

- **First integral**:

The first integral of Eq.(3.17) is given by:

$$\int_{\Omega_j} \frac{\partial \mathbf{u}_{jk}}{\partial t} b_{jk} b_{jm} d\Omega = \frac{d\mathbf{u}_{jk}}{dt} \int_{\Omega_j} b_{jk} b_{jm} d\Omega. \tag{3.30}$$

Employing the inverse of the linear map $\mathbf{x}^j$, denoted by $\boldsymbol{\xi}^j$ and defined by Eq.(3.26), and the basis functions $b_{jk}(\mathbf{x})$, we evaluate the remaining integral as:

$$\int_{\Omega_j} b_{jk}(\mathbf{x}) b_{jm}(\mathbf{x}) d\Omega = \int_{\hat{\Omega}} b_k(\boldsymbol{\xi}) b_m(\boldsymbol{\xi}) |J_j| d\hat{\Omega}. \tag{3.31}$$

Recall that we have assumed $|J_j| = constant$ per element in the previous section leading to:

$$\int_{\Omega_j} \frac{\partial \mathbf{u}_{jk}}{\partial t} b_{jk} b_{jm} d\Omega = \frac{d\mathbf{u}_{jk}}{dt} |J_j| M_{km}. \tag{3.32}$$

with

$$M_{km} \equiv \int_{\hat{\Omega}} b_k(\boldsymbol{\xi}) b_m(\boldsymbol{\xi}) d\hat{\Omega}, \tag{3.33}$$

so-called Mass matrix.

- **Second integral**:

The second integral of Eq.(3.17) is given by:

$$\int_{\Omega_j} \mathbf{f}_i(\mathbf{u}_h) \frac{\partial b_{jm}}{\partial x_i} d\Omega = \int_{\Omega_j} A_i \mathbf{u}_{jk} b_{jk} \frac{\partial b_{jm}}{\partial x_i} d\Omega. \tag{3.34}$$

Employing the relation $\frac{\partial}{\partial x_i} = \frac{\partial \xi_l}{\partial x_i} \frac{\partial}{\partial \xi_l}$ and $(J_j)_{il} = \frac{\partial x_i^j}{\partial \xi_l}$, we get

$$\int\limits_{\Omega_j} A_i \mathbf{u}_{jk} b_{jk} \frac{\partial b_{jm}}{\partial x_i} d\Omega = \int\limits_{\hat{\Omega}} A_i \mathbf{u}_{jk} b_k (J_j^{-T})_{il} |J_j| \frac{\partial b_m}{\partial \xi_l} d\hat{\Omega}. \tag{3.35}$$

Assuming the mean flow is approximated as piecewise constant per element ($A_i = constant$) the above equation can be evaluated as:

$$\int\limits_{\hat{\Omega}} A_i \mathbf{u}_{jk} b_k (J_j^{-T})_{il} |J_j| \frac{\partial b_m}{\partial \xi_l} d\hat{\Omega} = |J_j| F_{jkm} \mathbf{u}_{jk}. \tag{3.36}$$

where,

$$F_{jkm} = A_i (J_j^{-T})_{il} \int\limits_{\hat{\Omega}} b_k \frac{\partial b_m}{\partial \xi_l} d\hat{\Omega}. \tag{3.37}$$

- **Third integral**:

  The third integral in Eq.(3.17) is given by:

$$\begin{aligned}
\int\limits_{\partial\Omega_j} \mathbf{h}(\overline{\mathbf{u}}_j, \overline{\mathbf{u}}_l, \mathbf{n}_j) \overline{b}_{jm} d\Gamma &= \sum_{l\in I_j} \left\{ \int\limits_{\partial\Omega_{jl}} \left\{ \frac{1}{2} \left(\overline{\mathbf{f}}^n(\overline{\mathbf{u}}_j) + \overline{\mathbf{f}}^n(\overline{\mathbf{u}}_l) \right) - \frac{1}{2}\alpha \left(\overline{\mathbf{u}}_l - \overline{\mathbf{u}}_j \right) \right\} \overline{b}_{jm} d\Gamma \right\} \\
&= \sum_{l\in I_j} \left\{ \int\limits_{\partial\Omega_{jl}} \left\{ \frac{1}{2} \left(A_i n_{ji} \mathbf{u}_{jk} \overline{b}_{jk} + A_i n_{ji} \mathbf{u}_{lk} \overline{b}_{lk} \right) \right. \right. \\
&\qquad\qquad \left. \left. - \frac{1}{2}\alpha \left(\mathbf{u}_{lk} - \mathbf{u}_{jk} \right) \right\} \overline{b}_{jm} d\Gamma \right\}. \tag{3.38}
\end{aligned}$$

where $\alpha = \theta|a|_{max}$. ϵ is the index of the element faces where $\epsilon = 1, .., 6$ for hexahedra and, $\delta\Omega_\epsilon$ indicates the element surface. This integral is to be carried out over each surface of the 6 faces of the hexahedra. When an element boundary coincides with domain boundary than the flux term is calculated using the contribution from the boundary condition instead of the adjacent element "l". As discussed in the previous section we approximate $A_i = constant$ per element. On the interface between two elements we use the average of the two states:

$$\overline{A}^n = \frac{1}{2} \left((A_i^n)^L + (A_i^n)^R \right), \qquad A_i^n = A_i n_{ji}. \tag{3.39}$$

Rearranging Eq. (3.38) leads to

$$\int_{\partial\Omega_j} \mathbf{h}(\bar{\mathbf{u}}_j, \bar{\mathbf{u}}_l, \mathbf{n}_j)\bar{b}_{jm}d\Gamma \;=\; \sum_{l\in I_j}\left\{\frac{1}{2}\left[\bar{A}^n + \alpha I\right]\mathbf{u}_{jk}\int_{\partial\Omega_{jl}}\bar{b}_{jk}\bar{b}_{jm}d\Gamma\right.$$

$$\left. +\frac{1}{2}\left[\bar{A}^n - \alpha I\right]\mathbf{u}_{lk}\int_{\partial\Omega_{jl}}\bar{b}_{lk}\bar{b}_{jm}d\Gamma\right\}, \qquad (3.40)$$

where I is the (5×5)-identity matrix and the summation is over the faces of the hexahedra.

For convenience, the surface integrals in the right-hand-side of Eq.(3.40) are evaluated on the reference square $\hat{\Gamma}$, which is shown in Fig.(3.2). The local coordinates of the reference square are given by $\hat{\boldsymbol{\xi}} = (\hat{\xi}, \hat{\eta})^T$ and the local coordinate system has its origin at the centroid of the square. The six surfaces of the reference element are also all squares. The surface area of $\hat{\Gamma}$ is equal to the surface area of $\partial\hat{\Omega}_s$. The surface coordinates of $\partial\hat{\Omega}_s$, expressed in terms of the local element coordinates (ξ, η, ζ) of the reference element $\hat{\Omega}$, are related to the local surface coordinates of the reference square $\hat{\Gamma}$ by the map:

$$\boldsymbol{\phi}^s(\hat{\boldsymbol{\xi}}): \quad \hat{\Gamma} \mapsto \partial\hat{\Omega}_s,$$
$$\boldsymbol{\phi}^s(\hat{\boldsymbol{\xi}}) \equiv \boldsymbol{\xi}_{s0} + \Phi_s\hat{\boldsymbol{\xi}}, \qquad \Phi_s \in \mathbb{R}^2 \times \mathbb{R}^3, \qquad (3.41)$$

where $\boldsymbol{\xi}_{s0} = (\xi_0, \eta_0, \zeta_0)_s^T$ represents the location of the centroid of the surface $\partial\hat{\Omega}_s$, expressed in terms of the local element coordinates of the reference element $\hat{\Omega}$ and where the index $s \in \{1, 2, 3, 4, 5, 6\}$ depends on the indices of the two adjacent elements Ω_j and Ω_l by:

$$s = \bar{s}(j, l), \qquad (3.42)$$

and where $\bar{s}(j, l)$ is such that

$$\mathbf{x}^j(\boldsymbol{\phi}^s(\hat{\Gamma}))) = \partial\Omega_{jl}, \qquad s = \bar{s}(j, l). \qquad (3.43)$$

In Eq.(3.41) Φ_s is a (2×3)-matrix. In addition, we introduce $\boldsymbol{\psi}^s$, which is the inverse map of $\boldsymbol{\phi}^s$:

$$\boldsymbol{\psi}^s(\boldsymbol{\xi}): \quad \partial\hat{\Omega}_s \mapsto \hat{\Gamma},$$
$$\boldsymbol{\psi}^s(\boldsymbol{\xi}) \equiv (\Phi_s^T\Phi_s)^{-1}\Phi_s^T(\boldsymbol{\xi} - \boldsymbol{\xi}_{s0}) \quad \Rightarrow \quad \boldsymbol{\psi}^s(\boldsymbol{\phi}^s(\hat{\boldsymbol{\xi}})) = \hat{\boldsymbol{\xi}}, \qquad (3.44)$$

where it is required that $\det(\Phi_s^T\Phi_s) \neq 0$. It is noted that since the matrix Φ_s is not a square matrix it cannot be inverted. It can be shown that for all six maps from the faces $\partial\hat{\Omega}_s$ to the reference square that $\det(\Phi_s^T\Phi_s) \neq 0$.
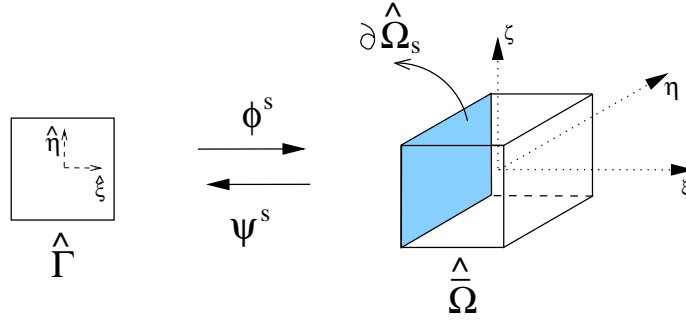
FIGURE 3.2: *Mapping from reference square $\hat{\Gamma}$ onto $\partial\hat{\Omega}_s$ and vise versa.*

Employing the map $\phi^s(\hat{\boldsymbol{\xi}})$ we can write for the basis functions defined in the reference element $\hat{\Omega}$, Eq.(3.27):

$$b_k(\phi^s(\hat{\boldsymbol{\xi}})) = \sum_{m=0}^{M(p,d-1)} T_{km}^s \hat{b}_m(\hat{\boldsymbol{\xi}}), \tag{3.45}$$

where the set $\{\hat{b}_m(\hat{\boldsymbol{\xi}})\} = \{1, \hat{\xi}, \hat{\eta}, \ldots, \hat{\eta}^p\}$ forms a basis for polynomials with degree less or equal to p on $\hat{\Gamma} \subset \mathbb{R}^2$. The matrices T^s are $(\hat{M} \times M)$-matrices, where

$$\hat{M}(p, d) \equiv M(p, d - 1), \tag{3.46}$$

and where $M(p, d)$ has been defined in Eq.(3.8). With this relation, Eq.(3.45), and the earlier obtained relation between the basis functions $\bar{b}_{jk}$ and b_k, Eq.(3.29), the first integral on the right-hand-side of Eq.(3.40) can be rewritten into an integral over basis functions $\hat{b}_k$ on $\hat{\Gamma}$ (with Einstein summation convention, except for index j):

$$\int_{\partial\Omega_{jl}} \bar{b}_{jk}\bar{b}_{jm}d\Gamma = \int_{\partial\hat{\Omega}_l} b_k b_m |J_j| d\boldsymbol{\xi} = \int_{\hat{\Gamma}} T_{kk'}^s \hat{b}_{k'} T_{mm'}^s \hat{b}_{m'} |J_j||\hat{J}_s| d\hat{\Gamma}, \tag{3.47}$$

where $|\hat{J}_s| = 1$, because the surface area of the square surfaces $\hat{\Gamma}$ and $\partial\hat{\Omega}_s$ are equal. So, we have:

$$\int_{\partial\Omega_{jl}} \bar{b}_{jk}\bar{b}_{jm}d\Gamma = |J_j| T_{kk'}^s T_{mm'}^s \int_{\hat{\Gamma}} \hat{b}_{k'}\hat{b}_{m'} d\hat{\Gamma}, \tag{3.48}$$

The integral in Eq.(3.48) has to be evaluated only once, as a pre-processing step in a numerical simulation. For the first term on the right-hand-side of Eq.(3.40) we can now write:

$$\frac{1}{2}\left[\overline{A}^n + \alpha I\right]\mathbf{u}_{jk}\int\limits_{\partial\Omega_{jl}}\overline{b}_{jk}\overline{b}_{jm}d\Gamma = |J_j|\left\{\frac{1}{2}\left[\overline{A}^n + \alpha I\right]T_{kk'}^s T_{mm'}^s\int\limits_{\hat{\Gamma}}\hat{b}_{k'}\hat{b}_{m'}d\hat{\Gamma}\right\}\mathbf{u}_{jk},$$

$$(3.49)$$

which, upon introducing the notation:

$$G_{jkm} \equiv \frac{1}{2}\left[\overline{A}^n + \alpha I\right]T_{kk'}^s T_{mm'}^s\int\limits_{\hat{\Gamma}}\hat{b}_{k'}\hat{b}_{m'}d\hat{\Gamma}, \qquad (3.50)$$

can be written as:

$$\frac{1}{2}\left[\overline{A}^n + \alpha I\right]\mathbf{u}_{jk}\int\limits_{\partial\Omega_{jl}}\overline{b}_{jk}\overline{b}_{jm}d\Gamma = |J_j|G_{jkm}\mathbf{u}_{jk}. \qquad (3.51)$$

The evaluation of the second integral on the right-hand-side of Eq.(3.40) involves integrating basis functions from both elements Ω_j and Ω_l. Although both can be mapped onto $\hat{\Gamma}$, the integration can not readily be performed because a common point on $\partial\Omega_\epsilon$ is mapped onto different points in $\hat{\Gamma}$ when mapping this point from, respectively, element Ω_j and Ω_l onto $\hat{\Gamma}$. Assuming that a point on the surface $\mathbf{x} \in \partial\Omega_\epsilon$ is part of element Ω_j, it is mapped onto the point $\hat{\boldsymbol{\xi}}_1$ on the reference square $\hat{\Gamma}$. However, assuming that $\mathbf{x} \in \partial\Omega_\epsilon$ is part of element Ω_l it is mapped onto $\hat{\boldsymbol{\xi}}_2$ on $\hat{\Gamma}$:

$$\hat{\boldsymbol{\xi}}_1 = \boldsymbol{\psi}^s \circ \boldsymbol{\xi}^j(\mathbf{x}) = \boldsymbol{\psi}^s(\boldsymbol{\xi}^j(\mathbf{x})), \qquad (3.52)$$
$$\hat{\boldsymbol{\xi}}_2 = \boldsymbol{\psi}^t \circ \boldsymbol{\xi}^l(\mathbf{x}) = \boldsymbol{\psi}^t(\boldsymbol{\xi}^l(\mathbf{x})), \qquad (3.53)$$

where

$$s = \overline{s}(j,l) \quad \text{and} \quad t = \overline{s}(l,j), \qquad (3.54)$$

and where $\overline{s}(j,l)$ is as in Eq.(3.43). In general $\hat{\boldsymbol{\xi}}_2 \neq \hat{\boldsymbol{\xi}}_1$. The above situation has been depicted in Fig. (3.3).

From Eqs.(3.52) and (3.53) and the maps Eq.(3.41) and (3.44) $\hat{\boldsymbol{\xi}}_2$ can be expressed in terms of $\hat{\boldsymbol{\xi}}_1$.

$$\hat{\boldsymbol{\xi}}_2 = \boldsymbol{\psi}^t \circ \boldsymbol{\xi}^l \circ \mathbf{x}^j \circ \boldsymbol{\phi}^s(\hat{\boldsymbol{\xi}}_1) = \boldsymbol{\psi}^t(\boldsymbol{\xi}^l(\mathbf{x}^j(\boldsymbol{\phi}^s(\hat{\boldsymbol{\xi}}_1)))), \qquad (3.55)$$
$$= \hat{N}(\theta,\mu)\hat{\boldsymbol{\xi}}_1, \qquad (3.56)$$

where the matrix $\hat{N}$ is given by:
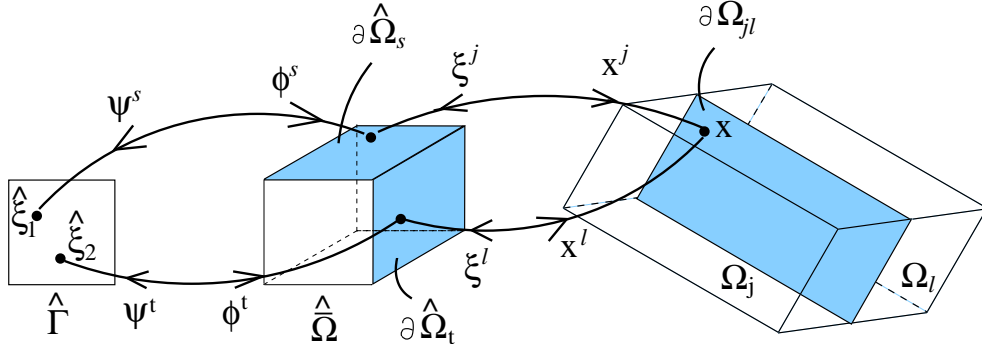
FIGURE 3.3: *Compound maps $\boldsymbol{\psi}^s \circ \boldsymbol{\xi}^j$ and $\boldsymbol{\psi}^t \circ \boldsymbol{\xi}^l$, mapping $\mathbf{x}$ onto $\hat{\boldsymbol{\xi}}_1$ and $\hat{\boldsymbol{\xi}}_2$, respectively.*

$$\hat{N}(\theta, \mu) = \begin{bmatrix} \mu\cos(\theta) & -\mu\sin(\theta) \\ \sin(\theta) & \cos(\theta) \end{bmatrix}, \tag{3.57}$$

with $\theta = 0, \pm\frac{\pi}{2}$ or π and $\mu = \pm 1$. The relation presented in Eq.(3.55) describes the path; First $\hat{\boldsymbol{\xi}}_1$ is mapped onto a point on $\partial\hat{\Omega}_s$ in the reference element $\overline{\hat{\Omega}}$ via the map ϕ^s, next this point on $\partial\hat{\Omega}_s$ is mapped onto $\mathbf{x}$ in $\partial\Omega_\epsilon$ via the map $\mathbf{x}^j$. Now we have expressed $\mathbf{x}$ in terms of $\hat{\boldsymbol{\xi}}_1$. Subsequently $\mathbf{x}(\hat{\boldsymbol{\xi}}_1)$ is mapped via $\boldsymbol{\xi}^l$ and $\boldsymbol{\psi}^t$ to $\hat{\boldsymbol{\xi}}_2$ in $\hat{\Gamma}$.

The basis functions evaluated for $\mathbf{x}$ can now be expressed in terms of the basis functions $\hat{b}_k$:

$$\begin{aligned} \bar{b}_{lk}(\mathbf{x}) = b_k(\boldsymbol{\xi}^l(\mathbf{x})) &= T^t_{kk'}\hat{b}_{k'}(\boldsymbol{\psi}^t(\boldsymbol{\xi}^l(\mathbf{x}))) = \\ &= T^t_{kk'}\hat{b}_{k'}(\boldsymbol{\psi}^t(\boldsymbol{\xi}^l(\mathbf{x}^j(\boldsymbol{\phi}^s(\hat{\boldsymbol{\xi}}))))), \\ &= T^t_{kk'}\hat{b}_{k'}(\hat{N}\hat{\boldsymbol{\xi}}) \end{aligned} \tag{3.58}$$

$$\begin{aligned} \bar{b}_{jm}(\mathbf{x}) = b_m(\boldsymbol{\xi}^j(\mathbf{x})) &= T^s_{mm'}\hat{b}_{m'}(\boldsymbol{\psi}^s(\boldsymbol{\xi}^j(\mathbf{x}))), \\ &= T^s_{mm'}\hat{b}_{m'}(\hat{\boldsymbol{\xi}}). \end{aligned} \tag{3.59}$$

For the second integral on the right-hand-side of Eq.(3.40) we now obtain:

$$\int_{\partial\Omega_{jl}} \bar{b}_{lk}(\mathbf{x})\bar{b}_{jm}(\mathbf{x})d\Gamma = |J_j|T^t_{kk'}T^s_{mm'}\int_{\hat{\Gamma}} \hat{b}_{k'}(\hat{N}\hat{\boldsymbol{\xi}})\,\hat{b}_{m'}(\hat{\boldsymbol{\xi}})d\hat{\Gamma}. \tag{3.60}$$

Employing Eq.(3.57), the basis functions $\hat{b}_k(\hat{N}\hat{\boldsymbol{\xi}})$ can be written as:

$$\hat{b}_k(\hat{N}\hat{\boldsymbol{\xi}}) \equiv N_{km}\hat{b}_m(\hat{\boldsymbol{\xi}}), \tag{3.61}$$

and we can write for Eq.(3.60):

$$\int_{\partial\Omega_{jl}} \bar{b}_{lk}(\mathbf{x})\bar{b}_{jm}(\mathbf{x})d\Gamma = |J_j|T^t_{kk'}T^s_{mm'}N_{k'n'}\int_{\hat{\Gamma}} \hat{b}_{n'}\hat{b}_{m'}d\hat{\Gamma}. \tag{3.62}$$

Hence, we have obtained for the second part of the right-hand-side of equation Eq.(3.40):

$$\frac{1}{2}\Big[\overline{A}^n - \alpha I\Big]\mathbf{u}_{lk}\int_{\partial\Omega_{jl}} \bar{b}_{lk}\bar{b}_{jm}d\Gamma = |J_j|\Big\{\frac{1}{2}\Big[\overline{A}^n - \alpha I\Big]T^t_{kk'}T^s_{mm'}$$

$$N_{k'n'}\int_{\hat{\Gamma}} \hat{b}_{n'}\hat{b}_{m'}d\hat{\Gamma}\Big\}\mathbf{u}_{lk}, \tag{3.63}$$

which, upon introducing the notation:

$$H^l_{jkm} \equiv \frac{1}{2}\Big[\overline{A}^n - \alpha I\Big]T^t_{kk'}T^s_{mm'}N_{k'n'}\int_{\hat{\Gamma}} \hat{b}_{n'}\hat{b}_{m'}d\hat{\Gamma}, \tag{3.64}$$

can be written as:

$$\frac{1}{2}\Big[\overline{A}^n - \alpha I\Big]\mathbf{u}_{lk}\int_{\partial\Omega_{jl}} \bar{b}_{lk}\bar{b}_{jm}d\Gamma = |J_j|H^l_{jkm}\mathbf{u}_{lk}. \tag{3.65}$$

In summary, we have obtain for the third term given by Eq.(3.38), employing Eq.(3.40) and the results of Eq.(3.51) and Eq.(3.65):

$$\int_{\partial\Omega_j} \mathbf{h}(\overline{\mathbf{u}}_j, \overline{\mathbf{u}}_l, \mathbf{n}_j)\bar{b}_{jm}d\Gamma = |J_j|G_{jkm}\mathbf{u}_{jk} + \sum_{l\in I_j}|J_j|H^l_{jkm}\mathbf{u}_{lk}. \tag{3.66}$$

• **Fourth integral**:

The fourth term of Eq.(3.17) is given by:

$$(\mathbf{s}_h, b_{jm})_{\Omega_j} = (b_{jk}, b_{jm})_{\Omega_j}\mathbf{s}_{jk}. \tag{3.67}$$

Clearly the integral which has to be evaluated here is exactly the same as the one which had to be evaluated for the first term. Employing Eq. (3.24) and Eq. (3.33) we therefore simply obtain:

$$(\mathbf{s}_h, b_{jm})_{\Omega_j} = |J_j| M_{km} \mathbf{s}_{jk}. \tag{3.68}$$

3.2.4   Resulting system of equations

In the preceding section, section 3.2.3 we performed all the required integrations of Eq.(3.17). Combining the results of Eqs.(3.32), (3.36), (3.66) and (3.68) we obtain for Eq.(3.17) $\forall \, \Omega_j \in \Omega, \forall \, m \in [0, M(p, d)]$:

$$|J_j| M_{km} \frac{d\mathbf{u}_{jk}}{dt} + |J_j| \{-F_{jkm} + G_{jkm}\} \mathbf{u}_{jk} + \sum_{l \in I_j} |J_j| H^l_{jkm} \mathbf{u}_{lk} \;\; = \;\; |J_j| M_{km} \mathbf{s}_{jk},$$

$$\tag{3.69}$$

Hence, the determinant $|J_j|$ can be divided out of the equation, to result in:

$$M_{km} \frac{d\mathbf{u}_{jk}}{dt} + \{-F_{jkm} + G_{jkm}\} \mathbf{u}_{jk} + \sum_{l \in I_j} H^l_{jkm} \mathbf{u}_{lk} = M_{km} \mathbf{s}_{jk}. \tag{3.70}$$

For the sake of completeness, the matrices M_{km}, G_{km}, F_{lkm} and H_{lkm} are given by (Eqs.(3.33), (3.50), (3.37) and (3.64), respectively):

$$M_{km} \equiv \int_{\hat{\Omega}} b_k b_m d\hat{\Omega},$$

$$F_{jkm} \equiv A_i (J_j^{-T})_{il} \int_{\hat{\Omega}} b_k \frac{\partial b_m}{\partial \xi_l} d\hat{\Omega},$$

$$G_{jkm} \equiv \frac{1}{2} \left[\overline{A}^n + \alpha I \right] T^s_{kk'} T^s_{mm'} \int_{\hat{\Gamma}} \hat{b}_{k'} \hat{b}_{m'} d\hat{\Gamma},$$

$$H^l_{jkm} \equiv \frac{1}{2} \left[\overline{A}^n - \alpha I \right] T^t_{kk'} T^s_{mm'} N_{k'n'} \int_{\hat{\Gamma}} \hat{b}_{n'} \hat{b}_{m'} d\hat{\Gamma},$$

where (Eq.(3.43)):

$$s = \overline{s}(j, l), \quad \mathbf{x}^j(\phi^s(\hat{\Gamma})) = \partial\Omega_{jl}.$$

3.2.5   Evaluation of integrals involving non-linear terms

In section (3.2.3) we have evaluated the integrals where the determinant of the transformation Jacobian (J) is assumed to be constant and the mean flow is approximated as piecewise constant per element. In general the transformation jacobian, J, and the mean flow can be in linear or non-linear form. Thus these terms can be expanded in terms of the basis functions leading to a general way of evaluating the integral terms. In order to demonstrate this we will re-evaluate the first and second integral terms using the mentioned expansion.

• **First integral**:

The first integral of Eq.(3.17) is given by:

$$\int_{\Omega_j} \frac{\partial \mathbf{u}_{jk}}{\partial t} b_{jk} b_{jm} d\Omega = \frac{d\mathbf{u}_{jk}}{dt} \int_{\Omega_j} b_{jk} b_{jm} d\Omega. \tag{3.71}$$

Employing the inverse of the non-linear map $\mathbf{x}^j$, denoted by $\boldsymbol{\xi}^j$ and defined by Eq.(3.26), and the basis functions $b_{jk}(\mathbf{x})$, we evaluate the remaining integral as:

$$\int_{\Omega_j} b_{jk}(\mathbf{x}) b_{jm}(\mathbf{x}) d\Omega = \int_{\hat{\Omega}} b_k(\boldsymbol{\xi}) b_m(\boldsymbol{\xi}) |J_j| d\hat{\Omega}. \tag{3.72}$$

Since the map is non-linear the determinant of the transformation jacobian is not a constant. The term $|J_j|$ can be expanded in terms of the basis functions. In general, as:

$$|J_j| = j_j^{000} + j_j^{100}\xi + j_j^{010}\eta + j_j^{001}\zeta + j_j^{110}\xi\eta + ..., \tag{3.73}$$

where, the number of terms is determined by the desired order of accuracy of the expansion. Inserting this expansion into the volume integral gives:

$$\int_{\hat{\Omega}} b_m b_k |J_j| d\hat{\Omega} = \int_{\hat{\Omega}} b_m b_k \left\{ j_j^{000} + j_j^{100}\xi + j_j^{010}\eta + j_j^{001}\zeta + j_j^{110}\xi\eta + ... \right\} d\hat{\Omega},$$

$$= j_j^{000} M_{mk}^{000} + j_j^{100} M_{mk}^{100} + j_j^{010} M_{mk}^{010} + j_j^{001} M_{mk}^{001} + ..., \tag{3.74}$$

where,

$$M_{mk}^{i_1,i_2,i_3} = \int_{\hat{\Omega}} \xi^{i_1}\eta^{i_2}\zeta^{i_3} b_m(\vec{\xi}) b_k(\vec{\xi}) d\zeta d\eta d\xi. \tag{3.75}$$

is so-called Mass matrix. Inserting Eq. (3.74) into Eq. (3.71) will result in

$$\int_{\Omega_j} \frac{\partial \mathbf{u}_{jk}}{\partial t} b_{jk} b_{jm} d\Omega = \frac{d\mathbf{u}_{jk}}{dt} \left\{ j_j^{000} M_{mk}^{000} + j_j^{100} M_{mk}^{100} + j_j^{010} M_{mk}^{010} + j_j^{001} M_{mk}^{001} + ... \right\}.$$

(3.76)

- **Second integral**:

    The second integral of Eq.(3.17) is given by:

$$\int_{\Omega_j} \mathbf{f}_i(\mathbf{u}_h) \frac{\partial b_{jm}}{\partial x_i} d\Omega = \int_{\Omega_j} A_i \mathbf{u}_{jk} b_{jk} \frac{\partial b_{jm}}{\partial x_i} d\Omega.$$

(3.77)

Employing the relation $\frac{\partial}{\partial x_i} = \frac{\partial \xi_l}{\partial x_i} \frac{\partial}{\partial \xi_l}$ and $(J_j)_{il} = \frac{\partial x_i^j}{\partial \xi_l}$, we get

$$\int_{\Omega_j} A_i \mathbf{u}_{jk} b_{jk} \frac{\partial b_{jm}}{\partial x_i} d\Omega = \int_{\hat{\Omega}} A_i \mathbf{u}_{jk} b_k (J_j^{-T})_{il} |J_j| \frac{\partial b_m}{\partial \xi_l} d\hat{\Omega}.$$

(3.78)

Following the discussion above, the term A_i can be expanded in terms of basis functions as:

$$A_i = A_i^{000} + A_i^{100}\xi + A_i^{010}\eta + A_i^{001}\zeta + A_i^{110}\xi\eta...,$$

(3.79)

and the inverse transpose of the transformation Jacobian, $(J_j^{-T})_{il}$, as:

$$(J_j^{-T})_i l = (J_j^{000})_{il}^{-T} + (J_j^{100})_{il}^{-T}\xi + (J_j^{010})_{il}^{-T}\eta + (J_j^{001})_{il}^{-T}\zeta + (J_j^{110})_{il}^{-T}\xi\eta + ...,$$

(3.80)

Inserting above expansions into Eq. (3.78) we get:

$$\int_{\hat{\Omega}} A_i \mathbf{u}_{jk} b_k (J_j^{-T})_{il} |J_j| \frac{\partial b_m}{\partial \xi_l} d\hat{\Omega} = \int_{\hat{\Omega}} \mathbf{u}_{jk} b_k \frac{\partial b_m}{\partial \xi_l} \left\{ \left[A_i^{000} + A_i^{100}\xi + A_i^{010}\eta + A_i^{001}\zeta... \right] \right.$$
$$\left[(J_j^{000})_{il}^{-T} + (J_j^{100})_{il}^{-T}\xi + (J_j^{010})_{il}^{-T}\eta + (J_j^{001})_{il}^{-T}\zeta... \right]$$
$$\left. \left[j_j^{000} + j_j^{100}\xi + j_j^{010}\eta + j_j^{001}\zeta... \right] \right\} d\hat{\Omega},$$

(3.81)

which can be rearranged to get

$$\int\limits_{\hat{\Omega}} A_i \mathbf{u}_{jk} b_k (J_j^{-T})_{il} |J_j| \frac{\partial b_m}{\partial \xi_l} d\hat{\Omega} = \left[A_i^{000} (J_j^{000})_{il}^{-T} j_j^{000} \right] F_{jkm}^{000} + \left[A_i^{100} (J_j^{000})_{il}^{-T} j_j^{000} + \right.$$

$$\left. A_i^{000} (J_j^{100})_{il}^{-T} j_j^{000} + A_i^{000} (J_j^{000})_{il}^{-T} j_j^{100} \right] F_{jkm}^{100} + ..., \quad (3.82)$$

with,

$$F_{jkm}^{i_1,i_2,i_3} = \int\limits_{\hat{\Omega}} \xi^{i_1} \eta^{i_2} \zeta^{i_3} \, b_k \frac{\partial b_m}{\partial \xi_l} d\zeta d\eta d\xi. \quad (3.83)$$

3.3 Boundary conditions

An important feature of the DG method is that the approximate Riemann flux is the only mechanism through which an element communicates with its environment (direct neighbor or domain boundary), regardless of whether the bounding surface of the element is in the interior of the domain or coincides with the domain boundary (Atkins [9]). This makes that the system presented in Eq.(3.70) is also applicable in elements adjacent to the domain boundary. In contrast, most higher-order finite-difference and finite-volume methods require a modification of the discretization stencils at points near the domain boundary. With increasing order, the modifications are needed for an increasing number of points, counted from the domain boundary inwards. The modification requires special attention because it might adversely affect the accuracy and might even give rise to instabilities. Employing the DG method complications such as these are avoided.

The boundary conditions can be imposed by either providing the desired solution $\overline{\mathbf{u}}_l$ at the exterior side of the boundary, to be used in the approximate Riemann flux in Eq.(3.17):

$$\int\limits_{\partial \Omega_{jl}} \mathbf{h}(\overline{\mathbf{u}}_j, \overline{\mathbf{u}}_l, \mathbf{n}_j) \overline{b}_{jm} d\Gamma, \quad (3.84)$$

or by reformulating the boundary normal flux, subjected to the specified boundary condition, such that only part of the interior data are needed (Atkins [9]). Since we usually do not have an exact solution at the exterior, we will specify the boundary condition by reformulating the boundary normal flux. In section 3.2.1 the integral involving the approximate Riemann flux, given by Eq.(3.84), replaced the surface integral term of Eq.(3.17) and was introduced to provide coupling. In this section we

will apply the different boundary conditions to boundary $\partial\Omega_{jb} \cap \partial\Omega$, where $\partial\Omega_{jb} \in \partial\Omega$, $\partial\Omega_{jb} \in \partial\Omega$, and reformulate the surface integral term of Eq.(3.17):

$$\int_{\partial\Omega_{jb}} \mathbf{f}_i(\bar{\mathbf{u}}_j)n_{ji}\bar{b}_{jm}d\Gamma, \tag{3.85}$$

where

$$\mathbf{f}_i(\bar{\mathbf{u}}_j)n_{ji} = n_{ji}A_i\bar{\mathbf{u}}_j = A^n\bar{\mathbf{u}}_j, \quad A^n \equiv n_{ji}A_i, \tag{3.86}$$

and where:

$$\bar{\mathbf{u}}_j(\mathbf{x}, t) = \mathbf{u}_{jk}(t)\bar{b}_{jk}(\mathbf{x}), \quad \mathbf{x} \in \partial\Omega_j.$$

Hence, we have:

$$\int_{\partial\Omega_{jb}} \mathbf{f}_i(\bar{\mathbf{u}}_j)n_{ji}\bar{b}_{jm}d\Gamma = A^n\mathbf{u}_{jk} \int_{\partial\Omega_{jb}} \bar{b}_{jk}\bar{b}_{jm}d\Gamma. \tag{3.87}$$

In analogy with section 3.2.3, the integration will be performed employing the reference square $\hat{\Gamma}$. The notation which will be used here has been introduced in section 3.2.3. Employing the result of Eq.(3.48), we recast Eq.(3.87) into an integral over the reference square:

$$\int_{\partial\Omega_{jb}} n_i\mathbf{f}_i(\bar{\mathbf{u}}_j)\bar{b}_{jm}d\Gamma = A_i^n\mathbf{u}_{jk}|J_j|T_{kk'}^sT_{mm'}^s \int_{\hat{\Gamma}_b} \hat{b}_{k'}\hat{b}_{m'}d\hat{\Gamma}, \tag{3.88}$$

where s is such that $\mathbf{x}^j(\phi^s(\hat{\Gamma}))) = \partial\Omega_{jb}$. Upon introducing the notation, which is closely related to the notation introduced in Eq.(3.50):

$$G_{jkm}^b \equiv A^nT_{kk'}^sT_{mm'}^s \int_{\hat{\Gamma}} \hat{b}_{k'}\hat{b}_{m'}d\hat{\Gamma}, \tag{3.89}$$

we obtain

$$\int_{\partial\Omega_{jb}} \mathbf{f}_i(\bar{\mathbf{u}}_j)n_{ji}\bar{b}_{jm}d\Gamma = G_{jkm}^b\mathbf{u}_{jk}. \tag{3.90}$$

The unit normal vector $\mathbf{n}$ to the boundary $\partial\Omega_{jb}$, which we will use frequently in this section, is derived from the unit normal vector to the boundary $\partial\hat{\Omega}_s$ in the reference element $\boldsymbol{\tau}_s$, employing the relation:

$$\mathbf{n} = \frac{J_j^{-T}\boldsymbol{\tau}_s}{\|J_j^{-T}\boldsymbol{\tau}_s\|}. \tag{3.91}$$

It is noted that $\mathbf{n}$ and $\boldsymbol{\tau}_s$ are constants on $\partial\Omega_{jb}$ and $\partial\hat{\Omega}_s$, respectively.

In the subsequent (sub-)sections the characteristics-based non-reflecting boundary condition for $\partial\Omega_{jb} \in \partial\Omega^{NR}$, solid wall boundary condition for $\partial\Omega_{jb} \in \partial\Omega^{SW}$ and vibrating wall boundary condition for $\partial\Omega_{jb} \in \partial\Omega^{VW}$, will be presented.

3.3.1 Characteristics-based non-reflecting boundary condition

We apply non-reflecting boundary conditions when we want to ensure that waves that are leaving the domain can do so, as if the boundary does not exist. The simplest form of non-reflecting inflow and outflow boundary conditions is obtained by splitting the boundary normal flux into characteristic components according to whether their associated wave is entering or leaving the domain. The Euler and the linearized Euler equations are hyperbolic and can therefore be transformed into a characteristic form which facilitates the boundary condition treatment.

The (5×5)- matrix A_0^n, defined in Eq.(3.39), has 5 eigenvalues $\lambda_1, \ldots, \lambda_5$, the corresponding eigenvectors $\mathbf{r}_1, \ldots, \mathbf{r}_5$ can be shown to be linearly independent. Now we can write (Råde & Westergren [89]):

$$A^n = R\Lambda R^{-1}, \tag{3.92}$$

where

$$\Lambda = \mathrm{diag}(\lambda_1, \ldots, \lambda_5), \quad R = [\mathbf{r}_1, \ldots, \mathbf{r}_5]. \tag{3.93}$$

We define:

$$\Lambda^+ = \mathrm{diag}(\max(0, \lambda_1), \ldots, \max(0, \lambda_5)), \tag{3.94}$$
$$\Lambda^- = \mathrm{diag}(\min(0, \lambda_1), \ldots, \min(0, \lambda_5)), \tag{3.95}$$

and note that:

$$\Lambda^+ + \Lambda^- = \Lambda, \tag{3.96}$$

such that:

$$A^n \overline{\mathbf{u}}_j = (R\Lambda^+ R^{-1})\overline{\mathbf{u}}_j + (R\Lambda^- R^{-1})\overline{\mathbf{w}}, \tag{3.97}$$

where $\overline{\mathbf{w}}$ can be used to describe an incoming wave. Usually we set $\overline{\mathbf{w}} = \mathbf{0}$.

Setting $\overline{\mathbf{w}} = \mathbf{0}$, we replace A_0^n in Eq.(3.89) by $R\Lambda^+ R^{-1}$. Upon introducing the notation:

$$G_{jkm}^{NR} \equiv (R\Lambda^+ R^{-1})T_{kk'}^s T_{mm'}^s \int_{\hat{\Gamma}} \hat{b}_{k'}\hat{b}_{m'} d\hat{\Gamma}, \tag{3.98}$$

we obtain for the characteristics-based non-reflecting boundary condition:

$$\int\limits_{\partial\Omega_{jb}} \mathbf{f}_i(\overline{\mathbf{u}}_j)n_{ji}\overline{b}_{jm}d\Gamma = G^{NR}_{jkm}\mathbf{u}_{jk}, \quad \partial\Omega_{jb} \in \partial\Omega^{NR} \subset \partial\Omega. \qquad (3.99)$$

3.3.2   Solid-wall boundary condition

The solid-wall condition states that no flow passes through the boundary. Assuming that the mean flow satisfies this condition, we have to set the normal velocity perturbation equal to zero in order to implement this condition .

In vector notation, a vector $\mathbf{V}$ can be modified to have zero normal component, relative to the normal $\mathbf{n}$, by replacing it by the vector $\mathbf{W}$:

$$\mathbf{W} = \mathbf{V} - \left(\mathbf{V} \cdot \mathbf{n}\right)\mathbf{n}, \quad \text{so that} \quad \mathbf{W} \cdot \mathbf{n} = 0. \qquad (3.100)$$

The three components of the velocity perturbation are given by the second, third and fourth component of $\overline{\mathbf{u}}_j$. Hence, to implement the solid-wall boundary condition for the velocity perturbation, we have to impose:

$$\overline{u}_j^{m+1}n_m = 0, \quad m = 1, 2, 3, \qquad (3.101)$$

where $\overline{u}_j^m$ denotes the mth-component of the solution vector $\overline{\mathbf{u}}_j$. Because the boundary normal vector is constant over the surface $\partial\Omega_{jb}$, the solid-wall boundary condition can be applied to Eq.(3.90) by replacing $\mathbf{u}_j$ by $\tilde{\mathbf{u}}_j$, where the second, third and fourth component are given by (in analogy with Eq.(3.100)):

$$\tilde{u}_{jk}^{m+1} = u_{jk}^{m+1} - \left(u_{jk}^{l+1}n_l\right)n_m, \quad m, l = 1, 2, 3, \ \forall\, k. \qquad (3.102)$$

The first and fifth component of $\mathbf{u}_j$ remain unchanged. For the solid-wall boundary condition we finally obtain:

$$\int\limits_{\partial\Omega_{jb}} \mathbf{f}_i(\overline{\mathbf{u}}_j)n_ij\overline{b}_{jm}d\Gamma = G^b_{jkm}\tilde{\mathbf{u}}_{jk}, \quad \partial\Omega_{jb} \in \partial\Omega^{SW} \subset \partial\Omega. \qquad (3.103)$$

3.3.3   Vibrating-wall boundary condition

When considering a vibrating wall it is assumed that the surface-vibration amplitude is small compared to a representative acoustic wavelength and representative dimensions describing the surface. Assuming that the vibrating wall condition, i.e.

the wall displacement, is introduced to the linearized Euler equations by a normal ve-
locity boundary condition $\mathbf{u}_{wall}$, the boundary condition can be imposed by simply
modifying Eq. (3.102):

$$\tilde{u}_{jk}^{m+1} = u_{jk}^{m+1} - \left(u_{jk}^{l+1}n_l + (u_{wall})_{jk}\right)n_m, \quad m, l = 1, 2, 3, \ \forall k, \qquad (3.104)$$

where $(u_{wall})_{jk}$ can be obtained by projecting $\mathbf{u}_{wall}$ onto the basis set $\left\{\hat{b}_k\right\}$. The
coefficients can then be obtained from solving:

$$\int_{\hat{\Gamma}} \mathbf{u}_{wall}\hat{b}_m d\hat{\Gamma} = (u_{wall})_{jk} \int_{\hat{\Gamma}} \hat{b}_k\hat{b}_m d\hat{\Gamma}. \qquad (3.105)$$

Although $\mathbf{u}_{wall}$ is known function of $\hat{\xi}$ and $\hat{\eta}$ in the entire surface, evaluation of the
integrals, presented at the left-hand-side of Eq. (3.105) might still be cumbersome.
As an alternative, the integrals can be evaluated employing numerical quadrature or
the projection coefficients can be obtained by expanding $\mathbf{u}_{wall}$ in terms of the local
basis functions $\hat{b}_k$.

3.4 Initial conditions

We can expand the initial conditions in terms of the basis functions. Suppose we
have the initial condition

$$\mathbf{u}(\mathbf{x}, 0) = \mathbf{u}_0(\mathbf{x}), \qquad \mathbf{u}_0(\mathbf{x}) \in \mathbb{R}^5. \qquad (3.106)$$

We would like to approximate this initial condition with a projection on to the basis
functions as:

$$\mathbf{u}_h = \sum_j \mathbf{u}_{jk}(t)b_{jk}(\mathbf{x}), \qquad (3.107)$$

We also require that the error between the exact function $\mathbf{u}_0$ and the approximation
$\mathbf{u}_h$ to be minimum. Hence;

$$\psi = \int_\Omega \|\mathbf{u}_h - \mathbf{u}_0\|^2 d\Omega, \qquad (3.108)$$

is minimized. We can write this norm as

$$\psi = \int_\Omega \|\mathbf{u}_h - \mathbf{u}_o\|^2 d\Omega = \int_\Omega (\mathbf{u}_h - \mathbf{u}_0, \mathbf{u}_h - \mathbf{u}_0 d\Omega). \qquad (3.109)$$

To minimize the above norm, the derivatives of ψ with respect to all u_{jk}^m must be equal to zero:

$$\frac{\partial \psi}{\partial u_{jk}^m} = 0, \ \forall j, k, m, \tag{3.110}$$

note that there is no summation over index j:

$$
\begin{aligned}
\frac{\partial \psi}{\partial u_{jk}^m} &= 2 \int_\Omega b_{jk}(u_h^m - u_0^m)d\Omega, \\
&= 2u_{jl}^m \int_\Omega b_{jk}b_{jl}d\Omega - 2 \int_\Omega b_{jk}u_0^m = 0, \\
\Rightarrow \ &(b_{jk}, b_{jl})u_{jl}^m = (b_{jk}, u_0^m), \ \forall j, m, k. \tag{3.111}
\end{aligned}
$$

For fixed values of $j \in \{1, 2, ..., N\}$, $m \in \{1, 2, ..., 5\}$ this is a $(p+1) \times (p+1)$ linear system for $u_{j0}^m, u_{j1}^m, ..., u_{jp}^m$.

3.5 Runge-Kutta time integration

The time integration is performed applying the low-storage Runga-Kutta ([61]) algorithm. The system, presented in Eq.(3.70), for each element Ω_j is written as:

$$\frac{d\mathbf{u}_j}{dt} = K\mathbf{u}_j. \tag{3.112}$$

The matrix K is comprised of the contributions of element Ω_j and its (at most) six direct neighbors, Ω_l, $l \in I_j$. The solution at time $t + \Delta t$ is obtained from the solution at time t, $\forall \Omega_j$, employing the following algorithm for the N-stage Runge-Kutta time integration:

$$
\begin{aligned}
\mathbf{u}_j^{n,0} &= \mathbf{u}_j^n, \\
\mathbf{u}_j^{n,k} &= \mathbf{u}_j^n + \gamma_k \Delta t K \mathbf{u}_j^{n,k-1}, \quad k = 1, ..., N, \\
\mathbf{u}_j^{n+1} &= \mathbf{u}_j^{n,N}. \tag{3.113}
\end{aligned}
$$

The coefficients γ_k can be chosen such to obtain the required accuracy in time. For the four step scheme we use $\gamma_1 = \frac{1}{4}$, $\gamma_2 = \frac{1}{3}$, $\gamma_3 = \frac{1}{2}$ and $\gamma_4 = 1$.

CONVECTION OF A GAUSSIAN PULSE

4.1 Introduction

The verification is always the first goal in developing a numerical algorithm. A verification procedure is achieved by applying the numerical method to a problem which the analytical solution is known or can be derived and verifying that the solution obtained by the numerical method is close to the analytical solution within "acceptable" limits. Verification procedure also makes it possible to get an idea about an actual accuracy of the numerical method developed both in space and time. Furthermore, post-processing is almost a "must" to get more insight of the method developed. Considering all these processes it is advantageous to chose a "simple" problem where the analytical solution can be derived and all these time consuming *numerical experiments* can be simulated in a shorter time. To this end, convection of a one-dimensional Gaussian pulse is chosen as a verification problem. Although the problem is one-dimensional the numerical solution is obtained by a three-dimensional method.

The discontinuous Galerkin space discretization is tested up to fourth-order of accuracy. The time integration is performed by the four-stage low-storage Runge-Kutta algorithm which is shown to be fourth-order accurate.

In the next section the problem is described. The analytical solution of the problem is presented in two alternative routes in section 4.3. The numerical results including the numerical dispersion and the CPU-time requirements are presented in section 4.4.

4.2 Problem Description

As a test case Eqs. (2.37) are solved on a rectangular domain in which a compact acoustic perturbation is imposed through the initial condition on the hexahedral grid. The solution domain has dimensions $x \in [-5, 5]$, while in the $y - z$ plane it contains only one element, which is sufficient in order to represent the solution of the present

1D problem. However, note that the unknown coefficients $\mathbf{u}_{jk}$ associated with the basis functions that have a variation with respect to the y and z-directions are not set to zero, but are computed as part of the solution. The initial acoustic perturbation is centered at $x = 0$, $y = 0$, $z = 0$. The simulations have been carried out with a quiescent background without sources ($\mathbf{s} = 0$) and the initial condition for the 3D solution vector is given by:

$$\mathbf{u}(\mathbf{x}, 0) = (\rho', u', v', w', p')^T = (f(x), 0, 0, 0, f(x))^T, \tag{4.1}$$

with,

$$f(x) = e^{-\beta x^2}, \quad \beta = -\frac{\log(10^{-6})}{2}. \tag{4.2}$$
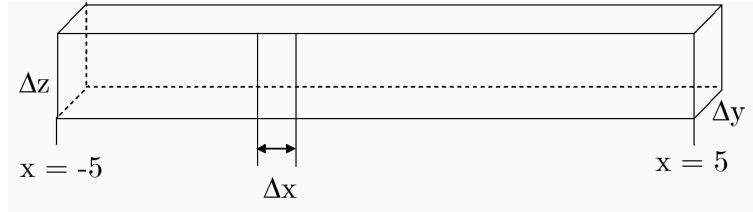
FIGURE 4.1: *The solution domain.*

In the remainder of this chapter we drop the primes, so the perturbed quantities are stated as ρ, u, v, w, and p.

4.3   Analytical Solution

In one-dimension the Linearized Euler Equations (Eq. (2.37)) can be written as follows:

$$\frac{\partial \mathbf{u}}{\partial t} + A \frac{\partial \mathbf{u}}{\partial x} = 0, \tag{4.3}$$

where,

$$\mathbf{u} = \begin{pmatrix} \rho \\ u \\ p \end{pmatrix}, \quad A = \begin{bmatrix} M & 1 & 0 \\ 0 & M & 1 \\ 0 & 1 & M \end{bmatrix}. \tag{4.4}$$

The matrix A has three linearly independent eigenvectors, corresponding to the eigenvalues $M + 1$, M and $M - 1$ of A, therefore matrix A can be diagonalized as;

$$A = R\Lambda R^{-1}, \quad R = \begin{bmatrix} 1 & 1 & 1 \\ 1 & 0 & -1 \\ 1 & 0 & 1 \end{bmatrix}. \tag{4.5}$$

with, $\Lambda = diag(M + 1, M, M - 1)$. We introduce a new unknown;

$$\mathbf{w} = \begin{pmatrix} w_1 \\ w_2 \\ w_3 \end{pmatrix}, \tag{4.6}$$

by means of the following transformation

$$\mathbf{u} = R\mathbf{w} \Rightarrow \mathbf{w} = R^{-1}\mathbf{u}, \tag{4.7}$$

with

$$R^{-1} = \begin{bmatrix} 0 & \frac{1}{2} & \frac{1}{2} \\ 1 & 0 & -1 \\ 0 & -\frac{1}{2} & \frac{1}{2} \end{bmatrix}. \tag{4.8}$$

Introducing this transformation into Eq. (4.3)gives

$$\frac{\partial \mathbf{u}}{\partial t} + A\frac{\partial \mathbf{u}}{\partial x} = R\frac{\partial \mathbf{w}}{\partial t} + AR\frac{\partial \mathbf{w}}{\partial x} = 0, \tag{4.9}$$

and multiplying each side of this equation by R^{-1} we get

$$R^{-1}R\frac{\partial \mathbf{w}}{\partial t} + R^{-1}AR\frac{\partial \mathbf{w}}{\partial x} = 0, \tag{4.10}$$

or,

$$\frac{\partial \mathbf{w}}{\partial t} + \Lambda\frac{\partial \mathbf{w}}{\partial x} = 0. \tag{4.11}$$

with,

$$\mathbf{w} = \begin{pmatrix} \frac{1}{2}(p + u) \\ \rho - p \\ \frac{1}{2}(p - u) \end{pmatrix}. \tag{4.12}$$

The components of $\mathbf{w}$ are called Riemann invariants. The analysis show that the first and third component of $\mathbf{w}$ corresponds to acoustic waves and the second component to the entropy wave. For the present initial solution the latter one is absent. The general solution of the above equation can be written as

$$\mathbf{w}(x, t) = \mathbf{f}(x - \Lambda t). \tag{4.13}$$

Now, consider the problem introduced in section 4.2 in one-dimension with the initial condition:

$$\mathbf{u}_0 = \begin{pmatrix} f(x) \\ 0 \\ f(x) \end{pmatrix}, \tag{4.14}$$

with $f(x)$ defined in Eq. (4.2). Applying the transformation introduced in Eq.(4.10) leads to:

$$\mathbf{w}_0 = R^{-1}\mathbf{u}_0 = \begin{bmatrix} 0 & \frac{1}{2} & \frac{1}{2} \\ 1 & 0 & -1 \\ 0 & -\frac{1}{2} & \frac{1}{2} \end{bmatrix} \begin{pmatrix} f(x) \\ 0 \\ f(x) \end{pmatrix} = \begin{pmatrix} \frac{1}{2}f(x) \\ 0 \\ \frac{1}{2}f(x) \end{pmatrix}. \tag{4.15}$$

Using the definition of $f(x)$ (Eq. (4.2)) we can write the general solution of the problem as:

$$\mathbf{w}(x,t) = \begin{pmatrix} \frac{1}{2}e^{-\beta(x-\Lambda_1 t)^2} \\ 0 \\ \frac{1}{2}e^{-\beta(x+\Lambda_3 t)^2} \end{pmatrix}. \tag{4.16}$$

Using the transformation introduced in Eq. (4.10) one more time we can write the general solution, $\mathbf{u}(x,t)$, to the Eq. (4.3) for $M=0$, $(\Lambda = diag(1,0,-1))$ as follows

$$\begin{aligned} \mathbf{u} = R\mathbf{w} \Rightarrow \mathbf{u}(x,t) &= \begin{bmatrix} 1 & 1 & 1 \\ 1 & 0 & -1 \\ 1 & 0 & 1 \end{bmatrix} \begin{bmatrix} \frac{1}{2}e^{-\beta(x-t)^2} \\ 0 \\ \frac{1}{2}e^{-\beta(x+t)^2} \end{bmatrix}, \\ &= \begin{bmatrix} \frac{1}{2}(e^{-\beta(x-t)^2} + e^{-\beta(x+t)^2}) \\ \frac{1}{2}(e^{-\beta(x-t)^2} - e^{-\beta(x+t)^2}) \\ \frac{1}{2}(e^{-\beta(x-t)^2} + e^{-\beta(x+t)^2}) \end{bmatrix}. \end{aligned} \tag{4.17}$$

The analytical solution of the problem considered is shown in figure (4.2) at various time instants. It shows that the initial Gaussian pulse splits up in two (condensation) waves, one moving to the left at speed $\frac{dx}{dt} = (M-1)$ and one moving to the right at speed $\frac{dx}{dt} = (M+1)$ with amplitude equal to half the amplitude of the initial pulse.

The induced velocity perturbations in both condensation waves is in the propagation direction of the wave, as known from classical 1D acoustics (see figure 4.3).

We can also derive an alternative route to the analytical solution. Rewrite the Linearized Euler Equations:

$$\begin{aligned} \frac{\partial \rho}{\partial t} + M\frac{\partial \rho}{\partial x} + \frac{\partial u}{\partial x} &= 0, \\ \frac{\partial u}{\partial t} + M\frac{\partial u}{\partial x} + \frac{\partial p}{\partial x} &= 0, \\ \frac{\partial p}{\partial t} + M\frac{\partial p}{\partial x} + \frac{\partial u}{\partial x} &= 0. \end{aligned} \tag{4.18}$$

We can differentiate Eqs. (4.18) to get

$$\left(\frac{\partial}{\partial t} + M\frac{\partial}{\partial x}\right)^2 p(x,t) - \frac{\partial^2 p}{\partial x^2} = 0,$$
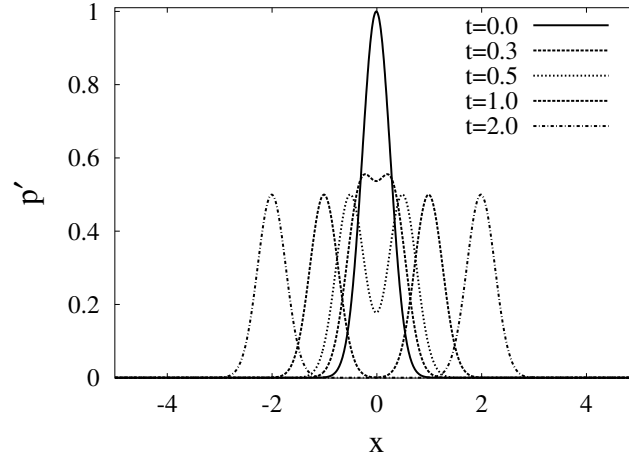
FIGURE 4.2: *Distribution of pressure perturbation at various dimensionless times (tc_0/H, with H the height of the duct). Analytical solution.*

$$\left(\frac{\partial}{\partial t} + M\frac{\partial}{\partial x}\right)^2 u(x,t) - \frac{\partial^2 u}{\partial x^2} = 0,$$

$$\left(\frac{\partial}{\partial t} + M\frac{\partial}{\partial x}\right)^2 (p(x,t) - \rho(x,t)) = 0. \tag{4.19}$$

Therefore d'Alembert's solution can be written as follows:

$$
\begin{aligned}
p(x,t) &= \hat{f}(x - (M+1)t) + \hat{g}(x - (M-1)t), \\
u(x,t) &= \hat{f}(x - (M+1)t) - \hat{g}(x - (M-1)t), \\
p(x,t) - \rho(x,t) &= \hat{h}(x - Mt).
\end{aligned}
\tag{4.20}
$$

The solution can be interpreted as in figure (4.4) Along the line $t = 0$ the initial condition is given in Eq. (4.1). From this it follows that along the initial line $t = 0$, $p - \rho = 0$. This implies that $p(x,t) - \rho(x,t) = 0$. Furthermore along the initial line $t = 0$ $p + u = f(x)$, so that $p(x,t) + u(x,t) = f(x - (M+1)t)$. Finally along the initial line $t = 0$ $p - u = f(x)$ leading to $p(x,t) - u(x,t) = f(x - (M-1)t)$. This is summarized in figure (4.5). From Eq. (4.22) the general solution can be written as:

$$
\begin{aligned}
p(x,t) &= \frac{1}{2}f(x - (M+1)t) + \frac{1}{2}f(x - (M-1)t) = \rho(x,t), \\
u(x,t) &= \frac{1}{2}f(x - (M+1)t) - \frac{1}{2}f(x - (M-1)t).
\end{aligned}
\tag{4.23}
$$

Finally, using the initial condition introduces in Eq. (4.2) we can write the solution as follows:

$$\rho(x,t) = p(x,t) = \frac{1}{2}\left(e^{-\beta(x-(M+1)t)^2} + e^{-\beta(x-(M-1)t)^2}\right),$$
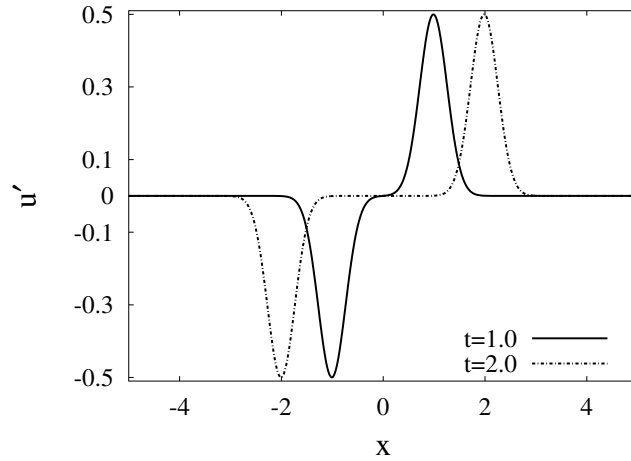
FIGURE 4.3: *Distribution of velocity perturbation at various dimensionless times* $(tc_0/H,$ *with H the height of the duct). Analytical solution.*
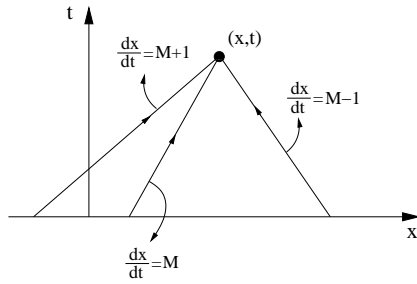
$$\frac{dx}{dt} = M \quad : \quad p - \rho = \text{constant},$$

$$\frac{dx}{dt} = (M+1) \quad : \quad p + u = \text{constant},$$

$$\frac{dx}{dt} = (M-1) \quad : \quad p - u = \text{constant}.$$

$$(4.21)$$

FIGURE 4.4: *Characteristic lines.*
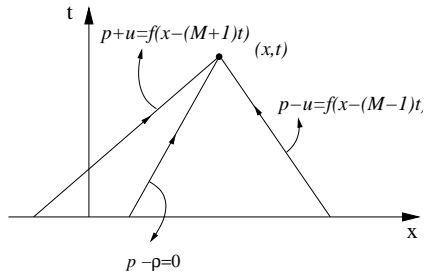
$$
\begin{aligned}
p(x,t) + u(x,t) &= f(x-(M+1)t), \\
p(x,t) - u(x,t) &= f(x-(M-1)t), \\
p(x,t) - \rho(x,t) &= 0.
\end{aligned}
$$

$$(4.22)$$

FIGURE 4.5: *Construction of solution of* *(x,t).*

$$u(x,t) \quad = \quad \frac{1}{2}\left(e^{-\beta(x-(M+1)t)^2} - e^{-\beta(x-(M-1)t)^2}\right). \qquad (4.24)$$

For $M = 0$ this solution is identical to the one presented in Eq. (4.17).

4.4 Numerical Results

The initial solution $\mathbf{u}(\mathbf{x}, 0)$, given by Eq. (4.1), has been approximated by a Taylor-series expansion in each element which has the same spatial order of accuracy as the numerical method itself. Alternatively the initial condition can be projected onto the basis functions as described in Section 3.4.

The 1D simulations have been performed with the present 3D method.At the boundaries in x-direction ($x = \pm5$) the characteristic based non-reflecting boundary conditions (see Section 3.3.1) are employed. Furthermore symmetry-plane boundary conditions are used in y- and z-directions. For the linear equation which we are considering, the symmetry-plane boundary condition is identical to solid-wall boundary condition, described in Section 3.3.2. The numerical solution is presented along the line in $x-$direction passing through the centroid of the elements.

The simulations have been carried out on different hexahedral meshes. The physical domain, Ω, is partitioned into 100, 200 and 400 equally sized cubes in $x-$direction, while one cube is used in y- and z-directions (figure (4.1)).

During the computations the results (function value ($p \geq 0$) and its first derivatives ($p \geq 1$), second derivatives ($p \geq 2$), etc.) are obtained at the cell centers and subsequently as a post-processing the values at all corner points of the mesh are evaluated using the basis functions. When a node point is common to more than one element the node value is obtained by averaging the corner point values .

4.4.1 Verification

Figures (4.6) and (4.7) shows a comparison of results for the first, second, third and fourth order accurate numerical method with the corresponding analytical solution for dimensionless times $t = 1$ and $t = 2$. The simulations have been performed on a relatively coarse mesh (number of element in $x-$ direction, N=50) to demonstrate the accuracy of the method. The results show that for the first-order method ($p = 0$) the pressure perturbation dissipates quickly, while the higher-order methods ($p \geq 1$) give much better results. A similar comparison for the velocity perturbation is shown in figures (4.8) and (4.9).

In figure (4.10) the reconstruction of the discontinuous solution is shown for various orders of accuracy. Here, the solution is evaluated at a large number (100) of points within each element, as a post processing, using the base functions. When only an element-wise constant basis function is used ($p = 0$) the solution can only be approximated element-wise constant. Increasing the polynomial degree to linear ($p = 1$) already gives better approximation as can be seen from figure (4.10) qualita-
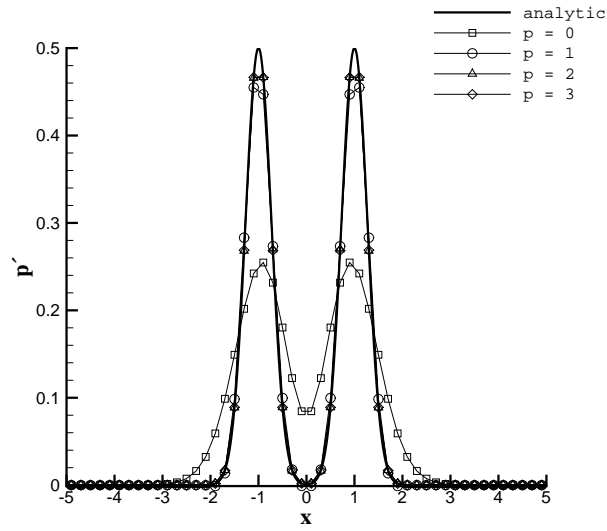
FIGURE 4.6: *Distribution of pressure perturbation at dimensionless time t=1 for $\Delta x = 0.2$, for the analytical and numerical solutions. The symbols indicate the numerical solutions, the solid line is the analytical result.*
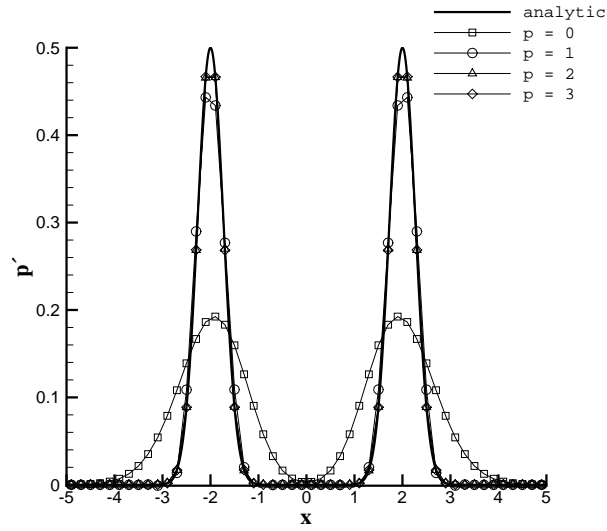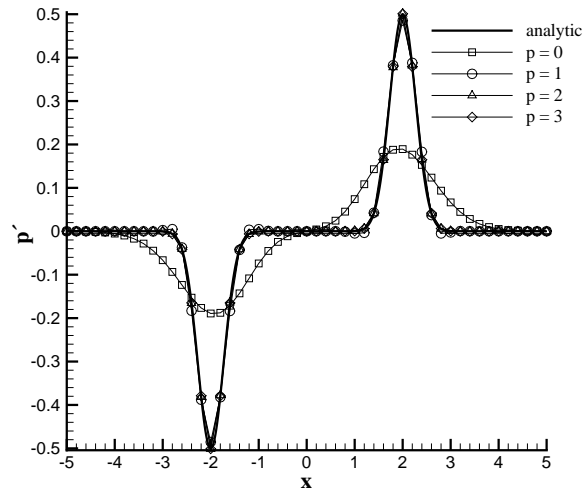

FIGURE 4.7: *Distribution of pressure perturbation at dimensionless time t=2 for $\Delta x = 0.2$, for the analytical and numerical solutions. The symbols indicate the numerical solutions, the solid line is the analytical result.*
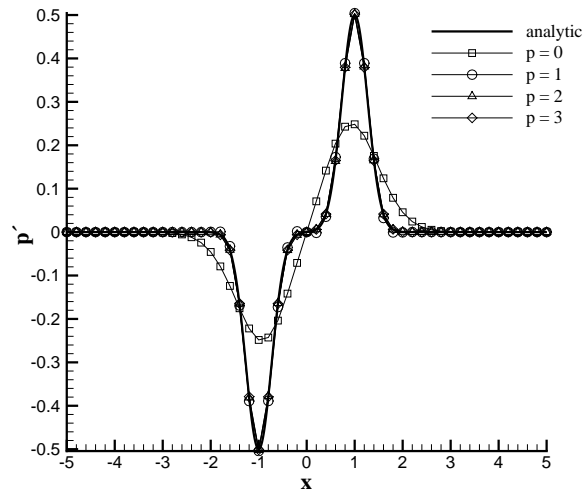
FIGURE 4.8: *Distribution of velocity perturbation at dimensionless time t=1 for $\Delta x = 0.2$, for the analytical and numerical solutions. The symbols indicate the numerical solutions, the solid line is the analytical result.*

FIGURE 4.9: *Distribution of velocity perturbation at dimensionless time t=2 for $\Delta x = 0.2$, for the analytical and numerical solutions. The symbols indicate the numerical solutions, the solid line is the analytical result.*
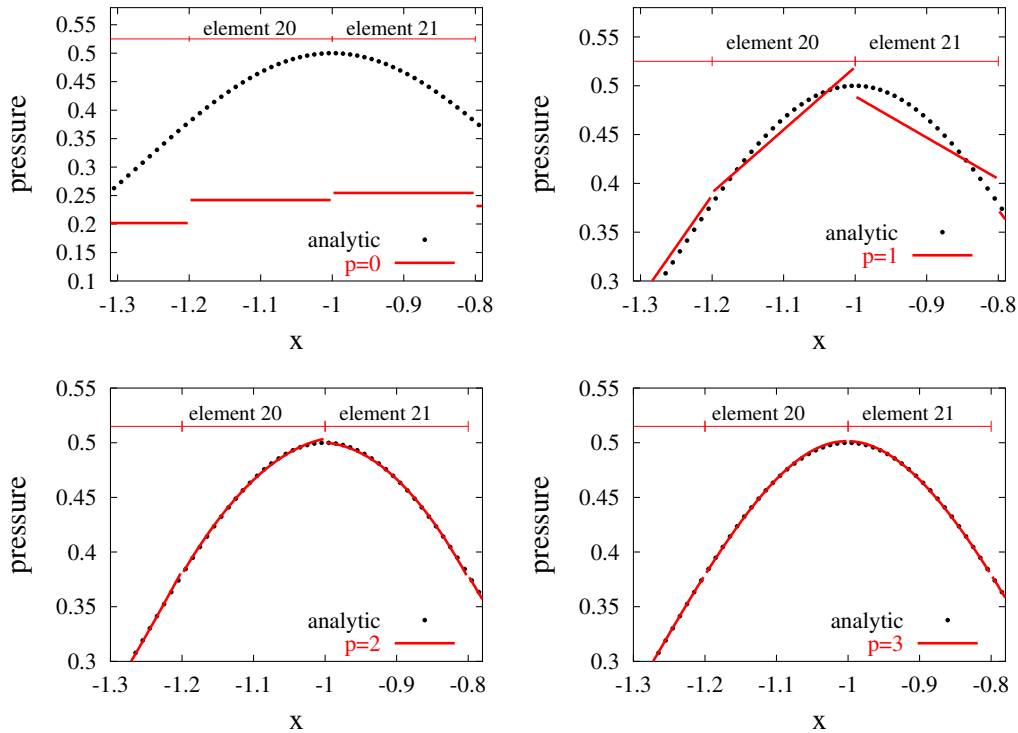
FIGURE 4.10: *Reconstruction of the discontinuous solution at dimensionless time t=1 and $\Delta x = 0.2$, for various values of p. The solid lines indicate the numerical solutions, the dashed line is the analytical result.*

tively. The fourth-order method ($p = 3$) gives the best results.

For the fourth-order method the difference between the analytical solution and the numerical solution is plotted in the left-hand side of figure (4.11). The right-hand side of figure (4.11) is a close-up of part of the plot illustrating the discontinuous numerical solution at the element interfaces. The sharp peaks in this plot correspond to the intersection points of the numerical solution evaluated at many points on the element and the analytic solution. At most $p + 1$ intersections are expected where p is the degree of the base functions.

The simulations performed for p-refinement study on the $100 \times 1 \times 1$ mesh is plotted in figure (4.12) where the comparison with the reconstructed result and the analytical solution is also shown. The reconstructed result is obtained using the numerical solution obtained by the fourth-order (p=3) method on the same mesh. A closer look (see figure (4.13)) shows that the reconstructed solution is in agreement with the analytical solution.
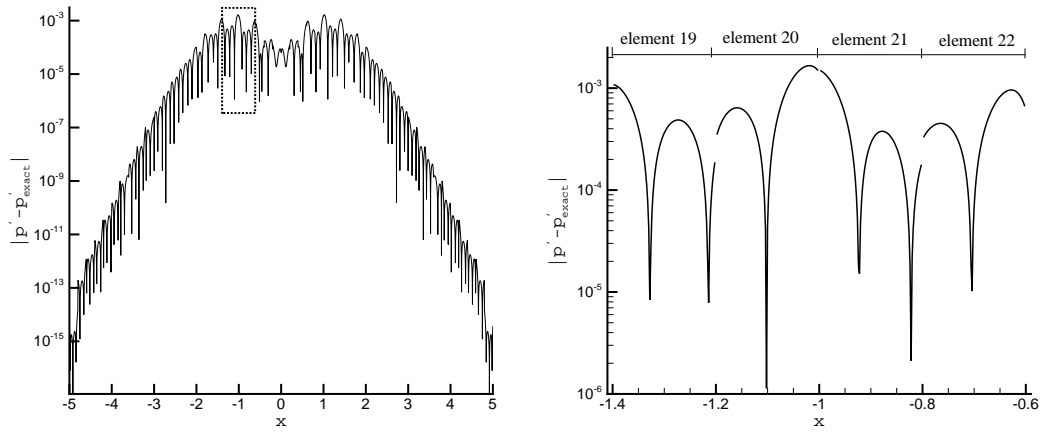
FIGURE 4.11: *Difference between the exact solution and numerical solution for the pressure perturbation at dimensionless time t=1, $\Delta x = 0.2$ (left). A detail of figure (5) showing the* DG *solution with the discontinuities at the element boundaries (right).*
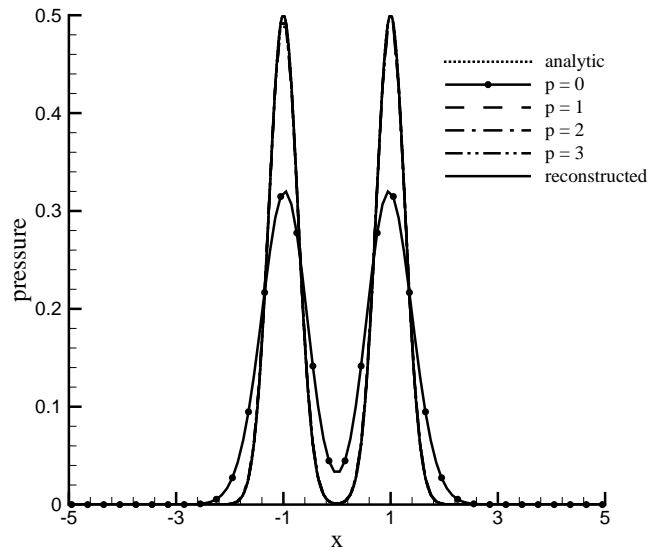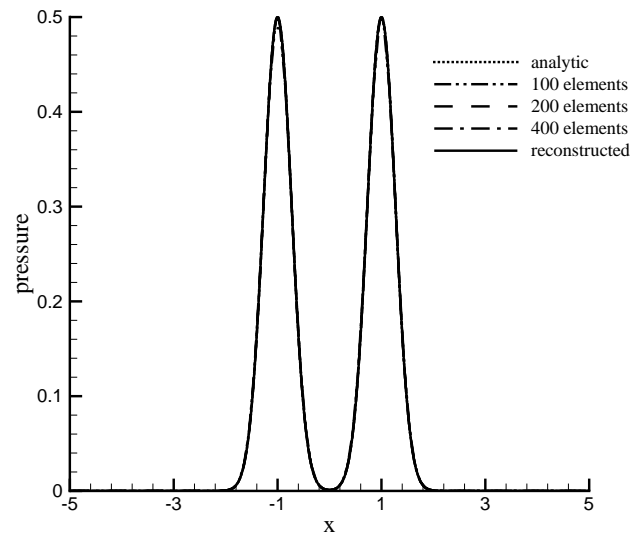

FIGURE 4.12: *Comparison of the distribution of pressure perturbations at dimensionless time $t = 1$ for $\Delta x = 0.1$ for p-refinement.*
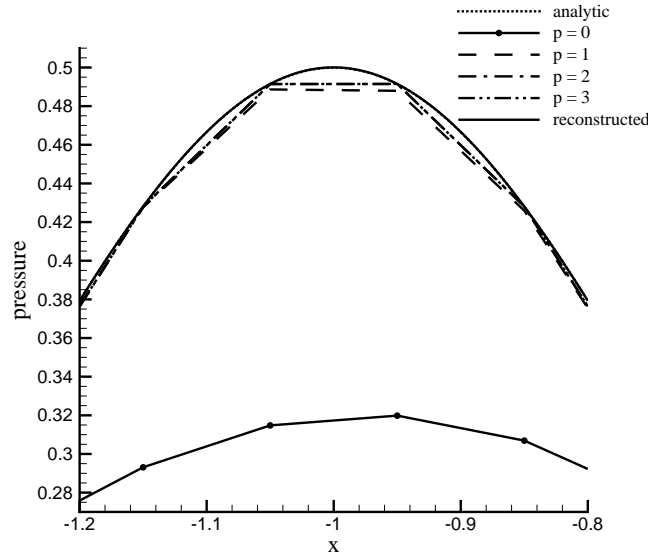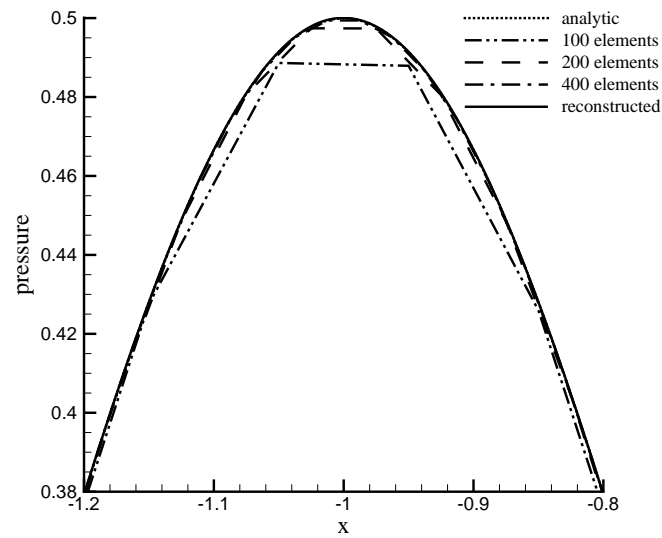
FIGURE 4.13: *A detailed view of comparison of the distribution of pressure perturbations at dimensionless time $t = 1$ for $\Delta x = 0.1$ for p-refinement.*

4.4.2 Accuracy

We obtained the time-converged solution by performing a time-refinement study. We can approximate the semi-discrete solution by employing Richardson extrapolation [89] as follows:

$$\left| p'_{\Delta t}(\mathbf{x}, t) - p'_{\Delta t=0}(\mathbf{x}, t) \right| = c\Delta t^{\alpha}, \qquad (4.25)$$

where, $p'_{\Delta t}$ is the fully-discrete solution, $p'_{\Delta t=0}$ is the semi-discrete solution, c is a constant, Δt is the dimensionless time step and α is the order of accuracy of the time discretization. Performing simulations for different values of the dimensionless time step, Δt, we can construct the semi-discrete solution $p'_{\Delta t=0}$ for any point with the way explained above. Figure (4.14) shows the order of accuracy of the time discretization obtained by employing equation (4.25) at each grid point. The dimensionless time is $t = 1$ and the domain is divided into 100 elements. Here, the result is shown only for the fourth-order ($p = 3$) accurate method, but a similar result is obtained for the first, second and third order methods. Recalling that a four-stage low-storage Runge-Kutta scheme is used for the time discretization, the time refinement study suggests that indeed the method is fourth-order accurate in time for the linear problem considered.

Next, a grid convergence study is performed using the time-converged semi-discrete
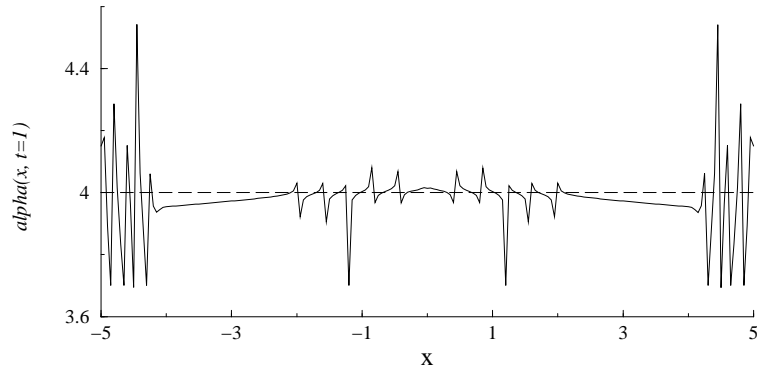
FIGURE 4.14: *Order of accuracy of the time discretization, obtained by the fourth-order method, at dimensionless time t=1 and for $\Delta x = 0.1$.*

solution. In order to perform this study, the solution is evaluated on an interrogation mesh with 10,000 common points used for the meshes with 100, 200 and 400 elements in $x-$direction, i.e. with 100, 50 and 25 interrogation points per element, respectively. The L_2-norm employed for each mesh, is of the form:

$$L_2 = \left\{ \frac{1}{L} \int_0^L \left[p'(x,t) - p'_{exact}(x,t) \right]^2 dx \right\}^{1/2}$$

$$\cong \left\{ \frac{1}{10000} \sum_{j=1}^{10000} \left[p'(x_j,t) - p'_{exact}(x_j,t) \right]^2 \right\}^{1/2} \tag{4.26}$$

with x_j the points of the interrogation mesh, which gives an accurate approximation of the integral norm. Note that the $p'(\mathbf{x},t)$'s used are the semi-discrete solutions for $\Delta t = 0$ on the mesh considered.

In figure (4.15) results obtained for three different meshes are compared with the reconstructed result and analytical solution. The reconstructed result is obtained using the numerical result obtained by the fourth-order (p=3) method on the 100x1x1 mesh. A detailed view is shown in figure (4.16).

The figure (4.17) shows the L_2-norm of the error in the pressure perturbation as a function of the number of elements N, with $\Delta x = L/N$, and $L = 10$. The results show that the present method is converging at a rate of h^{p+1} for $p = 1, 2$ and 3 and with a rate slightly higher than $h^{p+\frac{1}{2}}$ for $p = 0$, which agrees with the convergence rates derived in the literature, e.g. Ref. [60]. It is remarkable that in the range of Δx considered the line of the order p method is situated above the one for the order-$(p-1)$ method for any p considered.

FIGURE 4.15: *Comparison of the distribution of pressure perturbations at dimensionless time $t = 1$ for $\Delta x = 0.1$ for grid refinement.*

FIGURE 4.16: *A detailed view of comparison of the distribution of pressure perturbations at dimensionless time $t = 1$ for $\Delta x = 0.1$ for grid refinement.*

It is also observed that in case fewer points are used to evaluate the L_2-norm, e.g. common grid points of the coarsest or finest mesh considered (where the number of points used to evaluate the L_2 norm is of the order of the number of grid points) the rate of convergence for $p = 1$ is about h^3 (see figure (4.18)) which might suggest that this specific norm is based on some special points in the solution, namely, points close to the intersection points.
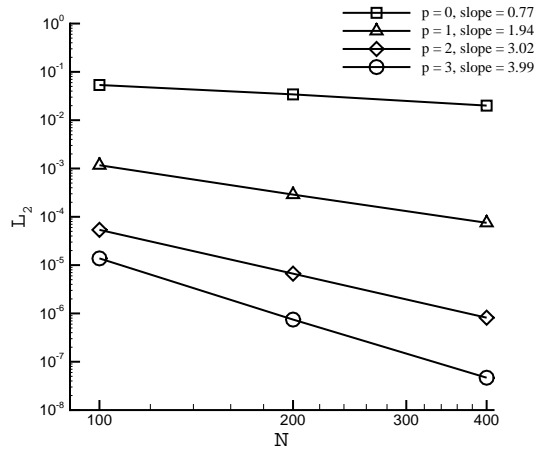
FIGURE 4.17: L_2-norm of error in pressure perturbation, Eq. (4.26), as function of N, with $\Delta x = L/N$, and $L = 10$, at dimensionless time t=1.
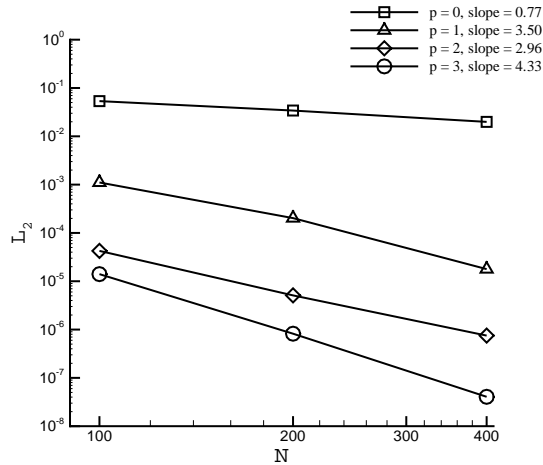
FIGURE 4.18: The L_2-norm of error in pressure perturbation as function of N, with $\Delta x = L/N$, with $L = 10$, at dimensionless time t=1 where fewer points are used to evaluate the L_2-norm.

4.4.3   Numerical Dispersion

The present method produces weak waves of small amplitude introduced by the numerics. Originating from the slope-discontinuity at the fronts of the initial wave, wave propagating at a higher speed than c_0 lead the acoustic wave.

Blom [25] has shown the numerical dispersion relation for the discontinuous Galerkin method applied to a one-dimensional model problem for $p = 0$ up to $p = 5$. Blom also discussed that the slope of the numerical dispersion as function of $k^* \Delta x$, with the scaled wave number, $k^* = \frac{k}{\pi(p+1)}$, represents the velocity at which the numerically induced waves propagate. In figure (4.19) this slope is shown as calculated from the numerical dispersion relation plot that is presented by Blom [25] (page 79, figure 4.4) for $p = 3$. It is seen from figure (4.19) that the numerically induced waves propagate at a speed between c_0 and about $2c_0$.
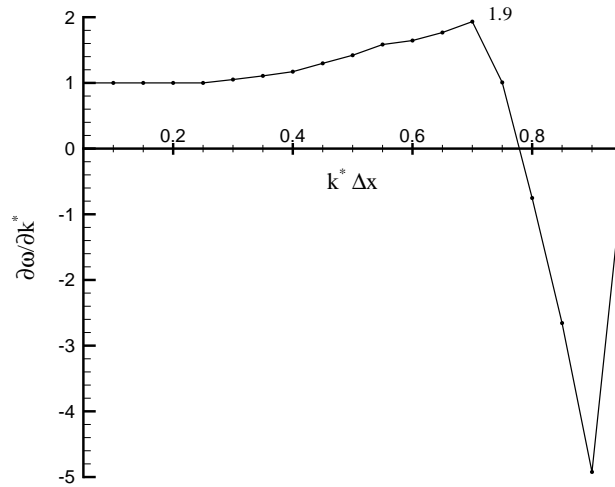
FIGURE 4.19: *Calculated slope of the numerical dispersion relation given by Blom[25] for $p = 3$ for plane-wave perturbations.*

The numerical dispersion can be demonstrated for a problem similar to the Gaussian pulse problem considered in the preceding sections. Consider a domain that has dimensions $x \in [-5, 5]$ and extends in the $y - z$ plane by only one element. The initial acoustic perturbation is symmetric with respect to the plane $x = 0$ and the initial condition for the 3D solution vector is given by:

$$\mathbf{u}(\mathbf{x}, 0) = \left(\rho', u', v', w', p'\right)^T = \left(g(x), 0, 0, 0, g(x)\right)^T, \qquad (4.27)$$
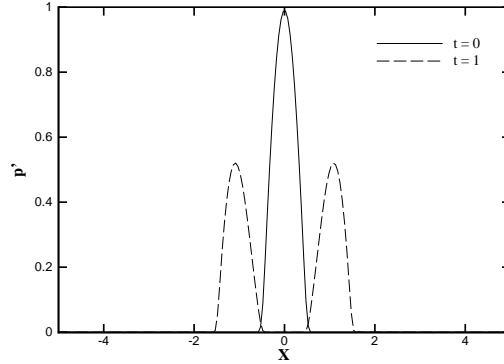
FIGURE 4.20: *Distribution of plane-wave pressure perturbation at dimensionless times $t = 0$ (initial condition) and $t = 1$. Numerical solution for $p = 3$, $\Delta x = \Delta y = \Delta z = 0.05$, $\Delta t = 1.0 \cdot 10^{-3}$.*

with,

$$g(x) = cos(\frac{2\pi x}{\lambda}), \qquad -0.5 \leq x \leq 0.5, \qquad (4.28)$$

$$g(x) = 0, \qquad x < -0.5, \qquad (4.29)$$

$$g(x) = 0, \qquad x > 0.5. \qquad (4.30)$$

with $\lambda = 2$, defining a half-sine wave with a slope discontinuity at the fronts initially at $x \pm 0.5$. Figure (4.20) shows the initial wave and the numerical solution at $t = 1$. From the numerical results, as well as from figures (4.20) and (4.21), it is evident that the amplitude of the numerically-induced waves is very small, smaller than 10^{-6}.

In figure (4.21) the contours of the pressure perturbation are plotted in the $x - t$ plane. In this figure the speed of the true wave can be calculated as $c_0 = 1.0$. What is also evident from this figure is that the weak numerically induced waves originate from the slope-discontinuity at the fronts of the imposed wave. The speed of these numerically induced waves can be determined from the figure as being in the range c_0 and a value slightly above $2c_0$. This result is in agreement with the numerical dispersion relation analysis shown by Blom [25] for $p = 3$.

4.4.4 CPU time requirements

The simulations have been performed on SGI Origin200 MIPS RISC R12000 processor with a clock speed of 270 MHz. The time required to advance the solution one time step is shown in table (4.1).

Although the CPU-time required per time step gives an idea about the simulation times, since the errors between the analytical solution and the numerical methods
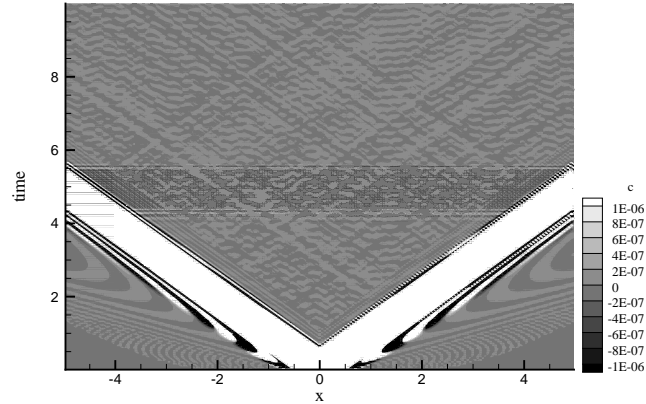
FIGURE 4.21: *Contours of plane-wave pressure perturbations in the $x - t$ plane. Numerical solution for $p = 3$, $\Delta x = \Delta y = \Delta z = 0.05$, $\Delta t = 1.0 \cdot 10^{-3}$.*

number of elements	order of accuracy ($p + 1$)	CPU time per time step (seconds)
100	2	0.0182
100	3	0.0247
100	4	0.0415
200	2	0.0356
400	2	0.0704

TABLE 4.1: *The time required for the numerical simulations on the hexahedral mesh.*

presented in Table (4.1) are different for each method it is not an exact comparison. To have a better idea of an optimum method in means of CPU-time it is more accurate to compare the time needed to reach a certain error level. This can be achieved by calculating the Δt required to obtain a certain error level (see figure (4.22)). In general the total error in the numerical method can be written as:

$$||\varepsilon|| = c_1 h^{\hat{\alpha}} + c_2 (\Delta t)^{\alpha}. \tag{4.31}$$

In figure (4.17) the error between the analytical solution and the numerical method is shown for $\Delta t \to 0$, thus,

$$||\varepsilon_{\Delta=0}|| = c_1 h^{\hat{\alpha}}. \tag{4.32}$$

Furthermore, in the previous section it is also shown that the order of accuracy of the time integration (α) is about 4. Hence, we can write for the total error:
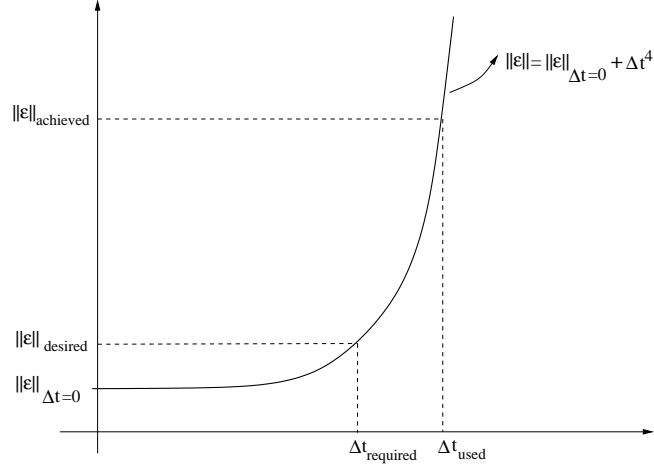
FIGURE 4.22: *A sketch of the calculation of the required time step to obtain a certain error level.*

$$||\varepsilon|| = ||\varepsilon_{\Delta=0}|| + c_2(\Delta t)^4. \tag{4.33}$$

The total error for the corresponding time step, Δt, can be calculated and then the constant, c_2, can be derived as:

$$c_2 = \frac{||\varepsilon|| - ||\varepsilon_{\Delta t=0}||}{(\Delta t)^4}. \tag{4.34}$$

Finally, the Δt required for the desired error level can be calculated as

$$\Delta t_{required} = \left(\frac{||\varepsilon_{desired}|| - ||\varepsilon_{\Delta t=0}||}{c_2} \right)^{\frac{1}{4}}. \tag{4.35}$$

In figure (4.23) the CPU-time needed to achieve a dimensionless time $t = 1$ is presented. For each method the time step required to obtain a certain error level is used as discussed. It can be concluded for the one-dimensional problem considered that the numerical method which is third-order accurate ($p = 2$) in space applied on the coarsest mesh considered is the optimum in means of CPU-time requirements.
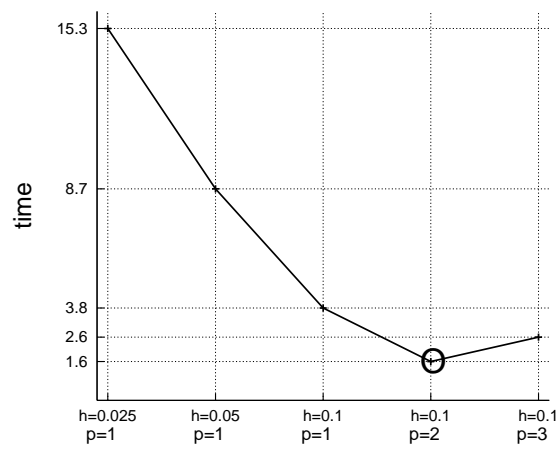
FIGURE 4.23: *CPU-time requirements for the methods considered to achieve the dimensionless time $t = 1$ under certain error level condition.*

ACOUSTIC RADIATION FROM VIBRATING WALL SEGMENT

5.1 Introduction

The problem of acoustic radiation from a vibrating wall segment inside an infinite rectangular duct is considered. The problem has been addressed by Blom[25, 26], who applied the DG method for a mesh of tetrahedral elements using second-order ($p = 1$) spatial accuracy. Blom also derived the analytical solution of the problem. In this chapter the DG method is applied for a mesh of hexahedral elements first using second-order spatial accuracy in order to compare the results with the method applied on a tetrahedral mesh by Blom. Furthermore a p-refinement study has been conducted using third- and fourth-order methods.

The vibrating wall problem is not an aeroacoustical problem, because the acoustic source is not of aerodynamic nature. However, the numerical algorithm has been developed to be applied for acoustic-wave propagation problems for given sources of sound. Therefore the vibrating wall problem at hand is well-suited as verification problem for the numerical algorithm.

The two main objectives of this chapter are to compare the results obtained for a hexahedral mesh to the results obtained for a tetrahedral mesh and to compare the numerical results obtained for a hexahedral mesh for values of p up to 3 (fourth-order) and the analytical solution in order to verify the numerical algorithm.

In section 5.2 the vibrating wall problem is described. A brief description of the analytical solution of the problem that has been derived by Blom[25, 26] is given in section 5.3. Numerical results are given in section 5.4 where a comparison with results obtained for a tetrahedral mesh is also discussed. Furthermore a grid convergence (h-refinement) and a p-refinement study is presented in section 5.4. In section 5.5 the numerical algorithm is applied by prescribing directly the wall displacement instead of prescribing the normal velocity profile and reconstructing the wall vibrations from that.

5.2   Problem Description

Consider an infinite rectangular duct of height $h = 1$ and width b, see figure (5.1). In the middle of the duct a finite part of the duct bottom wall, of length $2l$, is allowed to vibrate. The origin of the Cartesian coordinate system is in the mid-section of the duct at one of the lower corners. In the origin we define the orthogonal unit coordinate vectors $\mathbf{e}_x, \mathbf{e}_y$ and $\mathbf{e}_z$. In this study we consider the sound field generated by this vibrating wall segment inside the infinite duct. It is assumed that the problem can be described by the (non-dimensionalized) linearized Euler equations.
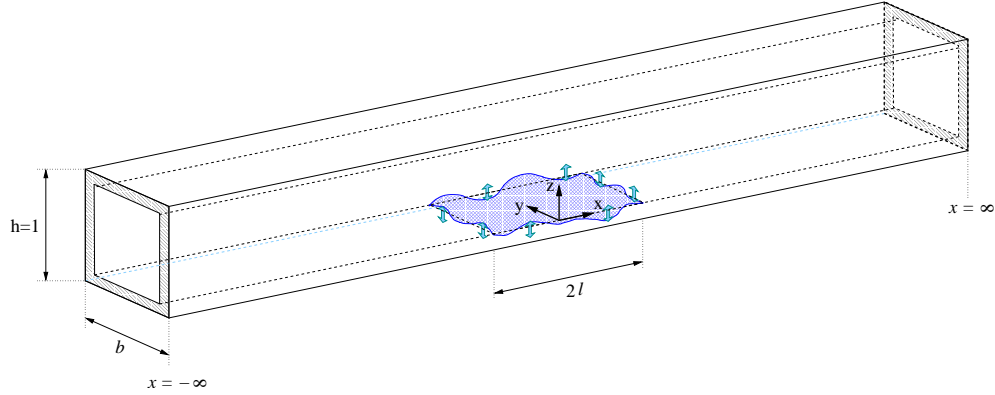
FIGURE 5.1: *Infinite rectangular duct with vibrating wall segment.*

The wall can be described by the position vector $\mathbf{x}_s$ (for $t > 0$) on the moving surface ($S = 2l \times b$):

$$\mathbf{x}_s(x, y, t) = x\mathbf{e}_x + y\mathbf{e}_y + \varepsilon z_s(x, y, t)\mathbf{e}_z, \quad x \in [-l, l], \quad y \in [0, b], \qquad (5.1)$$

with ε a measure for the amplitude of the wall vibration. The velocity vector $\mathbf{U}$ is given by:

$$\mathbf{U}(x, y, z, t) = (M + u')\mathbf{e}_x + v'\mathbf{e}_y + w'\mathbf{e}_z, \quad x \in [-l, l], \quad y \in [0, b], \qquad (5.2)$$

where M is the Mach number. Since the surface is assumed to be impenetrable, flow may not pass through the wall. This can be imposed by means of the kinematic condition $\frac{dF}{dt} = 0$, where $F(x, y, z, t) \equiv \varepsilon z_s(x, y, t) - z$ is the definition of the moving surface:

$$\left(\frac{dF}{dt}\right) = 0 \qquad \Rightarrow \qquad \left[\frac{\partial F}{\partial t} + \boldsymbol{\nabla} F \cdot \frac{d\mathbf{x}_s}{dt}\right]_s = 0,$$

$$\Rightarrow \qquad \left[\frac{\partial F}{\partial t} + \boldsymbol{\nabla} F \cdot \mathbf{U}\right]_s = 0. \qquad (5.3)$$

With

$$\frac{\partial F}{\partial t} = \varepsilon \frac{\partial z_s}{\partial t}, \qquad \boldsymbol{\nabla} F = \varepsilon \frac{\partial z_s}{\partial x}\mathbf{e}_x + \varepsilon\frac{\partial z_s}{\partial y}\mathbf{e}_y - \mathbf{e}_z, \qquad (5.4)$$

we obtain:

$$\left[\varepsilon\frac{\partial z_s}{\partial t} + \varepsilon(M + u')\frac{\partial z_s}{\partial x} + \varepsilon v'\frac{\partial z_s}{\partial y} - w'\right]_s = 0, \qquad (5.5)$$

We assume that the amplitude ε of the surface displacement is small compared to the acoustic wave length, the surface dimensions, l and b and the duct height h. Based on these assumptions it is consistent to linearize Eq.(5.5) with respect to the stationary reference surface $z = 0$ (Pierce [88]). This leads to:

$$w'(x, y, 0, t) = \varepsilon\left(\frac{\partial z_s}{\partial t} + M\frac{\partial z_s}{\partial x}\right). \qquad (5.6)$$

The perturbation velocity induced by the wall motion is scaled, i.e. $w = w'/\epsilon$. The displacement of the surface results in a normal velocity boundary condition for the linearized Euler equations to be imposed at $z = 0$:

$$u_n(x, y, t) = \psi(x, y, t)H(l - |x|), \quad x \in (-\infty, \infty), \quad y \in [0, b], \qquad (5.7)$$

whith

$$\psi(x, y, t) \equiv -w(x, y, 0, t) = -\left(\frac{\partial z_s}{\partial t} + M\frac{\partial z_s}{\partial x}\right), \qquad (5.8)$$

and where H is the Heaviside function.

The non-dimensionalized convected wave equation can be derived for the pressure as follows:

$$\frac{D^2 p}{Dt^2} - \nabla^2 p = 0, \quad \frac{D}{Dt} = \frac{\partial}{\partial t} + M\frac{\partial}{\partial x}, \quad \nabla^2 = \frac{\partial^2}{\partial x^2} + \frac{\partial^2}{\partial y^2} + \frac{\partial^2}{\partial z^2}. \qquad (5.9)$$

Taking the inner product of the momentum equation with the unit normal $\mathbf{n}_0 = -\mathbf{e}_z$, results in the following linearized boundary condition for the pressure at $z = 0$:

$$\frac{\partial p}{\partial z}\Big|_{z=0} = \frac{\partial u_n}{\partial t} + M\frac{\partial u_n}{\partial x}. \tag{5.10}$$

On the other walls, which are rigid and impenetrable, we apply the hard-wall conditions:

$$\frac{\partial p}{\partial z}\Big|_{z=h} = 0, \quad \frac{\partial p}{\partial y}\Big|_{y=0} = 0, \quad \frac{\partial p}{\partial y}\Big|_{y=b} = 0. \tag{5.11}$$

In the following sections we will solve Eq.(5.9) with the boundary conditions given by Eq.(5.10) and Eq.(5.11).

Plunging wall segment

Let us assume that the displacement of the vibrating wall segment is represented by the following function (see Eq. (5.7)):

$$\psi(t) = \sin(\omega_0 t)e^{-at}H(t), \tag{5.12}$$

where H is the Heaviside function. In this case the whole vibrating plate ($-l \leq x \leq l$, $0 \leq y \leq b$) moves up and down as a rigid plate (see figure (5.1)).

The simulations have been performed for $\omega_0 = \frac{4}{3}$, $l = 5$ and $a = 0.05$.

5.3   Analytical Solution

In this section the analytical solution is presented briefly, the reader is referred to Blom[25, 26] for a detailed description of the solution method.

The analytical solution of the described problem can be written in the following form:

$$p(x, y, z, t) \cong p_0(x, t) + \sum_{k=1}^{\infty} \cos(k\pi z)p_k(x, t). \tag{5.13}$$

The term p_0 represents a propagating (plane) wave or mode travelling to the right (in the positive x-direction), with the pressure perturbations p_k, represents waves affected by reflection, scattering, diffraction etc. Blom[25] did not find closed solutions for p_k, except for $t \to \infty$.

5.4   Numerical Results

For the verification of the computational method the numerical results are compared with the analytical solution obtained by Blom [25, 26].

When the mean flow is absent ($M = 0$), the problem is symmetrical with respect to the plane $x = 0$, which has also been verified numerically. The rectangular domain is given by $x \in [0, 40]$, $y \in [0, \Delta y]$ and $z \in [0, 1]$, where all lengths are nondimensional and Δy is the size of the element in y-direction. The location of x_{max} (=40) is chosen such that the plane wave does not reach the boundary in the time considered in the simulation. At the end planes of the duct, the characteristic non-reflecting boundary conditions are applied, while solid-wall boundary conditions are applied at the other walls except the vibrating wall segment.

The hexahedral mesh is obtained by partitioning the physical domain into equally sized cubes. The problem is two-dimensional but a three-dimensional method is applied to obtain the numerical results. In order to reduce the computation time, after verifying that there is indeed no effect of the third direction to the numerical solution, only one cell is used in the y-direction. In order to obtain the tetrahedral mesh, equally sized cubes are all divided into twelve identical tetrahedrons. Employing the centroid of the cubical basic element as additional point which yields a pyramid for each face of the cube. Dividing the faces in two by a diagonal gives the 12 equal tetrahedrons in total. In this way a reasonably regular tetrahedral mesh is obtained.

The results for the tetrahedral mesh are obtained for a cubical background mesh consisting of $200 \times 1 \times 5$ (1000) elements in x-, y- and z-directions, respectively. This results in 12000 tetrahedral elements.

During the computations the results are obtained at the cell centers and subsequently as a post-processing the values at all element corner points are evaluated using the basis functions. The node values are then obtained by averaging over all corner points of the cells that are common to more than one element. Additionally a time history of the perturbation variables is recorded at certain locations (not necessarily a node point) throughout the rectangular duct. These locations are called *microphone* (*mic*) locations.

5.4.1 Comparison with results obtained for tetrahedral mesh ($\omega_0 = \frac{4}{3}$, $l = 5$, $a = 0.05$)

The results obtained for the hexahedral mesh are compared with the analytical solution and with the existing results obtained for the tetrahedral mesh by Blom[25, 26]. Figure (5.2) shows the time histories of the pressure perturbation at the *mic* location $x = 5.025$, $y = \Delta y/2$, $z = 0.475$. It should be kept in mind that the analytical solution plotted in the figure represents only the propagating part of the solution (p_0 term, see Eq.(5.13)) while the other effects are neglected (p_k terms).

Although the result obtained for the hexahedral mesh seems to fit the analytic solution better than the result obtained for the tetrahedral mesh, it should be emphasized again that the analytical solution plotted is not complete. The deviation of the result obtained on the much finer (than the hexahedral mesh used) tetrahedral mesh from

the analytical solution suggests that the effects neglected in the analytical solution (p_k terms) are not captured in the solution obtained on the hexahedral mesh.

At a location further away from the vibrating wall segment the effect of the neglected terms is negligible. Figure (5.4) shows time histories of the pressure perturbations at the *mic* location $x = 20.075$, $y = \Delta y/2$ and $z = 0.475$. Now there is less detail in the signal and the results obtained on both meshes agree while also the deviation from the analytical solution (p_0) is small.
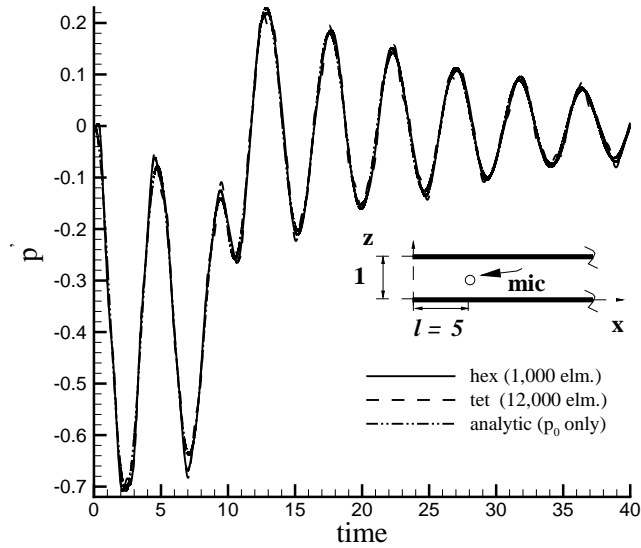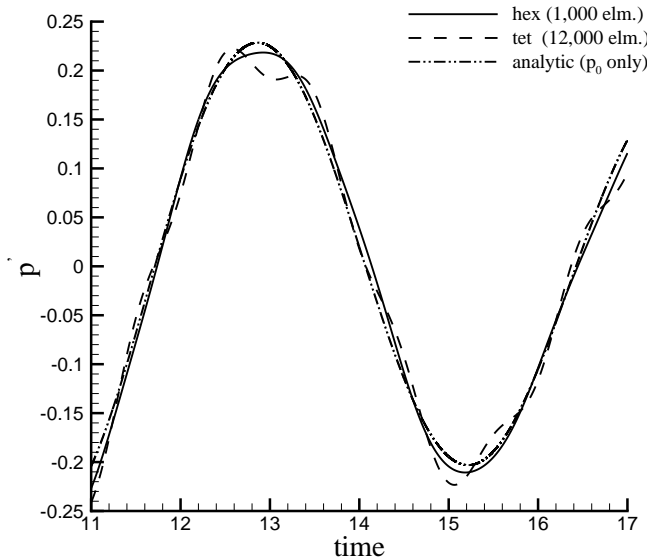

FIGURE 5.2: *Comparison of the time histories of the pressure perturbations at $x = 5.025$, $y=\Delta y/2$, $z = 0.475$. The order of approximation is $p = 1$, $\omega_0 = \frac{4}{3}$, $l = 5$, $a = 0.05$*

5.4.2   Grid Convergence

The results obtained for the hexahedral mesh suggest that a finer mesh is required. In order to determine the mesh that is fine enough a grid convergence study has been performed using three different hexahedral meshes: one with $400 \times 1 \times 10$, one with $800 \times 1 \times 20$ and the final one with $1600 \times 1 \times 40$ elements in x-, y- and z-directions, respectively. Since the analytical solution is not complete, using it as a reference to calculate the error for the different grids is not possible. Instead, using the time histories of the solutions at certain *mic* locations an approximation of the "exact" solution is calculated when $h \to 0$ by applying an extrapolation of the form:

$$p'(x = 5.025, y = \frac{\Delta y}{2}, z = 0.475, t) \quad - \quad p'_{exact}(x = 5.025, y = \frac{\Delta y}{2}, z = 0.475, t)$$

$$= \quad \tilde{a}(t)h + \tilde{b}(t)h^2, \tag{5.14}$$

for a given time step of the Runge-Kutta time integration scheme. This time step ($\Delta t = 0.001$) is assumed to be small enough that the solution is time converged on each grid used. The results on the 3 finest grids are used to compute p_{exact}, $\tilde{a}(t)$ and $\tilde{b}(t)$. It is observed that the magnitude of $\tilde{a}(t)$ is one order of magnitude smaller than the magnitude of $\tilde{b}(t)$. The time evaluation of $\tilde{a}(t)$ and $\tilde{b}(t)$ are shown in figure (5.6). After obtaining the approximate "exact" solution the absolute error for each grid is calculated by using an integral norm like the one introduced in Eq. (4.26) but now for the solution as function of time using the solution $t_n = n\Delta t$ as data where $n = 1, 2, .., 40000$. Figure (5.7) shows the absolute error for the three different grids used. It can be seen that the absolute error decreases slower than ch, the size of an element. Since the method applied is second-order accurate in space one would expect to get an accuracy (see figure (5.7)) close to second-order, i.e. h^2. However, the solutions used for the present analysis contain errors from the time discretization. For the three simulations on different meshes the time step has been kept constant
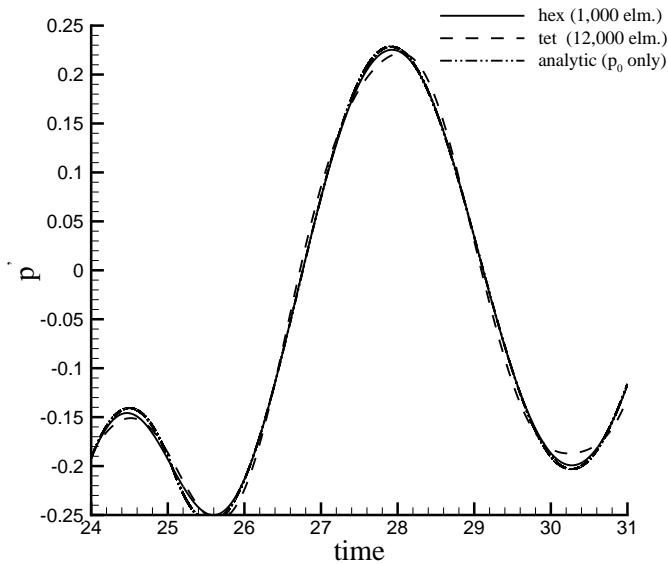

FIGURE 5.3: *A detailed view of the comparison of the time histories of the pressure perturbations at $x = 5.025$, $y = \Delta y/2$, $z = 0.475$. The order of approximation is $p = 1$, $\omega_0 = \frac{4}{3}$, $l = 5$, $a = 0.05$*
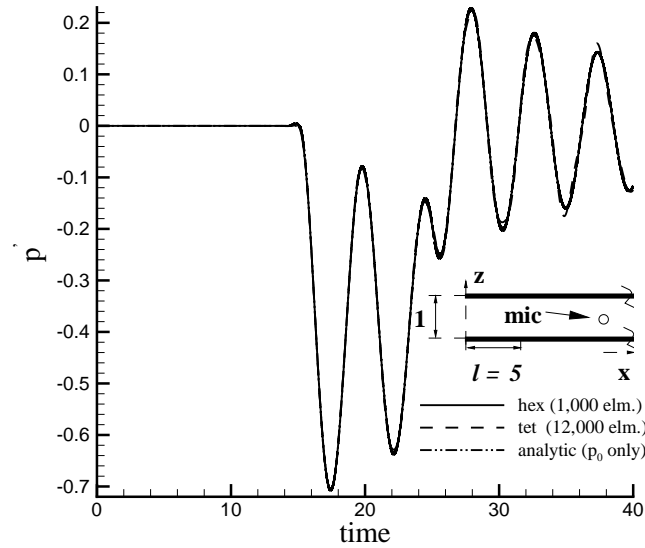
FIGURE 5.4: *Comparison of the time histories of the pressure perturbations at $x = 20.075$, $y=\Delta y/2$, $z = 0.475$. The order of approximation is $p = 1$, $\omega_0 = \frac{4}{3}$, $l = 5$, $a = 0.05$.*

leading to a different CFL number on each mesh. Although the CFL number is small enough for the procedure on the finest mesh to be stable the error due to time discretization has to be expected to be largest on the finest mesh. To truly check the spatial accuracy of the time-dependent solution the semi-discrete (time-converged) solutions have to be used. This has not been presented for the present case.

In figure (5.8) the results obtained for finer meshes are compared with the result obtained for the tetrahedral mesh and the analytical solution (p_0 part only). The figure shows that the results obtained for the hexahedral mesh using 4000 elements ($400 \times 1 \times 10$ mesh) is almost identical to the result obtained for the tetrahedral mesh using 12000 elements. It can be concluded that the DG method applied on hexahedral elements appears to converge faster for $h \to 0$ than the method applied on tetrahedral elements. Two detailed views for various time strips are plotted in figures (5.9) and (5.10).

Figures (5.11), (5.12) and (5.13) show contour plots for the pressure perturbation in the plane $y = \Delta y/2$ at different dimensionless times t_i, together with plots of the pressure perturbation $p(x, \Delta y/2, 0.25, t_i)$. In all three figures the same plotting levels for the contours are used. Only pressure levels between -0.01 and 0.01 have been presented, i.e. every value above $p = 0.01$ is white (see legend), every value below $p = -0.01$ is black. These small pressure levels are convenient to track the

(initially) small perturbations related to the p_d (or p_k) term of the analytical solution. It is noted that the horizontal and vertical coordinate axis used for the contour plot are not of the same scale. Next to each contour plot there is a figure showing the pressure perturbation $p(x, \Delta y/2, 0.25, t_i)$ obtained for the same dimensionless time t_i. The plotting levels in these figures have been adjusted to capture the minimum and maximum pressure perturbation in the duct.

Figure (5.11) presents results for dimensionless times $t = 0.4$, 0.8, 1.2, 1.6, 2.0 and 2.4. At these dimensionless times the flow is not (much) effected by reflections from the top wall of the duct. From $t > 0$ the vibrating wall introduces a perturbation travelling from the vibrating wall at $z = 0$ to the top wall at $z = 1$. The perturbation reaches the top wall at $z = 1$ (at and near $x = 0$) after approximately $t = 1$ dimensionless time units.

Figure (5.12) presents results for dimensionless times $t = 3.2$, 4.4, 5.2, 6.4, 7.2 and 8.0. At these dimensionless times the plane wave pulse p_0, which obtains its pulse shape after $t = 1$, can be observed to move away from the vibrating wall region.

Figure (5.13) presents results for dimensionless times $t = 10.0$, 12.0, 16.0, 20.0, 30.0 and 40.0. At these dimensionless times the plane wave pulse p_0 can be observed to propagate further away in x-direction from the vibrating wall region at the speed of
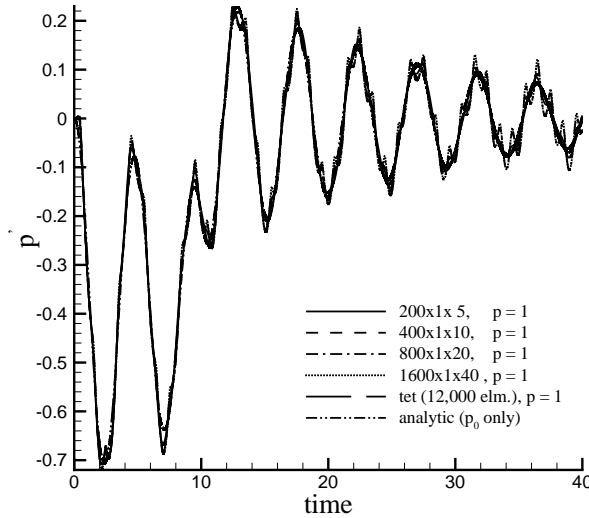

FIGURE 5.5: *A detailed view of the comparison of the time histories of the pressure pertur-bations at $x = 20.075$, $y=\Delta y/2$, $z = 0.475$. The order of approximation is $p = 1$, $\omega_0 = \frac{4}{3}$, $l = 5$, $a = 0.05$.*
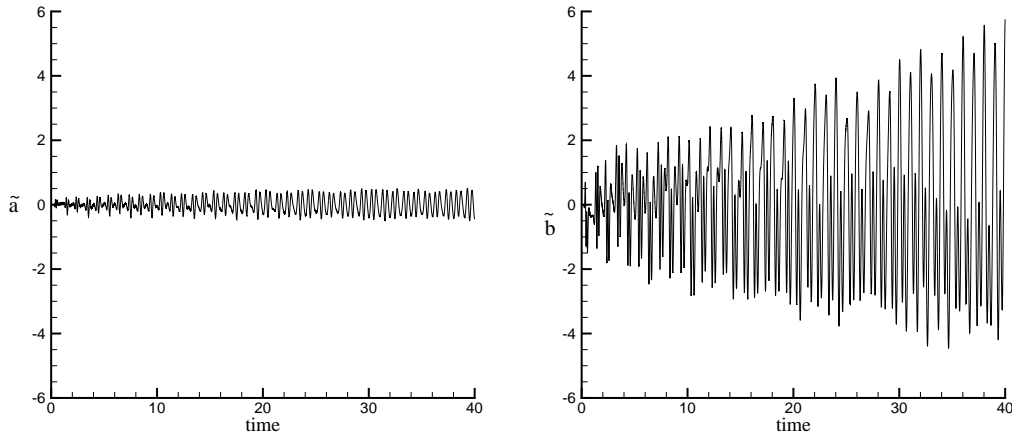
FIGURE 5.6: *The time evaluation of $\tilde{a}(t)$ (left) and $\tilde{b}(t)$ (right).*
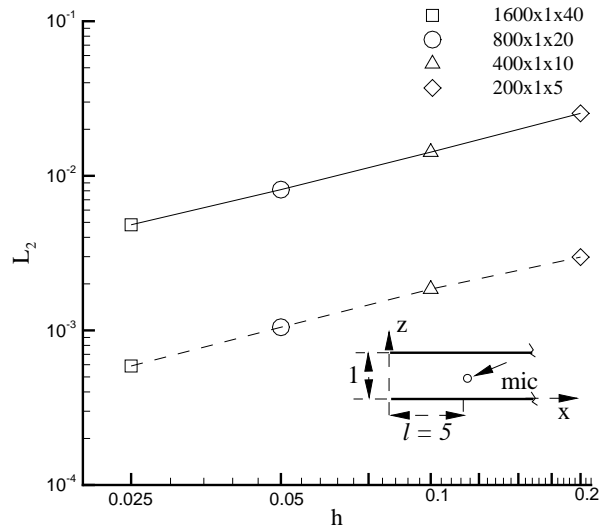
FIGURE 5.7: *L_2-norm of error in time signal of pressure perturbation as function of h at $x = 5.025$, $y = \Delta y/2$, $z = 0.475$ (solid line) and at $x = 20.075$, $y = \Delta y/2$, $z = 0.475$ (dashed line). The order of approximation is $p = 1$.*

sound ($= 1$; it only has a velocity component in x-direction). It should be noted that for the figures for the pressure perturbation $p(x, \Delta y/2, 0.25, t_i)$ the plotting scale for the pressure perturbation is different in all three figures.
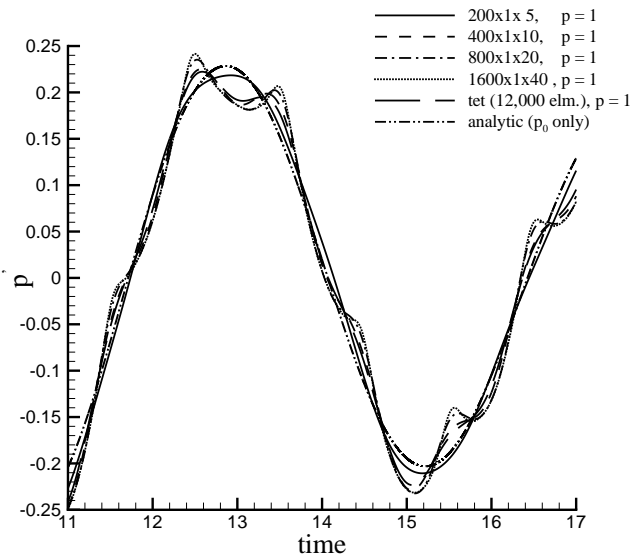
FIGURE 5.8: *Comparison of the time histories of the pressure perturbations at $x = 5.025$, $y=\Delta y/2$, $z = 0.475$ for grid refinement. The order of approximation is $p = 1$, $\omega_0 = \frac{4}{3}$, $l = 5$, $a = 0.05$, $\Delta t = 1.0 \cdot 10^{-3}$.*

In between the vibrating wall and the pulse, pressure perturbations are propagating with the ambient speed of sound as well. However, near the vibrating wall the velocity vector of the pressure perturbations have a significant component in z-direction, while just behind the pulse the velocity component in z-direction has reduced to zero. This can be seen in figure (5.13) by picking a black or white region (for $x > 5$) for $t = 10.0$ and following it until $t = 40.0$. When propagating further away from the vibrating wall the amplitude of the perturbations decreases (except p_0 of course). With increasing time the amplitude of the pressure perturbations, at a fixed x location, increase in amplitude (because of resonance). These pressure fluctuations form an anti-symmetric pattern with respect to $z = 0.5$ in the duct.

5.4.3 p-refinement

Finally, a p-refinement study has been performed. A hexahedral mesh of 1000 ($200 \times 1 \times 5$) elements is used for the second ($p = 1$), third ($p = 2$) and fourth-order ($p = 3$) accurate numerical method. The results are compared with the results obtained by the second-order method on the hexahedral mesh of 64000 ($1600 \times 1 \times 40$) elements and on the tetrahedral mesh of 12000 elements as well as the analytical solution (p_0 part only), see figure (5.14). A closer inspection of the solutions reveals that a fourth-order method on a mesh of 1000 elements gives results very close to the

results obtained using a second-order method on a mesh of 64000 elements. Noting that the time required to advance the numerical solution one time step for the fourth-order method on 1000 elements is about 17 times less (see table (5.1)) than for the second-order method on 64000 elements, it is a considerable gain in terms of computational time. Detailed views for various time strips are plotted in figures (5.15) and (5.16).

The simulations have been performed on SGI Origin200 MIPS RISC R12000 processor with a clock speed of 270 MHz. The time required to advance the solution one time step is shown in table (5.1).

FIGURE 5.9: *A detailed view of the comparison of the time histories of the pressure perturbations at $x = 5.025$, $y=\Delta y/2$, $z = 0.475$ for grid refinement. The order of approximation is $p = 1$, $\omega_0 = \frac{4}{3}$, $l = 5$, $a = 0.05$, $\Delta t = 1.0 \cdot 10^{-3}$.*
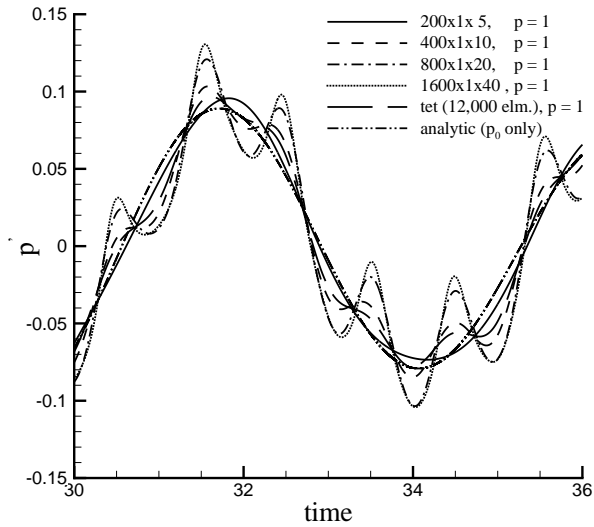
FIGURE 5.10: *A detailed view of the comparison of the time histories of the pressure pertur-bations at $x = 5.025$, $y=\Delta y/2$, $z = 0.475$ for grid refinement. The order of approximation is $p = 1$, $\omega_0 = \frac{4}{3}$, $l = 5$, $a = 0.05$, $\Delta t = 1.0 \cdot 10^{-3}$.*

number of elements	order of accuracy ($p+1$)	CPU time per time step (seconds)
1000	2	0.42
1000	3	0.76
1000	4	1.59
4000	2	1.68
9000	2	3.87
16000	2	6.87
64000	2	27.63

TABLE 5.1: *The time required for the numerical simulations on the hexahedral mesh.*
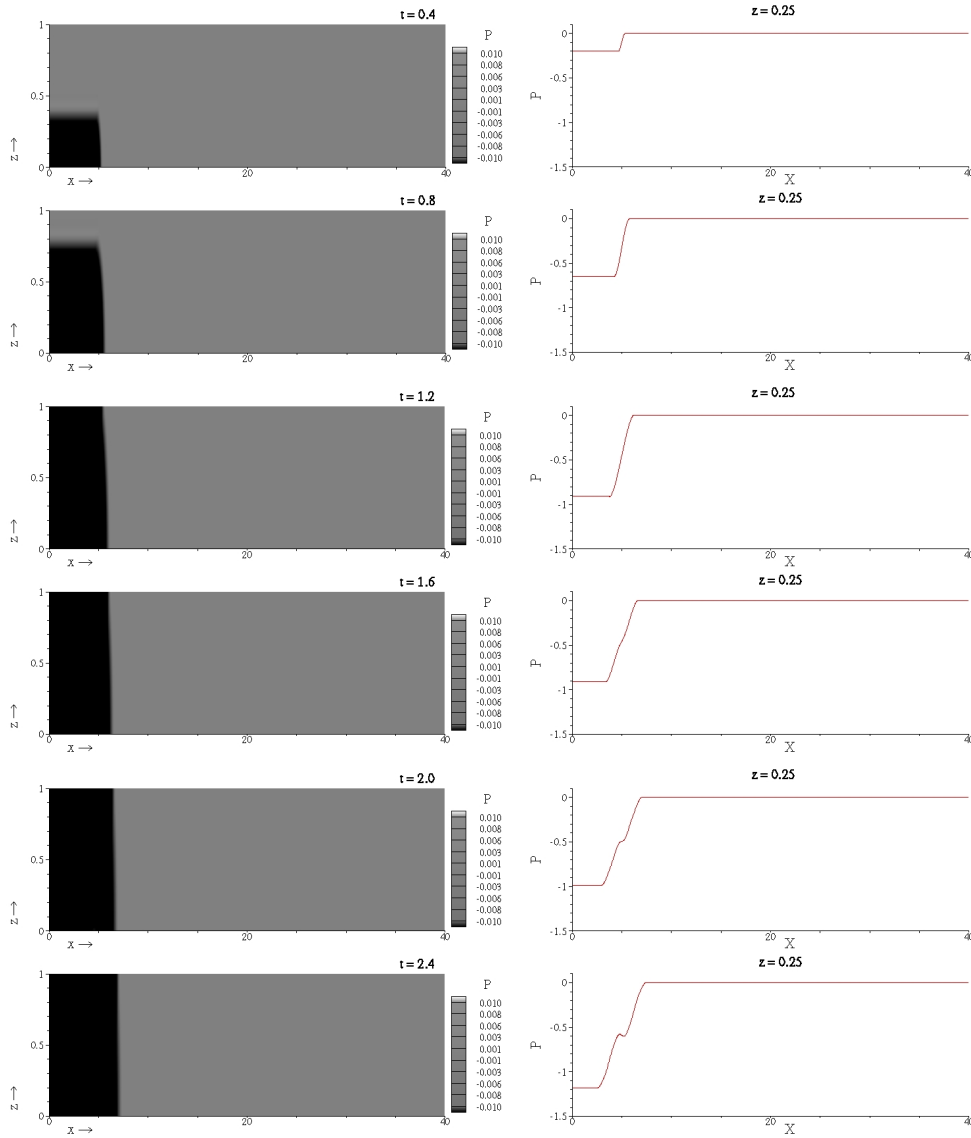
FIGURE 5.11: *Vibrating wall segment $x \in [0, 5]$. Left: Contour plots for the pressure perturbation in the plane $\Delta y/2$ for $t = 0.4$ to 2.4. ($\omega_0 = \frac{4}{3}$, $l = 5$, $a = 0.05$). Right: Pressure perturbation for $\Delta y/2$ and $z = 0.25$. Note the large difference in plotting scales for the pressure. $\Delta x = \Delta y = \Delta z = 0.025$, $\Delta t = 1.0 \cdot 10^{-3}$.*
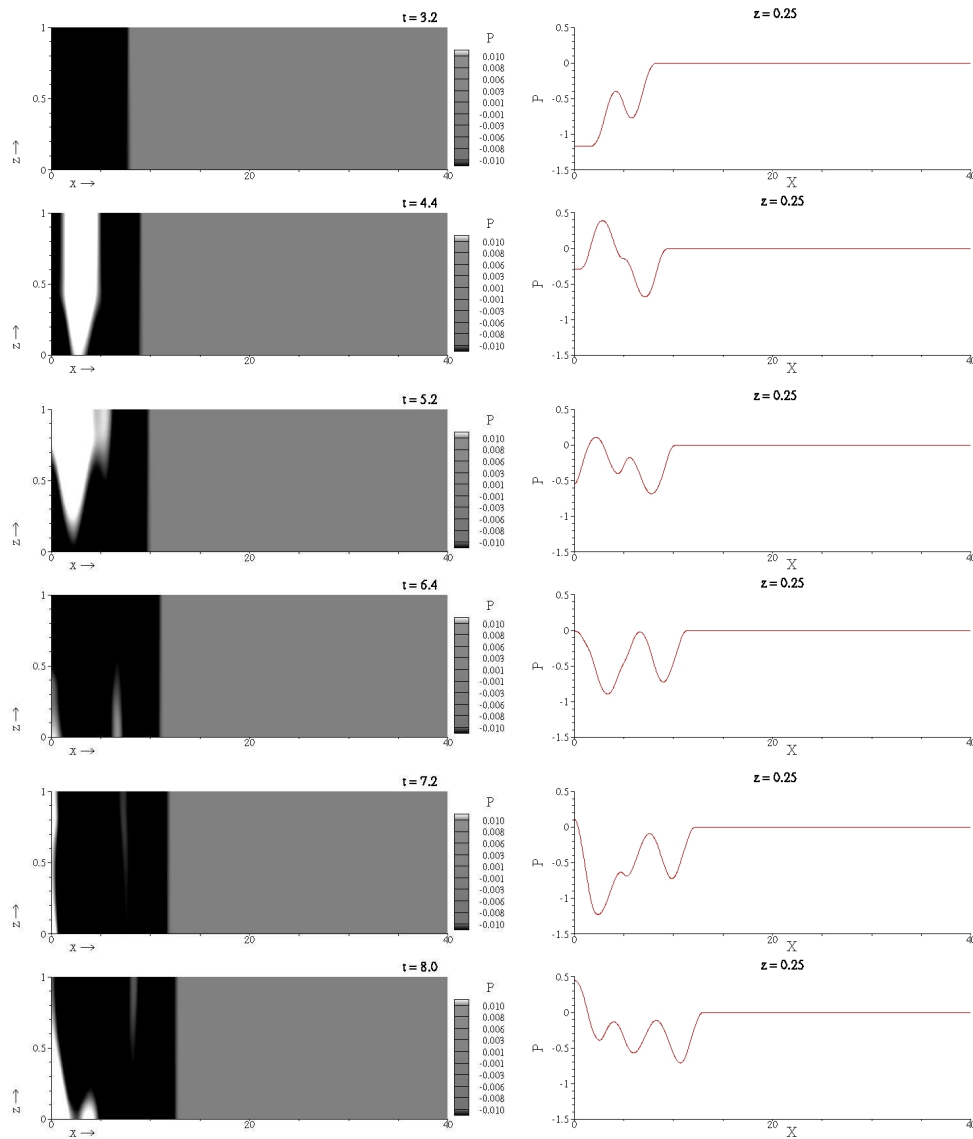
FIGURE 5.12: *Vibrating wall segment $x \in [0, 5]$. Left: Contour plots for the pressure perturbation in the plane $\Delta y/2$ for $t = 3.2$ to 8.0. ($\omega_0 = \frac{4}{3}$, $l = 5$, $a = 0.05$). Right: Pressure perturbation for $\Delta y/2$ and $z = 0.25$. Note the large difference in plotting scales for the pressure. $\Delta x = \Delta y = \Delta z = 0.025$, $\Delta t = 1.0 \cdot 10^{-3}$.*
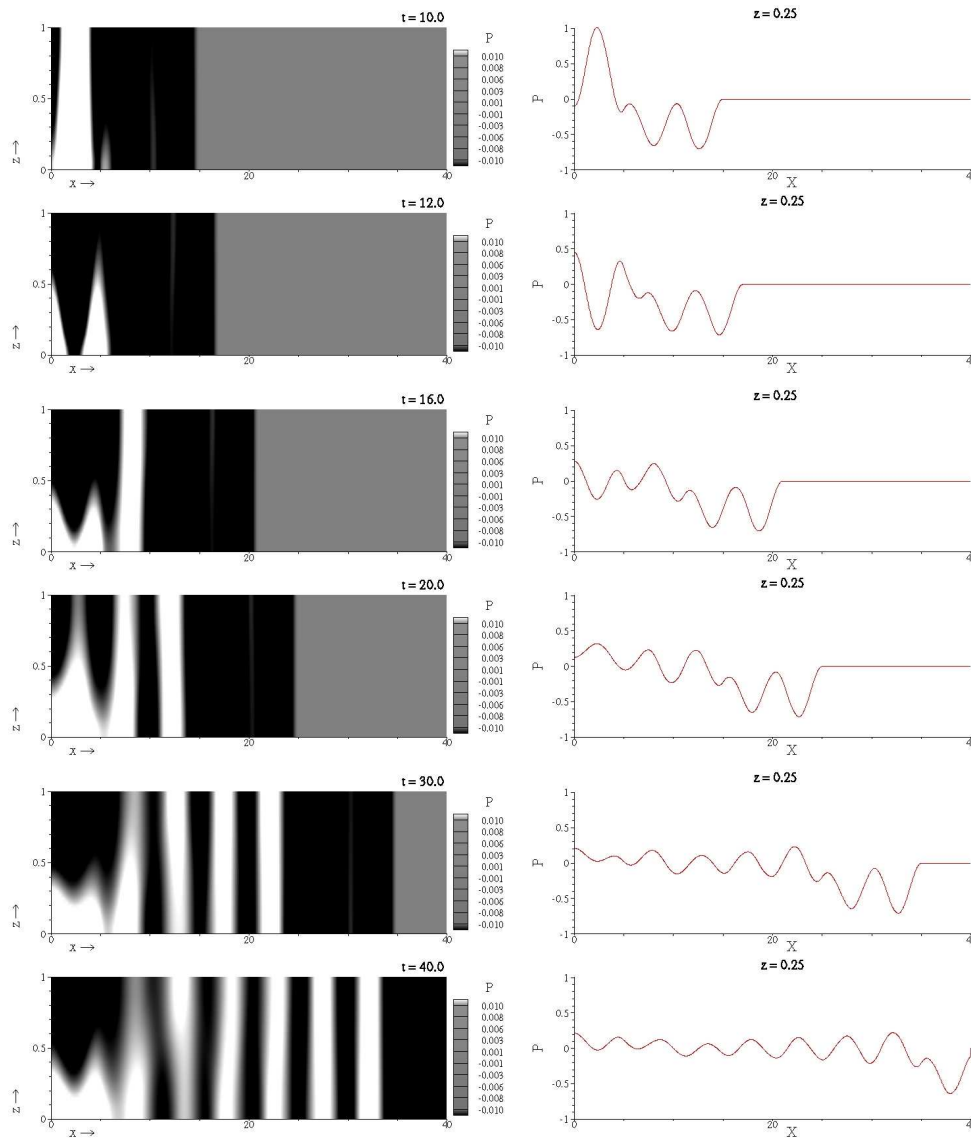
FIGURE 5.13: *Vibrating wall segment* $x \in [0, 5]$. *Left: Contour plots for the pressure perturbation in the plane* $\Delta y/2$ *for* $t = 10.0$ *to* 40.0. *(*$\omega_0 = \frac{4}{3}$, $l = 5$, $a = 0.05$*). Right: Pressure perturbation for* $\Delta y/2$ *and* $z = 0.25$. *Note the large difference in plotting scales for the pressure.* $\Delta x = \Delta y = \Delta z = 0.025$, $\Delta t = 1.0 \cdot 10^{-3}$.
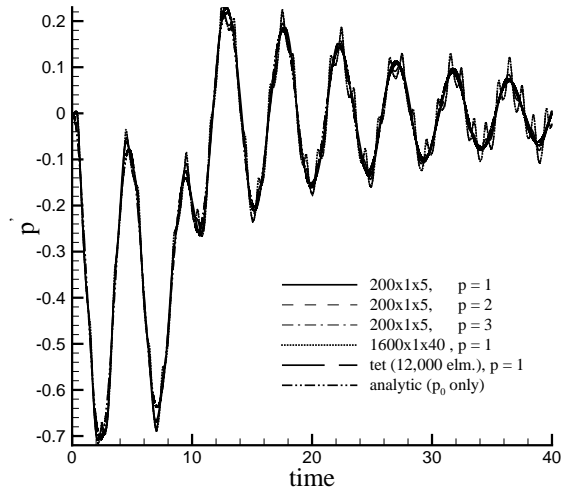
FIGURE 5.14: *Comparison of the time histories of the pressure perturbations at $x = 5.025$, $y = \Delta y/2$, $z = 0.475$ for p refinement. $\omega_0 = \frac{4}{3}$, $l = 5$, $a = 0.05$, $\Delta t = 1.0 \cdot 10^{-3}$.*
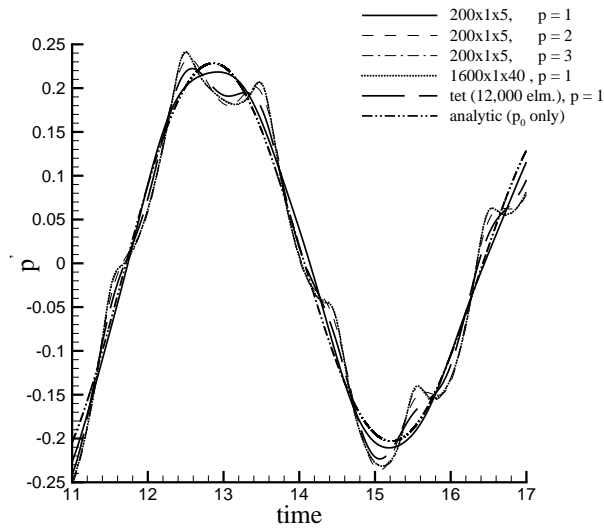
FIGURE 5.15: *A detailed view of the comparison of the time histories of the pressure perturbations at $x = 5.025$, $y = \Delta y/2$, $z = 0.475$ for p refinement. $\omega_0 = \frac{4}{3}$, $l = 5$, $a = 0.05$, $\Delta t = 1.0 \cdot 10^{-3}$.*
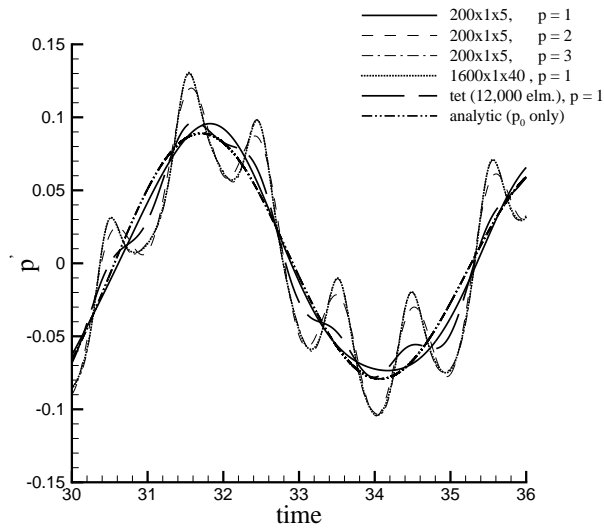
FIGURE 5.16: *A detailed view of the comparison of the time histories of the pressure pertur-*
bations at $x = 5.025$, $y=\Delta y/2$, $z = 0.475$ for p refinement. $\omega_0 = \frac{4}{3}$, $l = 5$, $a = 0.05$, $\Delta t =$
$1.0 \cdot 10^{-3}$.

5.5   Velocity Boundary Condition

5.5.1   Introduction

In the solution presented in the previous sections of this chapter the normal velocity profile $\psi(x, y, t)$ is described and the wall displacement $z_s(x, y, t)$ is reconstructed. In certain cases prescribing the velocity profile might lead to non-realistic wall displacements or it might not be possible to obtain the actual wall displacement without using numerical quadrature. Hence, it is more logical to choose the wall displacement $z_s(x, y, t)$ and derive the normal velocity profile $\psi(x, y, t)$ from it.

In this section the problem described in section 5.2 has been solved by prescribing the wall displacement $z_s(x, y, t)$ instead of the normal velocity profile $\psi(x, y, t)$. Note that, prescribing the wall displacement $z_s(x, y, t)$ as it is derived from the velocity profile $\psi(x, y, t)$ in the previous sections will result in identical results. Thus, the aim of this section is to choose a wall displacement $z_s(x, y, t)$ and perform the simulations accordingly.

5.5.2   Numerical Results

Let us now consider the following wall displacement:

$$z_s(x, y, t) = cos(\chi_n x) sin(\omega_0 t) H(t). \tag{5.15}$$

The normal velocity profile $\psi(x, y, t)$ can be derived from the wall displacement as follows:

$$-\psi(x, y, t) = \frac{\partial z_s}{\partial t} + M \frac{\partial z_s}{\partial x}, \tag{5.16}$$

inserting equation Eq. (5.15) into Eq. (5.16) leads in to the normal velocity profile $\psi(x, y, t)$ of the following form:

$$\psi(x, y, t) = \omega_0 \cos(\chi_n x) \sin(\omega_0 t) - M \chi_n \sin(\chi_n x) \sin(\omega_0 t) \tag{5.17}$$

together with $\omega_0 = 1$, $\chi_n = \frac{n\pi}{2l}$ and the length of the vibrating part of the wall $l = 1$. The simulations are performed on a hexahedral mesh with 400x1x5 elements in $x-$, $y-$ and $z-$directions respectively for a computational domain which is given by $x \in [-40, 40]$, $y \in [0, \Delta y]$ and $z \in [0, 1]$. The results are obtained for the case without mean flow ($M = 0.0$) as well as with the mean flow for $M = 0.1$ and 0.2 where the mean flow velocity vector, expressed as Mach-number components, is given by $(M, 0, 0)^T$.

Figure (5.17) presents the comparison of the time histories of the pressure perturbations at $x = 20.075$, $y = \Delta y/2$ and $z = 0.475$ for $M = 0.0$, 0.1 and 0.2. It is clear that with increased mean flow velocity M, the signal from the vibrating wall
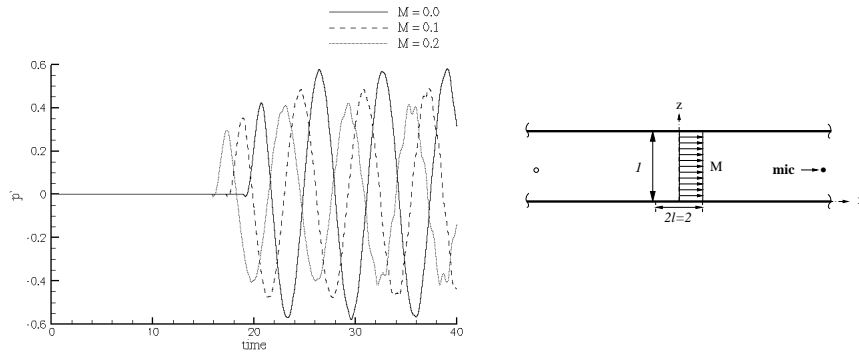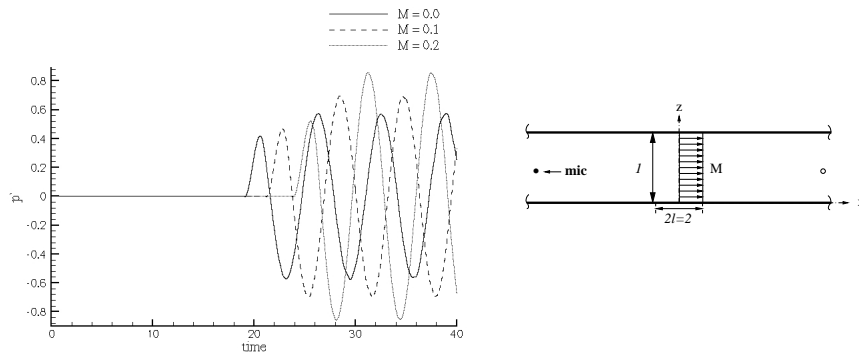
FIGURE 5.17: *Comparison of the time histories of the pressure perturbations at $x = 20.075$, $y=\Delta y/2$, $z = 0.475$ for $M = 0.0$, 0.1 and 0.2 for the case of prescribed wall displacement z_s. $\omega_0 = 1$, $l = 1$, $a = 0.0$, $\Delta x = \Delta y = \Delta z = 0.2$, $\Delta t = 1.0 \cdot 10-3$.*

reaches the microphone earlier, as expected. It is also observed that for $M > 0$ the amplitude has decreased while the observed frequency of the signal does not change.

Figure (5.18) presents the comparison of the time histories of the pressure perturbations at $x = -20.075$, $y = \Delta y/2$ and $z = 0.525$ for $M = 0.0$, 0.1 and 0.2. As expected, at a microphone location at a certain upstream distance from the vibrating wall, the signal is observed later than in the case $M = 0$. From the figure it is furthermore observed that for $M > 0$ the measured pressure amplitude is larger upstream than for $M = 0$. The observed frequency of the signal, again, is not changed.

FIGURE 5.18: *Comparison of the time histories of the pressure perturbations at $x = -20.075$, $y=\Delta y/2$, $z = 0.525$ for $M = 0.0$, 0.1 and 0.2 for the case of prescribed wall displacement z_s. $\omega_0 = 1$, $l = 1$, $a = 0.0$, $\Delta x = \Delta y = \Delta z = 0.2$, $\Delta t = 1.0 \cdot 10-3$.*
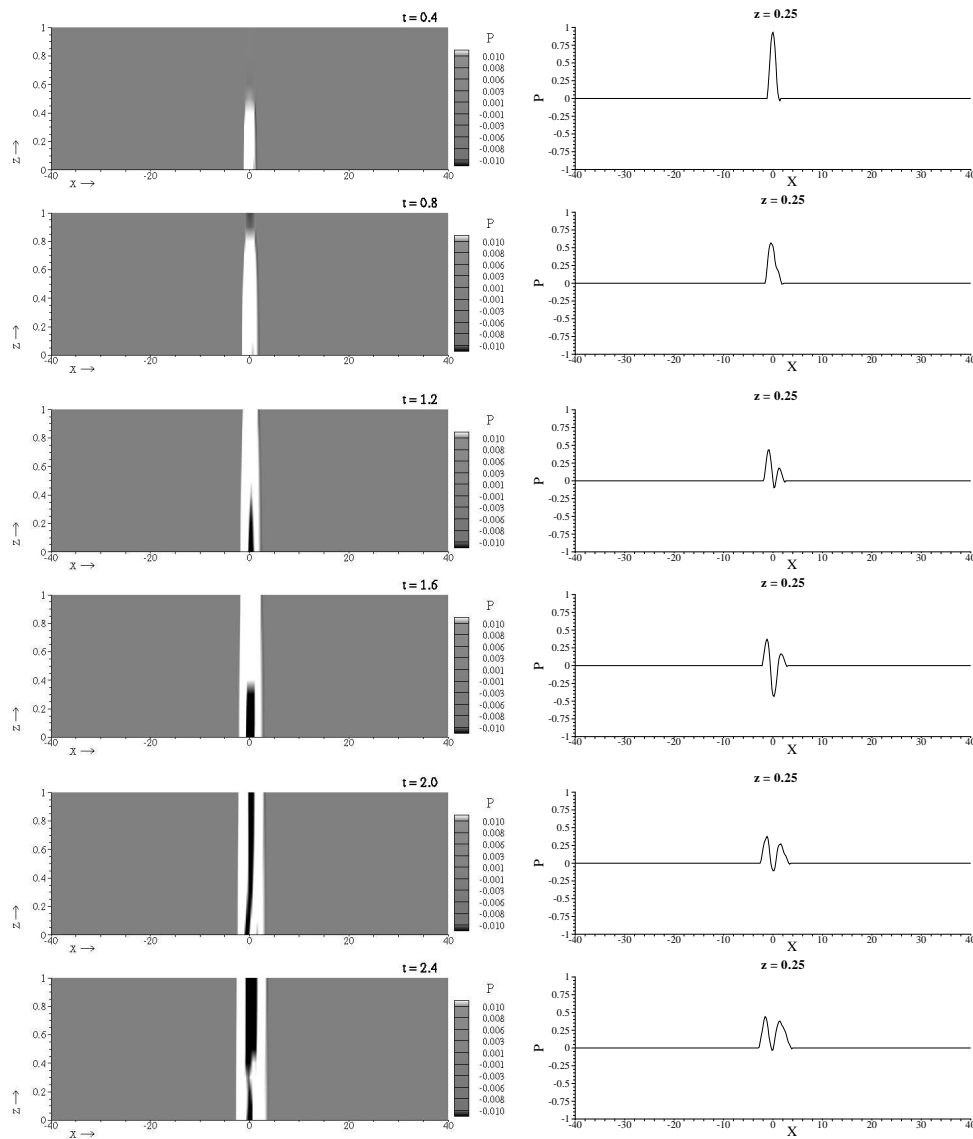
FIGURE 5.19: *Vibrating wall segment $x \in [-5, 5]$. Left: Contour plots for the pressure perturbation in the plane $\Delta y/2$ for $t = 0.4$ to 2.4. ($\omega_0 = \frac{4}{3}$, $l = 5$, $a = 0.05$). Right: Pressure perturbation for $\Delta y/2$ and $z = 0.25$. Note the large difference in plotting scales for the pressure ($\Delta x = \Delta y = \Delta z = 0.025$, $\Delta t = 1.0 \cdot 10^{-3}$).*
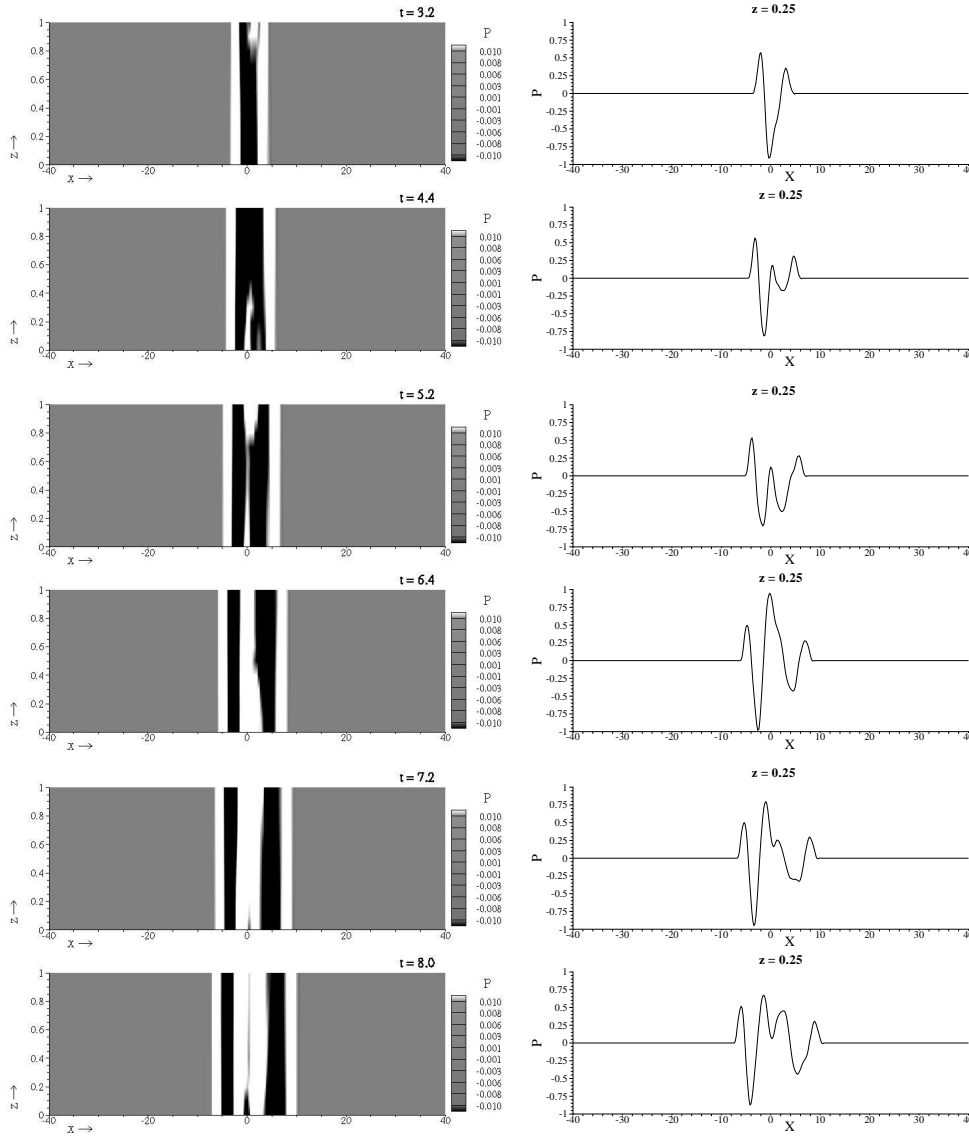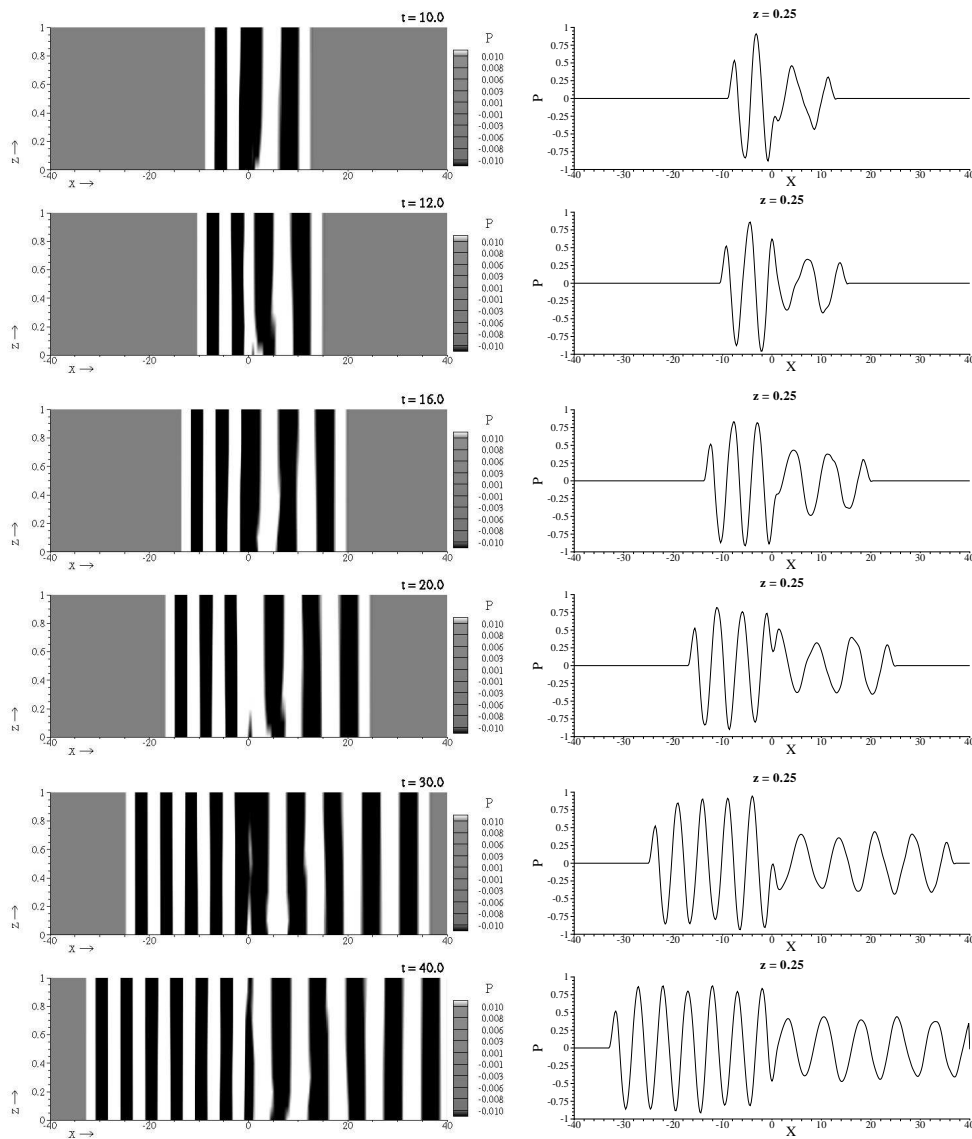
FIGURE 5.20: *Vibrating wall segment $x \in [-5, 5]$. Left: Contour plots for the pressure perturbation in the plane $\Delta y/2$ for $t = 3.2$ to 8.0. ($\omega_0 = \frac{4}{3}$, $l = 5$, $a = 0.05$). Right: Pressure perturbation for $\Delta y/2$ and $z = 0.25$. Note the large difference in plotting scales for the pressure ($\Delta x = \Delta y = \Delta z = 0.025$, $\Delta t = 1.0 \cdot 10^{-3}$).*

FIGURE 5.21: *Vibrating wall segment* $x \in [-5, 5]$. *Left: Contour plots for the pressure perturbation in the plane $\Delta y/2$ for $t = 10.0$ to 40.0. ($\omega_0 = \frac{4}{3}$, $l = 5$, $a = 0.05$). Right: Pressure perturbation for $\Delta y/2$ and $z = 0.25$. Note the large difference in plotting scales for the pressure ($\Delta x = \Delta y = \Delta z = 0.025$, $\Delta t = 1.0 \cdot 10^{-3}$).*

Effects of Grid Distortion

6.1 Introduction

Throughout this thesis hexahedral elements are used in the numerical algorithm, with the shape of the elements restricted to parallelepipeds, for the sake of retaining a linear transformation from physical to the computational coordinates. It is clear that for solution domains with complex geometries we have to resort to more general hexahedral elements and the approach of a linear(ized) transformation will be inadequate, or rather constitutes an approximation. In this chapter the effect of non-parallelepiped elements, i.e. of grid distortion is investigated considering two cases. In the first case the grid is skewed at a certain angle while keeping the shape of the elements as parallelepiped and in the second case the grid is randomly distorted, violating the restriction to parallelepiped elements. In the skewed mesh case both the *inflow* and the *outflow* boundaries of the domain are also skewed while in the randomly distorted mesh the domain boundaries are retained as (*y,z*)-planes.

In the context of this chapter the problem considered in the preceding chapter of the vibrating wall segment is re-visited since it is advantageous to consider a problem for which the results are similar and can be used as a guide line. Also the problem considered is 2D which allows us to investigate the effects of grid distortion more clearly.

Note that the present duct configuration is different from the one in chapter 5 in that of the duct is shorter, i.e. $x \in [0, 10]$ rather than $x \in [0, 40]$, which saves computing time, and we wish to consider the near-field wave pattern. Furthermore, the length of the vibrating wall segment has now been chosen as $x \in [0, 2.5]$ rather than $x \in [0, 5]$, in order to capture the near-field within the domain considered. The plane $x = 0$ is a plane of symmetry for the configuration, but as in chapter 5 whenever appropriate, we consider the whole configuration, i.e. $x \in [-10, 10]$. In all cases we take $\omega_0 = \frac{4}{3}$ and $a = 0.05$. In the following sections the effect of grid distortion is analyzed for the two types of grid distortion considered and the numerical results are discussed.
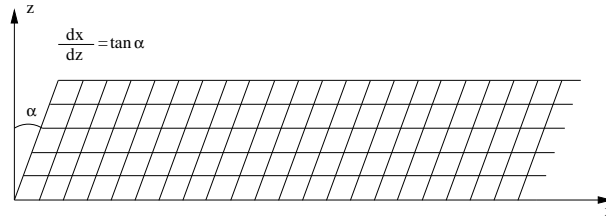
FIGURE 6.1: *Skewed mesh for $\alpha = 10$ deg.*

6.2 Skewed Mesh

In this section the effect of a skewed grid is analyzed. In the skewed grid case the elements are restricted to parallelepipeds as in the previous chapters. The faces of the solution domain that coincide with the $x - z$ plane are skewed at a certain angle "α" and then partitioned into equally sized cells with opposite faces that are parallel. The mesh is shown in figure (6.1). In total three angles are considered namely $\alpha = 2.5$, $\alpha = 5$ and $\alpha = 10$ deg.

6.2.1 Numerical Results

The simulations have been performed for a quiescent background ($M = 0$). For the skewed mesh case the problem cannot be assumed geometrically symmetrical with respect to the $x = 0$ plane, thus the whole domain is considered. The parallelepiped domain is given by $x \in [-10 + z tan\alpha, 10 + z tan\alpha]$, $y \in [0, \Delta y]$ and $z \in [0, 1]$, where all lengths are non-dimensional and Δy is the size of the element in y-direction. At the end planes of the duct, the characteristic non-reflecting boundary conditions are applied, while solid-wall boundary conditions are applied at the other walls except the vibrating wall segment. The location of $x_{max}(= 10)$ is chosen such that the plane wave does not reach the boundary in the time considered in the simulation. The hexahedral mesh is obtained as explained above. The problem is two-dimensional but the method for three-dimensional wave-propagation problems is applied to obtain the numerical results.

During the computations the solution obtained at the cell centers and subsequently as a post-processing the values at all element corner points are evaluated using the basis functions. The node values are then obtained by averaging over all corner points of the cells that are common to more than one element. Additionally a time history of the perturbation variables is recorded at certain locations (not necessarily a node point or a centroid) throughout the rectangular duct. These locations are called *microphone* locations. The solution at the microphone location is obtained directly from the solution using the base functions.

In the preceding chapter the need for a grid refinement study has already been discussed. In the light of that discussion a similar grid convergence study is also

performed here using three different hexahedral meshes: one with $200 \times 1 \times 10$, one with $400 \times 1 \times 20$ and the final one with $800 \times 1 \times 40$ elements in x-, y- and z-directions, respectively.

The upper part of figures (6.2) and (6.3) shows the time histories of the pressure perturbation for the skewness angle $\alpha = 2.5$ deg, recorded at ($x = 3.0125$, $y = \Delta y/2$, $z = 0.0125$) and ($x = 9.0125$, $y = \Delta y/2$, $z = 0.0125$), respectively, while the lower part shows a detailed view. These microphone positions are chosen such that they are at the centroid of an element of the finest mesh and away from the edges of the elements of the coarser meshes. In figures (6.2) and (6.3) results of the method for various mesh sizes are compared with the solution obtained on the finest cartesian mesh ($\alpha = 0$) at the same microphone positions. The results show that a grid distortion of $\alpha = 2.5$ deg skewness angle does not affect the solution very much. These time histories of the pressure perturbations at a location close to the vibrating segment, i.e. figure (6.2), clearly show the wave originating from the oscillatory segment and the wave reflected from the top wall. At the location further away from the vibrating segment the wave is almost one-dimensional.

Similar plots are shown for the grid distortion skewness angle $\alpha = 5$ and 10 deg in figures (6.4) to (6.7). These results indicate that the solution is affected somewhat more for larger values of α, but remains fairly limited for the degree of distortion considered.

In figures (6.8) and (6.9) the time histories of the pressure perturbation is plotted showing a comparison between the results for various values of the grid distortion angle for the finest mesh at $x = 3.0125$ and $x = 9.0125$, respectively. If the solution for $\alpha = 0$ (undistorted case) is taken as a reference then it can be concluded that when increasing the grid distortion angle the deviation from the undistorted case increases gradually.

In the left parts of figures (6.10, 6.11 and 6.12) contour plots for the pressure perturbation in the plane $y = \Delta y/2$ for $t = 0.4$ to 7.2 are shown while in the right parts the pressure perturbations along the (horizontal) line $y = \Delta y/2$, $z = 0.25$ as well as along the (vertical) line $x = 0$, $y = \Delta y/2$ are plotted. This data is for the mesh with $800 \times 1 \times 40$ elements in $x-$, $y-$ and $z-$directions, respectively. These plots show a similar wave pattern as found in chapter 5 for the longer vibrating wall segment. Above, as well as close to the vibrating wall segment, a relatively complex pattern develops, while away from this segment plane waves evolve.
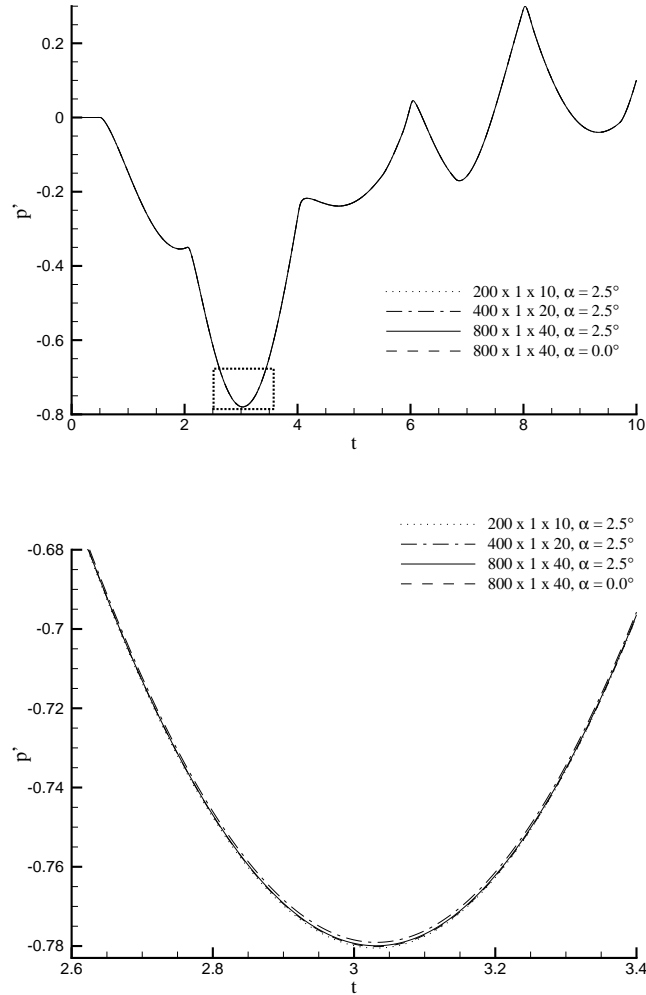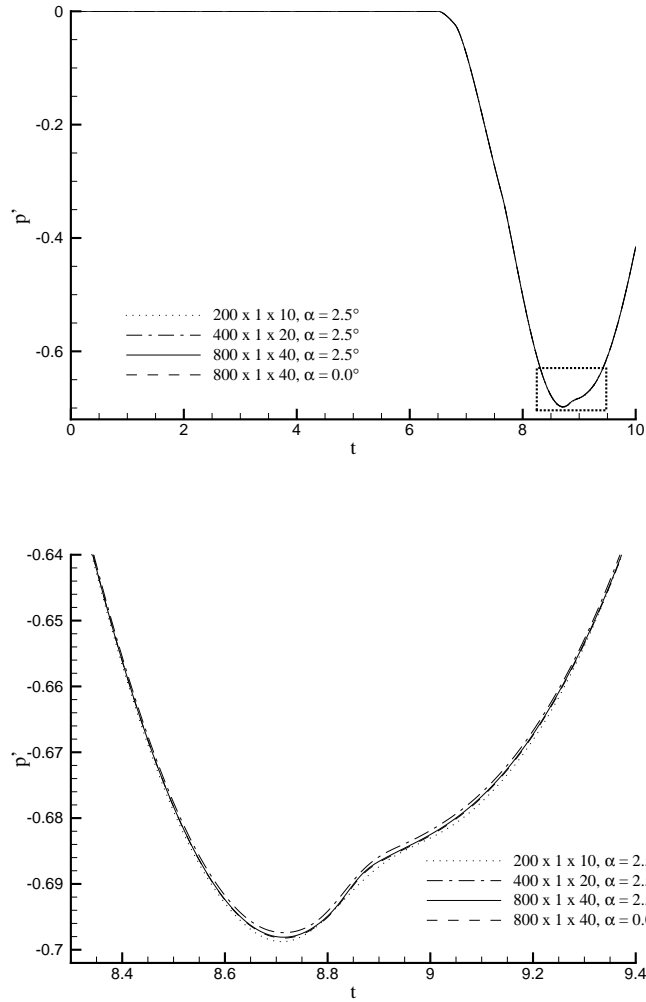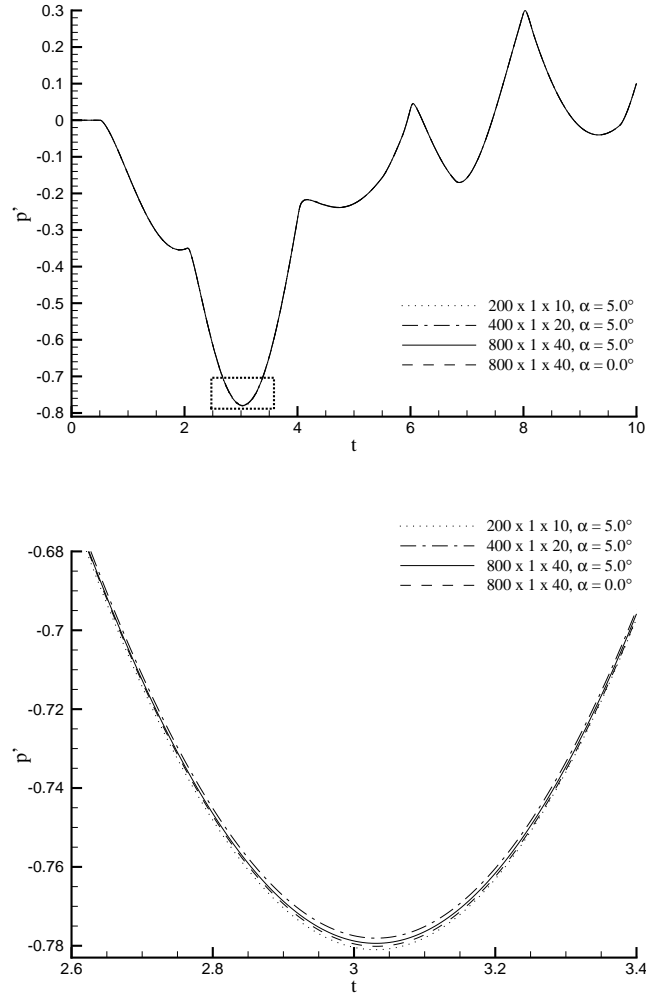
FIGURE 6.2: *Vibrating wall segment* $x \in [-2.5, 2.5]$, $\omega_0 = \frac{4}{3}$, $l = 2.5$, $a = 0.05$. *Comparison of the time histories of* p' *at* ($x = 3.0125$, $y = \Delta y/2$, $z = 0.0125$) *for various mesh sizes for* $\alpha = 2.5$ *deg. (top). Detailed view (bottom). The order of approximation is* $p = 3$.
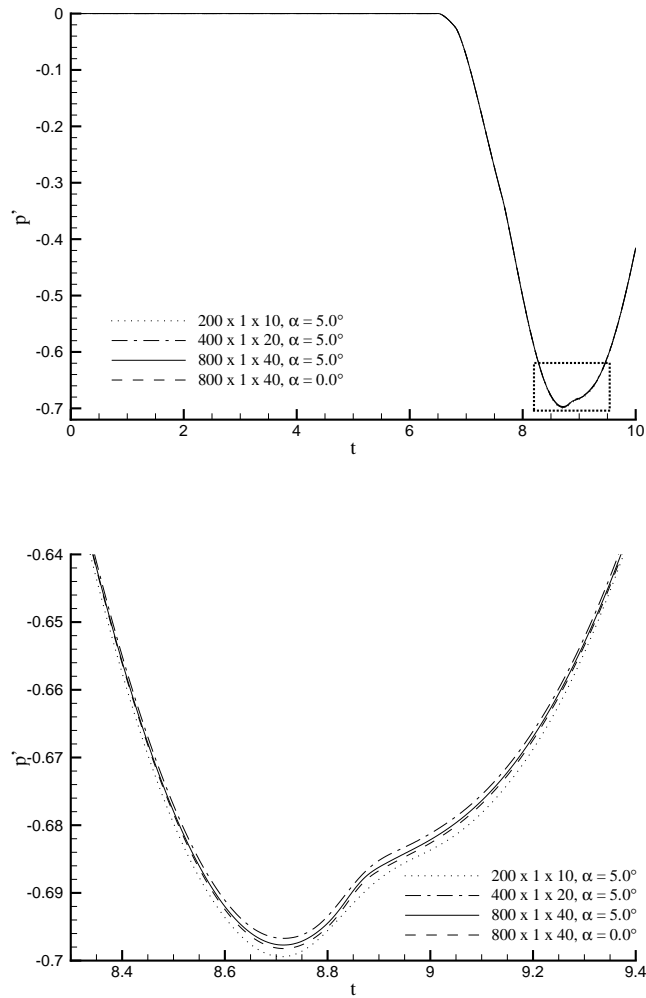
FIGURE 6.3: *Vibrating wall segment* $x \in [-2.5, 2.5]$, $\omega_0 = \frac{4}{3}$, $l = 2.5$, $a = 0.05$. *Comparison of the time histories of* p' *at* $(x = 9.0125$, $y = \Delta y/2$, $z = 0.0125)$ *for various mesh sizes for* $\alpha = 2.5$ *deg. (top). Detailed view (bottom). The order of approximation is* $p = 3$.
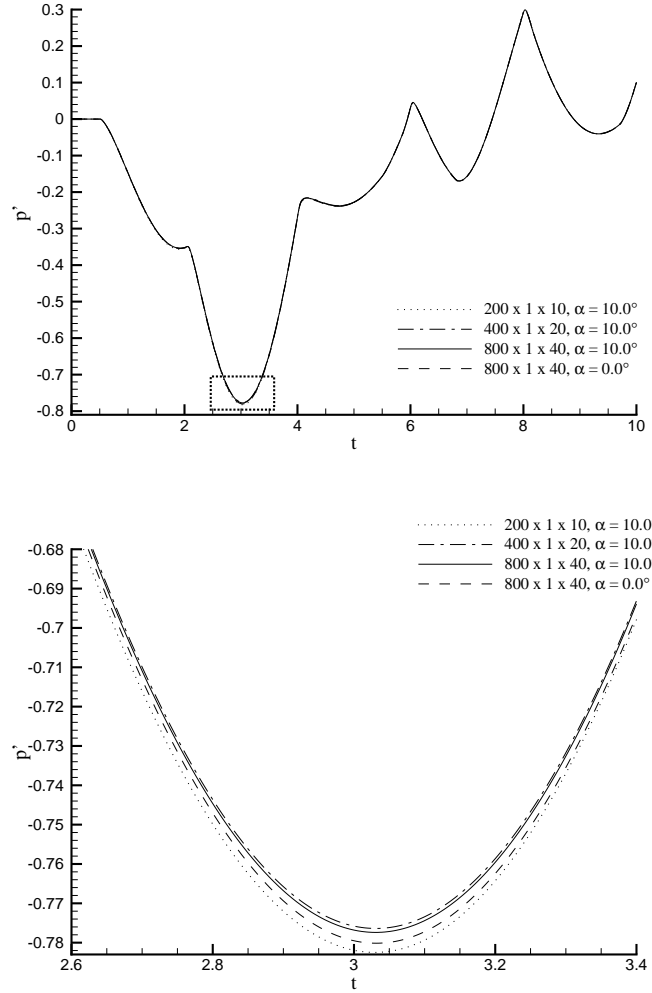
FIGURE 6.4: *Vibrating wall segment $x \in [-2.5, 2.5]$, $\omega_0 = \frac{4}{3}$, $l = 2.5$, $a = 0.05$. Comparison of the time histories of p' at ($x = 3.0125$, $y = \Delta y/2$, $z = 0.0125$) for various mesh sizes for $\alpha = 5$ deg. (top). Detailed view (bottom). The order of approximation is $p = 3$.*

FIGURE 6.5: *Vibrating wall segment $x \in [-2.5, 2.5]$, $\omega_0 = \frac{4}{3}$, $l = 2.5$, $a = 0.05$. Comparison of the time histories of p' at ($x = 9.0125$, $y = \Delta y/2$, $z = 0.0125$) for various mesh sizes for $\alpha = 5$ deg. (top). Detailed view (bottom). The order of approximation is $p = 3$.*
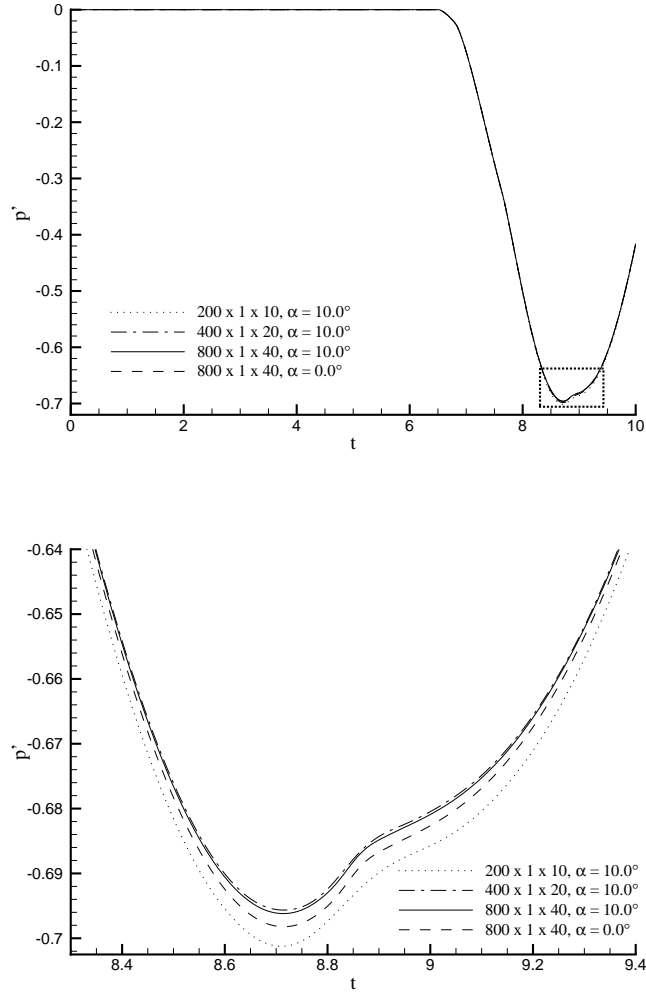
FIGURE 6.6: *Vibrating wall segment $x \in [-2.5, 2.5]$, $\omega_0 = \frac{4}{3}$, $l = 2.5$, $a = 0.05$. Comparison of the time histories of p' at ($x = 3.0125$, $y = \Delta y/2$, $z = 0.0125$) for various mesh sizes for $\alpha = 10$ deg. (top). Detailed view (bottom). The order of approximation is $p = 3$.*
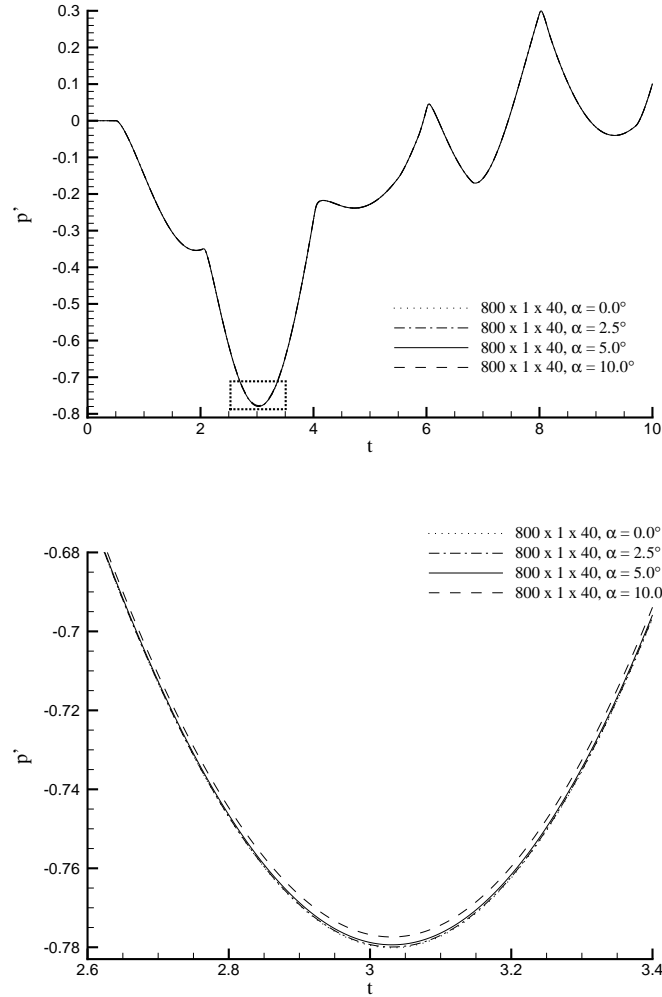
FIGURE 6.7: *Vibrating wall segment $x \in [-2.5, 2.5]$, $\omega_0 = \frac{4}{3}$, $l = 2.5$, $a = 0.05$. Comparison of the time histories of p' at ($x = 9.0125$, $y = \Delta y/2$, $z = 0.0125$) for various mesh sizes for $\alpha = 10$ deg. (top). Detailed view (bottom). The order of approximation is $p = 3$.*

FIGURE 6.8: *Vibrating wall segment* $x \in [-2.5, 2.5]$, $\omega_0 = \frac{4}{3}$, $l = 2.5$, $a = 0.05$. *Comparison of the time histories of* p' *at* $(x = 3.0125$, $y = \Delta y/2$, $z = 0.0125)$ *for 800x1x40 mesh for various values of grid distortion angle* α. *(top). Detailed view (bottom). The order of approximation is* $p = 3$.
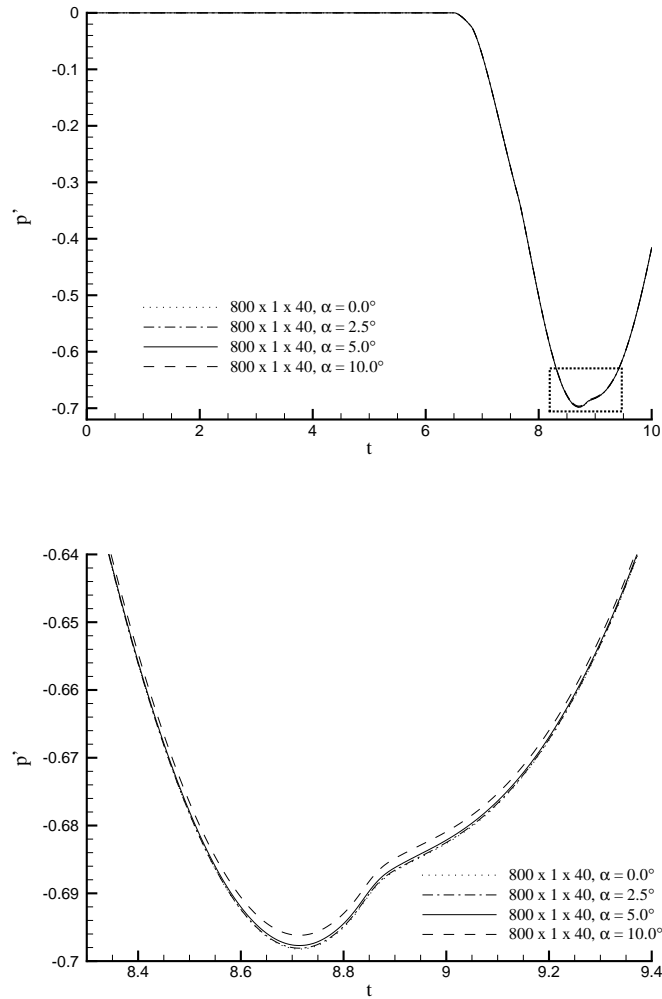
FIGURE 6.9: *Vibrating wall segment $x \in [-2.5, 2.5]$, $\omega_0 = \frac{4}{3}$, $l = 2.5$, $a = 0.05$. Comparison of the time histories of p' at ($x = 9.0125$, $y = \Delta y/2$, $z = 0.0125$) for 800x1x40 mesh for various values of grid distortion angle α. (left). Detailed view (right). The order of approximation is $p = 3$.*
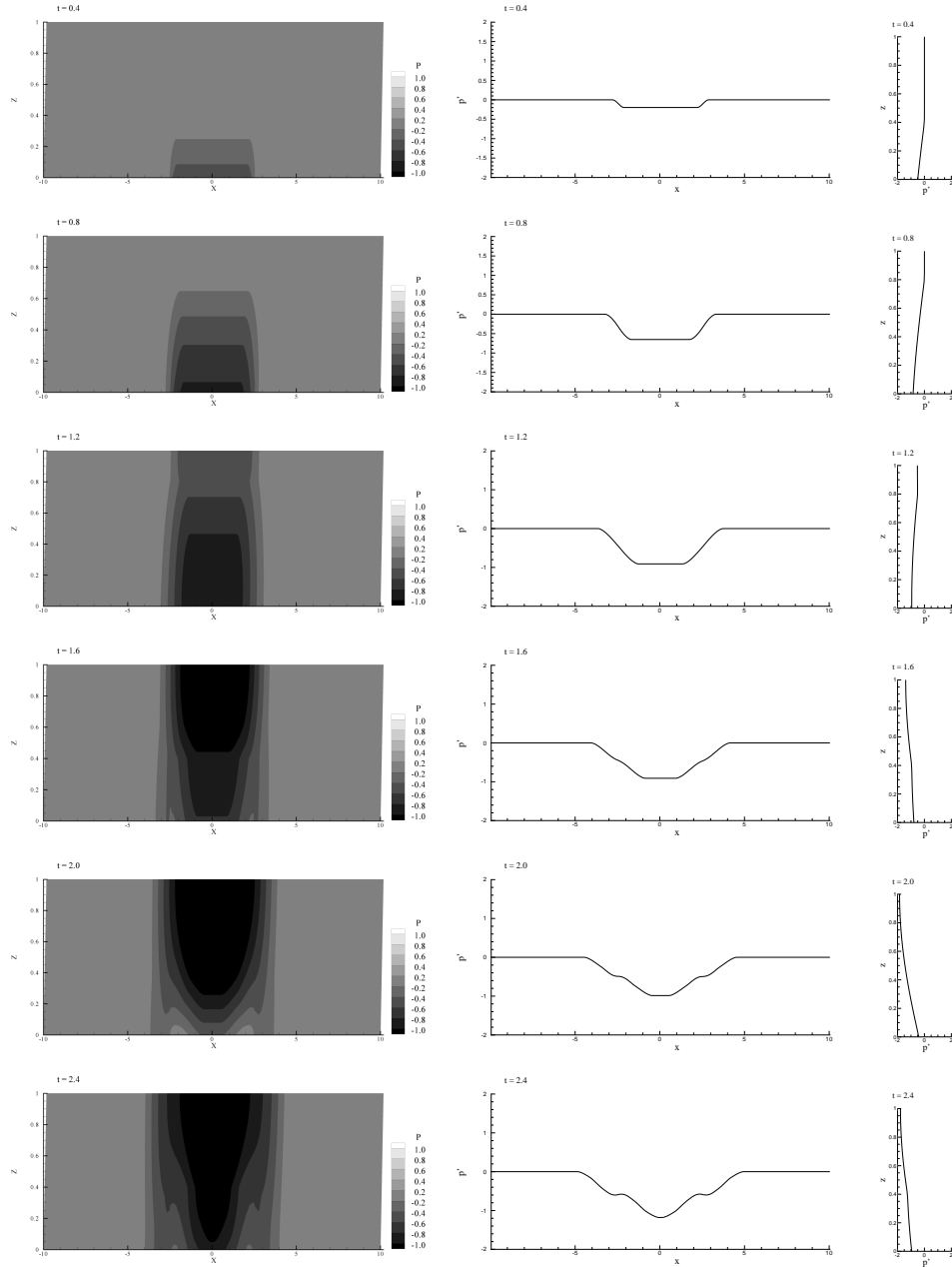
FIGURE 6.10: *Vibrating wall segment $x \in [-2.5, 2.5]$, $\omega_0 = \frac{4}{3}$, $l = 2.5$, $a = 0.05$, $\alpha = 10$ deg. Left: Contour plots for the pressure perturbation in the plane $y = \Delta y/2$ for $t = 0.4$ to 2.4. Middle: Pressure perturbation along line ($y = \Delta y/2$, $z = 0.25$). Right: Pressure perturbation along line ($x = 0$, $y = \Delta y/2$). $\Delta x = \Delta y = \Delta z = 0.025$, $\Delta t = 1.0 \cdot 10^{-3}$.*

FIGURE 6.11: *Vibrating wall segment* $x \in [-2.5, 2.5]$, $\omega_0 = \frac{4}{3}$, $l = 2.5$, $a = 0.05$, $\alpha = 10$ *deg. Left: Contour plots for the pressure perturbation in the plane* $y = \Delta y/2$ *for* $t = 2.8$ *to* 4.8. *Middle: Pressure perturbation along line* ($y = \Delta y/2$, $z = 0.25$). *Right: Pressure perturbation along line* ($x = 0$, $y = \Delta y/2$). $\Delta x = \Delta y = \Delta z = 0.025$, $\Delta t = 1.0 \cdot 10^{-3}$.
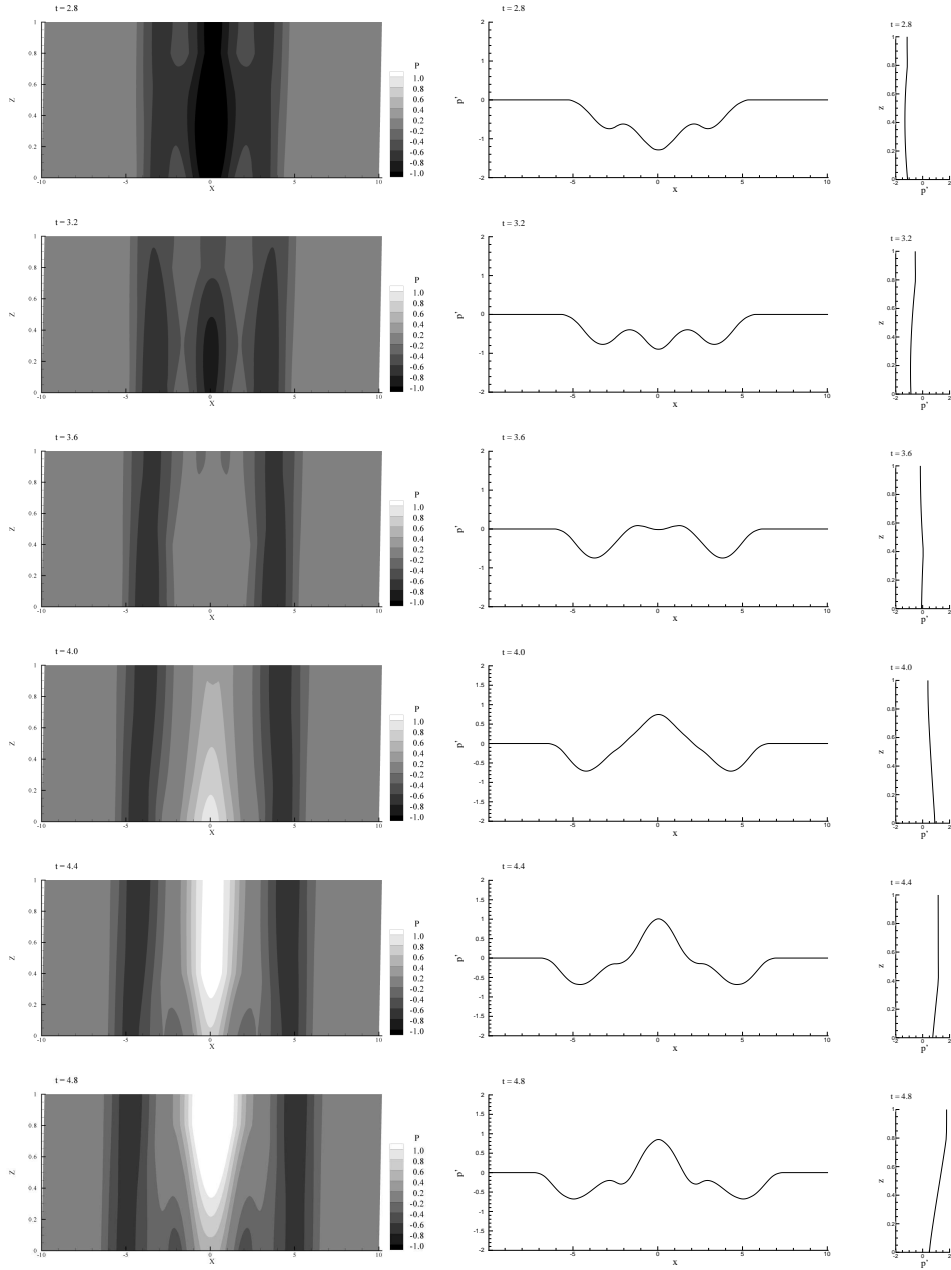
FIGURE 6.12: *Vibrating wall segment $x \in [-2.5, 2.5]$, $\omega_0 = \frac{4}{3}$, $l = 2.5$, $a = 0.05$, $\alpha = 10$ deg. Left: Contour plots for the pressure perturbation in the plane $y = \Delta y/2$ for $t = 5.2$ to 7.2. Middle: Pressure perturbation along line ($y = \Delta y/2$, $z = 0.25$). Right: Pressure perturbation along line ($x = 0$, $y = \Delta y/2$). $\Delta x = \Delta y = \Delta z = 0.025$, $\Delta t = 1.0 \cdot 10^{-3}$.*
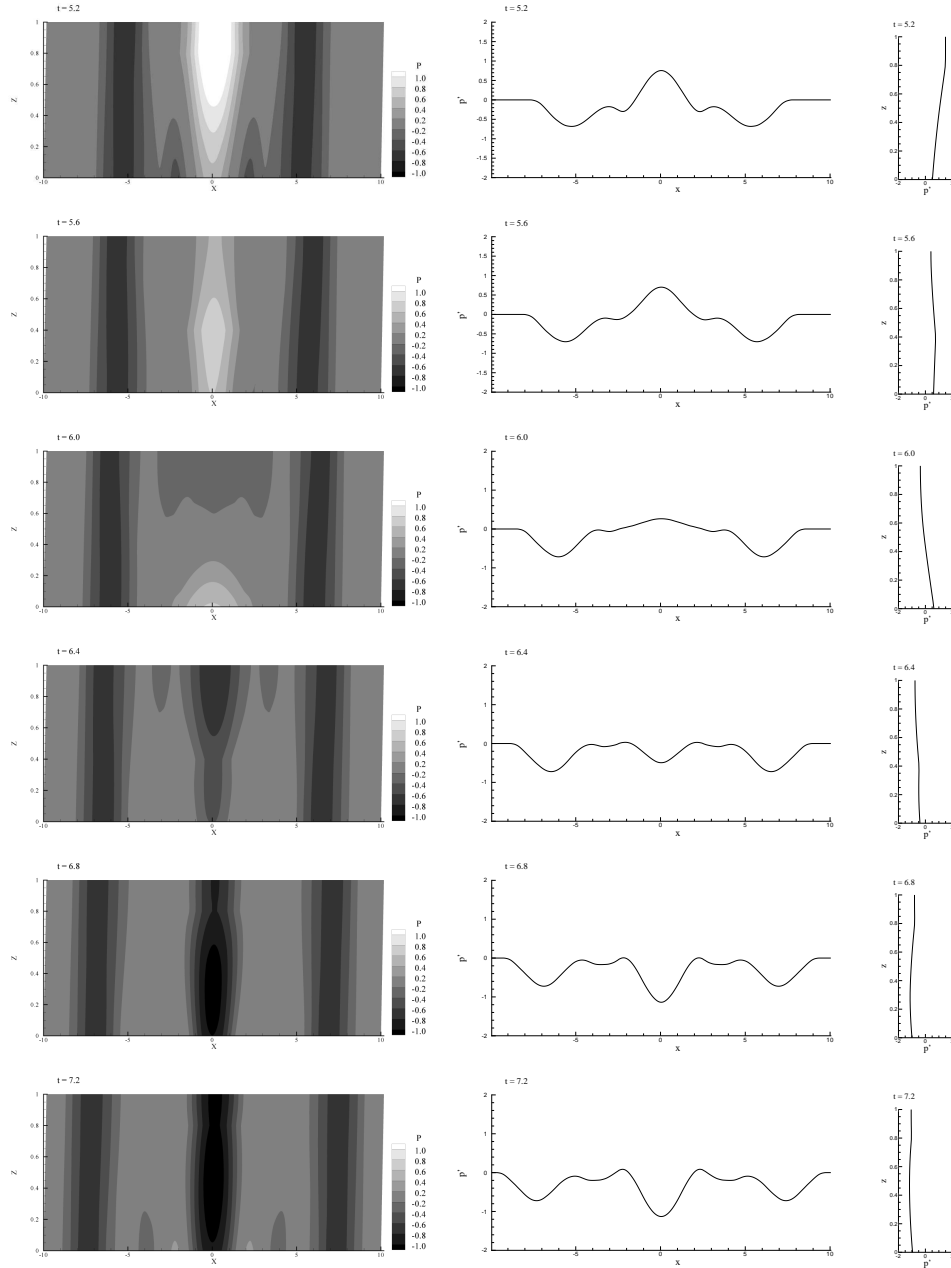
6.2.2   Accuracy

In the preceding section the effect of the skewness angle α is shown in terms of details of the perturbation pressure field. The following analysis is conducted to assess the effect of the grid distortion parameter in terms of L_2-norms of differences between the time histories at two microphone locations. For each angle $\alpha_0 (= 0)$, α_1, α_2 and α_3 and for each mesh size h_1, h_2 and h_3, with h_1 the coarsest and h_3 the finest mesh, we have signal $p'(t; h_i, \alpha_j)$, i.e. there are 12 signals in total for each microphone position considered. Taking the result of the simulation for h_3, $\alpha = 0$ as a reference solution the difference ("*error*") with respect to this solution can be calculated for each angle and mesh size considered, as follows:

$$||\varepsilon||_{ij} = \sqrt{\frac{1}{T} \int\limits_0^T \{p'(t; h_i, \alpha_j) - p'(t; h = h_3, \alpha = 0)\}^2 \, dt} \qquad (6.1)$$

The integral in Eq. (6.1) is approximated by Gaussian quadrature for $0 \leq t \leq T = 10$ using a fixed Δt of 1.0×10^{-3}.

The upper part of figure (6.13) shows the error as function of the angle α for the mesh sizes considered for the order of accuracy $p = 1$ and the lower part for the order of accuracy $p = 3$. It is clear from these figures that the "*error*" decreases with increasing order of accuracy as expected. It can be concluded that for each order, for each mesh considered, the difference increases with increasing grid distortion. The order of magnitude of the effect of grid distortion, for small grid distortions, is of the same order of magnitude as the difference between solutions for different mesh sizes.
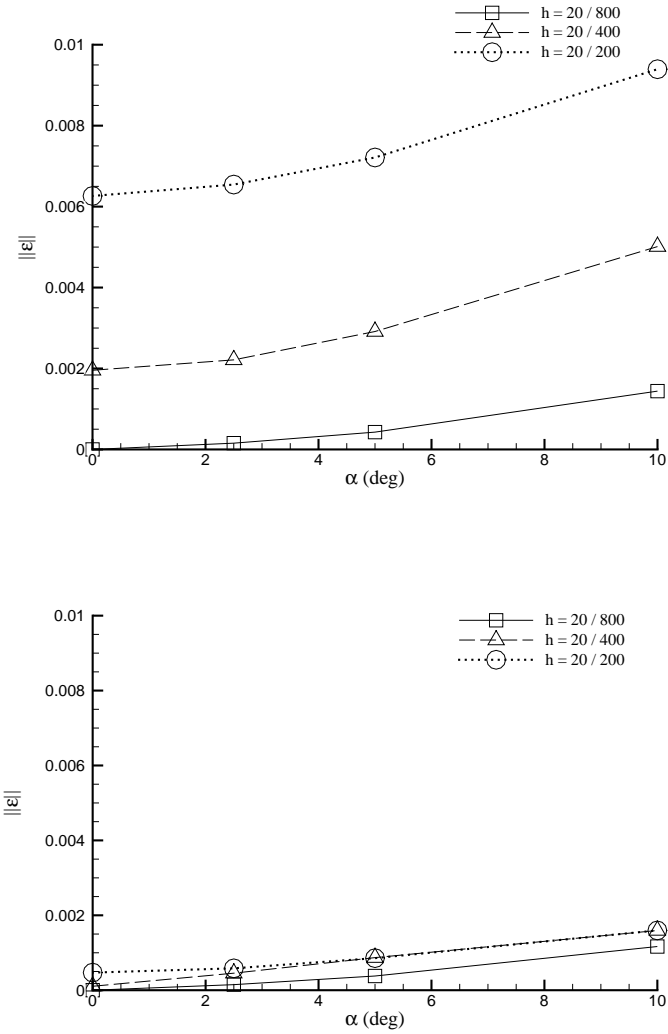
FIGURE 6.13: *Results for vibrating wall segment $x \in [-2.5, 2.5]$, $\omega_0 = \frac{4}{3}$, $l = 2.5$, $a = 0.05$. L_2-norm of difference of time history of pressure perturbation with that of reference solution as function of grid distortion angles for various grid sizes at location ($x = 3.0125$, $y = \Delta y/2$, $z = 0.0125$). Order of approximation is $p = 1$ (top), $p = 3$ (bottom).*

6.3 Randomly Distorted Mesh

In this section the effect of a randomly distorted grid is analyzed. In the randomly distorted grid case the elements are not restricted to parallelepipeds, which differs from the case considered in the preceding section. The hexahedral base mesh is obtained by partitioning the physical domain into equally sized cubes. The base mesh is shown in the left hand side of figure (6.14).
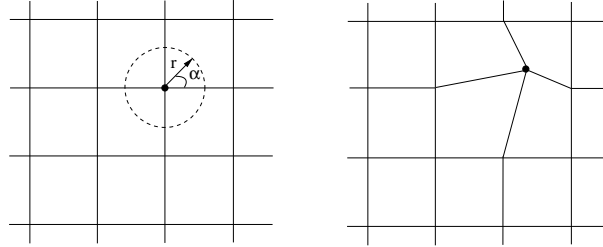

FIGURE 6.14: *Randomly distorted mesh generation.*

For each grid point that does not coincide with the boundary an angle "θ" and a radius "r" are chosen randomly and the new coordinate of the grid point is calculated with the distortion $(\Delta x, \Delta y)^T = r(cos\theta, sin\theta)^T$. The values of r are limited to 2.5, 5 and 10% of the length of the cell edge, here referred as the distortion parameter "d". The right hand side of figure (6.14) shows the distorted grid after one grid point has been processed. Figure (6.15) shows the distorted grid generated for the distortion parameters $d = 2.5$ and $d = 10$, respectively.
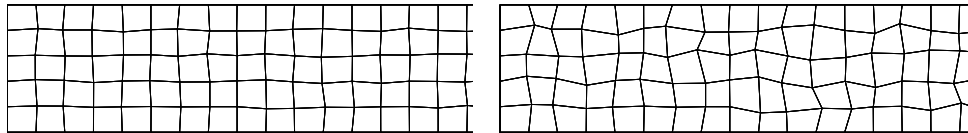

FIGURE 6.15: *Randomly generated mesh distortion for distortion parameters d=2.5 (left) and d=10 (right).*

As can be seen from the figures the grid generated in this way is 2D. Recall that the numerical algorithm used to solve the linearized Euler equations solves the problem in 3D. To keep the 2D nature of the problem the grid generated in 2D is copied in the

third direction while, as before, one cell used in that direction.

6.3.1   Numerical Results

The simulations are performed for a quiescent background ($M = 0$). For the randomly distorted mesh case the mesh is assumed to be symmetrical with respect to the plane $x = 0$. The rectangular domain is given by $x \in [0, 10]$, $y \in [0, \Delta y]$ and $z \in [0, 1]$, where all lengths are non-dimensional and Δy is the size of the element in y-direction. At the end planes of the duct, the characteristic non-reflecting boundary conditions are applied, while solid-wall boundary conditions are applied at the other walls except on the vibrating wall segment. The location of $x_{max}(= 10)$ is chosen such that the plane wave does not reach the boundary in the time considered in the simulation.

During the computations the solution is obtained at the cell centers and subsequently as a post-processing the values at all element corner points are evaluated using the basis functions. The node values are then obtained by averaging over all corner points of the cells that are common to more than one element. Additionally a time history of the perturbation variables is recorded at certain locations (not necessarily a node point) in the rectangular duct. These locations are called *microphone* locations.

In the preceding chapter the need for a grid refinement study has already been discussed. In the light of that discussion a similar grid convergence study is also performed here using three different hexahedral meshes: one with $100 \times 1 \times 10$, one with $200 \times 1 \times 20$ and the final one with $400 \times 1 \times 40$ elements in x-, y- and z-directions, respectively.

The upper parts of figures (6.16) and (6.17) show the time histories of the pressure perturbation for a distortion parameter $d = 2.5$ recorded at ($x = 3.0125$, $y = \frac{1}{2}\Delta y$, $z = 0.5125$) and ($x = 9.0125$, $y = \frac{1}{2}\Delta y$, $z = 0.5125$), respectively, while the lower parts show a detailed view.

A similar plot is shown for the distortion parameters $d = 5$ and 10 in figures (6.18) to (6.21).

In figures (6.22) and (6.23), the time histories of the pressure perturbation is plotted showing a comparison between the various values of the distortion parameter for the finest mesh at ($x = 3.0125$, $y = \frac{1}{2}\Delta y$, $z = 0.5125$) and ($x = 9.0125$, $y = \frac{1}{2}\Delta y$, $z = 0.5125$), respectively. If the solution for the distortion parameter $d = 0$ (undistorted case) is taken as a reference then it can be concluded that increasing the distortion parameter the deviation from the undistorted case increases.

In the left parts of figures (6.24, 6.25 and 6.26) contour plots for the pressure perturbation in the plane $y = \Delta y/2$ for $t = 0.4$ to 7.2 are shown, while in the right parts the pressure perturbation along the line ($y = \Delta y/2$, $z = 0.25$), and the line ($x = 0$, $y = \Delta y/2$) are plotted. This data is for the mesh with $400 \times 1 \times 40$
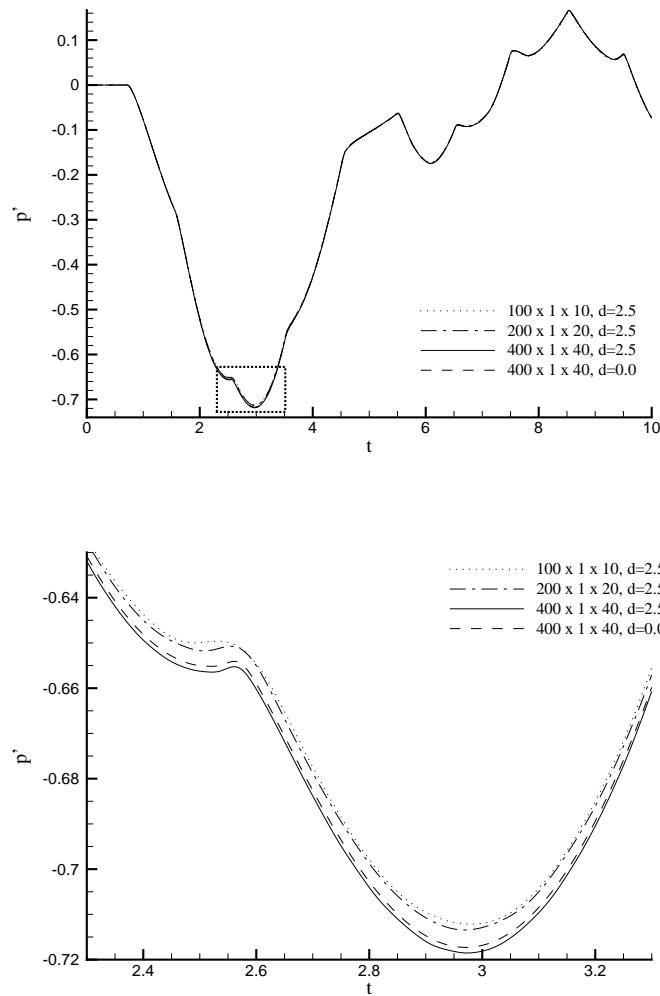
FIGURE 6.16: *Vibrating wall segment $x \in [0, 2.5]$, $\omega_0 = \frac{4}{3}$, $l = 2.5$, $a = 0.05$. Comparison of the time histories of p' at $(x = 3.0125$, $y = \Delta y/2$, $z = 0.5125)$ for various mesh sizes for $d = 2.5$. (top). Detailed view (bottom). The order of approximation is $p = 3$.*

elements in $x-$, $y-$ and $z-$directions, respectively. Comparison of these results with the corresponding results for the skewed mesh show that, judging from these plots, the differences are small.

However, in the results for the randomly distorted mesh small-amplitude wiggles are present in the time-history of the pressure perturbation, figures (6.16 - 6.23), as well as in the snapshots of the pressure perturbation, figures (6.24 - 6.26). Figures
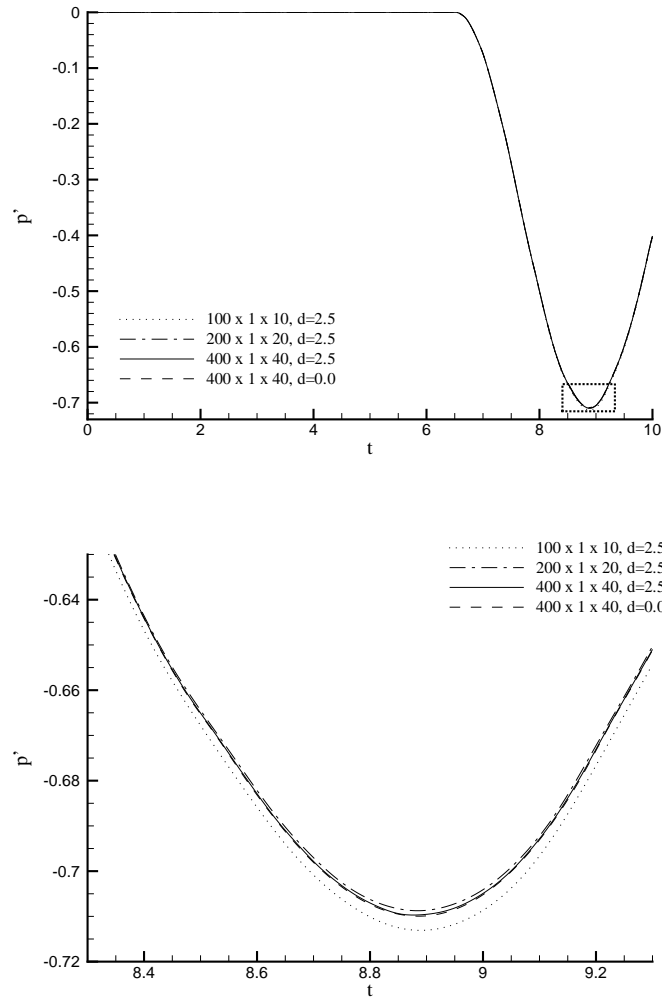
FIGURE 6.17: *Vibrating wall segment $x \in [0, 2.5]$, $\omega_0 = \frac{4}{3}$, $l = 2.5$, $a = 0.05$. Comparison of the time histories of p' at ($x = 9.0125$, $y = \Delta y/2$, $z = 0.5125$) for various mesh sizes for $d = 2.5$. (top). Detailed view (bottom). The order of approximation is $p = 3$.*

(6.16) to (6.23) indicate that the amplitude increases with increasing value of the distortion parameter d. The snapshots in figures (6.24) to (6.26) are for the largest value of d considered, i.e. $d = 10$. The wavelength of the wiggles appears to correspond with the element size $\Delta x (= \Delta y = \Delta z)$. For example in the bottom figure of figure (6.20), for $d = 10$, the element size of the finest mesh is $\Delta x = 1/40 = 0.025$, the wavelength of the small disturbance on the time history is about $T = 2c\Delta x = 0.05$.
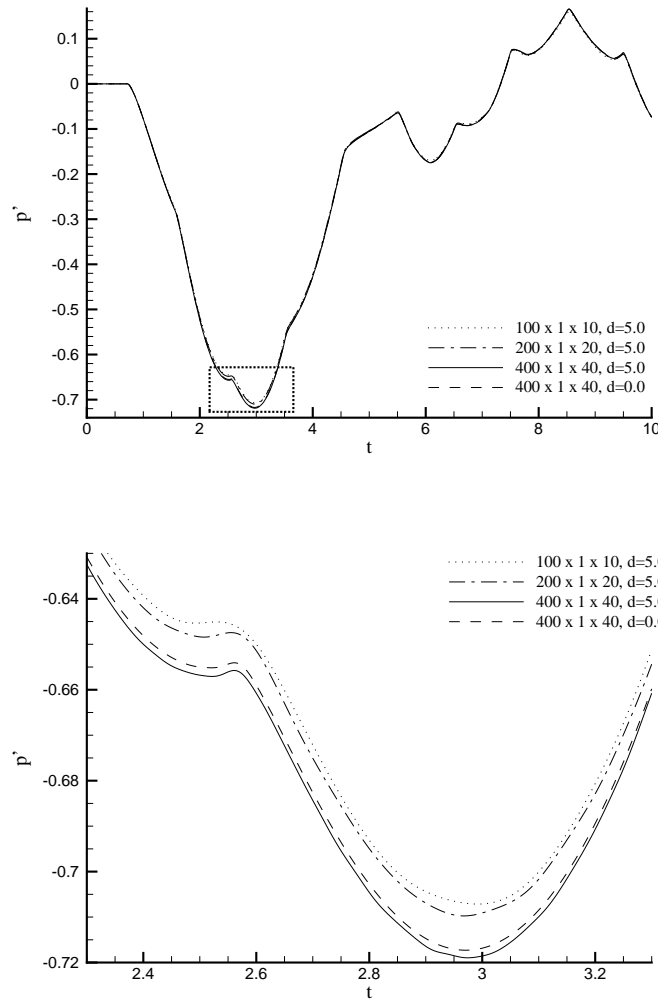
FIGURE 6.18: *Vibrating wall segment $x \in [0, 2.5]$, $\omega_0 = \frac{4}{3}$, $l = 2.5$, $a = 0.05$. Comparison of the time histories of p' at ($x = 3.0125$, $y = \Delta y/2$, $z = 0.5125$) for various mesh sizes for $d = 5$. (top). Detailed view (bottom). The order of approximation is $p = 3$.*

For the snapshot, e.g. figure (6.24), right figure, suggests a wave length of $L = 0.1$, twice the wavelength in longitudinal direction, which will be due to the boundary conditions at the duct walls.

FIGURE 6.19: *Vibrating wall segment $x \in [0, 2.5]$, $\omega_0 = \frac{4}{3}$, $l = 2.5$, $a = 0.05$. Comparison of the time histories of p' at ($x = 9.0125$, $y = \Delta y/2$, $z = 0.5125$) for various mesh sizes for $d = 5$. (top). Detailed view (bottom). The order of approximation is $p = 3$.*

FIGURE 6.20: *Vibrating wall segment $x \in [0, 2.5]$, $\omega_0 = \frac{4}{3}$, $l = 2.5$, $a = 0.05$. Comparison of the time histories of p' at ($x = 3.0125$, $y = \Delta y/2$, $z = 0.5125$) for various mesh sizes for $d = 10$. (top). Detailed view (bottom). The order of approximation is $p = 3$.*
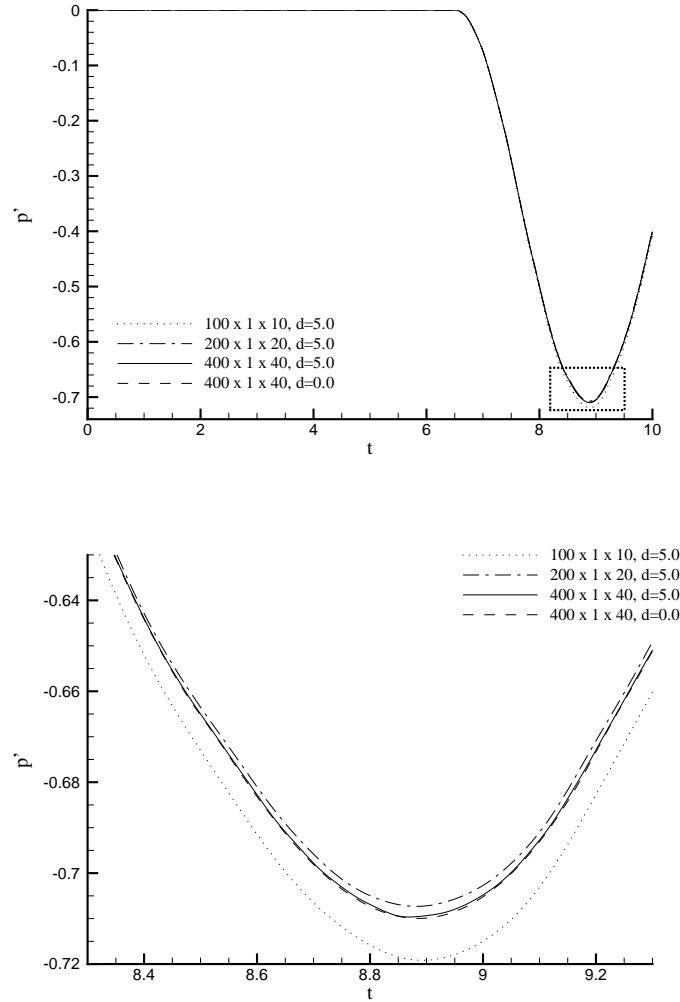
FIGURE 6.21: *Vibrating wall segment $x \in [0, 2.5]$, $\omega_0 = \frac{4}{3}$, $l = 2.5$, $a = 0.05$. Comparison of the time histories of p' at ($x = 9.0125$, $y = \Delta y/2$, $z = 0.5125$) for various mesh sizes for $d = 10$. (top). Detailed view (bottom). The order of approximation is $p = 3$.*
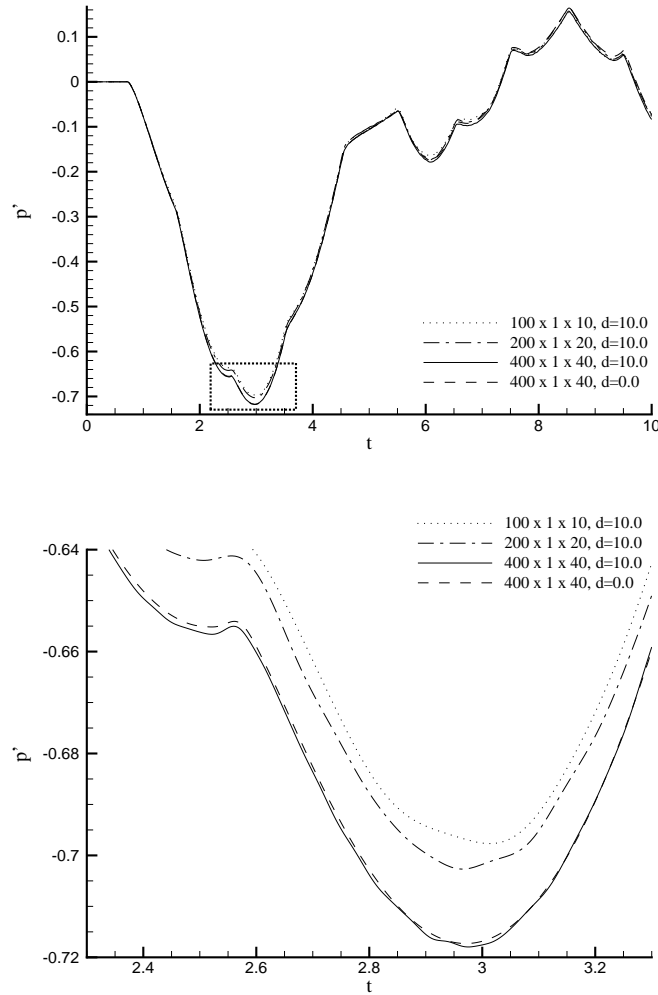
FIGURE 6.22: *Vibrating wall segment $x \in [0, 2.5]$, $\omega_0 = \frac{4}{3}$, $l = 2.5$, $a = 0.05$. Comparison of the time histories of p' at ($x = 3.0125$, $y = \Delta y/2$, $z = 0.0125$) for 400x1x40 mesh for various values of grid distortion parameters d (top). Detailed view (bottom). The order of approximation is $p = 3$.*
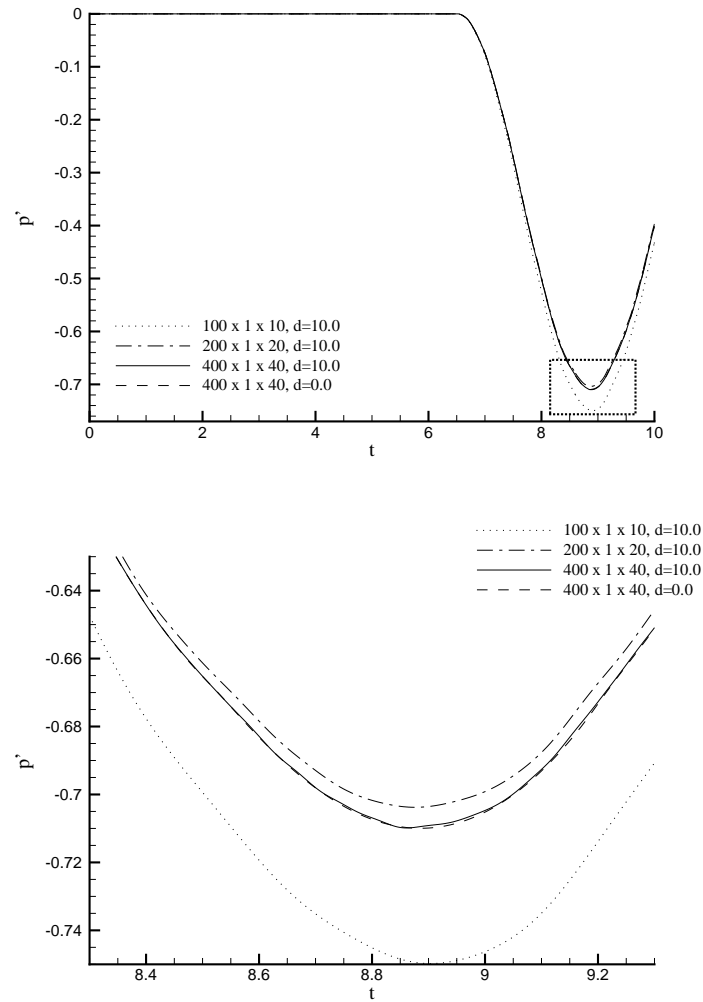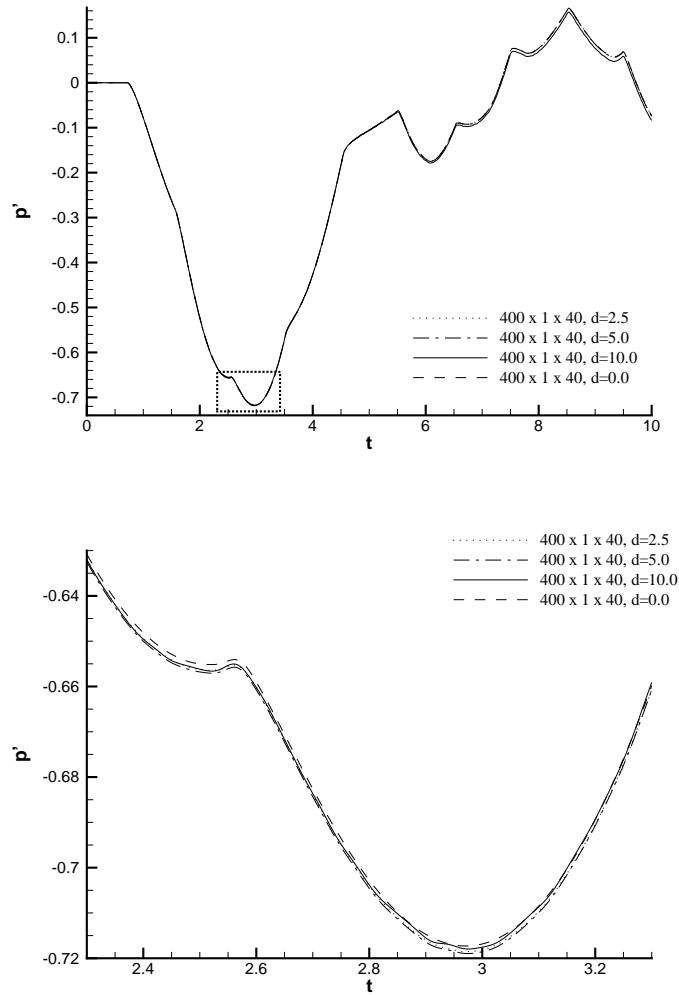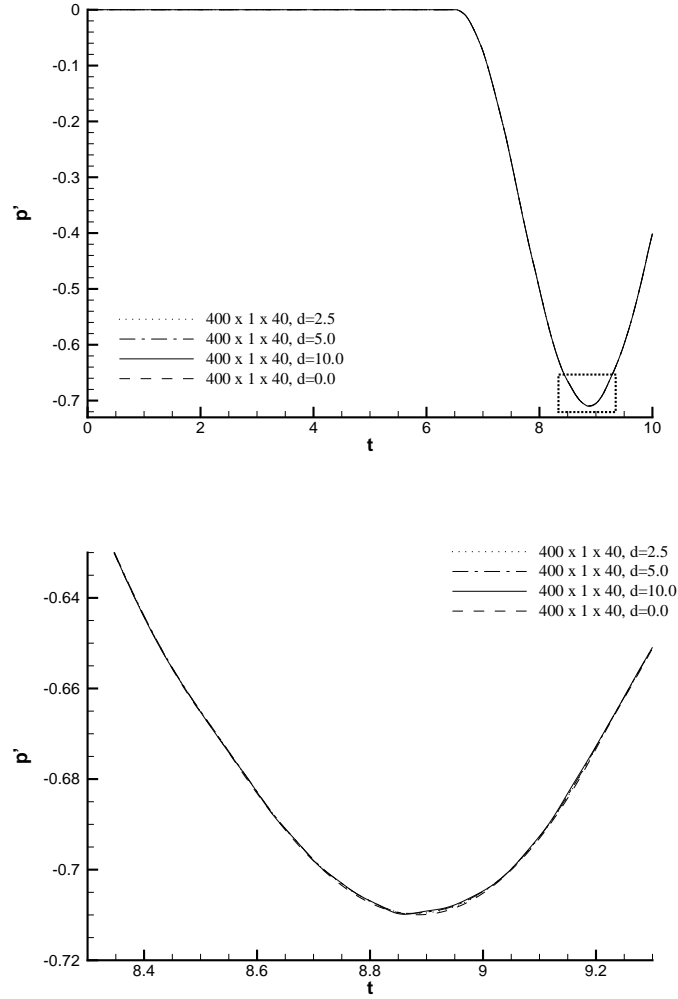
FIGURE 6.23: *Vibrating wall segment* $x \in [0, 2.5]$, $\omega_0 = \frac{4}{3}$, $l = 2.5$, $a = 0.05$. *Comparison of the time histories of* p' *at (*$x = 9.0125$ *,* $y = \Delta y/2$, $z = 0.0125$*) for 400x1x40 mesh for various values of grid distortion parameters* d *(top). Detailed view (bottom). The order of approximation is* $p = 3$.

FIGURE 6.24: *Vibrating wall segment $x \in [-2.5, 2.5]$, $\omega_0 = \frac{4}{3}$, $l = 2.5$, $a = 0.05$, d=10. Left: Contour plots for the pressure perturbation in the plane $y = \Delta y/2$ for $t = 0.4$ to 2.4. Middle: Pressure perturbation along line ($y = \Delta y/2$, $z = 0.25$). Right: Pressure perturbation along line ($x = 0.0$, $y = \Delta y/2$). $\Delta x = \Delta y = \Delta z = 0.025$, $\Delta t = 1.0 \cdot 10^{-3}$.*
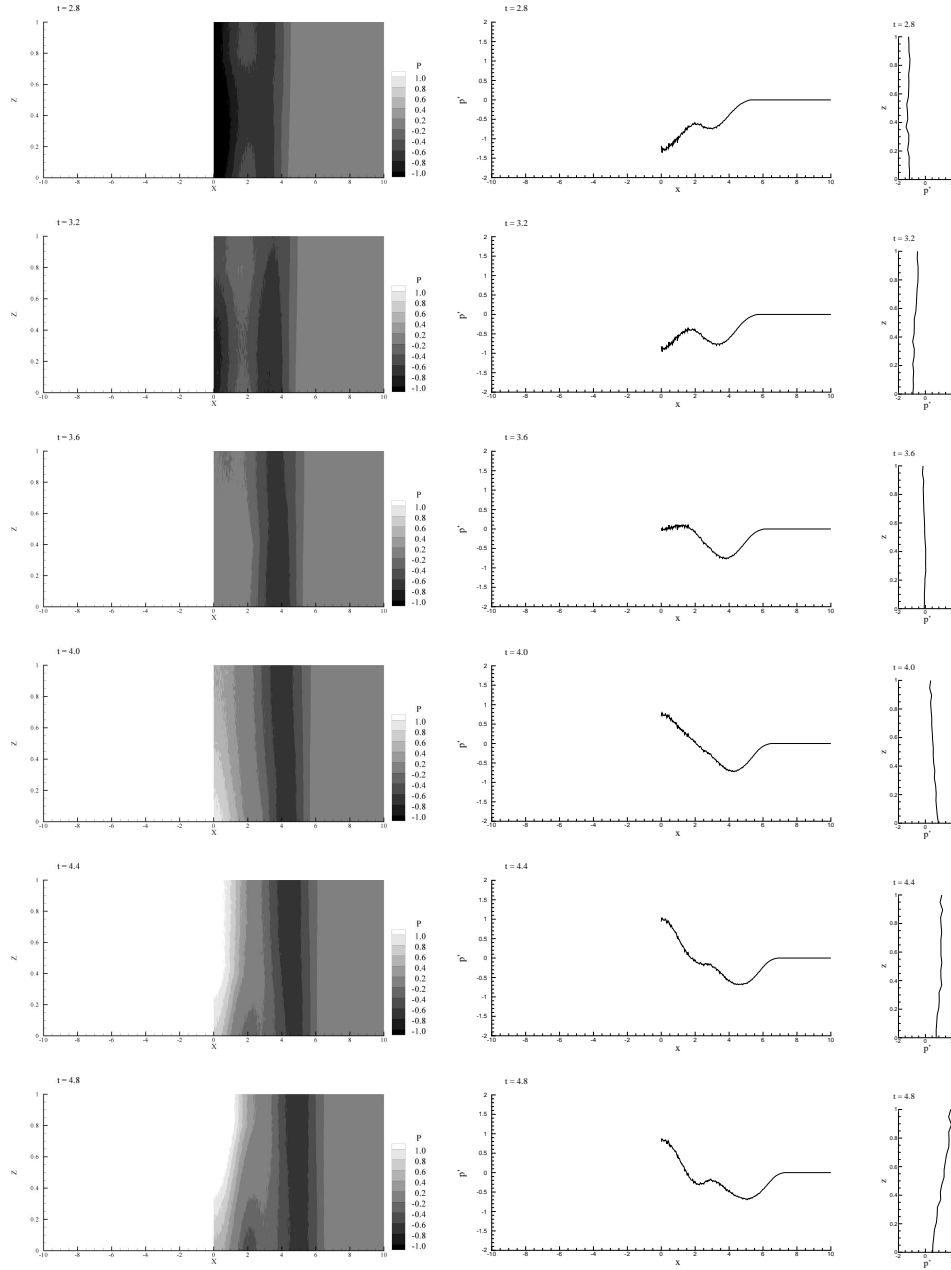
FIGURE 6.25: *Vibrating wall segment* $x \in [-2.5, 2.5]$, $\omega_0 = \frac{4}{3}$, $l = 2.5$, $a = 0.05$, $d=10$. *Left: Contour plots for the pressure perturbation in the plane* $y = \Delta y/2$ *for* $t = 2.8$ *to* 4.8. *Middle: Pressure perturbation along line* $(y = \Delta y/2$, $z = 0.25)$. *Right: Pressure perturbation along line* $(x = 0.0$, $y = \Delta y/2)$. $\Delta x = \Delta y = \Delta z = 0.025$, $\Delta t = 1.0 \cdot 10^{-3}$.
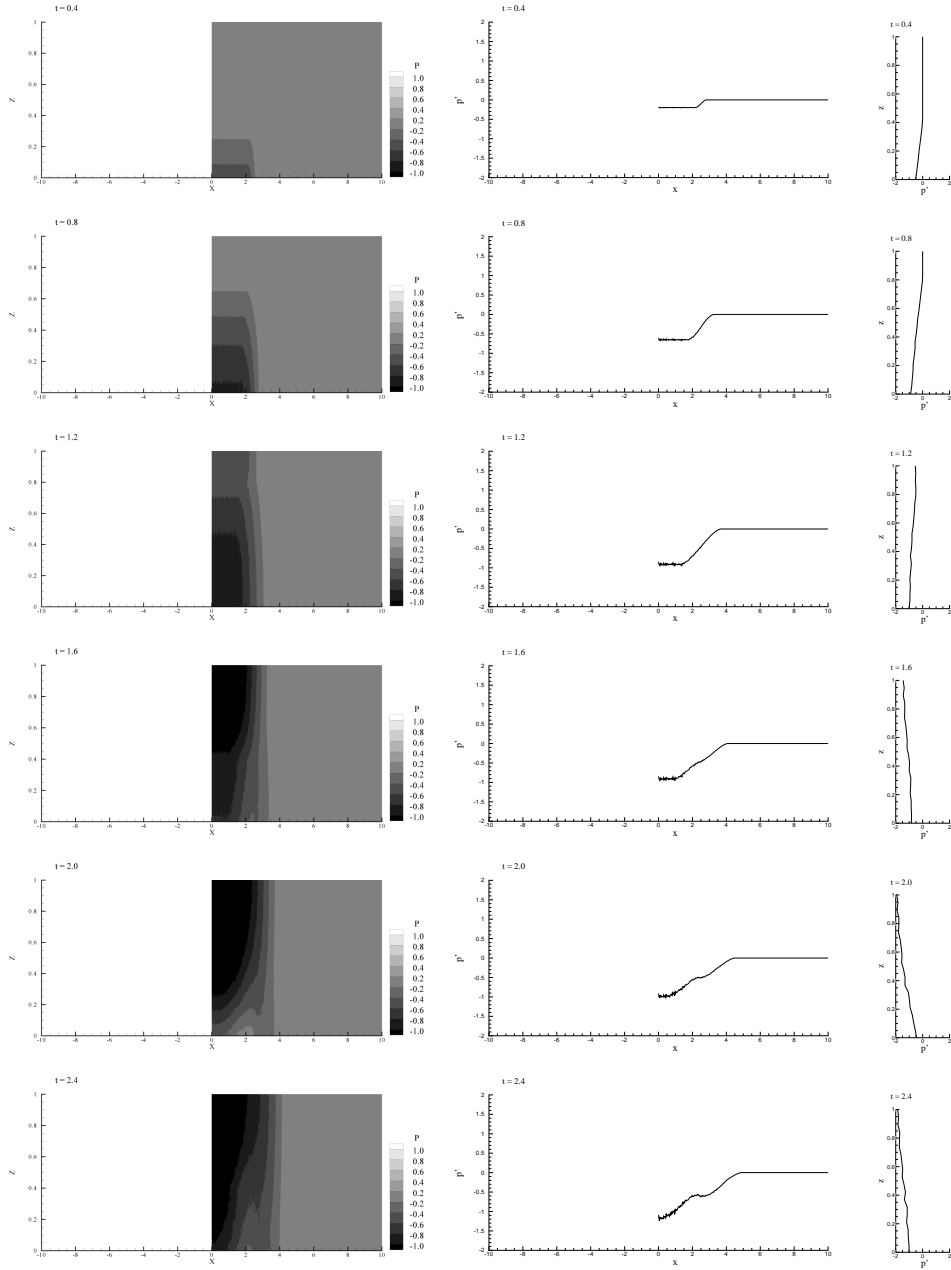
FIGURE 6.26: *Vibrating wall segment* $x \in [-2.5, 2.5]$, $\omega_0 = \frac{4}{3}$, $l = 2.5$, $a = 0.05$, *d=10.* *Left: Contour plots for the pressure perturbation in the plane* $y = \Delta y/2$ *for* $t = 5.2$ *to* *7.2. Middle: Pressure perturbation along line* ($y = \Delta y/2$, $z = 0.25$). *Right: Pressure perturbation along line* ($x = 0.0$, $y = \Delta y/2$). $\Delta x = \Delta y = \Delta z = 0.025$, $\Delta t = 1.0 \cdot 10^{-3}$.
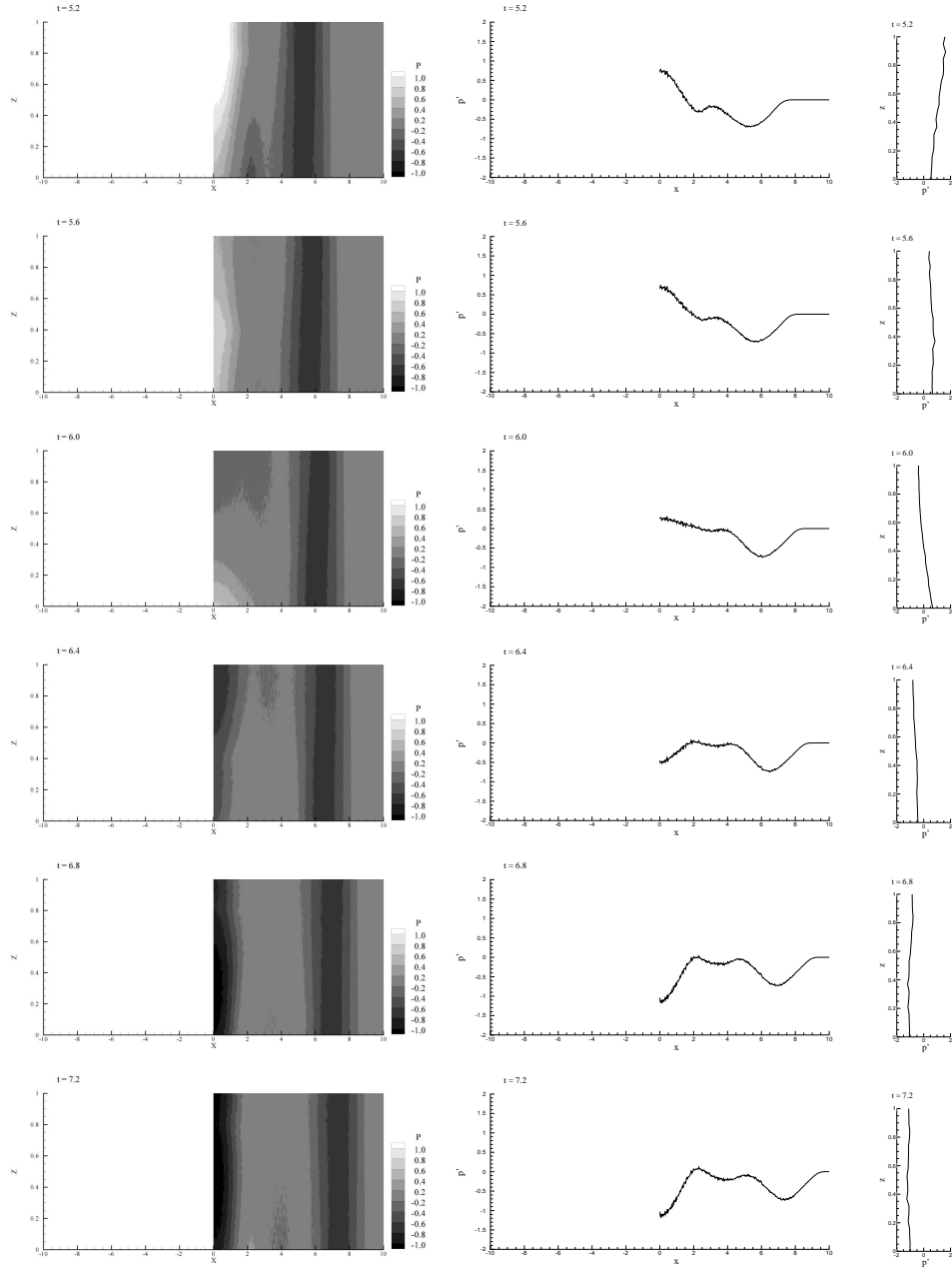
6.3.2   Accuracy

As in the preceding section the effect of the distortion parameter d is considered here in terms of the L_2-norms of the differences in the time history at a microphone position. For each value of the distortion parameter d_0 (=0), d_1, d_2 and d_3 and for each mesh size h_1, h_2 and h_3 we have a signal as function of time, i.e. there are 12 signals in total. Taking the result of the simulation for h_3, $d = 0$ as a reference solution the dependency of the difference with respect to distortion parameter can be calculated for each distortion parameter and mesh size considered, as follows:

$$||\varepsilon||_{ij} = \sqrt{\frac{1}{T} \int_0^T \{p'(t, h_i, d_j) - p'(t, h = h_3, d_0 = 0)\}^2 \, dt} \qquad (6.2)$$

The integral is approximated using Gaussian quadrature for $0 \leq t \leq T = 10$ using a fixed Δt of 1.0×10^{-3}. The present implementation of the method is restricted to meshes with parallelepiped elements since the the transformation of the elements in the physical space to the unit element in computational space is obtained by a linear approximation. This implies that the present mapping is exact for parallelepiped elements and approximate for more general elements. Using a randomly distorted mesh the restriction of using parallelepiped elements only is violated. In this case the linear approximation no longer holds and the truncation error due to the linear mapping can play a dominant role. The L_2-norm of the difference for each value of the mesh size as a function of distortion parameter d for order of approximation $p = 1$ is shown in the upper part of figure (6.27) and for order of approximation $p = 3$ it is shown in the lower part. One may expect that with increasing order of approximation a significant decrease in the error for a given mesh size h, and distortion parameter d as shown in chapter 4 of this thesis. From the comparison of upper and lower parts of figure (6.27) it is clear that for higher values of d there is no significant decrease in error with increasing order of approximation. This is because the truncation error due to the linear mapping plays a dominant role in case of meshes with non-parallelepiped elements.
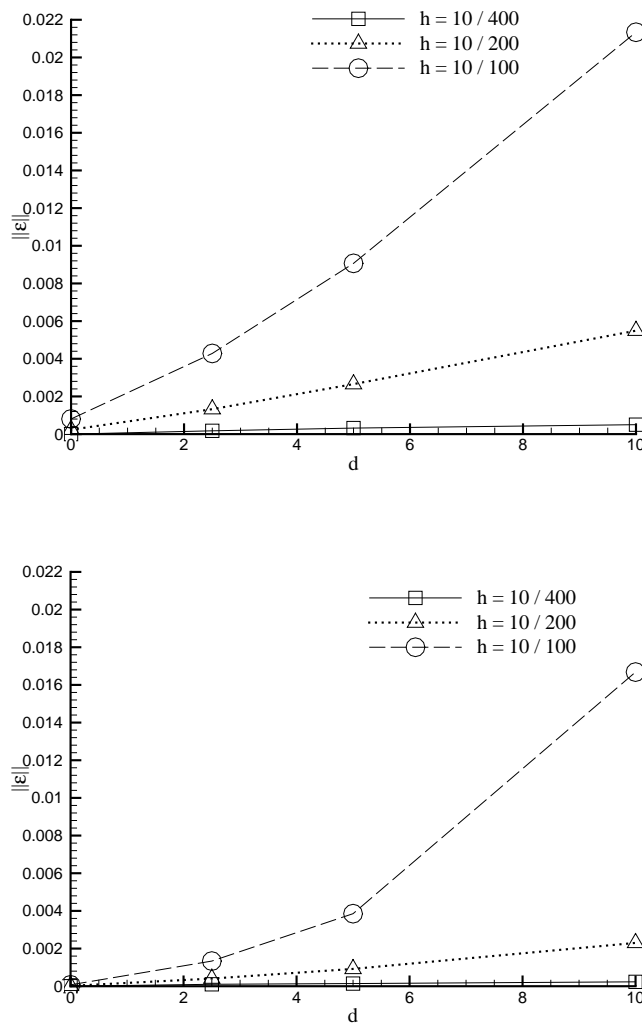
FIGURE 6.27: *Results for vibrating wall segment* $x \in [0, 2.5]$, $\omega_0 = \frac{4}{3}$, $l = 2.5$, $a = 0.05$. L_2-*norm of difference of pressure perturbation with reference solution as function of distortion parameters for various grid sizes at location* ($x = 3.0125$, $y = \Delta y/2$, $z = 0.0125$) *for order of approximations p=1 (top) and p=3 (bottom).*

PLATE WITH SLIT INSIDE INFINITE DUCT

7.1   Introduction

Acoustic liners are used in walls of exhaust systems of combustion engines and jet engine in- and outlets to reduce noise radiation. The liners consist of up to several layers of perforated plate backed with a honeycomb structure. It should be noted that when a liner is used the acoustic damping is nonlinear since it involves vortex shedding or turbulence generation in response to the incident sound, but its representation as an impedance boundary condition is linear.

In this chapter the DG method is applied to a generic acoustic liner problem. The configuration consists of a flat plate with a single orifice (slit) positioned inside a duct. The numerical results are compared to the analytical solution obtained for this configuration by Kooijman et al.[64].

The problem is prescribed in section 7.2. In section 7.3 a brief description of the analytical solution is given. The numerical results obtained for a quiescent background and the comparison of numerical results with the analytical solution are presented in section 7.4. In section 7.5 the duct modes are presented. The numerical dispersion of the method is demonstrated in section 7.6. Finally in section 7.7 the numerical results are presented for the solution obtained with the background flow and the comparison to the solution obtained for a quiescent background.

7.2   Problem Description

As a validation case the method is applied to a problem in which an infinitely long duct is split up longitudinally by a plate into two ducts. The plate has a transverse slit, referred to as an aperture here, which forms a connection between the two parts of the duct. The configuration is depicted in figure (7.1). The non-dimensional height of the two parts of the duct is identical, i.e. $h/2$, where $h = (\omega/c)h'$. Here ω is the radian frequency of sound, c the speed of sound and h' a height with dimension. The non-dimensional width of the aperture is $2s = 2(\omega/c)s'$, with s' a length with a

dimension. In the computation the non-dimensional length of the duct is taken to be equal to $2L = 2(\omega/c)L'$, with L' a length with dimension.

The configuration is symmetric with respect to the vertical plane $x = L$, i.e. the plane passing through the middle of the aperture. The complete geometry is split in 3 regions. An incoming wave is introduced at the open boundaries of region 2, region 1 is in the lower part of the duct, opposite to region 2. Region 3 is the aperture region. The time histories of the perturbations on the mean flow variables are recorded at *microphones* in vertical arrays at various locations in the duct.

We choose L to be equal to $L = 3$ and h equal to $h = 2$. When the mean flow is absent ($M = 0$), the flow problem is symmetrical with respect to the plane $x = L = 3$, i.e. in that case it is sufficient to consider the left half of the configuration only. It has also been verified that indeed for the no-flow case the numerical solution is symmetric with respect to the plane $x = L$ when computing the solution in the whole configuration.

The rectangular domain is now given by $x \in [0,3]$, $y \in [0, \Delta y]$ and $z \in [0,2]$, where all lengths are non-dimensional and Δy is the size of the element in y-direction. The aperture has a half-width of $s = 0.125$. At the end planes of the duct, the characteristic non-reflecting boundary conditions are applied, while solid-wall boundary conditions are applied on the other walls.

For the present diffraction problem a sine wave is introduced as an incoming wave from the open boundary of region 2, i.e. both from the left and from the right. At the open boundary at the left the Riemann invariant corresponding to the right running characteristic, $R_1(0, y, z, t) = \rho_0 c_0 u'(0, y, z, t) + p'(0, y, z, t)$, is prescribed as $A \sin \omega t$, while the Riemann invariant corresponding to the left running characteristic, $R_2(0, y, z, t) = \rho_0 c_0 u'(0, y, z, t) - p'(0, y, z, t) = 0$. At the right open boundary we require $R_1(2L, y, z, t) = \rho_0 c_0 u'(0, y, z, t) + p'(0, y, z, t) = 0$ while $R_2(2L, y, z, t) = \rho_0 c_0 u'(0, y, z, t) - p'(0, y, z, t)$ is prescribed as $A \sin \omega t$. Various frequencies are chosen, above as well as below the cut-off frequency of the duct which is $\omega_c = \pi$. Microphones are located in four vertical arrays close to the left end of region 1 and region 2 ($x = 0.5$, $y = \Delta y/2$, $z \in [0,1]$ and $z \in [1,2]$, respectively) and close to the aperture ($x = 2.5$, $y = \Delta y/2$, $z \in [0,1]$ and $z \in [1,2]$, respectively). Each array of microphones consists of 40 microphones (a total of 160 microphones in 2 regions).

7.3 Analytic Solution

The analytical solution is performed by Kooijman et al.[64] using a modal expansion of the pressure field in the three regions 1, 2 and 3 (see figure (7.1)). By matching the pressure and velocity at the interfaces between regions 1 and 3, and between regions 2 and 3, a scattering matrix for the left boundary of region 3 is obtained. This
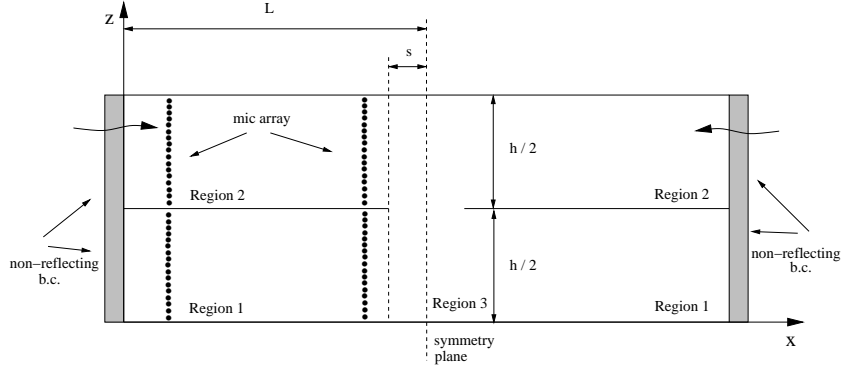
FIGURE 7.1: *Infinite plate with slit in duct.*

matrix relates the amplitudes of the outgoing modes p_1^-, p_2^-, p_3^+ to the amplitudes of the incoming modes p_1^+, p_2^+, p_3^-. By using these amplitudes reflection and transmission coefficients of the plane waves are calculated.

7.4 Numerical Results

For the verification of the computational method the numerical results are compared with the analytical solution.

The hexahedral mesh is obtained by partitioning the physical domain into equally sized cubes. The problem is two-dimensional but the method for three-dimensional wave-propagation problems is applied to obtain the numerical results. In order to reduce the computation time, after verifying that there is no effect of the third-direction in the numerical solution, only one cell is used in the y-direction. A detailed (not-equally scaled in x and z-directions) view of the hexahedral mesh around the aperture is included in figure (7.2).

During the computations the results are obtained in the cell centers and subsequently, as a post-processing, the values in all nodes are evaluated using the basis functions. The node values are averaged when the node points are common to more than one element. The time history of the perturbation variables is recorded at the 160 microphones in the four microphone arrays defined in figure (7.1).

Figure (7.3) presents for $\omega = \frac{1}{2}\omega_c$, which is below the cut-off frequency, the time evolution of the pressure and velocity perturbation recorded at the two array locations close to the left boundary. Shown are the array-averaged signals of the 40 microphones, e.g.

$$\overline{u'}\left(x, \frac{\Delta y}{2}, t\right) = \frac{1}{40} \sum_{i=1}^{40} u'\left(x, \frac{\Delta y}{2}, z_i, t\right), \tag{7.1}$$
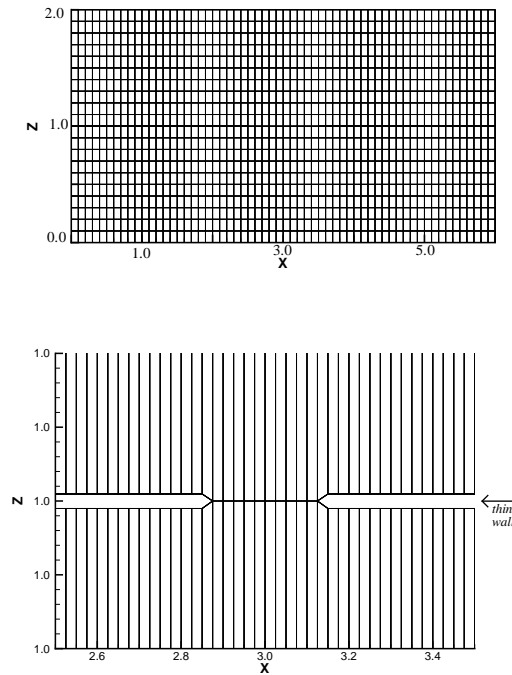
FIGURE 7.2: *The complete (coarsest) mesh (top). A close up of the (finest) mesh around the aperture (bottom).*

with $(x, \frac{\Delta y}{2}, z_i)$ the position of the i-th microphone within an array. Time is made dimensionless by h'/c, with c the speed of sound and h' the dimensional duct height. The array-averaging is done in order to filter out the plane-wave components of the acoustic field. When we have a closer look at the upper part of figure (7.3) we observe that the wave reaches the array of microphones located at ($x = 0.5$, $y = \Delta y/2$, $z \in [1,2]$) with a delay time (at $t = 0.5$, with the non-dimensional speed of sound $c = 1$) as expected. Furthermore, at dimensionless time $t = 5.5$ the effect of the incoming wave that originates from the right boundary of region 2 can be seen. This effect is a slight modulation of the wave in terms of the $\overline{u'}$ and a $\pi/2$ phase shift plus amplitude increase for $\overline{p'}$. The lower part of figure (7.3) shows the pressure and velocity perturbations recorded at and averaged over the microphone array in region 1 ($x = 0.5$, $y = \Delta y/2$, $z \in [0,1]$). The wave arrives at this array at $t = 5.5$. The array-averaged perturbation velocity $\overline{u'}$ shows an inverted sine wave moving to the left, with the same frequency as the incoming wave, but with about half the amplitude.

The array-averaged perturbation pressure $\overline{p'}$ has the same reduced amplitude and has a phase shift of π with respect to the velocity wave.

The time evolution of the pressure and velocity perturbations for the frequency $\omega = \frac{3}{2}\omega_c$ (which is above the cut-off frequency $\omega_c = \pi$) is shown in figure (7.4) for the same two arrays.

It is seen that in region 2 the interaction of the incoming u' wave and the u' wave reflected from the plane of symmetry now results in an increase of the amplitude by 50%. In region 1 the amplitude of the transmitted wave is about $1/4$ of that of the incoming wave.

Figure (7.5) shows the comparison between the time histories of the array-averaged pressure (top) and velocity (bottom) perturbations for two frequencies one below and one above the cut-off frequency $\omega_c = \pi$ This shows the differences in the interaction patterns.

Figure (7.6) shows the comparison between the time histories of the array-averaged pressure (top) and velocity (bottom) perturbations for three microphones in the array in region 2 for frequency $\omega = \frac{3}{2}\omega_c$. We observe that upon interaction with the wave from the right the amplitude of the pressure perturbation varies in z-direction while there is also a shift in the phase for the velocity perturbation.

The perturbations (on the mean flow variables) can be written in terms of left-travelling and right-travelling components. For the array-averaged pressure perturbation:

$$\overline{p'} = p^+ + p^-, \tag{7.2}$$

and for the array-averaged velocity perturbation:

$$\overline{u'} = (p^+ - p^-)/\rho_0 c_0, \tag{7.3}$$

where the mean density ρ_0 and the speed of sound c_0 are non-dimensional and equal to unity. With the help of equations (7.2) and (7.3) the reflection and transmission coefficients of the waves can be evaluated . For the linear problem considered we can write the reflection coefficient R, of the plane waves in region 2 as:

$$R = \frac{\overline{p'_2} - \rho_0 c_0 \overline{u'_2}}{\overline{p'_2} + \rho_0 c_0 \overline{u'_2}}, \tag{7.4}$$

where array-averaged pressure and velocity perturbations are $\overline{p'_2} = \overline{p'}(x = 0.5, y = \frac{\Delta y}{2}, t)$ and $\overline{u'_2} = \overline{u'}(x = 0.5, y = \frac{\Delta y}{2}, t)$, respectively, at the array in region 2 in which $z \in [1, 2]$. The transmission coefficient T, of the plane waves in region 1 can be expressed as:

$$T = \frac{\overline{p_1'} - \rho_0 c_0 \overline{u_1'}}{\overline{p_2'} + \rho_0 c_0 \overline{u_2'}}, . \tag{7.5}$$

where array-averaged pressure and velocity perturbations are $\overline{p_1'} = \overline{p'}(x = 0.5, y = \frac{\Delta y}{2}, t)$ and $\overline{u_1'} = \overline{u'}(x = 0.5, y = \frac{\Delta y}{2}, t)$, respectively, at the array in region 2 in which $z \in [0, 1]$.

Reflection and transmission coefficients R and T are shown in figure (7.7) showing the ratios of the amplitudes of the reflected and transmitted plane waves that are plotted versus ω/ω_c for the present slit width of $s/(h/2) = 0.125$. Below the cut-off frequency $\omega_c = \left(\frac{2\pi c}{h} \right) = \pi$ we find an excellent agreement between numerical and analytical results. Please note that because we consider plane waves, below the cut-off frequency we have $R^2 + T^2 = 1$, from energy conservation. Above the cut-off frequency this relationship does not hold because energy is transferred to a higher non-planar mode.

In the left parts of figures (7.8 and 7.9) contour plots are shown for the pressure perturbation in the plane $y = \Delta y/2$ for $t = 0.5$ to 7.5 while in the right parts the pressure perturbation along the line ($y = \Delta y/2$, $z = 1.5$), and the line ($x = 3.0$, $y = \Delta y/2$) are plotted, all for $\omega = \frac{3}{4}\omega_c$, below the *cut-off* frequency. This data is for the mesh with $120 \times 1 \times 80$ elements in $x-$, $y-$ and $z-$directions, respectively.

This data gives a clean overview of the diffraction of acoustic waves in the duct with the slitted flat plate without mean flow. The sine wave moves in from the left boundary and reflects from the plane of symmetry $x = L = 3$, with a reflected wave in region 2 and a wave moving into region 1. The reflected wave appears as a more or less planar wave, while the diffracted wave is much more two-dimensional.

For $\omega = \frac{3}{2}\omega_c$, above the *cut-off* frequency, similar contour plots are shown for the same mesh in the left parts of figures (7.10 and 7.11) for the pressure perturbation in the plane $y = \Delta y/2$ for $t = 0.5$ to 7.5 while in the right parts the pressure perturbation along the line ($y = \Delta y/2$, $z = 1.5$), and the line ($x = 3.0$, $y = \Delta y/2$) are plotted.

As in previous figures we can see the diffraction of acoustic waves in the duct with slitted flat plate without mean flow. The sine wave moving in from the left boundary reflects from the plane of symmetry $x = L = 3$. In the case of higher-frequency, i.e. $\omega = \frac{3}{2}\omega_c$, the reflected wave contains higher-modes and appears as a non-planar wave rather than a planar wave as in lower-frequency case. The diffracted wave moves in to region 1 and is also two-dimensional.

FIGURE 7.3: *Time evolution of the pressure and velocity perturbations recorded (and averaged over) the microphone array close to the boundary (top: mic(0.5, $\Delta y/2$, $z \in [1, 2]$) (Region 2), bottom: mic(0.5, $\Delta y/2$, $z \in [0, 1]$) (Region 1)) for $\omega = \frac{1}{2}\omega_c$. Numerical simulation with 4th-order ($p = 3$) method, $120 \times 1 \times 80$ mesh, $\Delta x = 0.025$, $\Delta y = 0.025$, $\Delta z = 0.025$, $\Delta t = 1.0 \cdot 10^{-3}$.*
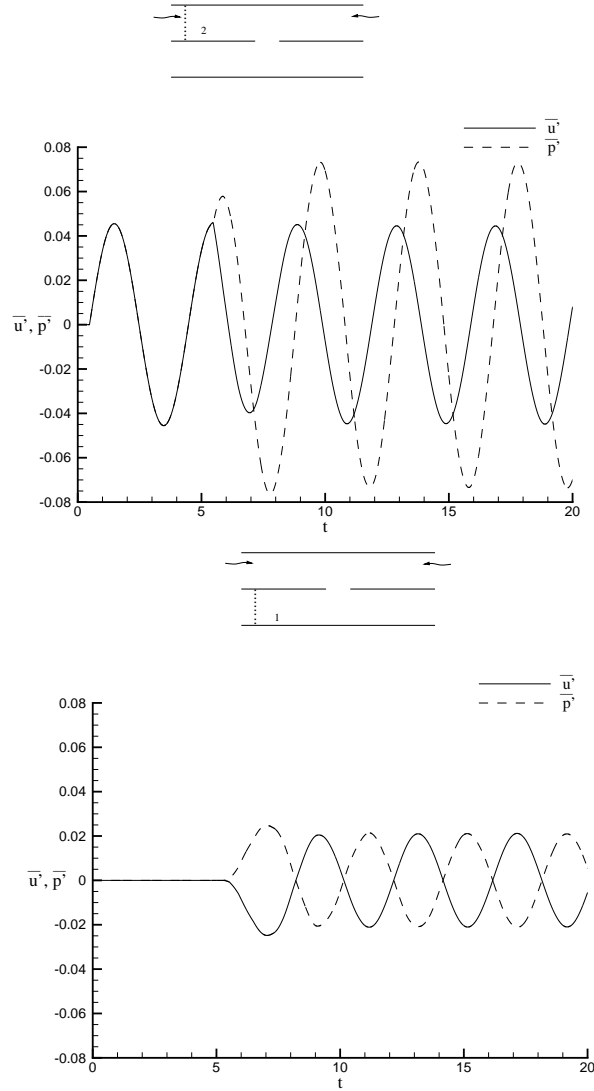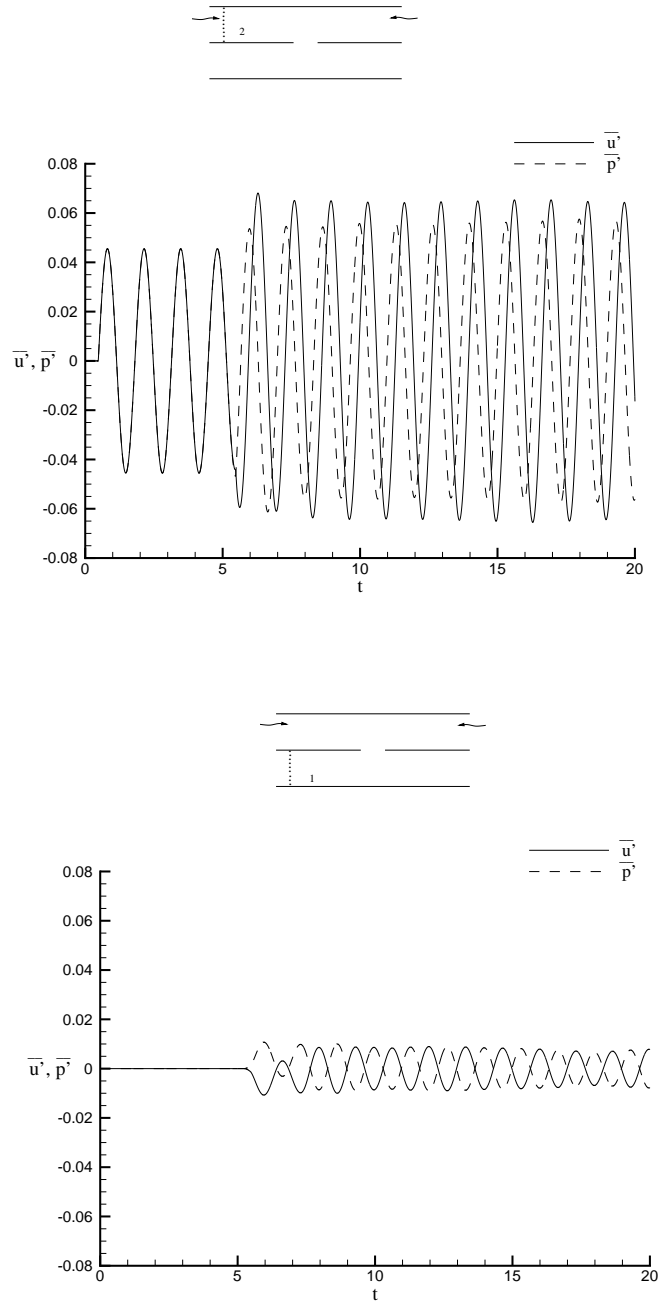
FIGURE 7.4: *Time evolution of the pressure and velocity perturbations recorded (and averaged over) the microphone array close to the boundary (top: mic(0.5, $\Delta y/2$, $z \in [1,2]$) (Region 2), bottom: mic(0.5, $\Delta y/2$, $z \in [0,1]$) (Region 1)) for $\omega = \frac{3}{2}\omega_c$. Numerical simulation with 4th-order ($p = 3$) method, $120 \times 1 \times 80$ mesh, $\Delta x = 0.025$, $\Delta y = 0.025$, $\Delta z = 0.025$, $\Delta t = 1.0 \cdot 10^{-3}$.*
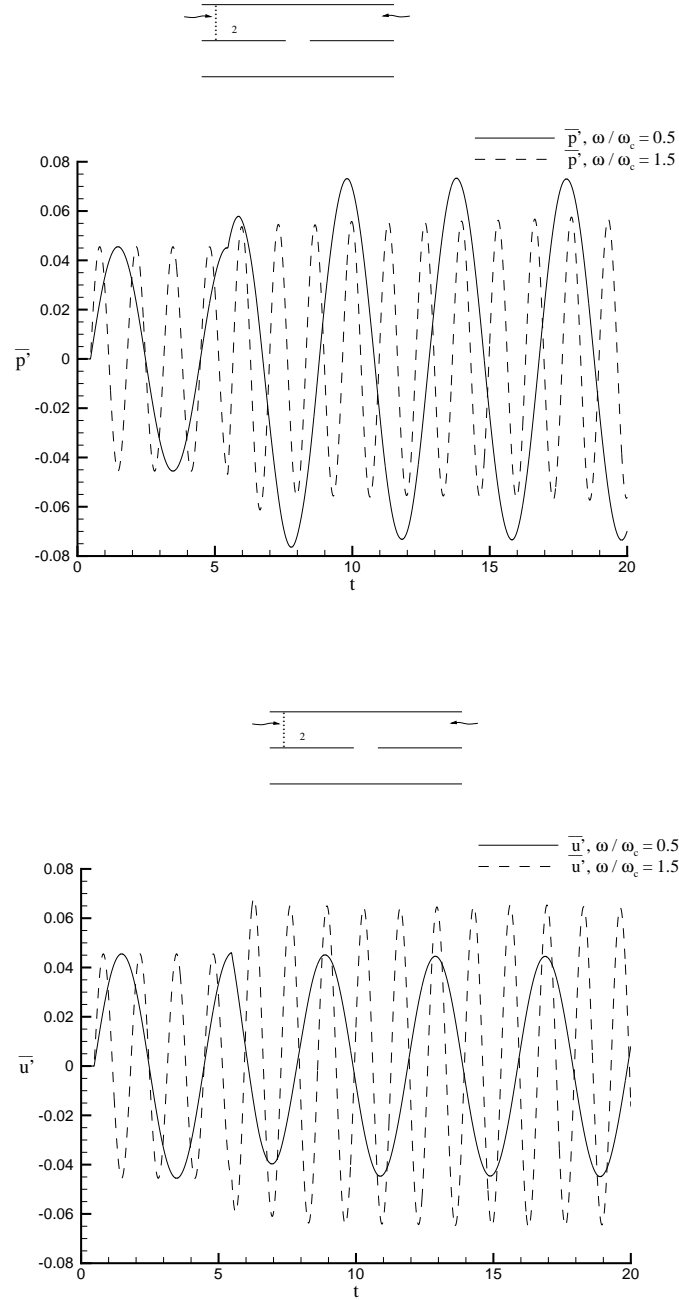
FIGURE 7.5: *Comparison of the time evolution of the array-averaged pressure (top) and velocity (bottom) perturbations recorded for $\omega = \frac{1}{2}\omega_c$ and $\omega = \frac{3}{2}\omega_c$ at microphone location mic(0.5, $\Delta y/2$, $z \in [1,2]$). Numerical simulation with 4th-order (p = 3) method, $120 \times 1 \times 80$ mesh, $\Delta x = 0.025$, $\Delta y = 0.025$, $\Delta z = 0.025$, $\Delta t = 1.0 \cdot 10^{-3}$.*
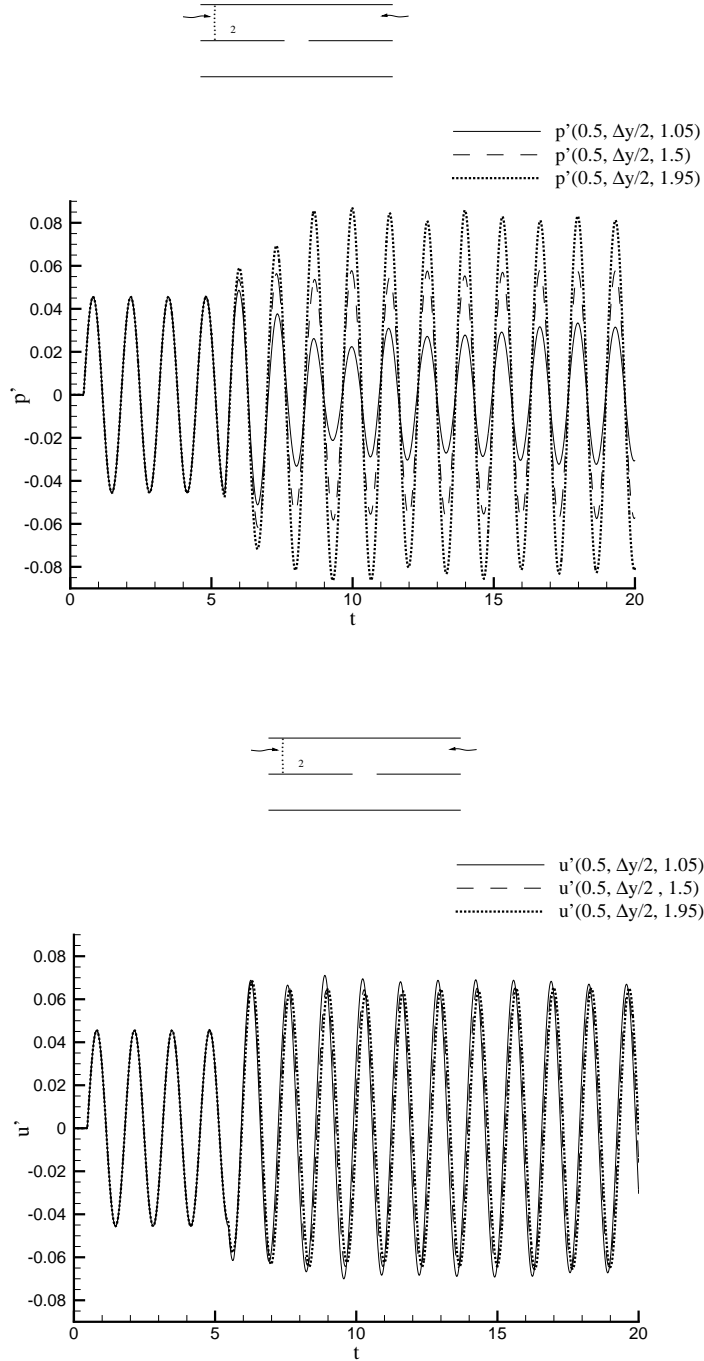
FIGURE 7.6: *Comparison of the time evolution of the pressure (top) and velocity (bottom) perturbations recorded at three microphones in the array in region 1 for* $\omega = \frac{3}{2}\omega_c$. *Numerical simulation with 4th-order (p = 3) method,* $120 \times 1 \times 80$ *mesh,* $\Delta x = 0.025$, $\Delta y = 0.025$, $\Delta z = 0.025$, $\Delta t = 1.0 \cdot 10^{-3}$.
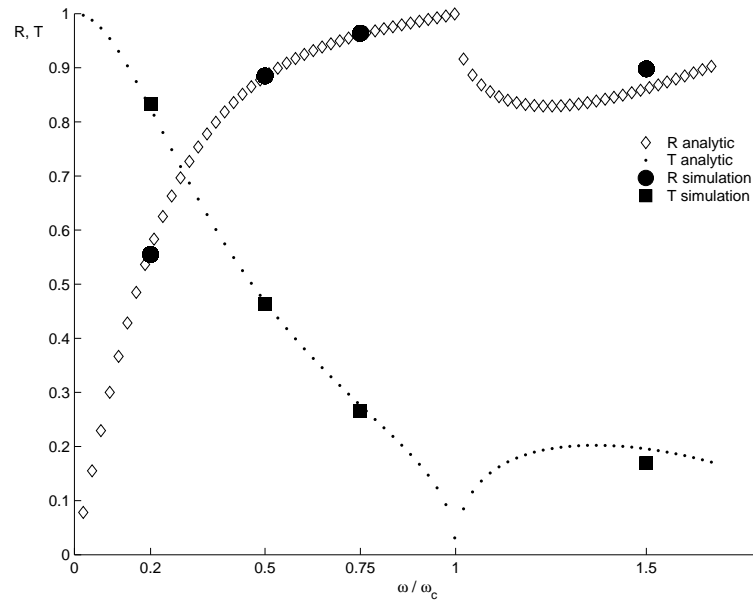
FIGURE 7.7: *The ratios of the amplitudes of the reflected and transmitted plane waves versus ω/ω_c. (R: Ratio of the amplitudes of the reflected wave and the incoming wave in region 2. T: Ratio of the amplitudes of the transmitted wave in region 1 and the incoming wave in region 2).*
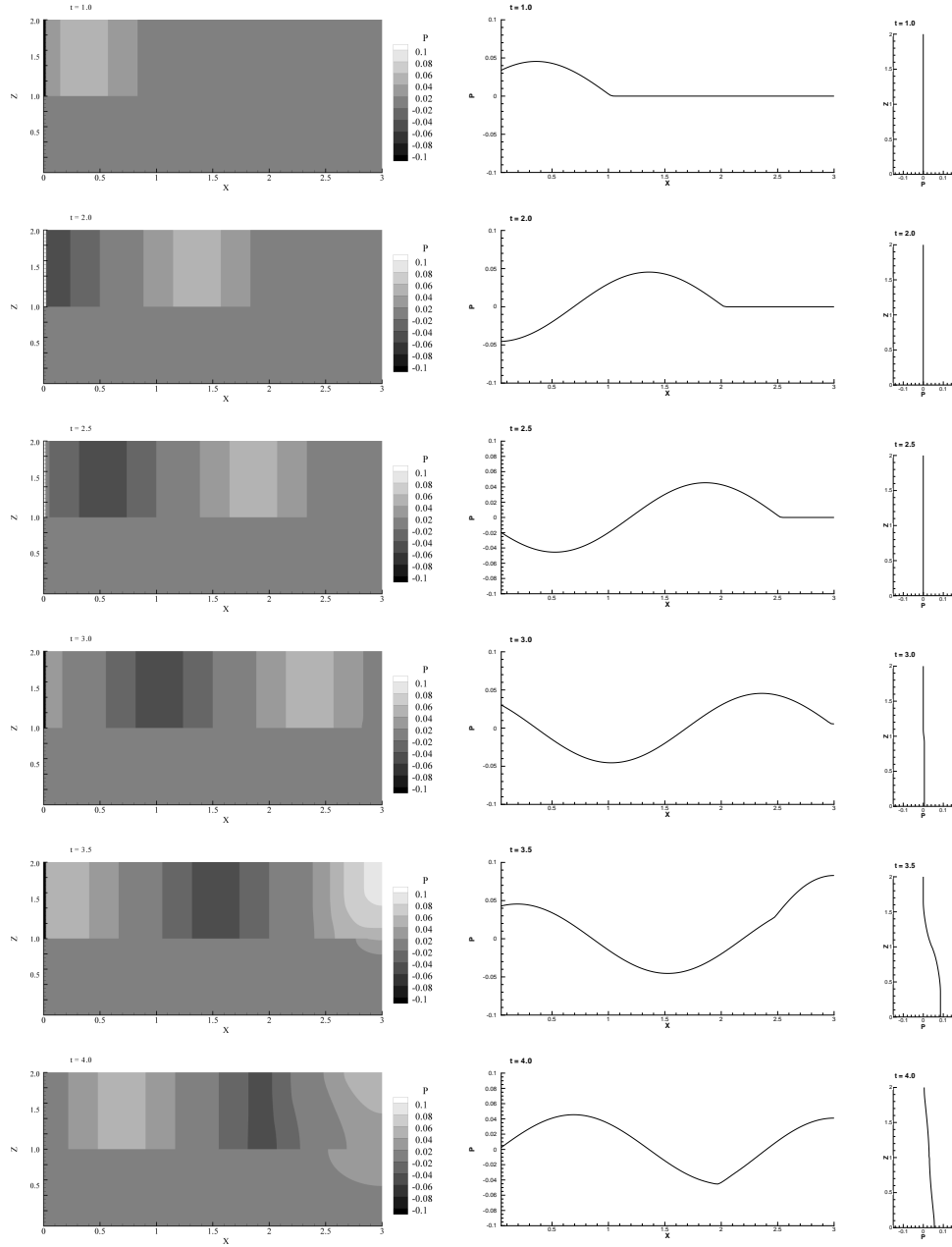
FIGURE 7.8: *Left: Contour plots for the pressure perturbation in the plane $y = \Delta y/2$ for $t = 1.0$ to 4.0. ($\omega = \frac{3}{4}\omega_c$). Middle: Pressure perturbation along line ($y = \Delta y/2$, $z = 1.5$). Right: Pressure perturbation along line ($x = 3.0$, $y = \Delta y/2$). $\Delta x = \Delta y = \Delta z = 0.025$, $\Delta t = 1.0 \cdot 10^{-3}$.*
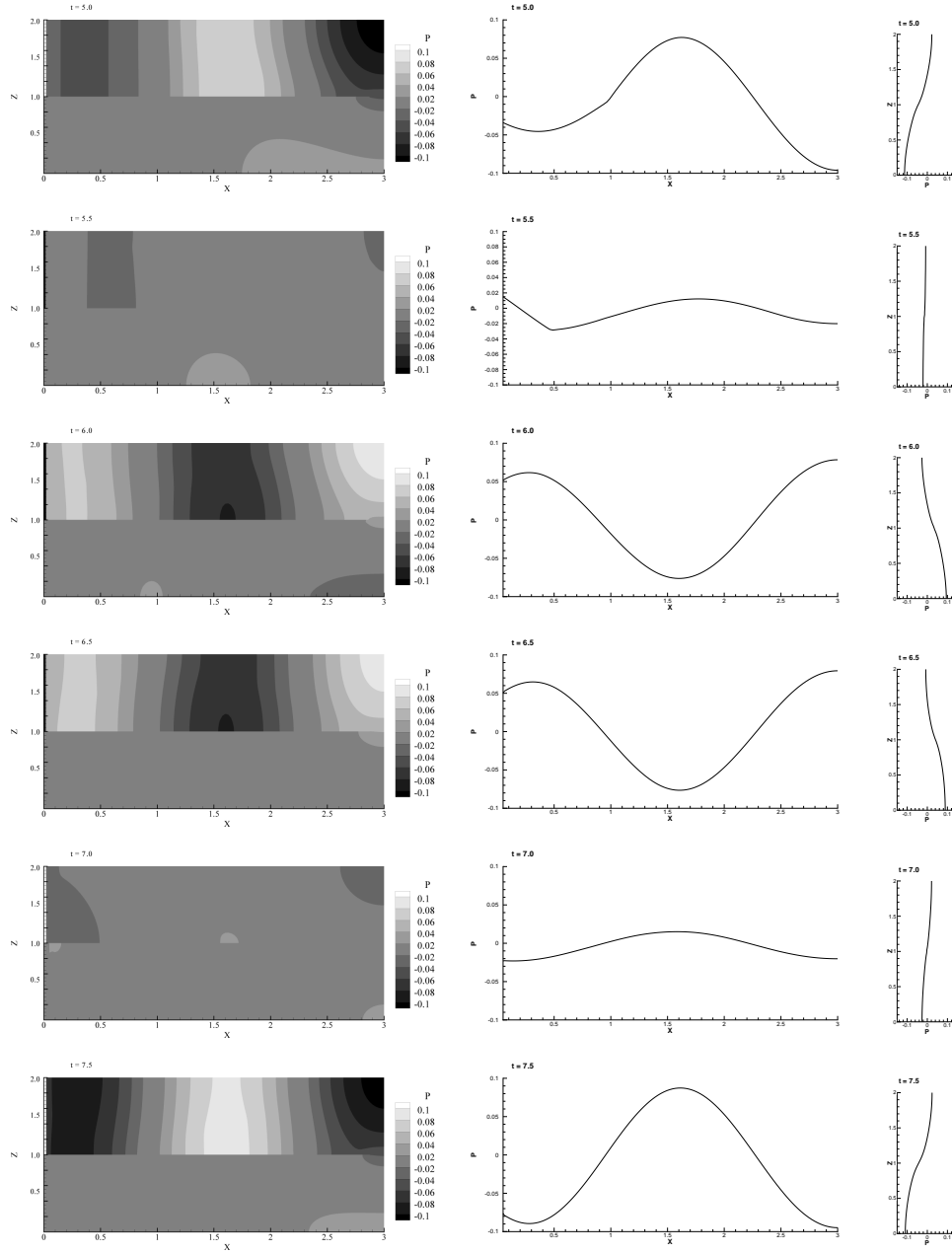
FIGURE 7.9: *Left: Contour plots for the pressure perturbation in the plane $y = \Delta y/2$ for $t = 5.0$ to 7.5. ($\omega = \frac{3}{4}\omega_c$). Middle: Pressure perturbation along line ($y = \Delta y/2$, $z = 1.5$). Right: Pressure perturbation along line ($x = 3.0$, $y = \Delta y/2$). $\Delta x = \Delta y = \Delta z = 0.025$, $\Delta t = 1.0 \cdot 10^{-3}$.*
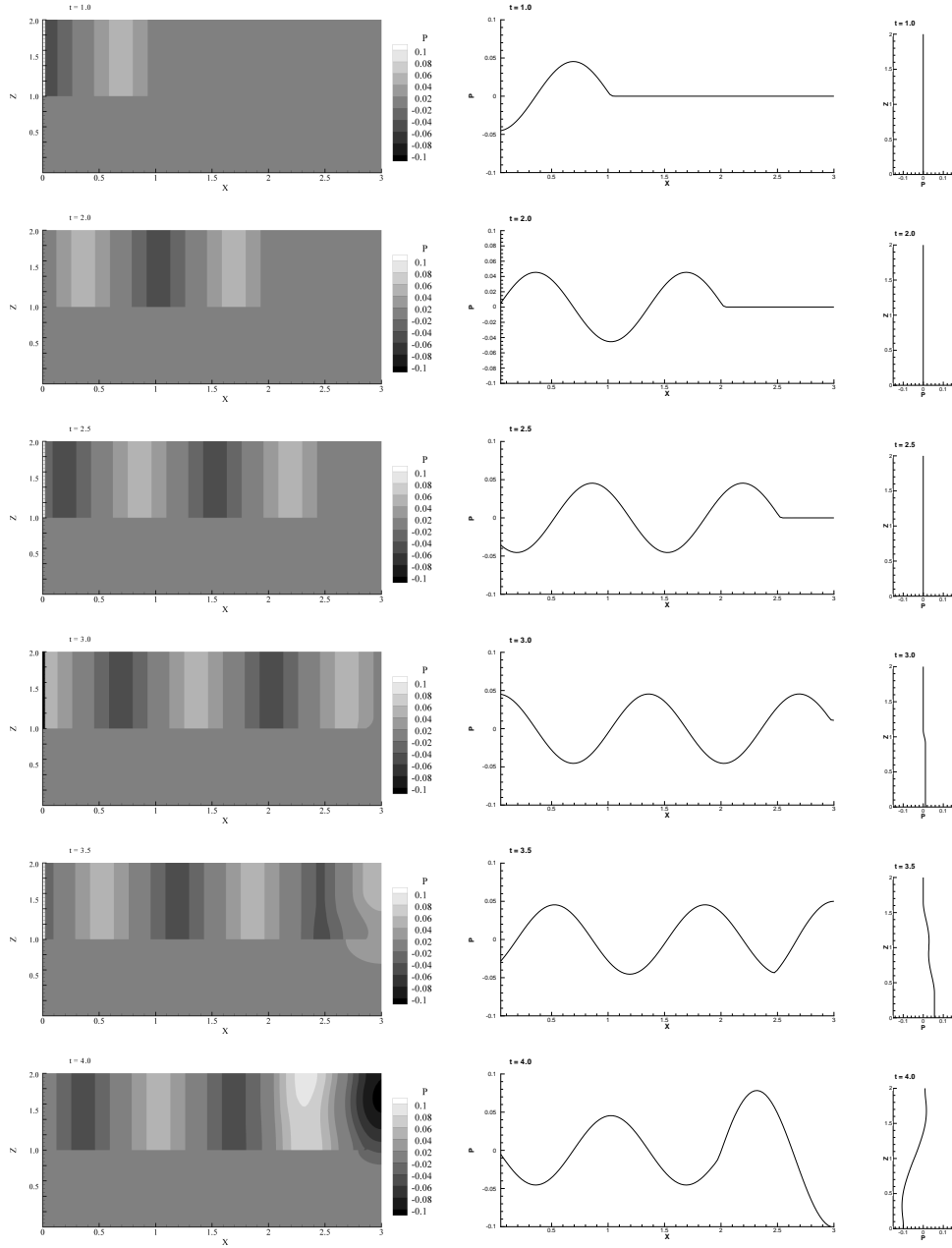
FIGURE 7.10: *Left: Contour plots for the pressure perturbation in the plane $y = \Delta y/2$ for $t = 1.0$ to 4.0. ($\omega = \frac{3}{2}\omega_c$). Middle: Pressure perturbation along line ($y = \Delta y/2$, $z = 1.5$). Right: Pressure perturbation along line ($x = 3.0$, $y = \Delta y/2$). $\Delta x = \Delta y = \Delta z = 0.025$, $\Delta t = 1.0 \cdot 10^{-3}$.*

FIGURE 7.11: *Left: Contour plots for the pressure perturbation in the plane $y = \Delta y/2$ for $t = 5.0$ to 7.5. ($\omega = \frac{3}{2}\omega_c$). Middle: Pressure perturbation along line ($y = \Delta y/2$), $z = 1.5$. Right: Pressure perturbation along line ($x = 3.0$, $y = \Delta y/2$). $\Delta x = \Delta y = \Delta z = 0.025$, $\Delta t = 1.0 \cdot 10^{-3}$.*

7.5   Duct Modes

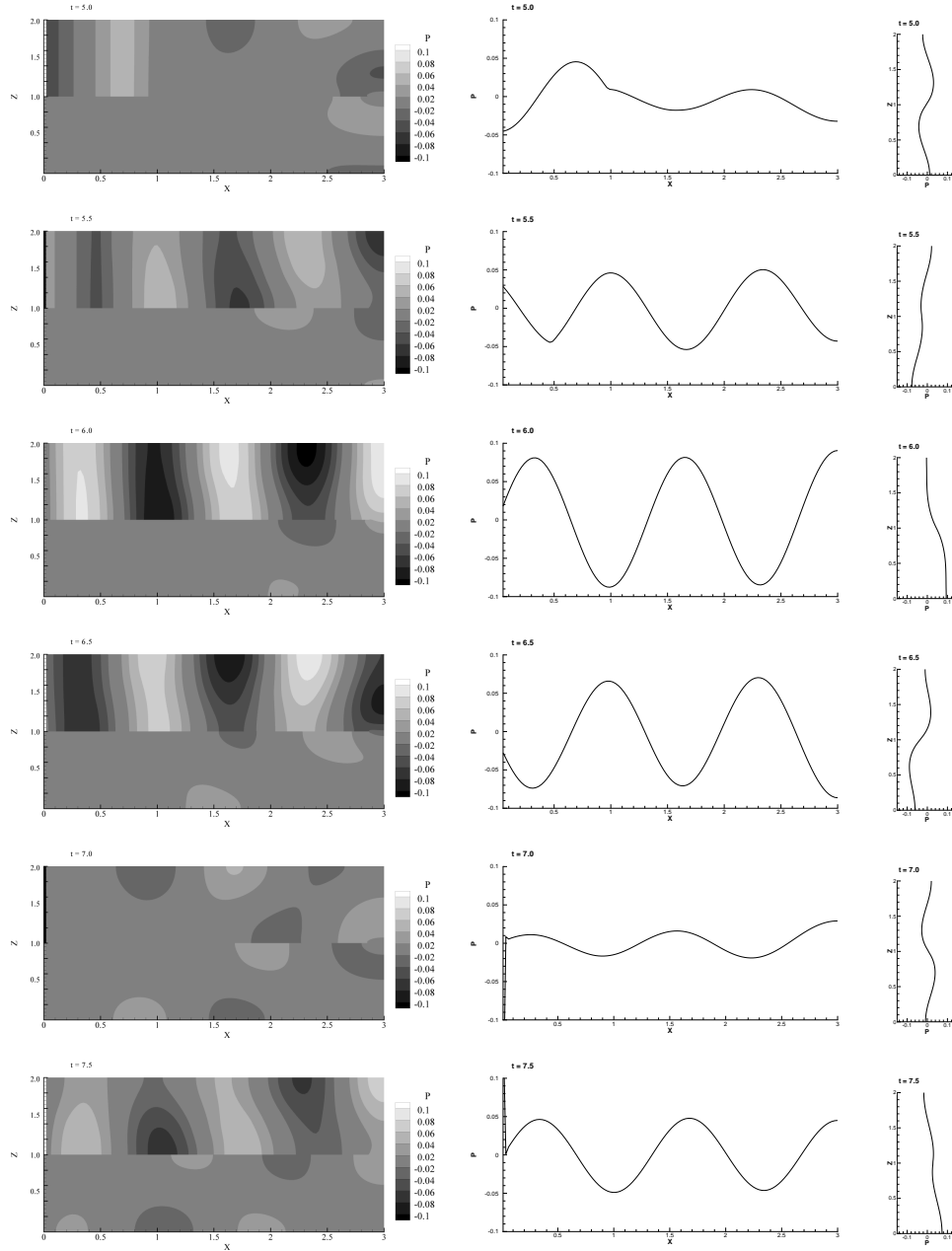At a given time $\hat{t}$, the pressure perturbation can be transformed to the frequency domain by writing

$$p'(x, \Delta y/2, z, \hat{t}) = \hat{p}(x, z, \omega)e^{i\omega\hat{t}}. \tag{7.6}$$

The duct modes for a channel as follow from the literature [88, 95] can be expressed as

$$\hat{p}(x, z, \omega) = \sum_{n=0}^{\infty} \cos(\frac{n\pi z}{h}) A_n e^{ik_n x}, \tag{7.7}$$

with

$$k_n = \sqrt{\frac{\omega^2}{c_0^2} - \left(\frac{n\pi}{h}\right)^2}, \tag{7.8}$$

where h is the height of a single duct, c_0 is the speed of sound, ω is the frequency of the signal. The nth term in the summation in equation (7.7) is called the nth *duct mode* and A_n is its modal amplitude. Modes for which $\left(\frac{n\pi}{h}\right)^2 > \frac{\omega^2}{c_0^2}$ are evanescent modes while those for which $\left(\frac{n\pi}{h}\right)^2 < \frac{\omega^2}{c_0^2}$ are propagating modes. For a given frequency there is a limited number of propagating modes, at least one being the *plane wave* or *fundamental mode* for which $n = 0$. For $n > 0$, if the frequency ω is below the cut-off frequency $w_c = c_0 \frac{n\pi}{h}$, the mode is evanescent, but above the cut-off frequency the mode is propagating.

From the time-dependent pressure perturbation computed by the present method the modal amplitude can be derived as follows.

Write the perturbation pressure as

$$p'(x, \Delta y/2, z, \hat{t}) = \sum_{n=0}^{\infty} P_n(x; \hat{t}) \cos\left(\frac{n\pi z}{h}\right), \tag{7.9}$$

so that

$$P_n(x; \hat{t}) = \frac{2}{h} \int_{z/h=1}^{z/h=2} p'(x, \Delta y/2, z, \hat{t}) \cos(\frac{n\pi z}{h}) dz. \tag{7.10}$$

It can be shown that the integration in equation (7.10) leads to

$$P_n(x; \hat{t}) = A_n e^{i\omega\hat{t}} e^{ik_n x}. \tag{7.11}$$

ω	λ_1 (eq. 7.12)	λ (fig. 7.12)
$5/4\pi$	2.667	2.738
$3/2\pi$	1.789	1.792
$7/4\pi$	1.392	1.401
2π	1.154	1.140

TABLE 7.1: *Comparison of wavelengths calculated from equation (7.12) and the wavelengths measured from figure (7.12) for $n = 1$, $c_0 = 1$, $h = 1$.*

This implies that we find the wave number k_n of the duct mode by plotting, for a given time $\hat{t}$, $P_n(x; \hat{t})$ and determining the wavelength of the waves, and there with k_n.

At a given time $\hat{t} = 30$, equation (7.10) is evaluated for $x \in [3, 6]$ and $P_n(x; \hat{t})$ is plotted in figure (7.12). It is clear from the figure that there are decaying modes for which $\omega < \omega_c = \pi$ and propagating modes for which $\omega > \omega_c = \pi$.

The quantity k_n in equation (7.7) is the wave number of the duct modes, i.e. $k_n = \frac{2\pi}{\lambda_n}$, so that

$$\lambda_n = \frac{2\pi}{\sqrt{\frac{\omega^2}{c_0^2} - \left(\frac{n\pi}{h}\right)^2}}. \tag{7.12}$$

In table (7.1) the evaluated values of λ_n for $n = 1$, $c_0 = 1$, $h = 1$ determined from equation (7.12) are compared to the measured wave lengths from figure (7.12) for various values of ω. The calculated wave lengths of the propagating modes are in agreement with the wavelengths measured from figure (7.12).

7.6 Numerical Dispersion

It is discussed in Chapter 4 that the present method produces weak artificial waves of small amplitude. In the line plots presented, they are not evident because the scale is chosen in order to show the real waves. In the contour plots presented, they are not evident because in the contour levels we did not include the zero-level of the perturbation pressure. Figure (7.13) for $\omega = \frac{3}{4}\omega_c$ and figure (7.14) for $\omega = \frac{3}{2}\omega_c$, presents the contour plots including the zero-level. It shows that, originating from the slope-discontinuity at the front of the incoming wave, waves propagating at a higher speed than c_0 lead the acoustic wave and diffract at the slit in the plate.

7.7 Plate with slit inside infinite duct with mean flow

In this section the DG method is applied to a generic acoustic liner problem, discussed in the preceding sections, with mean flow. The mean flow profile is given
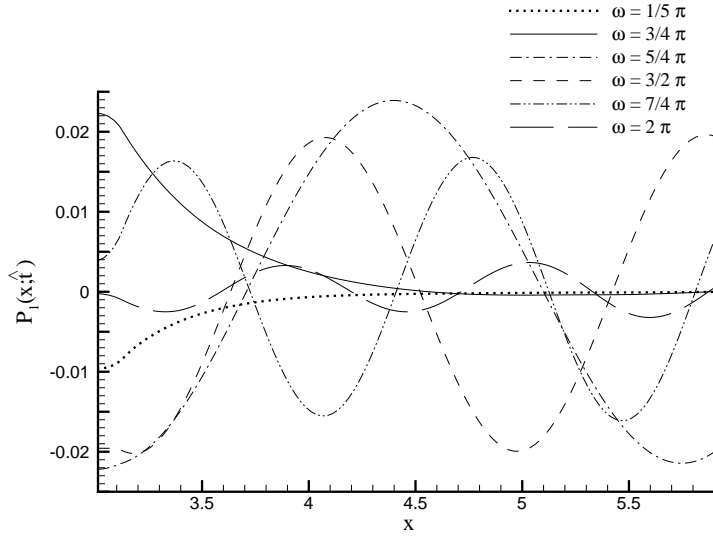
FIGURE 7.12: *Decaying and propagating duct modes ($n = 1$) computed from results for $p = 3$, $\Delta x = \Delta y = \Delta z = 0.025$, $\Delta t = 1.0 \cdot 10^{-3}$, $\hat{t} = 30$.*

as

$$M = M_0 f(z), \tag{7.13}$$

with

$$f(z) = \frac{1}{2} \left(1 - tanh \left(\frac{z - 1}{\theta} \right) \right), \tag{7.14}$$

where θ denotes a momentum thickness, chosen as $\theta/h = 0.125$. The profile $f(z)$ is given in figure (7.15).

The simulations are performed on a hexahedral mesh with $240 \times 1 \times 80$ elements in $x-$, $y-$ and $z-$directions, respectively, for a computational domain which is given by $x \in [-3, 3]$, $y \in [-\Delta y/2, \Delta y/2]$ and $z \in [0, 2]$. The results are obtained for a frequency of $\omega = \frac{3}{4}\pi$, aperture width of $s = 0.25$ and the Mach number of $M_0 = 0.1$.

In the upper part of figure (7.16) the time histories of the pressure perturbation is plotted showing a comparison between the result for the case without mean flow ($M_0 = 0$) and the one with mean flow ($M_0 = 0.1$) at $x = -2.5$, $y = 0.0$, and $z = 1.5$, while the lower part shows a detailed view. As expected, at the microphone location the signal is observed earlier when the mean flow is present. It is also observed that the amplitude has decreased while the observed frequency of the signal does not change when the mean flow is introduced.

In the left parts of figures (7.17 and 7.18) contour plots are shown for the pressure
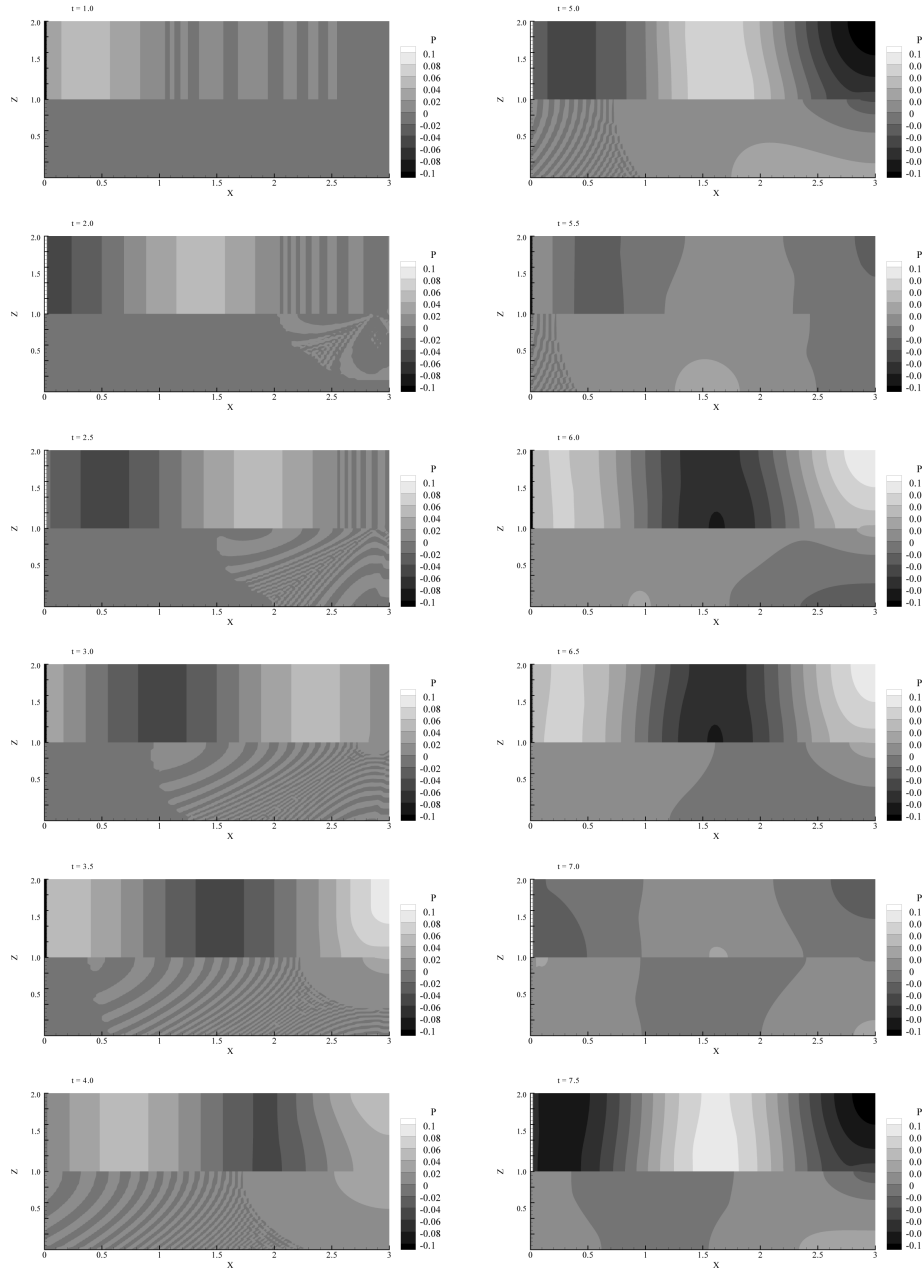
FIGURE 7.13: *Left: Contour plots for the pressure perturbation in the plane $y = \Delta y/2$ for $t = 1.0$ to 7.5 including zero-level. ($\omega = \frac{3}{4}\omega_c$). $\Delta x = \Delta y = \Delta z = 0.025$, $\Delta t = 1.0 \cdot 10^{-3}$.*
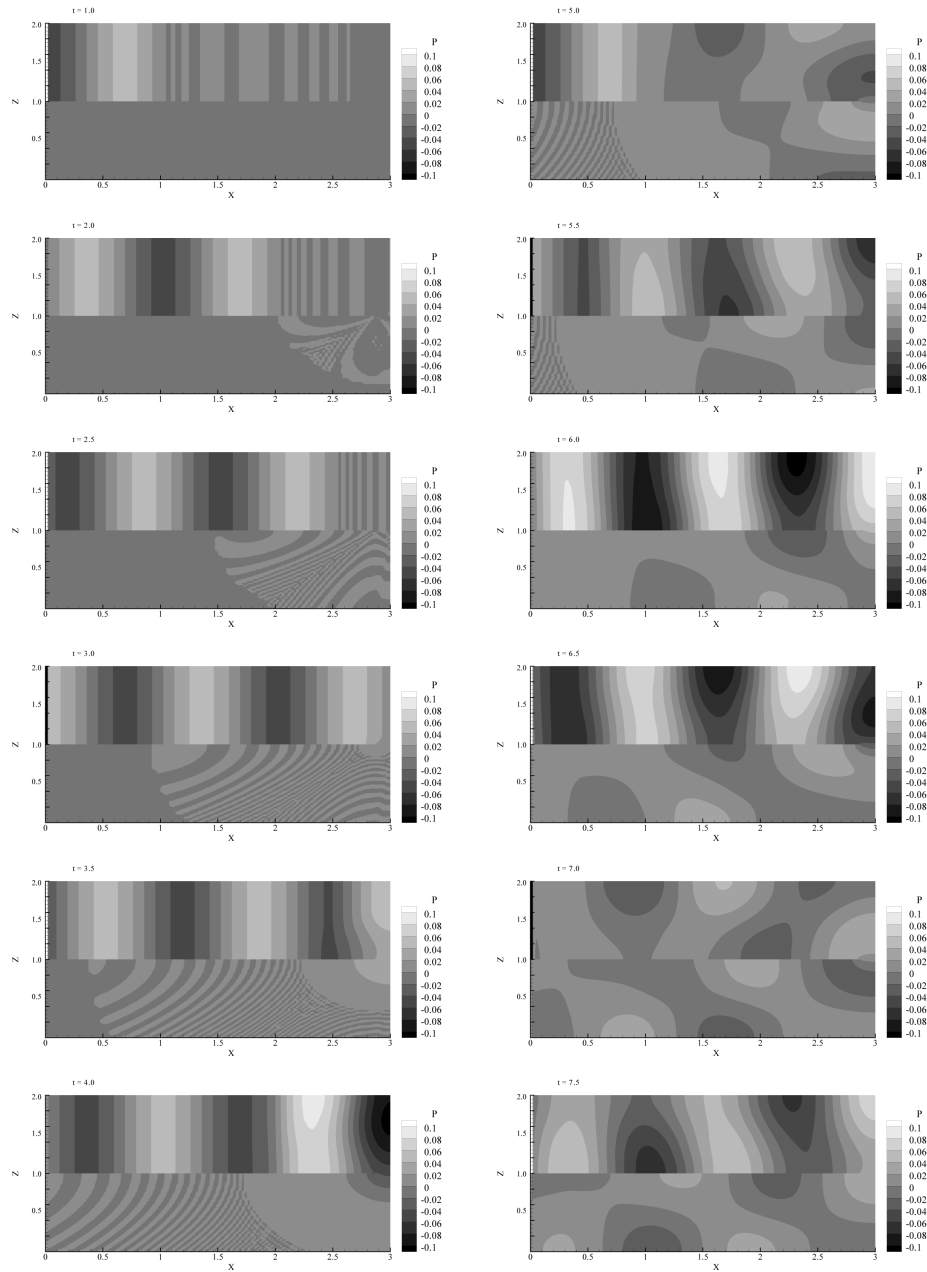
FIGURE 7.14: *Left: Contour plots for the pressure perturbation in the plane $y = \Delta y/2$ for $t = 1.0$ to 4.0 including zero-level. ($\omega = \frac{3}{2}\omega_c$). $\Delta x = \Delta y = \Delta z = 0.025$, $\Delta t = 1.0 \cdot 10^{-3}$.*
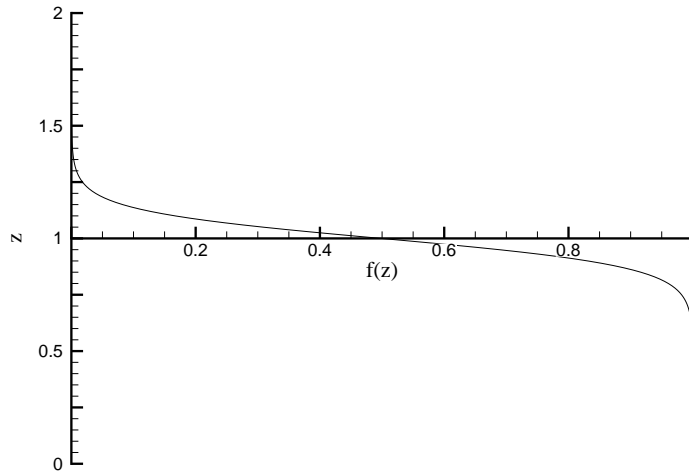
FIGURE 7.15: *The mean flow profile.*

perturbation in the plane $y = \Delta y/2$ for $t = 0.5$ to 7.5 while in the right parts the pressure perturbation along the line ($y = \Delta y/2$, $z = 1.5$), and the line ($x = 0.0$, $y = \Delta y/2$) are plotted.

As in the case without mean flow ($M_0 = 0$) we see the diffraction of acoustic waves in the duct with the slitted flat plate. The sine waves entering the domain from the left and right boundaries of the upper duct reach the geometric plane of symmetry at slightly different times due to the mean flow, which is evident from the non-symmetry of the left parts of the figures (7.17 and 7.18). The reflected wave is seen in region 2 while a wave moves into region 1. Again, as in the case without mean flow the reflected wave appears as a planar wave, while the diffracted wave is two-dimensional.
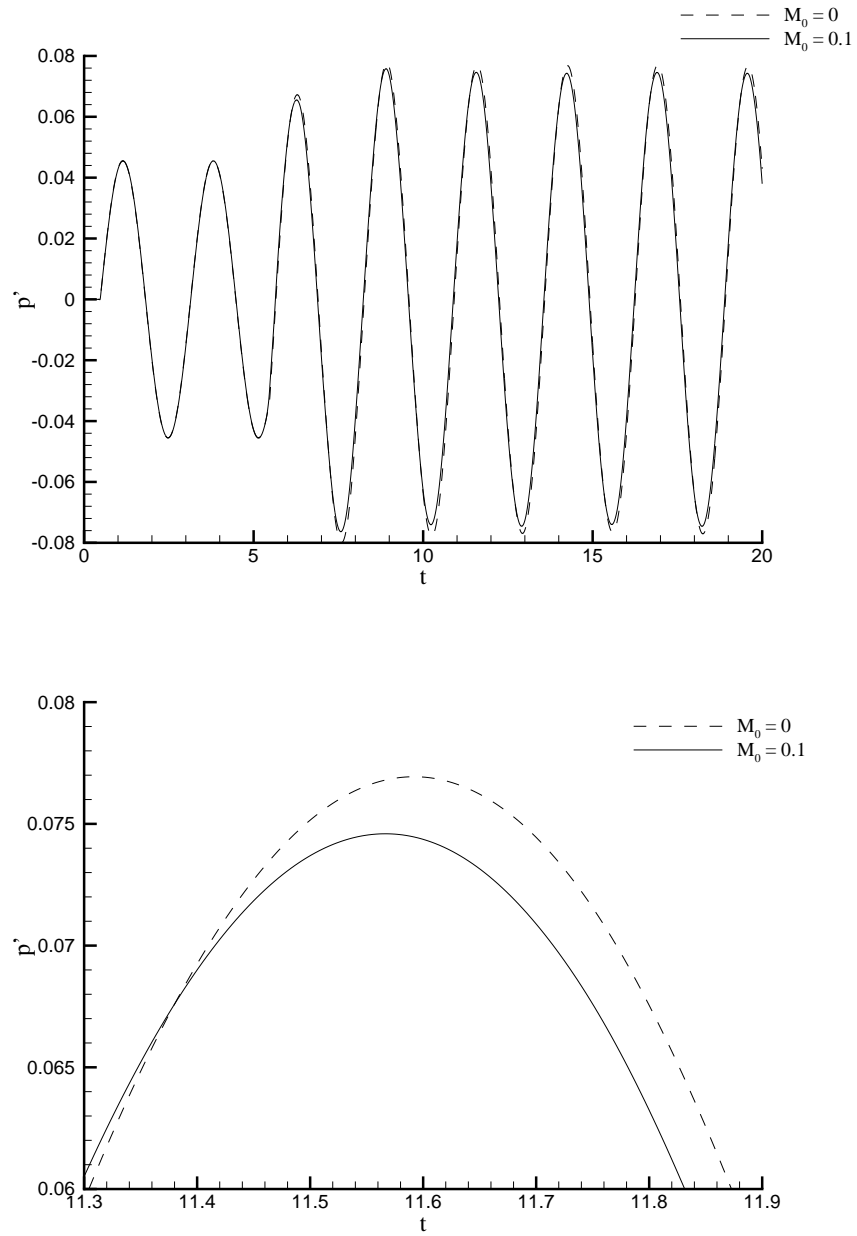
FIGURE 7.16: *Comparison of the time histories of the pressure perturbation with ($M_0 = 0.1$) and without ($M_0 = 0.0$) mean flow recorded at $x = -2.5$, $y = \Delta y/2$ and $z = 1.5$ $\omega = 3/4\pi$, $\Delta x = \Delta y = \Delta z = 0.025$, $\Delta t = 1.0 \cdot 10^{-3}$.*
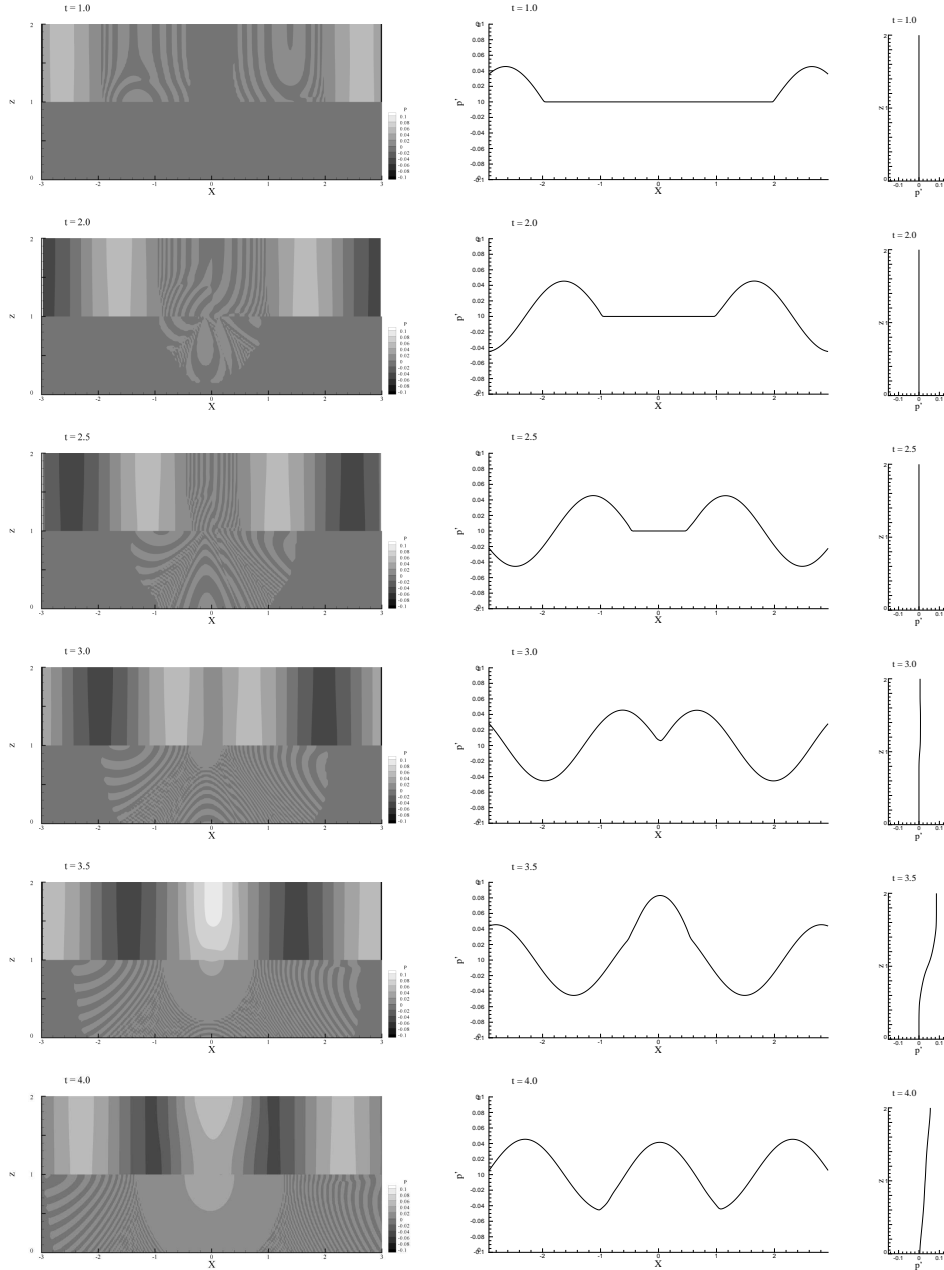
FIGURE 7.17: *Solution with mean flow ($M_0 = 0.1$, $\omega = \frac{3}{4}\pi$). Left: Contour plots for the pressure perturbation in the plane $y = \Delta y/2$ for $t = 1.0$ to 4.0. Middle: Pressure perturbation along line ($y = \Delta y/2$, $z = 1.5$). Right: Pressure perturbation along line ($x = 3.0$, $y = \Delta y/2$). $\Delta x = \Delta y = \Delta z = 0.025$, $\Delta t = 1.0 \cdot 10^{-3}$.*
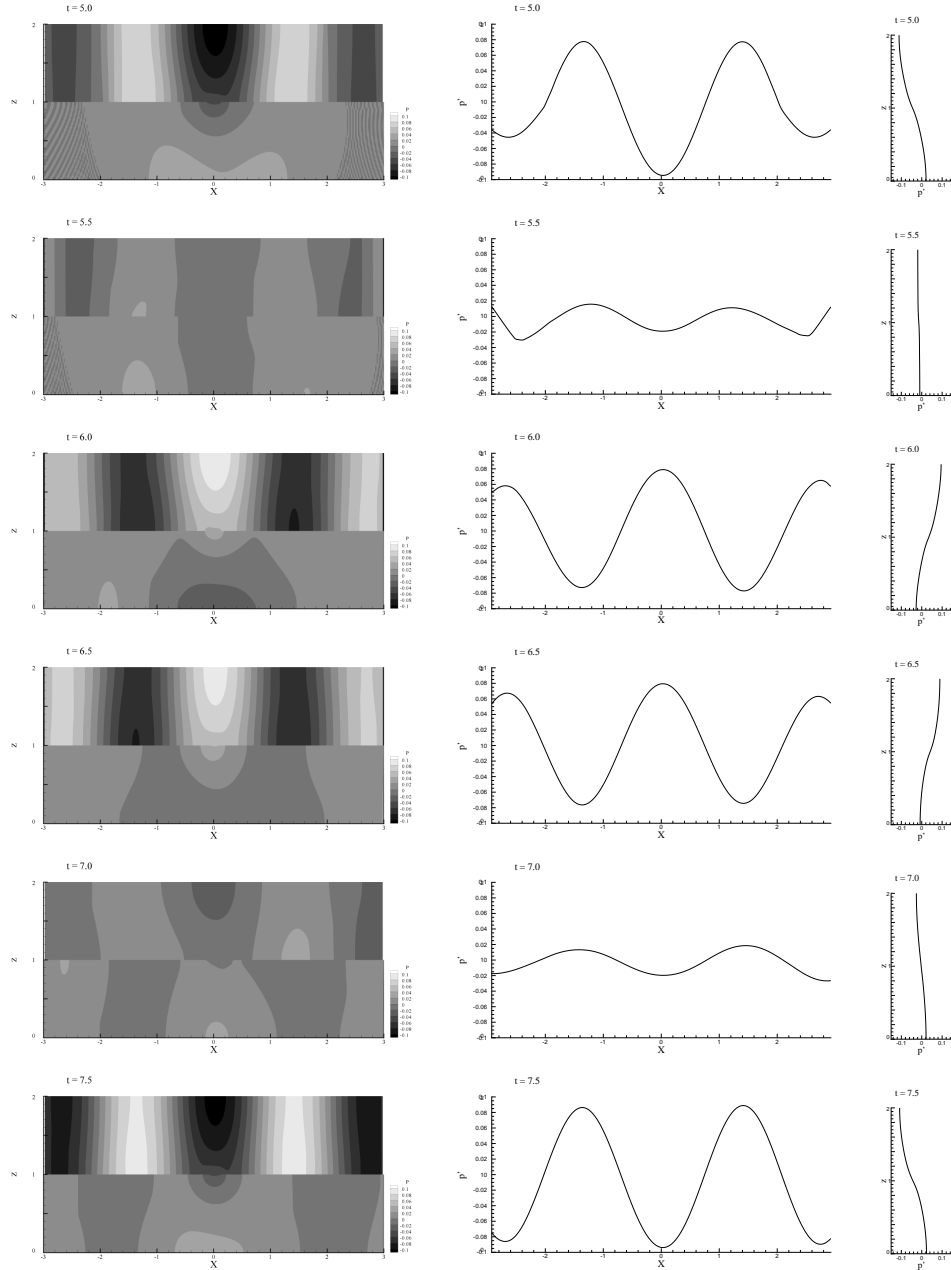
FIGURE 7.18: *Solution with mean flow ($M_0 = 0.1$, $\omega = \frac{3}{4}\pi$). Left: Contour plots for the pressure perturbation in the plane $y = \Delta y/2$ for $t = 5.0$ to 7.5. Middle: Pressure perturbation along line ($y = \Delta y/2$), $z = 1.5$. Right: Pressure perturbation along line ($x = 3.0$, $y = \Delta y/2$). $\Delta x = \Delta y = \Delta z = 0.025$, $\Delta t = 1.0 \cdot 10^{-3}$.*

CONCLUDING REMARKS AND RECOMMENDATIONS

8.1 Concluding Remarks

In this thesis the propagation of acoustic waves in non-uniform flows in three- dimensional space is considered employing a higher-order discontinuous Galerkin method on unstructured hexahedral grids.

The propagation of acoustic waves in non-uniform flows can be described by the linearized Euler equations under the assumptions that there is no feedback from the acoustic field to the background flow field and that the distance of propagation is not too large compared to the acoustic wave length.

The discontinuous Galerkin method has some remarkable advantages with respect to flexibility in discretization of domains with complex geometries. The discontinuous Galerkin method is a highly compact finite-element projection method, which provides a practical framework for the development of a higher-order method, on non-smooth unstructured grids, as desired for computational aeroacoustics ([9], [59], [23], [24], [82], [83], [85]). In recent studies it has been shown that the spatial dispersion error is of order $2p+3$, while the spatial dissipation error is of order $2p+2$ ([60], [50], [4]) with p the degree of the polynomial basis functions. In chapter 3, the higher-order discontinuous Galerkin method is presented for solving the three-dimensional linearized Euler equations on an unstructured hexahedral grid. The method has been implemented for values of p up to $p = 3$.

In chapter 4, the convection of a Gaussian pulse in one-dimension is considered with the present algorithm for three-dimensional wave propagation. The numerical results have been compared to the analytical solution. It has been shown that using polynomial basis functions of higher-degree (> 1) within each element the solution can be obtained with a higher accuracy. This implies that for a given accuracy a smaller number of elements in the solution domain maybe required. An error analysis is performed by using not only the solution at the grid points but also the reconstructed solution at points of an interrogation mesh employed to obtain an accurate approximation of the integral norm. It has been shown that the present method is converging at a rate of h^{p+1} for polynomial basis functions of degree 1,2 and 3

and at a rate slightly higher than $h^{p+1/2}$ for polynomial basis functions of degree 0, which agrees with the convergence rates derived in the literature, e.g. Ref. [60]. It is remarkable that in the plot for the error as function of number of elements, in the range of mesh sizes considered, the line of the order $p-1$ method is situated below the one for the order-(p) method for any p considered. It is also observed that in case fewer points are used to approximate the integral norm, e.g. common grid points of the coarsest or finest mesh considered (where the number of points used to evaluate the integral norm is of the order of the number of grid points) the rate of convergence for polynomial basis functions of degree 1 is about h^3, which might suggest that this specific norm is based on some special points in the solution, namely, points close to the intersection points.

In the low-storage Runge-Kutta time integration scheme four stages have been used and performing a time-refinement study it is shown that the discontinuous Galerkin method implemented is fourth-order accurate in time, as expected for this linear problem.

The present method produces weak waves of small amplitude introduced by the numerics. Originating from the slope-discontinuity at the fronts of the initial wave, wave propagating at a higher speed than c_0 lead the acoustic wave. It is shown in chapter 4 that the numerical dispersion of the method obtained from the numerical solutions is in good agreement with the numerical dispersion relation for the discontinuous Galerkin method applied to a one-dimensional model problem by Blom [25].

CPU-time requirements for the method, using polynomial basis functions of degree 1, 2 and 3, have been determined and a required number of elements and order of accuracy optimization table has been presented.

The problem of acoustic radiation from a vibrating wall segment is solved and the results of the present method are compared to the results obtained by the unstructured tetrahedral grid method developed by Blom [25]. It is concluded that the discontinuous Galerkin method applied on hexahedral elements appears faster for $h \to 0$ than the method applied on tetrahedral elements.

The effect of grid distortion is investigated by considering two types of distorted grids: skewed and randomly distorted grids. For the case of a randomly-distorted mesh the effect of the distortion on the difference between the solution with and the solution without distortion is relatively large. This is attributed to the fact that in the present implementation the mapping of the elements from physical to computational space is assumed to be linear.

The method is applied to a generic acoustic liner problem, i.e. the acoustics of a flat plate with a slit placed in a duct. The results for quiescent background are compared to the analytical solution obtained by Kooijman [64]. It is shown that the ratios of the amplitudes of the reflected and transmitted plane waves are in good agreement with

the analytical results. The results obtained for which a background flow is present is compared to the results obtained for a quiescent background.

8.2 Recommendations

Although a general derivation of the method is given in chapter 3, the discontinuous Galerkin method implemented assumes a piecewise constant background flow. In the considered verification problems the background flow is uniform. In order to apply the method to more general, non-uniform background flows, it is recommended to extend the implementation to account for strongly varying background flows.

In this thesis only characteristic-based non-reflecting boundary conditions have been applied. It is known from the literature that these boundary conditions may result in numerically induced reflections which may contaminate the solution at later times. It is recommended to analyze the performance of other types of boundary conditions such as perfectly matched layers (PML) or sponge layers.

In this thesis an unstructured hexahedral mesh is used and in the implementation it is assumed that the mapping from the element to the unit element is linear. This implies that in order to achieve higher-order accuracy for $p > 1$, formally the shape of the hexahedral elements is restricted to a parallelepiped. Although in chapter 3 the more general case is considered of a high-order approximation of the mapping it is not implemented in the numerical algorithm. It is recommended to investigate the higher-order approximation for the mapping in order to attack problems involving meshes with non-parallelepiped elements using the method for $p > 1$. Furthermore it is recommended to implement the discontinuous Galerkin method applied on a hybrid grid consisting of both tetrahedral and hexahedral elements. This will result in a more versatile method.

REFERENCES

[1] M. Abramowitz and I.A. Segun, *Handbook of Mathematical Functions*, Dover Publications, Inc., New-York, 1968.

[2] R. Abgrall, *An Essentially Non-Oscillatory Reconstruction Procedure on Finite-Element Type Meshes: Application to Compressible Flows*, Computational Methods in Applied Mechanical Engineering, Vol. 116, pp. 95-101, 1994.

[3] S. Adjerid, M. Aiffa and J.E. Flaherty, *High-Order Finite Element Methods for Singularly Perturbed Elliptic and Parabolic Problems*, SIAM Journal of Applied Mathematics, Vol. 55, pp. 520-543, 1995.

[4] M. Ainsworth *Dispersive and dissipative behaviour of high order discontinuous Galerkin finite element methods*, Journal of Computational Physics, Vol 198, 106-130, 2004.

[5] J.D. Anderson, Jr., *Modern Compressible Flow. With Historical Perspective*, McGraw-Hill Series in Aeronautical and Aerospace Engineering, 1990.

[6] ANSI S1.1960 (R1976) American National Standard Acoustical Terminology, American National Standards Institute, Inc. (ANSI), New York, 1976.

[7] H.L. Atkins, *Application of Essentially Nonoscillatory Methods to Aeroacoustic Flow Problems*, Proceedings of ICASE/LaRC Workshop on Benchmark Problems in Computational Aeroacoustics, Edited by J.C. Hardin, J.R. Ristorcelli and C.K.W. Tam, NASA CP-3300, pp. 15-26, 1995.

[8] H.L. Atkins and C.W. Shu, *Quadrature-Free Implementation of Discontinuous Galerkin Method for Hyperbolic Equations*, AIAA-Paper 96-1683, 1996.

[9] H.L. Atkins, *Continued Development of the Discontinuous Galerkin Method for Computational Aeroacoustic Applications*, AIAA-Paper 97-1581, 1997.

[10] H.L. Atkins and C.W. Shu, *Quadrature-Free Implementation of Discontinuous Galerkin Method for Hyperbolic Equations*, AIAA Journal, Vol. 36, pp. 775-782, 1998.

[11] H.L. Atkins and D.P. Lockard, *A High-Order Method Using Unstructured Grids for the Aeroacoustic Analysis of Realistic Aircraft Configurations*, AIAA-Paper 99-1945, Fifth AIAA/CAES Aeroacoustics Conference, May 10-12, 1999.

[12] A. Baggag, H.L. Atkins, C. Özturan and D. Keyes, *Parallelization of an Object-Oriented Unstructured Aeroacoustic Solver*, NASA/CR-1999-209098, ICASE Report No. 99-11, February 1999.

[13] C. Bailly, P. Lafon and S. Candel, *A Stochastic Approach to Compute Noise Generation and Radiation of Free Turbulent Flows*, AIAA Paper 95-092, 1995.

[14] C. Bailly and D. Juvé, *Numerical Solution of Acoustic Propagation Problems Using Linearized Euler Equations*, AIAA Journal, Vol. 38, Nr. 1, pp. 22-29, Jan. 2000.

[15] F. Bassi and S. Rebay, *Accurate 2D Euler Computations by means of a High-Order Discontinuous Finite Element Method*, Proceedings of the 14th International Conference on Numerical Methods in Fluid Dynamics, Bangalor, India, 1994.

[16] F. Bassi and S. Rebay, *Discontinuous Finite Element High Order Accurate Numerical Solution of the Compressible Navier-Stokes Equations*, ICFD Conference on Numerical Methods in Fluid Dynamics, University of Oxford, Oxford, England, 1995.

[17] C.E. Baumann and J.T. Oden, *A Discontinuous hp-Finite Element Method for the Euler and Navier-Stokes Equations*, International Journal for Numerical Methods in Fluids, Vol. 31, pp. 79-95, 1999.

[18] C.E. Baumann and J.T. Oden, *A Discontinuous hp-Finite Element Method for Convection-Diffusion Problems*, Computational Methods in Applied Mechanical Engineering, Vol. 175, pp. 311-341, 1999.

[19] W.M. Beltman, *Viscothermal Wave Propagation Including Acoustic-Elastic Interaction, Part I: Theory*, Journal of Sound and Vibration, Vol. 227(3), pp. 555-586, 1999.

[20] R. Biswas, K.D. Devine and J.E. Flaherty, *Parallel, Adaptive Finite Element Methods for Conservation Laws*, Applied Numerical Methods, Vol. 14, pp. 255-283, 1994.

[21] N. Bleistein and R.A. Handelsman, *Asymptotic Expansions of Integrals*, Dover Publications, Inc., New York, 1976.

[22] C.P.A. Blom, B.T. Verhaar, J.C. van der Heijden and B.I. Soemarwoto, *A Linearized Euler Method Based Prediction of Turbulence Induced Noise Using Time-averaged Flow Properties*, AIAA-Paper 2001-1100, 39th AIAA Aerospace Sciences Meeting and Exhibit, Reno, Jan. 2001.

[23] C.P.A. Blom, R. Hagmeijer, A. Biesheuvel and H.W.M. Hoeijmakers, *Three-dimensional Quadrature-free Discontinuous Galerkin Method for Computational Aeroacoustics*, AIAA-Paper 2001-2198, 7th AIAA/CEAS Aeroacoustics Conference, Maastricht, May 2001.

[24] C.P.A. Blom, R. Hagmeijer and E. Védy, *Development of Discontinuous Galerkin Method for the Linearized Euler Equations*, RTA/AVT Symposium on Developments in Computational Aero- and Hydro-Acoustics, Manchester, United Kingdom, 8-11 October 2001.

[25] C.P.A. Blom, *Discontinuous Galerkin Method on Tetrahedral Elements for Aeroacoustics*, PhD thesis, Department of Mechanical Engineering, Engineering Fluid Dynamics, University of Twente, 2003.

[26] C. P. A. Blom, R. Hagmeijer and H. W. M. Hoeijmakers, Analytical and Numerical Analysis of Duct Acoustics Generated by a Vibrating Wall Segment, 10th AIAA/CEAS Aeroacoustics Conference, Manchester, UK, May 2004.

[27] S.C. Brenner and L. Ridgway Scott, *The Mathematical Theory of Finite Element Methods*, Springer-Verlag, New-York, 1994.

[28] N.A.A. Castelo Branco, *Low Frequency Noise: A Major Risk Factor in Military Operations*, RTA/AVT Symposium on Developments in Computational Aero- and Hydro-Acoustics, Manchester, United Kingdom, 8-11 October 2001.

[29] G. Chavent and B. Cockburn, *The Local Projection P^0P^1-Discontinuous-Galerkin Method for Scalar Conservation Laws*, RAIRO, Model. Math. Anal. Numeri., Vol. 25, 1991

[30] B. Cockburn and C.-W. Shu, *TVB Runge-Kutta Local Projection Discontinuous Galerkin Finite Element Method for Conservation Laws II: General Framework*, Mathematics of Computation, Vol. 52, pp. 411-435, 1989.

[31] B. Cockburn, S.Y. Lin and C.-W. Shu, *TVB Runge-Kutta Local Projection Discontinuous Galerkin Finite Element Method for Conservation Laws III: One-Dimensional Systems*, Journal of Computational Physics, Vol. 84, pp. 90-113, 1989.

[32] B. Cockburn, B. Hou and C.-W. Shu, *TVB Runge-Kutta Local Projection Discontinuous Galerkin Finite Element Method for Conservation Laws IV: The Multidimensional Case*, Mathematics of Computation, Vol. 54, pp. 545-581, 1990.

[33] B. Cockburn and C.-W. Shu, *The P^1-RKDG Method for Two-Dimensional Euler Equations of Gas Dynamics*, ICASE Report 91-32, 1991.

[34] B. Cockburn and C.-W. Shu, *The Runge-Kutta Discontinuous Galerkin Finite-Element Method for Conservation Laws V: Multidimensional System*, Journal of Computational Physics, Vol. 141, pp. 199-224, 1998.

[35] B. Cockburn, M. Luskin, C.-W. Shu and E. Süli, *Post-Processing of Galerkin Methods for Hyperbolic Problems*, Discontinuous Galerkin Methods (Cockburn et al. eds), Springer, pp. 291-300, 2000.

[36] B. Cockburn, G.E. Karniadakis and C.-W. Shu, *Discontinuous Galerkin Methods; Theory, Computation and Applications*, Lecture Notes in Computational Science and Engineering 11, Springer-Verlag Berlin Heidelberg, 2000.

[37] T. Colonius, *Aeroacoustics and Active Noise Control*, Lectures on Computational Aeroacoustics, von Karman Institute for Fluid Dynamics, Lecture Series 1997-07, September 15-18, 1997.

[38] T. Colonius, S.K. Lele, *Computational Aeroacoustics: Progress on Nonlinear Problems of Sound Generation*, Progress in Aerospace Sciences, Vol. 40(6), pp. 345-416, 2004.

[39] J.B. Conway, *Functions of One Complex Variable*, Springer-Verlag, New York, 1986.

[40] D.G. Crighton, A.P. Dowling, J.E. Ffowcs Williams, M. Heckl and F.G. Leppington, *Modern Methods in Analytical Acoustics*, Lecture Notes, Springer-Verlag, London, 1996.

[41] L. Debnath and P. Mikusiński, *Introduction to Hilbert Spaces with Applications*, Academic Press, Inc., San Diego, 1990.

[42] A.P. Dowling and J.E. Ffowcs Williams, *Sound and Sources of Sound*, Ellis Horwood Limited, 1983.

[43] R. Ewert, M. Meinke and W. Schröder, *Computation of Aeroacoustic Sound Via Hybrid CFD/CAA-Methods*, AIAA-Paper 2001-2200, 7th AIAA/CEAS Aeroacoustics Conference, Maastricht, May 2001.

[44] R. Ewert, M. Meinke and W. Schröder, *Aeroacoustic Source Terms for the Linearized Euler-Equations*, AIAA-Paper 00-2046, 2000.

[45] P. Filippi, D. Habault, J.P. Lefebvre and A. Bergassoli, *Acoustics; Basic Physics, Theory and Methods*, Academic Press, London, 1999.

[46] J.E. Flaherty, L. Krivodonova, J-F. Remacle and M.S. Shephard, *Aspects of Discontinuous Galerkin Methods for Hyperbolic Conservation Laws*, Finite Elements in Analysis and Design, Vol. 38, pp. 889-908, 2002.

[47] M.E. Goldstein, *Aerocoustics*, McGraw-Hill International Book Company, New York, 1976.

[48] S.W. Goth, *A Brief Ethymology of Words in the Teaching of Physics*. http://www.smccd.net/accounts/goth/MainPages/wordphys.htm

[49] I.S. Gradshteyn and I.M. Ryzhik, *Table of Integrals, Series, and Products*, Academic Press, inc. 1980.

[50] R. Hagmeijer, C.P.A. Blom and H.W.M. Hoeijmakers, *Wave-Speed Analysis of Discontinuous Galerkin Finite Element Method for Aeroacoustics*, ECCOMAS Computational Fluid Dynamics Conference, 2001.

[51] D.W. Halt and R.K. Agarwal, *Compact Higher-Order Characteristic-Based Euler Solver for Unstructured Grids*, AIAA Journal, Vol. 30, pp. 1993-1999, 1992.

[52] J.C. Hardin and D.S. Pope, *An Acoustic/Viscous Splitting Technique for Computational Aeroacoustics*, Theoretical and Computational Fluid Dynamics, Vol. 6, pp. 323-340, 1996.

[53] A. Harten, B. Engquist, S. Osher and S.R. Chakravarthy, *Uniformly High Order Accurate Essentially Non-Oscillatory Schemes III*, Journal of Computational Physics, Vol. 71, pp. 231-303, 1987.

[54] C. Hirsch, *Numerical Computation of Internal and External Flows, Volume 1: Fundamentals of Numerical Discretization*, John Wiley & Sons Ltd., 1988.

[55] A. Hirschberg, S.W. Rienstra, *Elements of Aeroacoustics*, VKI Lecture Series 1994-04: Applied Aeroacoustics, Brussels, Belgium, 1994.

[56] M.S. Howe, *Acoustics of Fluid-Structure Interactions*, Cambridge University Press, Cambridge, 1998.

[57] M.S. Howe, *Theory of Vortex Sound*, Cambridge University Press, Cambridge, 2003.

[58] F.Q. Hu, M.Y. Hussaini and J.L. Manthey, *Low-Dissipation and Low-Dispersion Runge-Kutta Schemes for Computational Acoustics*, Journal of Computational Physics, Vol. 124, pp. 177-191, 1996.

[59] F.Q. Hu, M.Y. Hussaini and P. Rasetarinera, *An Analysis of the Discontinuous Galerkin Method for Wave Propagation Problems*, Journal of Computational Physics, Vol. 151, pp. 921-946, 1999.

[60] F.Q. Hu and H.L. Atkins, *Eigensolution Analysis of the Discontinuous Galerkin Method with Non-Uniform Grids, Part I:One Space Dimension*, Journal of Computational Physics, Vol. 182, 516-145, 2002.

[61] A. Jameson, W. Schmidt and E. Turkel, *Numerical Solution of the Euler Equations by Finite Volume Methods Using Runge-Kutta Time-Stepping Schemes*, AIAA 14th Fluid and Plasma Dynamics Conference, 1981-1259, California, June 1981.

[62] C. Johnson and J. Pitkäranta, *An Analysis of the Discontinuous Galerkin Method for a Scalar Hyperbolic Equation*, Mathematics of Computation, Vol. 46, No. 176, pp. 1-26, 1986.

[63] D.S. Jones, *Acoustic and Electromagnetic Waves*, Clarendon Press, Oxford, 1986.

[64] G. Kooijman, Y. Aurégan and A. Hirschberg, *Orifice Impedance under Grazing Flow: Modal Expansion Approach*, AIAA 2005-2857, 11th AIAA/CEAS Aeroacoustics Conference (26th AIAA Aeroacoustics Conference), Monterey, CA, USA, 2005.

[65] E. Kreyszig, *Introductory Functional Analysis With Applications*, John Wiley & Sons, 1978.

[66] D. Kröner, *Numerical Schemes for Conservation Laws*, Wiley Teubner, Chichester, 1997.

[67] A.H.W.M. Kuijpers, S.W. Rienstra, G. Verbeek and J.W. Verheij, *The Acoustic Radiation of Baffled Finite Ducts with Vibrating Walls*, Journal of Sound and Vibration, Vol. 216, No. 3, pp. 461-493, 1998.

[68] A.H.W.M. Kuijpers, *Acoustic Modeling and Design of MRI Scanners*, PhD thesis, Technische Universiteit Eindhoven, Eindhoven, the Netherlands, 1999.

[69] K.A. Kurbatskii, R.R. Mankbadi, *Review of Computational Aeroacoustics Algorithms*, International Journal of Computational Fluid Dynamics, Vol. 18(6), pp. 533-546, 2004.

[70] L.D. Landau and E.M. Lifshitz, *Fluid Mechanics, Course of Theoretical Physics, Volume 6*, Butterworth-Heinemann, reprint 2000.

[71] S.K. Lele, *Computational Aeroacoustics: A Review*, AIAA-Paper 97-0018, 35th AIAA Aerospace Sciences Meeting and Exhibit, Reno, Jan. 1997.

[72] P. Lesaint and P.A. Raviart, *On a Finite Element Method for Solving the Neutron Transport Equation*, Mathematical Aspects of Finite Elements in Partial Differential Equations, Academic Press, pp. 89-145, 1974.

[73] M.J. Lighthill, *On Sound Generated Aerodynamically. I. General Theory*, Proceedings of the Royal Society of London. Series A, Mathematical and Physical Sciences, Vol. 211, pp. 564-587, 1952.

[74] M.J. Lighthill, *On Sound Generated Aerodynamically. II. Turbulence as a Source of Sound*, Proceedings of the Royal Society of London. Series A, Mathematical and Physical Sciences, Vol. 222, pp. 1-32, 1954.

[75] M.J. Lighthill, *Waves in Fluids*, Cambridge University Press, Cambridge, 1978.

[76] Q. Lin, N. Yan and A.-H. Zhou, *An Optimal Error Estimate of the Discontinuous Galerkin Method*, Journal of Engineering Mathematics, Vol. 13, pp. 207-210, 1993.

[77] R.B. Lowrie, P.L. Roe and B. van Leer, *A Space-Time Discontinuous Galerkin Method for the Time-Accurate Numerical Solution of Hyperbolic Conservation Laws*, AIAA-Paper 95-1658, 1995.

[78] R.B. Lowrie, *Compact Higher-Order Numerical Methods for Hyperbolic Conservative Laws*, PhD thesis, University of Michigan, 1996.

[79] P.M. Morse and H. Feshbach, *Methods of Theoretical Physics*, Vol. I & II, McGraw-Hill Book Company, Inc., 1953.

[80] P.M. Morse and K.U. Ingard, *Theoretical Acoustics*, McGraw-Hill Book Company, 1968.

[81] *Noise in Europe: A Briefing from the NGO Community*.

[82] H. Özdemir, R. Hagmeijer and H. W. M. Hoeijmakers, *Development of Higher-Order Discontinuous Galerkin Method on Hexahedral Elements*, Euromech Colloquium 449: Computational Aeroacoustics, Chamonix, France, December 2003.

[83] H. Özdemir, C.P.A. Blom, R. Hagmeijer and H. W. M. Hoeijmakers, *Development of Higher-Order Discontinuous Galerkin Method on Hexahedral Elements*, 10th AIAA/CEAS Aeroacoustics Conference, Manchester, UK, May 2004.

[84] H. Özdemir, G. Kooijman, R. Hagmeijer, A. Hirschberg, H.W.M. Hoeijmakers, *Validation of Higher-Order Discontinuous Galerkin Method for the Linearized Euler Equations*, AIAA 2005-2821, 11th AIAA/CEAS Aeroacoustics Conference (26th AIAA Aeroacoustics Conference), Monterey, CA, USA, 2005.

[85] H. Özdemir, R. Hagmeijer, H.W.M. Hoeijmakers, *Verification of Higher-Order Discontinuous Galerkin Method on Hexahedral Elements*, Comptes Rendus Mecanique, Vol. 333, pp. 719-725, 2005.

[86] A. Papoulis, *The Fourier Integral and Its Applications*, McGraw-Hill Book Company, Inc., 1962.

[87] T. Peterson, *A Note on the Convergence of the Discontinuous Galerkin Method for a Scalar Hyperbolic Equation*, SIAM J. Numer. Anal., Vol. 28, pp. 133-140, 1991.

[88] A.D. Pierce, *Acoustics. An Introduction to Its Physical Principles and Applications*, the Acoustical Society of America, New York, 1994.

[89] L. Råde and B. Westergren, *Mathematics Handbook, for Science and Engineering*, 4th Edition, 1999.

[90] P. Rasetarinera, M.Y. Hussaini and F.Q. Hu, *Some Remarks on the Accuracy of a Discontinuous Galerkin Method*, Discontinuous Galerkin Methods (Cockburn et. al eds), Springer, pp. 425-431, 2000.

[91] W.H. Reed and T.R. Hill, *Triangular Mesh Methods for the Neutron Transport Equation*, Technical Report LA-UR-73-479, Los Alamos Scientific Laboratory, 1973.

[92] S. Redonnet, E. Manoha and P. Sagaut, *Numerical Simulation of Small Perturbations Interacting with Flows and Solid Bodies*, AIAA-Paper 01-2223, 2001.

[93] G.R. Richter, *An Optimal-Order Error Estimate for the Discontinuous Galerkin Method*, Mathematics of Computations, Vol. 50, pp. 75-88, 1988.

[94] L. Råde, *Mathematics Handbook*, for Science and Engineering, Fourth Edition, Springer-Verlag Berlin Heidelberg, 1999.

[95] S.W. Rienstra, A. Hirschberg, *An Introduction to Aeroacoustics*, Report IWDE 01-03 May 2001 (extended and revised version of IWDE 92-06, also available at http://www.win.tue.nl/ sjoerdr/), Eindhoven University of Technology, 2001.

[96] W. Rudin, *Real and Complex Analysis*, McGraw-Hill, 1986.

[97] S. Schreier, *Compressible Flow*, John Wiley & Sons Inc., New York, 1982.

[98] S. Sherwin, *Dispertion Analysis of the Continuous and Discontinuous Galerkin Formulations*, Discontinuous Galerkin Methods (Cockburn et al. ads), Springer, pp. 425-431, 2000.

[99] M. Snellen, L. van Lier, C. Rops, M.H.A. Janssens, J. van Heck and G.S. Strumolo, *Flow Induced Noise Around the A-pillar of an Idealized Car Greenhouse*, AIAA-Paper 2002-2548, 8th AIAA/CEAS Aeroacoustics Conference, Breckenridge, 2002.

[100] E. Süli, P. Houston and B. Senior, *hp-Discontinuous Galerkin Finite Element Methods for Hyperbolic Problems: Error Analysis and Adaptivity*, Journal for Numerical Methods in Fluids, Vol. 40(1-2), pp. 153-169, 2002.

[101] Y. Takahashi, Y. Yonekawa and K. Kanada, *A New Approach to Assess Low Frequency Noise in the Working Environment*, Industrial Health, Vol. 39, pp. 281-286, 2001.

[102] C.K.W. Tam and J.C. Webb, *Dispersion-Relation-Preserving Finite Difference Schemes for Computational Acoustics*, Journal of Computational Physics, Vol. 107, pp. 262-281, 1993.

[103] C.K.W. Tam, *Computational Aeroacoustics: Methods and Applications*, AIAA-Journal, Vol. 33, No. 10, pp. 1788-1796, 1995.

[104] C.K.W. Tam, *Computational Aeroacoustics: Methods and Applications*, An AIAA Professional Development Short Course, Lahaina, Hawaii, June 2000.

[105] C.K.W. Tam, *Computational Aeroacoustics: An Overview of Computational Challanges and Applications*, International Journal of Computational Fluid Dyamics, Vol. 18(6), pp. 546-567, 2004.

[106] Teras, 1024-CPU SGI Origin 3800 system. http://www.sara.nl.

[107] J.J.W. van der Vegt, *Anisotropic Grid Refinement Using an Unstructured Discontinuous Galerkin Method for the Three-Dimensional Euler Equations of Gas Dynamics*, Procedings 12th AIAA CFD Conference, San Diego, California, AIAA-Paper 95-1657, 1995.

[108] J.J.W. van der Vegt and H. van der Ven, *Discontinuous Galerkin Finite Element Method with Anisotropic Grid Refinement for Inviscid Compressible Flows*, Journal of Computational Physics, Vol. 141, pp. 46-77, 1998.

[109] J.J.W. van der Vegt and H. van der Ven, *Space-time Discontinuous Galerkin Finite Element Method with Dynamic Grid Motion for Inviscid Compressible Flows. I. General Formulation*, Journal of Computational Physiscs, Vol. 182, pp. 546-585, 2002.

[110] H. van der Ven and J.J.W. van der Vegt, *Space-time Discontinuous Galerkin Finite Element Method with Dynamic Grid Motion for Inviscid Compressible Flows. II. Efficient Flux Quadrature*, Computational Methods in Applied Mechanical Engineering, Vol. 191, pp. 4747-4780, 2002.

[111] J.J.W. van der Vegt and H. van der Ven, *Slip Flow Boundary Conditions in Discontinuous Galerkin Discretizations of the Euler Equations of Gas Dynamics*, WCCM V, Fifth World Congress on Computational Mechanics, 2002.

[112] M. Wang, J.B. Freund and S.K. Lele, *Computational Predictions of Flow Generated Sound*, Annual Review of Fluid Mechanics, Vol. 38, pp. 483-512, 2006.

[113] V.L. Wells, R.A. Renaut, *Computing Aerodynamically Generated Noise*, Annual Review of Fluid Mechanics, Vol. 29, pp. 161-199, 1997.

[114] F.M. White, *Viscous Fluid Flow*, McGraw-Hill, Inc., 1991.

[115] C.R. Wylie, *Advanced Engineering Mathematics*, McGraw-Hill, Japan, 1975.

TRANSFORMATION TO COMPUTATIONAL SPACE

A.1 The transformation from the physical to the computational space

Vectors tangential to the ξ, η, ζ coordinate lines are $\frac{\partial \vec{x}}{\partial \xi}$, $\frac{\partial \vec{x}}{\partial \eta}$, $\frac{\partial \vec{x}}{\partial \zeta}$, respectively, denoted by $\vec{x}_\xi$, $\vec{x}_\eta$, $\vec{x}_\zeta$, respectively, the so-called co-variant directions.

The surface $\xi = constant$, $\eta = constant$, $\zeta = constant$ have their normal in the direction $\vec{x}_\eta \times \vec{x}_\zeta$, $-\vec{x}_\xi \times \vec{x}_\zeta$, $\vec{x}_\xi \times \vec{x}_\eta$ respectively.

From differentiating $x = x(\xi, \eta, \zeta)$, $y = y(\xi, \eta, \zeta)$, $z = z(\xi, \eta, \zeta)$ with respect to x, we find $\frac{\partial \xi}{\partial x}$, $\frac{\partial \eta}{\partial x}$, $\frac{\partial \zeta}{\partial x}$ in terms of $\vec{x}_\xi$, $\vec{x}_\eta$ and $\vec{x}_\zeta$. Differentiation with respect to y yields $\frac{\partial \xi}{\partial y}$, $\frac{\partial \eta}{\partial y}$, $\frac{\partial \zeta}{\partial y}$. Differentiation with respect to z yields $\frac{\partial \xi}{\partial z}$, $\frac{\partial \eta}{\partial z}$, $\frac{\partial \zeta}{\partial z}$. An example:

$$\begin{cases} 1 = x_\xi \xi_x + x_\eta \eta_x + x_\zeta \zeta_x \\ 0 = y_\xi \xi_x + y_\eta \eta_x + y_\zeta \zeta_x \\ 0 = z_\xi \xi_x + z_\eta \eta_x + z_\zeta \zeta_x \end{cases} \Rightarrow \begin{cases} \xi_x = (y_\eta z_\zeta - y_\zeta z_\eta)/|J| \\ \eta_x = -(y_\xi z_\zeta - y_\zeta z_\xi)/|J| \\ \zeta_x = (y_\xi z_\eta - y_\eta z_\xi)/|J| \end{cases} \quad \text{(A.1)}$$

where,

$$J = \begin{pmatrix} x_\xi & x_\eta & x_\zeta \\ y_\xi & y_\eta & y_\zeta \\ z_\xi & z_\eta & z_\zeta \end{pmatrix} \equiv \frac{\partial(x, y, z)}{\partial(\xi, \eta, \zeta)}, \quad \text{(A.2)}$$

and,

$$|J| = det(J) = \vec{x}_\xi \cdot (\vec{x}_\eta \times \vec{x}_\zeta). \quad \text{(A.3)}$$

This leads to the expression for the normal directions on the surface $\xi = constant$, which is $\vec{\nabla}\xi$, that for the surface $\eta = constant$, which is $\vec{\nabla}\eta$ and finally that for the normal direction on the surface $\zeta = constant$, which is $\vec{\nabla}\zeta$:

$$\begin{aligned} \vec{\nabla}\xi &= (\vec{x}_\eta \times \vec{x}_\zeta)/|J| \\ \vec{\nabla}\eta &= -(\vec{x}_\xi \times \vec{x}_\zeta)/|J| \\ \vec{\nabla}\zeta &= (\vec{x}_\xi \times \vec{x}_\eta)/|J| \end{aligned}$$

$$\text{(A.4)}$$

These vectors give the so-called contra-variant vectors.

A.1.1 Transformation of $\vec{\nabla}_{\vec{x}}$ to $\vec{\nabla}_{\vec{\xi}}$

In case we have $\vec{\nabla}_{\vec{x}} f$ we find

$$
\begin{aligned}
\frac{\partial f}{\partial x} &= \frac{\partial f}{\partial \xi}\xi_x + \frac{\partial f}{\partial \eta}\eta_x + \frac{\partial f}{\partial \zeta}\zeta_x \\
\frac{\partial f}{\partial y} &= \frac{\partial f}{\partial \xi}\xi_y + \frac{\partial f}{\partial \eta}\eta_y + \frac{\partial f}{\partial \zeta}\zeta_y \qquad \Rightarrow \vec{\nabla}_{\vec{x}} f = J^{-1}\vec{\nabla}_{\vec{\xi}} f, \qquad (A.5) \\
\frac{\partial f}{\partial z} &= \frac{\partial f}{\partial \xi}\xi_z + \frac{\partial f}{\partial \eta}\eta_z + \frac{\partial f}{\partial \zeta}\zeta_z
\end{aligned}
$$

with

$$
J^{-1} = \begin{pmatrix} \xi_x & \xi_y & \xi_z \\ \eta_x & \eta_y & \eta_z \\ \zeta_x & \zeta_y & \zeta_z \end{pmatrix} \equiv \frac{\partial(\xi, \eta, \zeta)}{\partial(x, y, z)}; \quad |J^{-1}| = \vec{\nabla}\xi \cdot (\vec{\nabla}\eta \times \vec{\nabla}\zeta) = \frac{1}{|J|} \quad (A.6)
$$

A.1.2 Transformation of an infinitesimal volume element

$$
\begin{aligned}
d\Omega &= dxdydz && \text{in Cartesian coordinates} \\
&= \vec{x}_\xi \cdot (\vec{x}_\eta \times \vec{x}_\zeta)d\xi d\eta d\zeta && \text{in } (\xi, \eta, \zeta) \text{ coordinates} \\
&= |J|d\xi d\eta d\zeta \\
&= |J|d\hat{\Omega} && (A.7)
\end{aligned}
$$

A.1.3 Transformation of a vector

Any vector $\vec{a}$ can be expressed in terms of the three vectors $\vec{e}_\xi$, $\vec{e}_\eta$ and $\vec{e}_\zeta$ as:

$$
\begin{aligned}
\vec{a} &= \frac{\vec{a} \cdot (\vec{e}_\eta \times \vec{e}_\zeta)}{|J|}\vec{e}_\xi + \frac{\vec{a} \cdot (\vec{e}_\xi \times \vec{e}_\zeta)}{|J|}\vec{e}_\eta + \frac{\vec{a} \cdot (\vec{e}_\xi \times \vec{e}_\eta)}{|J|}\vec{e}_\zeta \\
&= a^\xi \vec{e}_\xi + a^\eta \vec{e}_\eta + a^\zeta \vec{e}_\zeta && (A.8)
\end{aligned}
$$

which can also be written as:

$$
\begin{pmatrix} a^\xi \\ a^\eta \\ a^\zeta \end{pmatrix} = J^{-1} \begin{pmatrix} a^x \\ a^y \\ a^z \end{pmatrix}, \qquad (A.9)
$$

or,

$$
\begin{aligned}
\vec{a} &= a^x \vec{e}_x + a^y \vec{e}_y + a^z \vec{e}_z \\
&= a^\xi \vec{e}_\xi + a^\eta \vec{e}_\eta + a^\zeta \vec{e}_\zeta && (A.10)
\end{aligned}
$$

TRANSFORMATION OF THE ELEMENTS
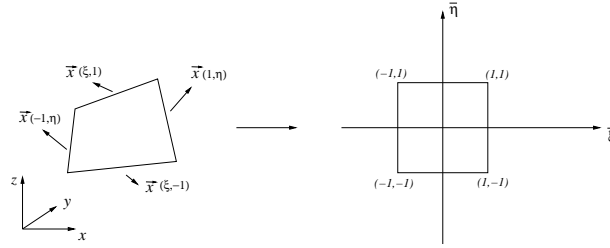
B.1 Bilinear transformation

FIGURE B.1: *Transformation of a 2D surface.*

Bilinear transformation from the physical space to the computational plane can be constructed as follows:

$$
\begin{aligned}
\vec{x}(\bar{\xi}, -1) &= \vec{x}(-1, -1)Q_1(\xi) + \vec{x}(1, -1)Q_2(\xi), \\
\vec{x}(\bar{\xi}, 1) &= \vec{x}(-1, 1)Q_1(\xi) + \vec{x}(1, 1)Q_2(\xi), \\
\vec{x}(-1, \bar{\eta}) &= \vec{x}(-1, -1)Q_1(\eta) + \vec{x}(-1, 1)Q_2(\eta), \\
\vec{x}(1, \bar{\eta}) &= \vec{x}(1, -1)Q_1(\eta) + \vec{x}(1, 1)Q_2(\eta).
\end{aligned}
\tag{B.1}
$$

Combining the above equations we can derive the following relation:

$$
\begin{aligned}
\vec{x}(\bar{\xi}, \bar{\eta}) &= \vec{x}(-1, -1)Q_1(\xi)Q_1(\eta) + \vec{x}(1, -1)Q_2(\xi)Q_1(\eta) \\
&\quad + \vec{x}(-1, 1)Q_1(\xi)Q_2(\eta) + \vec{x}(1, 1)Q_2(\xi)Q_2(\eta)
\end{aligned}
\tag{B.2}
$$

with,

$$
\begin{aligned}
Q_1(\bar{\xi}) = \frac{1 - \bar{\xi}}{2}, && Q_2(\bar{\xi}) = \frac{1 + \bar{\xi}}{2}, \\
Q_1(\bar{\eta}) = \frac{1 - \bar{\eta}}{2}, && Q_2(\bar{\eta}) = \frac{1 + \bar{\eta}}{2}.
\end{aligned}
\tag{B.3}
$$

Finally we get for the bilinear coordinate transformation:

$$
\begin{aligned}
\vec{x}(\bar{\xi},\bar{\eta}) \;=\;& \vec{x}(-1,-1)\frac{(1-\bar{\xi})(1-\bar{\eta})}{4} + \vec{x}(1,-1)\frac{(1+\bar{\xi})(1-\bar{\eta})}{4} \\
& +\vec{x}(-1,1)\frac{(1-\bar{\xi})(1+\bar{\eta})}{4} + \vec{x}(1,1)\frac{(1+\bar{\xi})(1+\bar{\eta})}{4}. \quad \text{(B.4)}
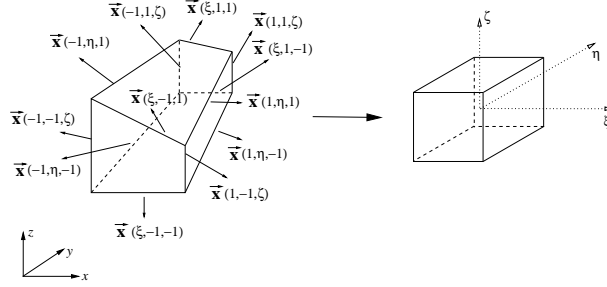\end{aligned}
$$

B.2   Trilinear transformation

FIGURE B.2: *Trilinear transformation of a 3D volume element.*

Trilinear transformation from the physical to the computational space can be constructed as follows:

$$
\begin{aligned}
\vec{x}(\xi,-1,-1) &= \vec{x}(-1,-1,-1)Q_1(\xi) + \vec{x}(1,-1,-1)Q_2(\xi), \\
\vec{x}(\xi,1,-1) &= \vec{x}(-1,1,-1)Q_1(\xi) + \vec{x}(1,1,-1)Q_2(\xi), \\
\vec{x}(\xi,-1,1) &= \vec{x}(-1,-1,1)Q_1(\xi) + \vec{x}(1,-1,1)Q_2(\xi), \\
\vec{x}(\xi,1,1) &= \vec{x}(-1,1,1)Q_1(\xi) + \vec{x}(1,1,1)Q_2(\xi), \\
\vec{x}(-1,\eta,-1) &= \vec{x}(-1,-1,-1)Q_1(\eta) + \vec{x}(-1,1,-1)Q_2(\eta), \\
\vec{x}(1,\eta,-1) &= \vec{x}(1,-1,-1)Q_1(\eta) + \vec{x}(1,1,-1)Q_2(\eta), \\
\vec{x}(-1,\eta,1) &= \vec{x}(-1,-1,1)Q_1(\eta) + \vec{x}(-1,1,1)Q_2(\eta), \\
\vec{x}(1,\eta,1) &= \vec{x}(1,-1,1)Q_1(\eta) + \vec{x}(1,1,1)Q_2(\eta), \\
\vec{x}(-1,-1,\zeta) &= \vec{x}(-1,-1,-1)Q_1(\zeta) + \vec{x}(-1,-1,1)Q_2(\eta), \\
\vec{x}(1,-1,\zeta) &= \vec{x}(1,-1,-1)Q_1(\zeta) + \vec{x}(1,-1,1)Q_2(\eta), \\
\vec{x}(-1,1,\zeta) &= \vec{x}(-1,1,-1)Q_1(\zeta) + \vec{x}(-1,1,1)Q_2(\eta), \\
\vec{x}(1,1,\zeta) &= \vec{x}(1,1,-1)Q_1(\zeta) + \vec{x}(1,1,1)Q_2(\eta). \quad \text{(B.5)}
\end{aligned}
$$

Combining the above equations we can derive the following relation:

$$
\vec{x}(\xi,\eta,\zeta) \;=\; \vec{x}(-1,-1,-1)Q_1(\xi)Q_1(\eta)Q_1(\zeta) + \vec{x}(1,-1,-1)Q_2(\xi)Q_1(\eta)Q_1(\zeta)
$$

$$+\vec{x}(-1,1,-1)Q_1(\xi)Q_2(\eta)Q_1(\zeta) + \vec{x}(1,1,-1)Q_2(\xi)Q_2(\eta)Q_1(\zeta)$$
$$+\vec{x}(-1,-1,1)Q_1(\xi)Q_1(\eta)Q_2(\zeta) + \vec{x}(1,-1,1)Q_2(\xi)Q_1(\eta)Q_2(\zeta)$$
$$+\vec{x}(-1,1,1)Q_1(\xi)Q_2(\eta)Q_2(\zeta) + \vec{x}(1,1,1)Q_2(\xi)Q_2(\eta)Q_2(\zeta)$$

$$(B.6)$$

with,

$$Q_1(\xi) = \frac{1-\xi}{2}, \qquad Q_2(\xi) = \frac{1+\xi}{2},$$
$$Q_1(\eta) = \frac{1-\eta}{2}, \qquad Q_2(\eta) = \frac{1+\eta}{2},$$
$$Q_1(\zeta) = \frac{1-\zeta}{2}, \qquad Q_2(\zeta) = \frac{1+\zeta}{2}. \qquad (B.7)$$

Finally we get for the trilinear coordinate transformation:

$$\vec{x}(\xi,\eta,\zeta) = \vec{x}(-1,-1,-1)\frac{(1-\xi)(1-\eta)(1-\zeta)}{8}$$
$$+\vec{x}(1,-1,-1)\frac{(1+\xi)(1-\eta)(1-\zeta)}{8}$$
$$+\vec{x}(-1,1,-1)\frac{(1-\xi)(1+\eta)(1-\zeta)}{8}$$
$$+\vec{x}(1,1,-1)\frac{(1+\xi)(1+\eta)(1-\zeta)}{8}$$
$$+\vec{x}(-1,-1,1)\frac{(1-\xi)(1-\eta)(1+\zeta)}{8}$$
$$+\vec{x}(1,-1,1)\frac{(1+\xi)(1-\eta)(1+\zeta)}{8}$$
$$+\vec{x}(-1,1,1)\frac{(1-\xi)(1+\eta)(1+\zeta)}{8}$$
$$+\vec{x}(1,1,1)\frac{(1+\xi)(1+\eta)(1+\zeta)}{8}. \qquad (B.8)$$

SUMMARY

The propagation of acoustic waves in non-uniform flow in three-dimensional space is investigated by means of a numerical method based on the discontinuous Galerkin finite-element formulation. The propagation of acoustic waves in non-uniform flows can be described by the linearized Euler equations under the assumptions that there is no feedback from the acoustic field to the background flow field and the distance of propagation is not too large compared to the acoustic wave lengths.

The discontinuous Galerkin method has some remarkable advantages with respect to flexibility in discretization of domains with complex geometries. The discontinuous Galerkin method is a highly compact finite-element projection method which provides a practical framework for the development of higher-order methods desired for computational aeroacoustics on non-smooth unstructured grids, as discussed in the literature. In the present study the higher-order discontinuous Galerkin method is presented for solving the three-dimensional Linearized Euler Equations on an unstructured hexahedral grid.

The implementation of the method is verified by considering the convection of a Gaussian pulse in one-dimension, with the present three-dimensional numerical algorithm, and comparing the numerical results to the analytical solution. The numerical results have been obtained using polynomial basis functions in the discontinuous Galerkin method of degree ≤ 3. It has been shown that using polynomial basis functions of higher-degree (> 1) the solution can be reconstructed with a higher accuracy within each element, which implies that for given accuracy fewer elements maybe required in the solution domain. An error analysis has been performed using not only the solution at the grid points but also the reconstructed solution at grid points of the interrogation mesh, this to obtain an accurate approximation of the integral norm. It shows that the method is converging at a rate of h^{p+1} for polynomial basis functions of degree 1,2 and 3 and at a rate slightly higher than $h^{p+1/2}$ for polynomial basis functions of degree 0, which agrees with the convergence rates derived in the literature. It is remarkable that in the range of h considered the line of the order p method is situated below the one for the order-$(p-1)$ method for any p considered. It is also observed that in case fewer points are used to evaluate the L_2-norm, e.g.

common grid points of the coarsest or finest mesh considered (where the number of points used to evaluate the L_2 norm is of the order of the number of grid points) the rate of convergence for polynomial basis functions of degree 1 is about h^3 which might suggest that this specific norm is based on some special points in the solution, namely, points close to the intersection points of analytical and numerical solution.

The low-storage Runge-Kutta time integration scheme with four stages has been used. Performing a time-refinement study showed that the Discontinuous Galerkin method implemented is fourth-order accurate in time which is as expected for this linear problem.

The present method produces weak waves of small amplitude introduced by the numerics. Originating from the slope-discontinuity at the fronts of the initial wave, waves propagating at a higher speed than c_0 lead the acoustic wave. It is shown that the numerical dispersion of the method obtained from the numerical solutions obeys the numerical dispersion relation for the discontinuous Galerkin method found earlier by Blom for a one-dimensional model problem.

CPU-time requirements for the methods, using polynomial basis functions of degree 1, 2 and 3, to reach a certain dimensionless time, for a certain error-level condition are discussed and the required number of elements and order of accuracy optimization table is given for the test problem considered.

The acoustic radiation from a vibrating wall segment in a duct is numerically simulated as a second verification problem. The results obtained are compared to the results obtained by the DG method developed by Blom for a tetrahedral grid. It is concluded that the discontinuous Galerkin method applied on a mesh consisting of hexahedral elements appears faster for $h \rightarrow 0$ than the method applied on a mesh consisting of tetrahedral elements.

The effects of grid distortion is investigated solving the problem of acoustic radiation from a vibrating wall segment in a duct. Two types of distorted grid have been considered: skewed and randomly distorted grids. It is shown that the method is able to handle problems involving grid irregularities up to certain skewness/distortion levels.

As a validation problem the method is applied to a generic acoustic liner problem, i.e. acoustics of a flat plate with a slit placed in a 2D duct. The results for quiescent background is compared to the analytical solution obtained by Kooijman. It is shown that the ratios of the amplitudes of the reflected and transmitted plane waves are in good agreement with the analytical results. Furthermore results are presented for the case where a mean flow is present. The results are compared to results obtained for a quiescent background.

SAMENVATTING

De voortplanting van akoestische golven in niet-uniforme driedimensionale stromingen is onderzocht door middel van een numerieke methode die is gebaseerd op de Discontinue Galerkin Eindige-Elementen formulering, geïmplementeerd op een niet-gestructureerd rekenrooster bestaande uit hexahedra. De voortplanting van akoestische golven in niet-uniforme stromingen wordt beschreven met de gelineariseerde Euler vergelijkingen voor het perturbatie druk-, snelheids- en dichtheidsveld op een niet-uniforme tijdsgemiddelde stromingsveld. Deze linearisatie is geldig onder de aannames dat er geen terugkoppeling is van het akoestische veld naar het tijdsgemiddelde stromingsveld en dat de afstand waarover het geluid zich voortplant niet te groot is ten opzichte van de akoestische golflengte.

De Discontinue Galerkin (DG) Eindige Elementenmethode heeft opmerkelijke voordelen wat betreft flexibiliteit in de keuze van de discretisatie van rekendomeinen om geometrisch complexe configuraties. De methode is een uiterst compacte eindige-elementen projectie formulering. Voor een aëro-akoestische rekenmethode biedt de DG formulering een praktisch raamwerk voor de ontwikkeling van een hogere-orde methode voor niet-gestructureerde niet-gladde rekenroosters. In dit proefschrift wordt een hogere-orde DG methode gepresenteerd voor het numeriek oplossen van de gelineariseerde Euler vergelijkingen op een niet-gestructureerd rekenrooster bestaande uit hexahedra.

De implementatie van de rekenmethode is geverifieerd aan de hand van de numerieke simulatie, met de rekenmethode voor driedimensionale golfvoortplanting, van de convectie van een eendimensionale Gaussische puls. De resultaten van de numerieke simulatie, met de methode gebaseerd op DG formulering voor graad $p = 3$, zijn vergeleken met die van de analytische oplossing. De vergelijking geeft aan dat, gebruikmakend van basis functies van hogere orde (> 1), de oplossing, voor een vast aantal elementen, met een hogere graad van nauwkeurigheid kan worden berekend, of dat voor een gekozen niveau van nauwkeurigheid het aantal elementen waarin het rekengebied is opgedeeld kan worden beperkt. Voor de methoden die gebruikmaken van polynoom basisfuncties van de graad $p = 1$, 2 en 3 zijn de benodigde reken (CPU) tijd bepaald om in een testgeval de golfvoortplanting tot een bepaald tijdstip

numeriek te simuleren, dit op een aantal rekenroosters van toenemende resolutie. Deze informatie kan worden gebruikt om bij de toepassing van de rekenmethode, voor een gekozen niveau van nauwkeurigheid, een optimale keuze te maken van de resolutie van het rekenrooster en de orde van de methode.

Er is een foutenanalyse uitgevoerd waarin de integraalnorm is bepaald met een numerieke integratie waarin het aantal punten veel groter is dan het aantal punten van het rekenrooster, dit om een nauwkeurigheid van de benadering van de integraalnorm op te voeren. Deze analyse laat zien dat de methode convergeert als h^{p+1} voor polynoom basis functies van orde 1, 2 en 3. Voor $p = 1$ is de convergentiesnelheid iets hoger dan $h^{p+1/2}$. Dit is in overeenstemming met de waarden gevonden in de literatuur. Het is opmerkelijk dat, voor de hs beschouwd, de fout voor de $p-$de orde methode altijd kleiner is dan die voor de $(p - 1)$-ste orde methode. Het is ook geconstateerd dat in geval dat er minder punten worden gebruikt voor het benaderen van de L_2-norm, bijvoorbeeld het aantal punten van het fijnste of van het grofste rekenrooster, de convergentiesnelheid van de $p = 1$ methode gelijk is aan h^3, hetgeen de suggestie wekt dat de benadering van die specifieke norm gebruik maakt van speciale punten, namelijk punten die dicht bij de punten liggen waar de numerieke oplossing de analytische oplossing snijdt.

In de numerieke methode wordt gebruik gemaakt van het "low-storage" 4-staps Runge-Kutta tijdsintegratieschema. Een studie naar de afhankelijkheid van de fout van de tijdstap heeft aangetoond dat de implementatie van de tijdsintegratie in de huidige DG-methode is inderdaad vierde-orde nauwkeurig is in tijd.

Als gevolg van de numerieke benaderingen in de methode genereert de huidige rekenmethode zwakke golven met een kleine amplitude. Deze golven hebben hun oorsprong in discontinuïteiten (in functiewaarde, eerste afgeleide) in de golf die als beginwaarde wordt gekozen. Uitgaande van zulke discontinuteiten ontspringen er pseudo-akoestische golven die zich met een hogere snelheid voortplanten dan de geluidssnelheid. Het kon worden gedemonstreerd dat de voortplantingssnelheid van deze golven voldoet aan de dispersierelatie van de huidige methode, zoals die is afgeleid door Blom in een eerder proefschrift.

Het testgeval van de akoestische radiatie van een bewegend wandsegment in een kanaal is gebruikt als tweede verificatie, via de vergelijking van de resultaten van de huidige methode met de methode van Blom: de DG methode geïmplementeerd voor niet-gestructureerde rekenroosters bestaande uit tetrahedra. De conclusie van deze vergelijking is dat de huidige methode voor rekenroosters bestaand uit hexahedra is sneller voor $h \to 0$ dan de methode voor rekenroosters bestaande uit tetrahedra. Om een indruk te krijgen van het effect van de vervorming (afwijking van orthogonaliteit) van het rekenrooster op de nauwkeurigheid van de numerieke oplossing zijn twee soorten vervorming bestudeerd: scheve rekenroosters en oorspronkelijk orthogonale rekenroosters waarvan de coordinaten van de roosterpunten random zijn verstoord.

Deze studie laat zijn dat de huidige methode onregelmatigheden in het rekenrooster aankan, maar dat de nauwkeurigheid van de oplossing afhangt van de grootte van de onregelmatigheid.

Als validatie wordt het testgeval bestudeerd van een generiek probleem van een akoestisch-gedempte wand ("acoustic liner"). Het betreft een vlakke plaat met een spleet, geplaatst in een kanaal. De plaat is in het midden van het kanaal geplaatst. De spleet is halverwege het kanaal en de richting van de spleet is loodrecht op de middellijn van het kanaal. Vanuit beide einden van het kanaal wordt een akoestische golf het kanaal ingestuurd. De tijdsafhankelijke voortplanting en diffractie van de randen van de spleet wordt numeriek gesimuleerd en resultaten worden vergeleken met de analytische oplossing verkregen door Kooijman. De resultaten betreffen onder meer de verhouding van de amplitude van de gereflecteerde golf en die van de getransmitteerde golf. Voor het geval zonder hoofdstroming wordt een goede overeenstemming tussen de analytische en de numerieke resultaten bereikt. Voor het geval met stroming worden de numerieke resultaten vergeleken met die voor het geval zonder hoofdstroming.

ACKNOWLEDGMENT

This thesis is the result of research carried within the Engineering Fluid Dynamics group at the University of Twente during an important period of my life. During this period a number of people have made a contribution to this work who I owe many thanks for their involvement.

First of all I would like to express my sincere gratitude to my promotor Harry Hoeijmakers. I am grateful for your support, guidance and advice over the past years. You also gave me an opportunity to get all the experience of living in this beautiful country which I felt its beauty day to day. I would like to thank Mico Hirschberg not only because he put an additional effort in my thesis as being my co-supervisor but also being one of the milestones to help me start this not so short adventure towards the Netherlands. I do appreciate his two key advices directing me first to Jerome Anthoine in von Karman Institute in Belgium and then to Steve Hulshoff in Engineering Fluid Dynamics group at the University of Twente. Furthermore, I am very grateful to Rob Hagmeijer for his support and guidance throughout this work.

Gratefully I like to acknowledge TNO TPD, Delft, the Netherlands, for sponsoring the research on aeroacoustics in our group at the University of Twente. Jan Bruggeman and René Parchen were the initiators of this enterprise. This research has been part of the collaboration within the TNO/UT "Kenniscentrum Geluid en Trillingen". During the course of my PhD study there have been contacts with many people of TNO TPD, who I all thank for the pleasant collaboration. Especially, I would like to thank Eric Védy, always enthusiastic, very dedicated and more than willing to cooperate.

I would like to thank the staff, fellow PhD students and MSc students of Engineering Fluid Dynamics group for providing an enjoyable working environment and for their direct or indirect contribution to this work.

Finally, I would like to thank to my parents and my family back in Turkey for

opening the path to build my career. My last words go to two dearest people in my life. Belgin and Duru thank you very much for all your patience and support during this long and tough period.

ABOUT THE AUTHOR

Hüseyin Özdemir was born on March 3, 1973 in Sivas Turkey. The author attended secondary school in Istanbul and started studying Mechanical Engineering at University of Istanbul. After obtaining his bachelors degree after four years he has started his MSc. studies within the same university, under the supervision of Prof. Dr. C.R. Kaykayoğlu, on the topic of computational heat and mass transfer. He completed this study with the thesis entitled: the computer aided simulation of a temperature distribution in cabin of a bus on ride.

In October 1998 he has started his post graduate course in Von Karman Institute for Fluid Dynamics in Brussels, Belgium. He has carried out his project work about an unsteady numerical simulation of vortex generation behind an obstacle and graduated in June 1999.

Hüseyin started his research work within Engineering Fluid Dynamics group at University of Twente where he later on continued as a Ph.D. student under supervision of prof. dr. ir. H.W.M. Hoeijmakers and co-supervision of prof. dr. ir. A. Hirschberg which has resulted in this thesis. Hüseyin has attended several courses during his studies from which he obtained certificates. In September 1997 he has attended the Lecture Series 'Aeroacoustics and Active Noise Control' of the von Karman Institute for Fluid Dynamics in Belgium. In June 2000 he participated in the two-weeks course on 'Sound-Flow Interaction' in Institut d'Études Scientifiques de Cargése in France, which was organized by Y. Aurégan, A. Maurel, V. Pagneux and J.-F. Pinton (the lectures of this course is published in: 'Sound Flow Interaction', Aurégan et al. (Eds.), Springer-Verlag, Berlin Heidelberg, 2002). Hüseyin has also attended two JMBC-courses; 'Computational Fluid Dynamics 3' in Enschede and 'Aero-Acoustics' in Eindhoven, the Netherlands.

Hüseyin is married to Belgin and they have a daughter, Duru, who was born in may 4th 2002.